Structure-Property Correlations in Fluoride-Sulfate-Phosphate Glasses

Kumulative Dissertation

zur Erlangung des akademischen Grades doctor rerum naturalium

(Dr. rer. nat.)

vorgelegt dem Rat der Chemisch-Geowissenschaftlichen Fakultät der

Friedrich-Schiller-Universität Jena

Von M. Ing. Quyen Huyen Le

Geboren am 02.02.1983 in Soc Trang, Viet Nam.

Dissertation, Friedrich-Schiller-Universität Jena, 2020

Gutachter:

1. Prof. Dr.-Ing. Wondraczek, FSU Jena, Jena, DE
2. HDoz. Dr. Doris Ehrt, FSU Jena, Jena, DE

Tag der Verteidigung: 27. Februar 2020

Content

Acknowledgements iii

LIST OF ABBREVIATIONS AND SYMBOLS iv

List of Table vi

List of Figure vii

1 Introduction 1
  1.1 General introduction and objective 1
    1.1.1 Definition of glass 1
    1.1.2 The glass transition 2
    1.1.3 Common commercial glass types and their applications 3
    1.1.4 The purpose and scope of the investigation 5
  1.2 The structure of phosphate and fluoroaluminate -phosphate glasses 6
    1.2.1 Phosphate network structure 6
    1.2.2 Fluoroaluminate-phosphate network structure 8
  1.3 Cu^{2+} as probe ions in oxide and mixed oxide/fluoride glasses 10
  1.4 Ionic conduction in glasses 11
    1.4.1 Conduction mechanism 11
    1.4.2 Model of ionic conduction in glass 13
2 Experimental 13
  2.1 Glass compositions and physical properties 13
  2.2 Analytical Methods for Structural Analysis 20
    2.2.1 Ultraviolet–visible (UV-Vis) spectroscopy 20
    2.2.2 Raman spectroscopy 20
    2.2.3 Infrared spectroscopy 21

2.2.4 NMR spectroscopy 21

2.2.5 EPR spectroscopy 21

3 Results and Discussion 22

3.1 Effect of structural change in fluoride-sulfate-phosphate glasses on copper doped and their electrical conductivity 22

3.1.1 NAPFS glasses $(100 - x - y)\text{NaPO}_3/x\text{AlF}_3/y\text{Na}_2\text{SO}_4$ (x = 0–40, y = 0–30) 22

3.1.2 FPS glasses $(100 - x - y)\text{MF}_n/x\text{Sr(PO}_3)_2/y\text{SrSO}_4$ (x = 10–20, y = 3–20) 23

3.1.3 Cu^{2+} in FPS glasses 24

3.1.4 Electrical conductivity in NAPFS glasses 26

3.2 Index of publications 27

3.2.1 Formation, structure, and properties of fluoro-sulfo-phosphate poly-anionic glasses 27

3.2.2 Fluoride-sulfophosphate glasses as hosts for broadband optical amplification through transition metal activators 45

3.2.3 Spectroscopic properties of Cu^{2+} in alkaline earth metaphosphate, fluoride-phosphate and fluoride-phosphate-sulfate glasses 55

3.2.4 Optimization of electrical conductivity in the Na_2O-P_2O_5-AlF_3-SO_3 glass system . 65

4 Summary 104

5 Zusammenfassung 106

6 Bibliography 109

Acknowledgements

Firstly, I would like to express my deepest appreciation to my advisor Prof. Dr. Lothar Wondraczek, who continuously encourages and assists in regard to research. His motivation, patience, immense knowledge and guidance helped me during the experiments and while preparing the papers as well as the thesis. Without his guidance and persistent help this dissertation could not have been completed.

Secondly, I gratefully acknowledge the financial support from Vietnam government (Project 911) for my living cost during my Ph.D. research.

In addition, I want to express my thanks to my coworkers at the Otto Schott Institute of Materials Research, both the current (Courtney, Ferdinand, Sindy, Nutty, Omar, Yang, Ru, Elham, Thien, René, Mariana, Aaron, Peter, Chia-en, Zhang) and former (Kristin, Jelena, Weichao, Arnulf, Benjamin, Caio, Bruno, Felix). It was fantastic to have the opportunity to work and discuss majority of my research with all of you. Particularly, I would like to acknowledge Prof. Doris Möncke, Prof. Efstratios I. Kamitsos, Dr. Doris Ehrt, Prof. Delia S Brauer for their lectures and many fruitful discussions about glass structure. Furthermore, I am very grateful to Mrs. Ute Böttger for her encouragement and help in my life and Mrs. Gabriele Möller for her patience to prepare and polish a great number of my glasses. I also want to express my thanks to the laboratory technicians Nadja Büchert, Christian Zeidler, Dietmar Güttler, Claudia Siedler, Steffi Ebbinghaus, Thomas Kittel for their technical assistance.

Finally, a very special gratitude goes out to my highly beloved parents (Quyen Ton Le and Ha Thi Do) and older brothers (Trung Nam Le and Kien Trung Le), especially my beloved husband (Thien Si Le), who have provided me through moral and emotional support in my life. I also want to thank my “little angel” Trí Trí who gave me the most powerful motivation to complete this dissertation. I dedicate this work to them, because none of my achievements would be possible without their generous love, encouragement, support and patience.

LIST OF ABBREVIATIONS AND SYMBOLS

Abbreviations

ASTM	American Society for Testing Materials
DBO	Double-bonded oxygen
BOs	Bridging oxygens
NBOs	Non-bridging oxygens
MP	Metaphosphate
FP	Fluoride phosphate
FPS	Fluoride phosphate sulfate
NAPF	Sodium aluminum fluoride phosphate
NAPFS	Sodium aluminum fluoride phosphate sulfate
UV-Vis-NIR	Ultra-violet, visible and near infra-red
EDX	Energy-dispersive X-ray
IR	Infrared
MAS	Magic-angle-spinning
NMR	Nuclear magnetic resonance
EPR	Electron Paramagnetic Resonance

Symbols and units

T_m	Melting point [K]
T_g	Glass transition temperature [K]
$g_\parallel$	Parallel to a unique symmetry axis
$g_\perp$	Perpendicular to a unique symmetry axis
$A_\parallel$	Hyperfine coupling constant parallel to a unique symmetry axis [G]
$A_\perp$	Hyperfine coupling constant perpendicular to a unique symmetry axis [G]
σ	Electrical conductivity [S/cm]
μ	The mobility of ions (charge carriers)
Ze	Electric charge
n	The volume concentration [mol/cm^3]
n_c	The concentration of mobile carriers
N_0	The total number of mobile ions
k_B	Boltzmann's constant
T	the absolute temperature [K]
ΔE_{crn}	The creation energy of mobile carriers [eV]
D	The diffusion coefficient
d	The ionic jumping distance
υ_0	The thermal vibration frequency
ΔE_{mig}	The migration energy [eV]
ΔE_{act}	The activation energy [eV]
ρ	The density [cm^3/mol]
B	The magnetic field.

List of Table

Table 1-1 Compositions, properties and applications of silica, borosilicate, soda-lime silicate and phosphate glasses. 4

Table 2-1 Transition temperature T_g and density ρ of all investigated glasses with their nominal compositions (mol%) and synthesis conditions. 15

Table 2-2 The nominal composition and true composition analyzed after the melt of the FPS and NAPFS glasses 19

List of Figure

Figure 1-1 The volume-temperature diagram for a glass-forming liquid[1] 3
Figure 1-2 Schematic structure of phosphate glass. 7
Figure 1-3 Schematic structure of phosphate glass after addition of modifier oxides (Na_2O and CaO).[12] 7
Figure 1-4 Schematic structure of FP glasses 9
Figure 1-5 Schematic structure of NAPF glasses 10
Figure 1-6 Schematic structure of sodium phosphate glass 13
Figure 2-1 The process of experiment and analysis of samples. 14
Figure 2-2 Splitting of the energy levels of Cu^{2+} in octahedral, tetragonal and rhombic fields. 20
Figure 3-1 Schematic structure of NAPFS glass 23
Figure 3-2 Schematic structure of FPS glass 24
Figure 3-3 Cu^{2+} absorption wavelengths correspond to the optical basicity of MP, FP and FPS glasses. 25

1 Introduction

1.1 General introduction and objective

1.1.1 Definition of glass

Before learning how to make glass, people used naturally occurring glasses, especially obsidians (volcanic glasses). Obsidians were utilized for the production of knives, arrowheads, and jewelry. These glasses were formed from the cooling process of molten rock, or lava, and like many naturally occurring minerals, contain a wide variety of components, including alkali, alkaline earths, and transition metal oxides. Yet for every specimen, silica is the main constituent found in these materials.

Archaeologists have found evidence of furnaces depicted on the pottery of ancient Egypt (4000 years old), which signifies the birth of glass produced by man. Throughout most of human history, it can be found that like mother earth (*e.g.* obsidian), mankind also used silica as a required component of glass and, again like the molten lava of the earth, manmade glasses were traditionally formed by cooling from a melt. In modern times glass is defined as "an inorganic product of fusion which has been cooled to a rigid condition without crystallizing" by the American Society for Testing Materials (ASTM).[1] Even this definition is too restrictive, as several other types of glassy materials have been discovered and invented (organic molecules, oligomers, and polymers, chalcogenides, ionic and metallic)[2], and are synthesized and processed in various techniques without of fusion (chemical vapor deposition, sol-gel).[2-4] As a result of this explosion in compositions and manufacturing techniques, and consequent glass' property development, glasses are utilized daily in a wide variety of fields, such as architecture, industrial equipment, medicine, electronics, data transmission and storage, foodstuffs, vessels and containers, agriculture and insulation, among many others.

Therefore, a general and broader definition of glass is also designed to accord with these developments, glasses are amorphous solids that show a glass transition regardless of their preparation method.[1, 5] Amorphous solids are disordered materials in which the atoms and molecules are not organized in a definite lattice pattern. They possess no long-range translational order (periodicity), as characteristic of a crystal. Thus, glass is a subset of all amorphous solids constrained by this definition.

1.1.2 The glass transition

When an amorphous material changes from a solid-state to a liquid state on heating or from a liquid to a solid-like state on cooling, if these thermal processes exhibit sudden changes in the derivative of thermodynamic properties (i.e., heat capacity and thermal expansion), this phenomenon is called glass transition.[6]

If a small volume of material is considered at a high temperature in liquid form. This state is represented by the point “a” on the volume-temperature (V-T) diagram (Fig. 1-1). During cooling, one of two events can happen: either crystallization can occur at the melting point T_m or the liquid will become supercooled liquid on below T_m.

The gradual shrinking of the liquid volume occurs in along the cooling path “abc”. The melting point T_m at the point “b” corresponds to the temperature at which the solid and the liquid states have equal vapor pressure or equal Gibbs free energy. The crystallization process happens in two steps as the melt cools (i) the appearance of nuclei in the mass, followed by (ii) a crystal growth stage. If both steps are kinetically favoured compared to the cooling rate, bulk crystallization will occur. This process is described by an abrupt decrease in volume at T_m along line “bd”. Upon further cooling, the volume continues shrinking along the crystalline line to the point “e”.

In the absence of crystallization below T_m, the liquid mass becomes a supercooled liquid along the path “bcf”, which is an extrapolation of the line “abc”. As cooling continues, the viscosity of the system increases dramatically, and the molecules become less and less mobile. The relationship between the solid volume and temperature then will no longer have the slope of the starting line “bcf” and soon becomes a near-straight line (often approximately parallel to the crystalline “de”), ending at point “g” if cooled fast, or at point “h” if cooled more slowly. The region where the change of slope occurs is termed the “glass transition temperature” T_g. It can be seen from Figure 1-1, clearly, the difference in cooling rates from the molten liquid causes a shift in the position of the T_g. Slower cooling rates gives lower T_g (T_g1) whereas faster cooling gives higher T_g (T_g2).[7] Thus, the characteristics of glass depend on the process by which it is formed.

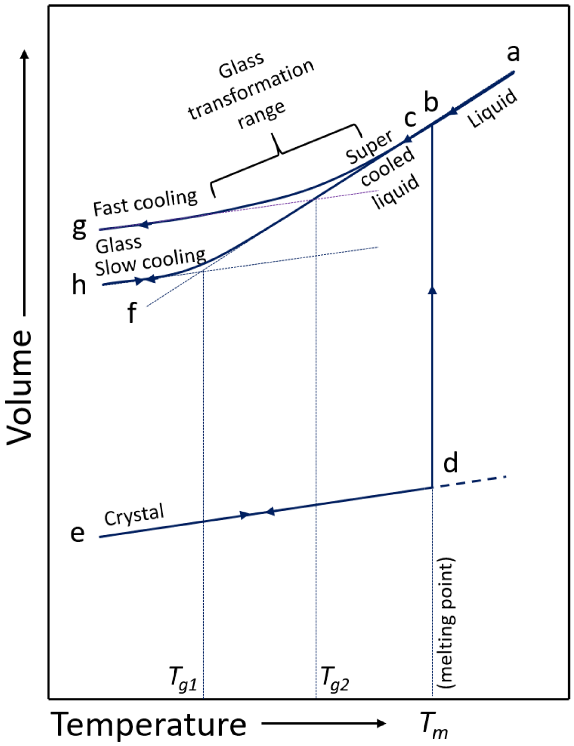

Figure 1-1: The volume-temperature diagram for a glass-forming liquid.[1]

1.1.3 Common commercial glass types and their applications

In commercial glass manufacturing, several glass compositions are commonly used such as silica, borosilicate, soda-lime silicate, and phosphate glasses. Depending on their compositions, glasses exhibit different physical, chemical, and optical properties. Some compositions, properties, and typical applications are shown in detail in Table 1-1.

Table 1-1: Compositions, properties and applications of silica, borosilicate, soda-lime silicate and phosphate glasses.

Glass type	Primary components	Properties	Applications
Silica	SiO_2	- Can withstand high temperatures. - High chemical durability. - High thermal shock resistance. - High radioactive radiation resistance. - Low coefficient of thermal expansion - Very low electrical conductivity.	- Semiconductor fabrication furnaces - In telescopes as surface mirrors - Optical glasses
Borosilicate	SiO_2, at least 5% Boric acid	- Can withstand high temperatures. - Chemical corrosion resistance. - High thermal shock resistance. - High hydrolytic resistance. - Low coefficient of thermal expansion. - Better thermal shock resistance. - Chemical durability. - Higher electrical resistivity.	- Industrial equipment. - Laboratory glassware as beakers, test tubes and conical flask. - Kitchen utensils (especially microwave glass cookware due to its resistance to heat) - Optical glasses
Soda-lime silicate	SiO_2, Na_2O, CaO	- High mechanical strength - High thermal shock resistance - Chemically stable - Hard	- Windows (flat glass) and containers. - Commonly used for beverages, food and pharmaceutical containers. - Used for glass recycling. - Optical glasses - Light bulbs - Art objects.
Phosphates	P_2O_5	- Low chemical resistance (except high resistance to hydrofluoric acid) - Some of this type of glass are soluble in water and biocompatible - Low glass transition temperature of 365°C - Lower thermal conductivity. - Lower optical damage.	- Bone transplants - Optical glasses - Heat absorbers.

1.1.4 The purpose and scope of the investigation

Nowadays, the progress of the optical industry is essential for the strong development of research activities in virtually all technologies, and therefore, in the end, essential for modern life in general. The optical industry requires glass compostions with high reproducibility and homogeneity. Optical glass as a practical product was first shaped around 130 years ago by the fortuitous collaboration of chemist Otto Schott and physicist Ernst Abbe, both at Jena.

All of the above-mentioned glass compositions exhibit useful optical properties and have been instrumental to the development of optics industry today. However, phosphate glasses were of more interest in this project because they generally have high thermal expansion coefficients, low transition temperature, low optical dispersion, high refractive indices and high electric conductivity compared to silicate and borate glasses.[8] Phosphate glasses have found a wide range of applications in glass-to-metal seals, sensing and laser technologies, optical data transmission, solid state batteries, and bio-compatible materials.[9-12]

In addition, more than silicate or borate glasses, phosphate can much more easily incorporate fluoride to form a good glass. Many studies have shown that fluoride glasses are characterized by low refractive index, an exceptional partial dispersion and high transmission from the ultraviolet (UV) to the infrared (IR) range.[13-16] These properties are attractive glasses for special optical applications.[16-18] However, compared to the standard oxide, fluoride glasses are an atypical network-forming anion and because of their high tendency towards crystallization,[16, 18-20] can be very difficult to form glass, which limits their wider utilization in applications. In order to avoid crystallization, special techniques are required for glass preparation. The strong ionic character of fluoride glasses leads to these disadvantages, thus, phosphate glasses with covalent 2d chains of corner-sharing PO_4 tetrahedra forming a polymer-like structure are a good choice to combine with fluoride glasses to improve glass forming ability. [16, 20-22] Literature has shown that small amounts of phosphates drastically increases not only the chemical durability but also the glass-forming ability of fluoride–phosphate glasses in comparison to pure fluorides,[16, 18-20, 23] while the important optical characteristics of the fluoride glass can be retained to a large extent.[24]

Moreover, phosphate glasses possess high solubility for secondary anion species such as sulfate, fluoride or nitride ions and enable the preparation of poly-anionic glasses. In this study, we consider fluoro-sulfo-phosphates. Equimolar secondary anion mixing in this system can be achieved without notably compromising the glass-forming ability. Their surprising stability to crystallization enables the fabrication of bulk samples without rapid quenching techniques.

The aims of this project were to study the formation, structure, and properties of fluoro-sulfo-phosphate poly-anionic glasses as well as investigate their optical properties and electrical conductivity. Especially, the broadly tunable interionic competition between the varying anion species provides an interesting variety of ligand situations leading to a wide variety of physical properties. These glass systems containing multiple anions hold promise as a novel class of laser gain media, for nonlinear optical applications, or for encapsulating crystalline phases, e.g., in solid-state light sources.

1.2 The structure of phosphate and fluoroaluminate -phosphate glasses

The structural information of the studied glasses as provided by Raman, infrared and, standard magic angle-spinning (MAS) NMR spectroscopy is presented in Sections 3.2.1 and 3.2.4, but first a brief summary of the fundamental glass structure theory will be given below.

1.2.1 Phosphate network structure

P_2O_5 is considered a good glass network former as it can form a glass itself. However, vitreous (v-)P_2O_5 is extremely hygroscopic, thus it is difficult both to prepare and keep water free during an experiment. (v-)P_2O_5 glass network is formed by a pattern of corner-sharing PO_4 tetrahedra, as is the case for all other phosphate glasses.[25-28] These groups are linked to adjacent units by covalent P–O–P bonds through three of their four oxygen atoms, because the remaining oxygen atom is a terminal, double-bonded oxygen atom (DBO).[29-30] The oxygens in these P–O–P linkages are commonly called bridging oxygens (BOs). Therefore, vitreous P_2O_5 exhibits a tendency to form a glass in two or three-dimensional networks such as chains, rings or branching networks (Fig. 1-2).[11, 29-30]

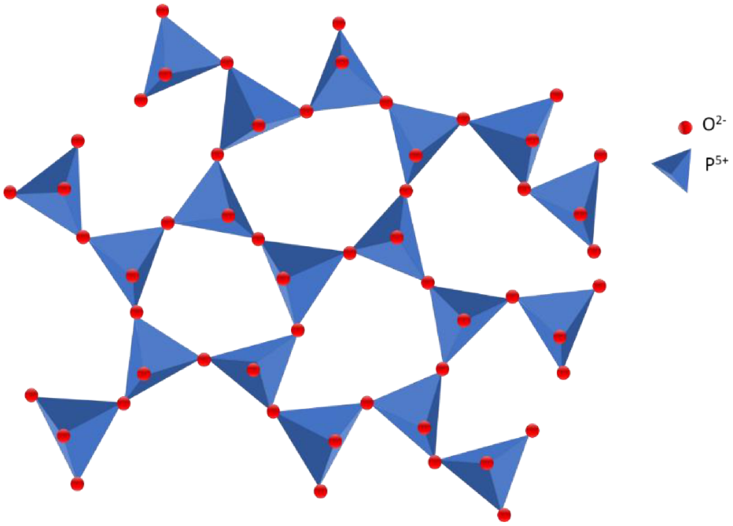

Figure 1-2: Schematic structure of phosphate glass.

Pure P_2O_5 glass is very reactive and hygroscopic, which seriously affects its wider utilization in applications. These weak points can be surmounted by adding other components such as alkali and alkaline earth oxides (called network modifiers). The addition of network modifier oxides (Me_nO) leads to the cleavage of P–O–P linkages (depolymerization of the network) and the presence of non-bridging oxygens (NBOs) in the glass network.[30-31] Consequently, the modified glass structure contains not only covalent P–O–P bonds but also ionic cross-linking between NBOs and modifying cations (Fig. 1-3)

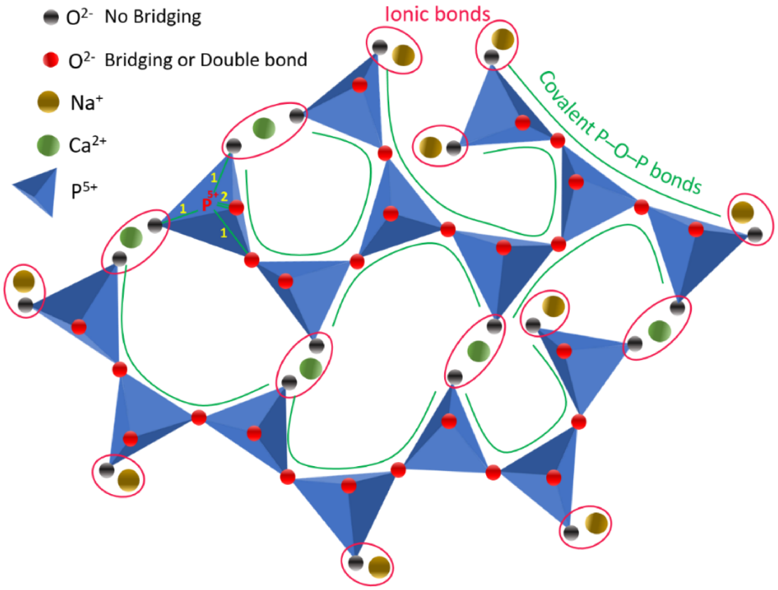

Figure 1-3: Schematic structure of phosphate glass after addition of modifier oxides (Na_2O and CaO).[12]

Depending on the number of modifiers introduced in phosphate glasses, the tetrahedra groups are converted and classified using the Q^i terminology,[32] where *"i"* denotes the number of bridging oxygens per a PO_4 tetrahedron. As the [O]/[P] ratio increases the networks of phosphate glasses can, for example, transform from a 3d cross-linked network of Q^3 tetrahedra (vitreous P_2O_5) to chain-like metaphosphate chains of Q^2 tetrahedra to "invert" glasses composed of short pyro- (Q^1) and orthophosphate (Q^0) anions.[11-12, 33]

1.2.2 Fluoroaluminate-phosphate network structure

The structure and properties of these glasses depend mainly on the molar relation between metal fluorides and phosphates, which can be varied in a wide range between pure metal fluoride and phosphate glasses. Based on the [F]/[P] ratio, glass structures can be formed in the following two was:

1.2.2.1 Fluoride >> phosphate content (FP glasses)
$(100–x)MF_n$ / $x Sr(PO_3)_2$ ($x \leq 20\%$, M = Mg^{2+}, Ca^{2+}, Sr^{2+}, Al^{3+})

Given the special optical properties of FP glasses, they have been studied and melted commercially in the past decades.[20-21, 23-24, 34] Their structural model has been described based on an ionic fluoride network. The fluoride ions favor Al–F over P–F bonds, therefore, mixed chains of $Al(F,O)_6$-octahedra and PO_4-tetrahedra were proposed in these glasses.[20] With small amount of phosphate content in these glass compositions, mostly only orthophosphate (Q^0) and pyrophosphate (Q^1) groups exist in glass network. According to previous publications,[20-21, 23-24, 34] the main network of FP glasses is chains of $Al(F,O)_6$ octahedra, which are connected to phosphate monomers and dimers, and cations. Schema of the FP structural model is illustrated in Figure 1-4.

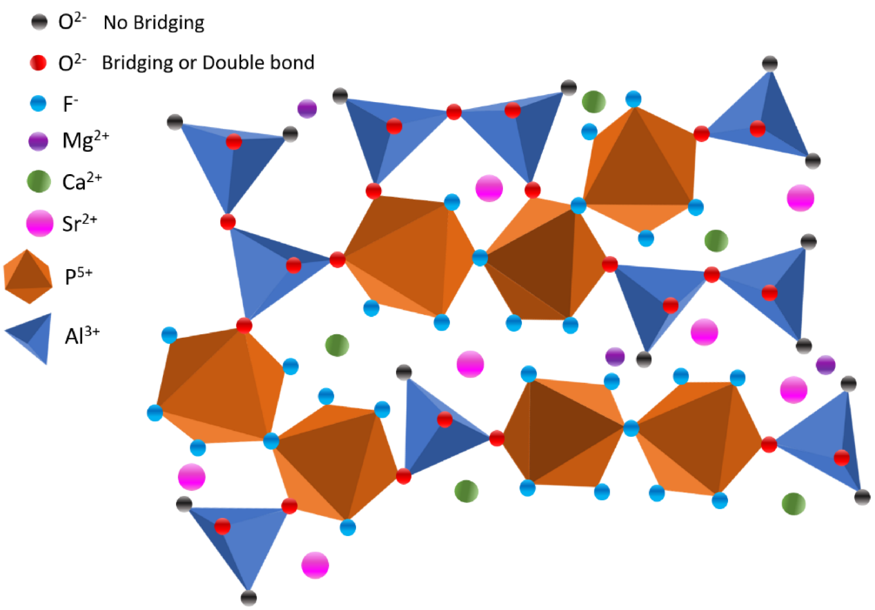

Figure 1-4: Schematic structure of FP glasses

1.2.2.2 Fluoride < phosphate content (NAPF glasses) (100–x)$NaPO_3$ / $x$$AlF_3$ ($x \leq 40\%$)

Contrary to FP glasses, the Raman spectra of glasses with high phosphate contents (NAPF glasses), show that the structure is dominated by metaphosphate chains. AlF_3 additions replace the P–O–P bridges of metaphosphate chains with oxide bridges between phosphate tetrahedra and aluminium octahedra (Al–O–P), which is dominant in both FP and NAPF glasses.[23] Two terminal fluoride types (P–F_T and Al–F_T) and a small amount of a bridging fluoride species (Al–F–Al) were found by ^{19}F MAS NMR in NAPF glasses.[23] The presence of P–F bond was found in NAPF but not in FP glasses.[23] According to Bradtmuller *et al.*,[35] of the six possible bonds in an Al octahedra two to three Al−F and three to four Al−O−P linkages occur in NAPF glasses, independent of AlF_3 content. Depending on the concentration of AlF_3, $Al(F,O)_6$ can link together in the short chains (Al–F–Al bonds, not Al–O–Al) or the octahedra can remain isolated and form bridges between the phosphate groups (Fig.1-5).

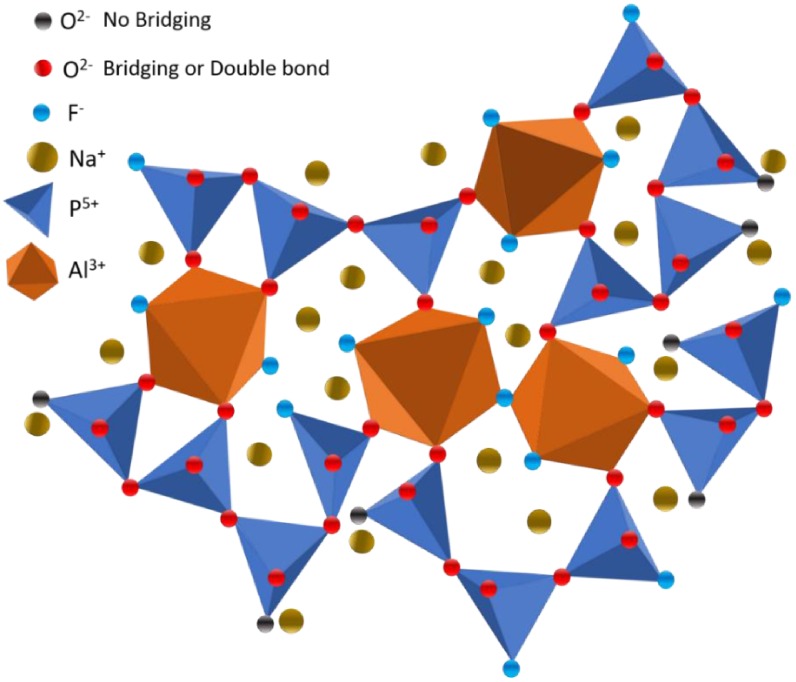

Figure 1-5: Schematic structure of NAPF glasses

1.3 Cu^{2+} as probe ions in oxide and mixed oxide/fluoride glasses

CuO-containing glasses melted in the air (oxidizing conditions) give rise to both the diagmagnetic Cu^+ and paramagnetic Cu^{2+} ions; the redox reaction is described by:

$$Cu^{2+} + O^{2-} \leftrightarrow Cu^{+} + 1/2\ O_2$$

The state of copper ions in oxide glasses has been studied extensively because the glasses containing a large number of copper ions exhibit desriable semiconducting, optical, and magnetic properties which can be important for many potential applications.[36-37] Besides these promising technological applications, studies by Electron Paramagnetic Resonance (EPR) and optical absorption spectra measure the coordination, bonding characteristics and covalency of copper ion environment in glasses which also gives helpful indirect information regarding the structure of the glass network. Simply put, Cu^{2+} is an advantageous probe ion. EPR and optical spectra of Cu^{2+} ions in various glasses have been extensively studied: Changes in the chemical composition of glass may change the local geometry of Cu^{2+} ion sites incorporated into the glass matrix resulting in ligand field changes, which may be reflected in the optical absorption and EPR spectra.[38-46]

Depending on the type of glasses, Cu^{2+} will absorb light from around 750 to 930 nm, and the color of the glasses will be pale blue (cyan).[41, 46-50] The Cu^{2+} ions in oxide glasses are preferentially coordinated with six O^{2-} in an octahedral site with elongated tetragonal distortion (due to Jahn–Teller effect).[41, 46-50] Even in mixed oxide/fluoride glasses, if the oxygen/fluorine ratio is higher than 1, Cu^{2+} ions seem to ignore fluoride ligands, and CuO_6 is also found in a tetragonally distorted octahedral environment.[42, 51] These assumptions are further proven by analyzing data from UV-Vis-NIR and EPR spectroscopies, once UV-Vis-NIR data showed a broad asymmetric absorption band at the red region of the spectrum)[41-42, 46-51] and all parameters $g_{\parallel}$, $g_{\perp}$, $A_{\parallel}$ and $A_{\perp}$ from EPR studies conclude that the coordination sphere is an elongated octahedron.[41-43, 46, 50, 52-55]

However, the conclusions as deduced from UV-Vis-NIR studies and EPR studies in oxide glasses and mixed oxide/fluoride glasses (with $[O]/[F]>1$) are not applicable for mixed oxide/fluoride glasses when the oxygen/fluorine ratio is lower than unity ($[O]/[F]<1$). When $[O]/[F]<<1$ in mixed oxide/fluoride glasses, the site geometry around Cu^{2+} ions has octahedral coordination with rhombic distortion (rather than tetragonal), which is discussed in more details in publication 3.2.3.

1.4 Ionic conduction in glasses

1.4.1 Conduction mechanism

Glasses can be both ionically and electronically conducting, however, for most glasses conduction is solely due to the movement of a single ionic species, anionic or cationic. The conductivity, σ, is related to the mobility of the charge carriers, μ, by[56]

$$\sigma = Zen\mu \tag{1}$$

where n and Ze are the carrier charge concentration and their charge, respectively. This equation shows that the conductivity is proportional to both the ion concentration and ion mobility i.e. how easily an ion moves through the solid.

The most general expression for the concentration of mobile carriers (n_c) in a nondegenerate semiconductor can be written following Maxwell–Boltzmann statistics,[57-58]

$$n_c(T) = N_0 \exp\left(-\frac{\Delta E_{crn}}{k_B T}\right) \tag{2}$$

where N_0 is the total number of possible mobile ions, k_B and T are Boltzmann's constant and the absolute temperature and ΔE_{crn} is the creation energy of mobile carriers. The mobility can be obtained from the diffusion coefficient of the ions by the familiar Nernst-Einstein equation,[57, 59]

$$\mu(T) = \frac{(Ze).D(T)}{k_B\, T} \tag{3}$$

with $D(T)$ is the diffusion coefficient. For an ionic conductor, the ionic jumping distance, d, can be related to the diffusion coefficient by random walk calculation,[56, 60-61]

$$D(T) = d^2\, \upsilon_0\, exp\left(-\frac{\Delta E_{mig}}{k_B T}\right) \tag{4}$$

where υ_0 is the thermal vibration frequency and ΔE_{mig} is the energy that must be overcome for the jump process to take place or in other words, it is the migration energy.

From Eq. (3) and (4) we obtain

$$\mu(T) = \frac{d^2 \upsilon_0 (Ze)}{k_B T}\, exp\left(-\frac{\Delta E_{mig}}{k_B T}\right) \tag{5}$$

Combining Eq. (1), (2) and (5) we obtain

$$\sigma(T) = \frac{N_0\, d^2\, \upsilon_0\, (Ze)^2}{k_B\, T}\, exp\left(-\frac{(\Delta E_{mig} + \Delta E_{crn})}{k_B\, T}\right) \tag{6}$$

And set $\sigma_0 = \dfrac{N_0 d^2\, \upsilon_0 (Ze)^2}{k_B}$

Eq. (6), the dc conductivity, can then be rewritten more simply in the familiar Arrhenius form:

$$\sigma_{dc} = \frac{\sigma_0}{T}\, exp\left(-\frac{\Delta E_{act}}{k_B\, T}\right) \tag{7}$$

Despite a complex pre-exponential factor in Eq. (6), the ionic conductivity of most glasses is dominated by Arrhenius behaviour. The activation energy (ΔE_{act}) includes both the energy required for creation (ΔE_{crn}) and migration (ΔE_{mig}) of mobile charge carriers, which are respectively related directly to the concentration of mobile ion and mobility.

1.4.2 Model of ionic conduction in glass

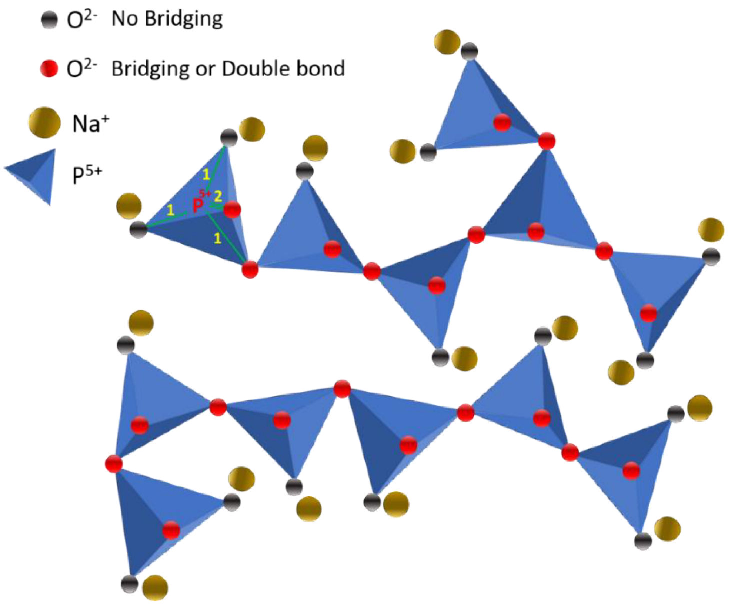

Figure 1-6: Schematic structure of sodium phosphate glass

The ionic transport mechanism in glass can be easily understood from Figure 1-6. The addition of a modifier, e.g. sodium oxide, to an amorphous, constrained phosphate network results in the creation of non-bridging oxygens (NBOs) and disruption of the P–O–P linkages.[30-31] The more Na_2O content introduced into the glass matrix, the more NBOs created. The NBOs are polarized ions and act as coordinating sites for the hopping of the cations (Na^+). Sodium transport only occurs when the glass is put in the presence of an electrical field. In order for electrical conduction to occur, the cation must overcome an barrier energy to move through the material and this barrier energy depends on the glass network. Thus, a change in glass composition will affect the barrier energy as well as electrical conduction in glass.

2 Experimental

2.1 Glass compositions and physical properties

The nominal compositions and synthesis conditions of all glasses studied are summarized in Table 2-1, together with selected physical properties, including the glass transition temperature T_g and density ρ. Here, selected compositions of the FP, NAPFS, and all FPS series were analyzed by energy-dispersive X-ray spectroscopy (EDX) to estimate glass components after melting (shown in Tab. 3). Detailed information on the preparation of the FP glasses were provided by Ehrt *et al.*[21, 24, 34] and the preparation details for the rest of the glasses in this work can be found in publications 3.2.1, 3.2.3 and 3.2.4. The process of glass melting and sample prepration (for analysis) are briefly depicted in Figure 2-1. The glass transition temperatures T_g were measured by differential scanning calorimetry and the densities were determined with the Archimedes method in distilled water (for MP, FP and FPS glasses) and in ethanol (for NAPFS glasses) at RT.

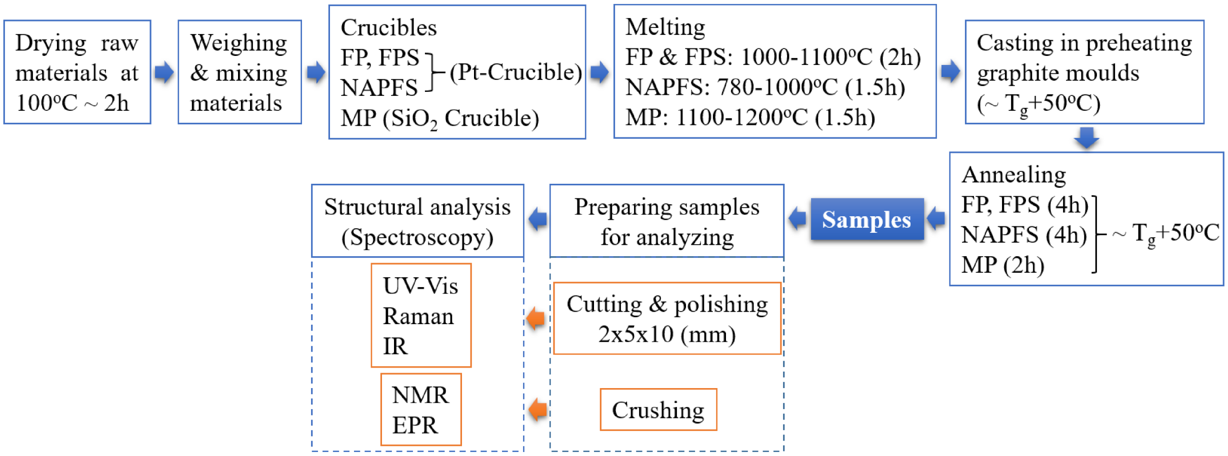

Figure 2-1: The process of experiment and analysis of samples.

Table 2-1: Transition temperature T_g and density ρ of all investigated glasses with their nominal compositions (mol%) and synthesis conditions.

	Symbol	Compositions									Synthesis conditions (°C)	T_g (°C)	ρ (g/cm³)
Glasses were mentioned in publications 3.2.1, 3.2.2, 3.2.3													
Metal Phosphate	**MP**	**MgO**	**CaO**	**SrO**	**BaO**	**P_2O_5**		**CuO**		**Cr_2O_3**			
	MgMP	50	0	0	0	50		0.1			1200, 1.5 h	543	2.437
	CaMP	0	50	0	0	50		0.1			1100, 1.5 h	528	2.645
	SrMP	0	0	50	0	50		0.1			1100, 1.5 h	490	3.130
	BaMP	0	0	0	50	50		0.1			1100, 1.5 h	465	3.620
Fluoride Phosphate	**FP**	**MgF_2**	**CaF_2**	**SrF_2**	**AlF_3**	**$Sr(PO_3)_2$**	**$SrSO_4$**						
	FP0	10	28.3	23.1	38.6	0	0	0.05	or	0.05	1000-1100-1000, 2h	400	3.454
	FP2	9.5	27.8	22.9	37.8	2	0	0.05	or	0.05	1000-1100-900, 2h	429	3.472
	FP3	9.5	27.5	22.5	37.5	3	0	0.05			1000-1100-900, 2h	436	3.467
	FP4	9.5	27.5	21.5	37.5	4	0	0.05	or	0.05	1000-1100-900, 2h	440	3.457
	FP6	9.5	27	21	36.5	6	0	0.05			1000-1100-900, 2h	448	3.478
	FP10*	10	30	15	35	10	0	0.05	or	0.05	1000-1100-900, 2h	461	3.427
	FP15*	10	23.4	19.4	32.2	15	0	0.05	or	0.05	1000-1100-900, 2h	488	3.503
	FP20*	10	21.8	18.2	30	20	0	0.05			1000-1100-900, 2h	485	3.512
Fluoride Sulfate Phosphate	**FPS10***												
	FP7S3	10	30	15	35	7	3	0.05			1000-1100-900, 2h	457	3.471
	FP5S5	10	30	15	35	5	5	0.05			1000-1100-900, 2h	447	3.479
	FP3S7	10	30	15	35	3	7	0.05			1000-1100, 1.5h	432	3.562
	FS10	10	30	15	35	0	10	0.05			1000-1100, 1.5h	400	3.527
	FPS15*												
	FP10S5	10	23.4	19.4	32.2	10	5	0.05	or	0.05	1000-1100-900, 2h	474	3.527
	FP7.5S7.5	10	23.4	19.4	32.2	7.5	7.5	0.05	or	0.05	1000-1100-900, 2h	456	3.531
	FP5S10	10	23.4	19.4	32.2	5	10	0.05	or	0.05	1000-1100, 1.5h	437	3.547
	FS15	10	23.4	19.4	32.2	0	15	0.05	or	0.05	1000-1100, 1.5h	403	3.555
	FPS20*												

	FP15S5	10	21.8	18.2	30	15	5	0.05	1000-1100-900, 2h	470	3.527
	FP10S10	10	21.8	18.2	30	10	10	0.05	1000-1100-900, 2h	451	3.531
	FP5S15	10	21.8	18.2	30	5	15	0.05	1000-1100, 1.5h	430	3.547
	FS20	10	21.8	18.2	30	0	20	0.05	1000-1100, 1.5h	396	3.555
Sodium-Aluminum Fluoride Phosphate	**NAPF***	**$NaPO_3$**	**Na_2SO_4**	**AlF_3**							
	NAPF100	100	0	0					800, 1.5h	289	2.500
	NAPF90	90	0	10					850, 1.5h	311	2.553
	NAPF80	80	0	20					900, 1.5h	325	2.616
	NAPF70	70	0	30					1000, 1.5h	367	2.682
	NAPF60	60	0	40					1000, 1.5h	412	2.753
Sodium-Aluminum Fluoride Sulfate Phosphate	**NAPFS1**										
	NAPF75S5	75	5	20					850, 1.5h	327	2.725
	NAPF70S10	70	10	20					850, 1.5h	330	2.628
	NAPF65S15	65	15	20					850, 1.5h	314	2.624
	NAPF60S20	60	20	20					850, 1.5h	313	2.618
	NAPF50S30	50	30	20					800, 1.5h	288	2.631
	NAPFS2*										
	NAPF70S5	70	5	25					850, 1.5h	336	2.634
	NAPF70S10	70	10	20					850, 1.5h	330	2.628
	NAPF70S15	70	15	15					850, 1.5h	307	2.589
	NAPF70S20	70	20	10					850, 1.5h	298	2.559
Glasses were mentioned in publication 3.2.4											
	NAPFS (Group)	**Na_2O**	**P_2O_5**	**AlF_3**	**SO_3**						
Sodium-Aluminum Fluoride Sulfate	**IA**	44	43	8	5				780, 1.5h	327	2.549
		44	41	8	7				780, 1.5h	328	2.546
		44	38	8	10				780, 1.5h	321	2.552
		44	36	8	12				780, 1.5h	319	2.556
	IB	44	39	12	5				780, 1.5h	339	2.582
		44	37	12	7				780, 1.5h	335	2.582
		44	34	12	10				780, 1.5h	332	2.587

	44	32	12	12	780, 1.5h	331	2.591
IC	44	40	16	0	780, 1.5h	366	2.627
	44	35	16	5	780, 1.5h	360	2.626
	44	33	16	7	780, 1.5h	355	2.629
	44	30	16	10	780, 1.5h	350	2.625
	44	28	16	12	780, 1.5h	347	2.624
ID	44	36	20	0	780, 1.5h	386	2.659
	44	31	20	5	780, 1.5h	380	2.659
	44	29	20	7	780, 1.5h	375	2.657
	44	26	20	10	780, 1.5h	372	2.657
	44	24	20	12	780, 1.5h	369	2.655
IIA	47	45	8	0	780, 1.5h	326	2.549
	47	40	8	5	780, 1.5h	325	2.555
	47	38	8	7	780, 1.5h	322	2.555
	47	35	8	10	780, 1.5h	316	2.566
	47	33	8	12	780, 1.5h	311	2.567
IIB	47	41	12	0	780, 1.5h	334	2.588
	47	36	12	5	780, 1.5h	341	2.599
	47	34	12	7	780, 1.5h	337	2.597
	47	31	12	10	780, 1.5h	337	2.588
	47	29	12	12	780, 1.5h	330	2.590
IIC	47	37	16	0	780, 1.5h	361	2.627
	47	32	16	5	780, 1.5h	356	2.632
	47	30	16	7	780, 1.5h	352	2.633
	47	27	16	10	780, 1.5h	353	2.627
	47	25	16	12	780, 1.5h	349	2.627
IID	47	33	20	0	780, 1.5h	397	2.667
	47	28	20	5	780, 1.5h	380	2.664
	47	26	20	7	780, 1.5h	367	2.657
	47	23	20	10	780, 1.5h	362	2.649

	47	21	20	12	780, 1.5h	358	2.648
IIIA	50	42	8	0	780, 1.5h	328	2.566
	50	37	8	5	780, 1.5h	326	2.566
	50	35	8	7	780, 1.5h	324	2.566
	50	32	8	10	780, 1.5h	317	2.564
	50	30	8	12	780, 1.5h	315	2.567
IIIB	50	38	12	0	780, 1.5h	343	2.606
	50	33	12	5	780, 1.5h	342	2.601
	50	31	12	7	780, 1.5h	343	2.601
	50	28	12	10	780, 1.5h	342	2.600
	50	26	12	12	780, 1.5h	341	2.607
IIIC	50	34	16	0	780, 1.5h	369	2.642
	50	29	16	5	780, 1.5h	369	2.633
	50	27	16	7	780, 1.5h	365	2.627
	50	24	16	10	780, 1.5h	361	2.624
	50	22	16	12	780, 1.5h	348	2.617
IIID	50	30	20	0	780, 1.5h	377	2.664
	50	25	20	5	780, 1.5h	363	2.659
	50	23	20	7	780, 1.5h	361	2.649
	50	20	20	10	780, 1.5h	359	2.644
	50	18	20	12	780, 1.5h	358	2.635
Experimental error						± 2	± 0.005

* Glass composition was analyzed by energy-dispersive X-ray spectroscopy (EDX) after melting.

Table 2-2 lists both the nominal compositions and compositions analyzed by EDX. All the mol percents of MgF_2, CaF_2, SrF_2 and AlF_3 in FPS glasses are rewritten under total MF_n (MF_n=MgF_2+CaF_2+SrF_2+AlF_3). Since a great amount of fluoride evaporates during the melting process,[21, 24] we assume that when fluoride escapes the rest of these metals form bonds with oxygen in glass network (and are assigned as M_2O_n).

Table 2-2: The nominal composition and true composition analyzed after the melt of the FPS and NAPFS glasses

Series	Glass	Written in simple oxides and fluoride compounds (in mol%)								
		Nominal composition				Analyzed after melting				
		P_2O_5	SO_3	SrO	MF_n	P_2O_5	SO_3	SrO	M_2O_n	MF_n
FPS20	FP10	9	0	9	82	10.6	0	11.9	7.3	70.2
	FP7S3	6.3	2.7	9	82	8.3	0.7	12.4	8	70.6
	FP5S5	4.5	4.5	9	82	6.2	1.1	12.7	6.9	73.1
	FP3S7	2.7	6.3	9	82	3.8	1.4	13.3	8	73.4
	FS10	0	9	9	82	0	3.8	14.6	6.9	74.6
FPS15	FP15	13	0	13	74	16	0	15.2	10.2	58.6
	FP10S5	8.7	4.3	13	74	10.4	2	16.1	7.5	64
	FP7.5S7.5	6.5	6.5	13	74	8.1	3.6	15.6	8.3	64.3
	FP5S10	4.3	8.7	13	74	5.2	4.8	16.8	9.2	64
	FS15	0	13	13	74	0	6.5	18.1	7.5	67.9
FPS10	FP20	16.7	0	16.7	66.6	19.3	0	16.7	11.6	52.4
	FP15S5	12.5	4.2	16.7	66.6	14.7	2.3	17	8.4	57.6
	FP10S10	8.3	8.3	16.7	66.6	9.6	6.2	16.7	8.9	58.6
	FP5S15	4.2	12.5	16.7	66.6	5	9.3	17	7.6	61.1
	FS20	0	16.7	16.7	66.6	0	14.4	16.4	8.8	60.3
		P_2O_5	SO_3	Na_2O	AlF_3	P_2O_5	SO_3	Na_2O	Al_2O_3	AlF_3
NAPF	NAPF100	50	0	50	0	49.3	0	50.7	0	0
	NAPF90	45	0	45	10	48.4	0	41.2	2.7	7.7
	NAPF80	40	0	40	20	46.4	0	40.2	3.4	10
	NAPF70	35	0	35	30	41.9	0	36.9	5	16.2
	NAPF60	30	0	30	40	38.7	0	33.3	7.1	20.9
NAPFS	NAPF70S5	31.8	4.5	40.9	22.7	41.8	4.4	40.4	5.3	8.1
	NAPF70S10	29.2	8.3	45.8	16.7	35.9	10	40.4	4.1	9.6
	NAPF70S15	26.9	11.5	50	11.5	35.3	13.9	42.6	2.6	5.6
	NAPF70S20	25	14.3	53.6	7.1	36.1	13.6	43.4	2.3	4.6

For NAPFS glasses, there is no evidence in the ^{19}F NMR of fluorine in an environment like the NaF crystal,[62] so we assume that the fluoride remaining in the glass after melting will link to Al^{3+} and the rest of Al^{3+} will connect to oxygen to become Al_2O_3. Then, it is easy to compare the nominal and real compositions after compositional analysis.

2.2 Analytical Methods for Structural Analysis

2.2.1 Ultraviolet–visible (UV-Vis) spectroscopy

UV-Vis-NIR absorption spectra of Cu^{2+} ion were recorded on a Cary 5000 (Agilent) double-beam spectrophotometer with a spectral resolution of 1.0 nm in the range from 200 to 3000 nm in direct transmission mode. From the obtained spectra, the broad and asymmetric absorption bands of the Cu^{2+} *d-d* transition were deconvoluted by using the Multiple Peak Fit method in Origin. In MP glasses, three bands are expected for the tetragonal distortion of the CuO_6 octahedra due to the energy transitions between orbitals $d_{z^2} \rightarrow d_{x^2-y^2}$, $d_{xy} \rightarrow d_{x^2-y^2}$, and d_{xz}, $d_{yz} \rightarrow d_{x^2-y^2}$. While in FP and FPS glasses, Cu^{2+} exhibited rhombic distortion; $\lambda_{\max,Cu^{2+}}$ bands were fitted with four peaks corresponding to transitions from d_{z^2}, d_{xy}, d_{yz} and d_{xz} to $d_{x^2-y^2}$ (Fig. 2-2).

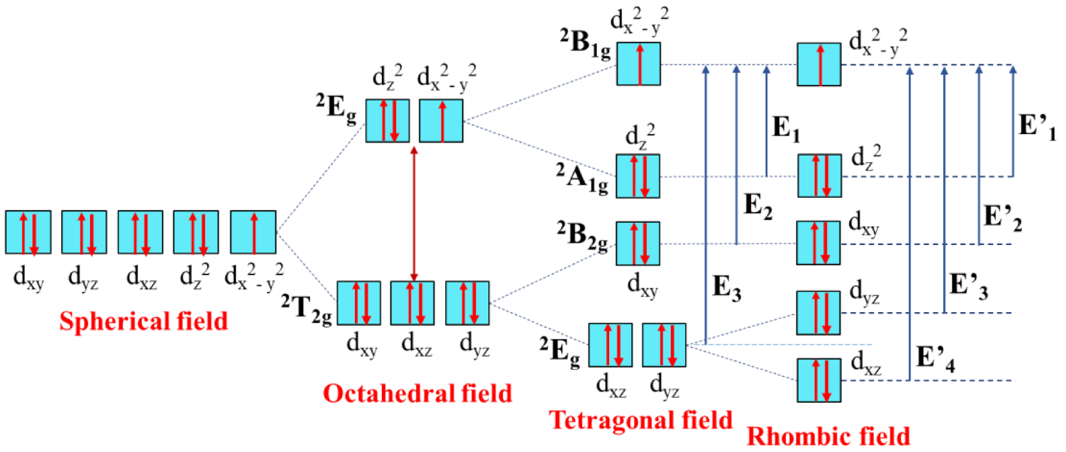

Figure 2-2: Splitting of the energy levels of Cu^{2+} in octahedral, tetragonal, and rhombic fields.

2.2.2 Raman spectroscopy

Both polished and unpolished samples can be measured by Raman spectroscopy to determine vibrational modes of molecules. Micro-Raman spectra were recorded over the spectral range of 50–1500 cm^{-1}, using an excitation wavelength of 514.5 nm in 90° scattering geometry.

The spectra in the region 800 to 1300 cm^{-1} were resolved into nine Gaussian peaks to quantify the Q^n , $Q^n{}_m$ and $SO_4{}^{2-}$ groups.

Low-frequency Raman spectra were collected using a Renishaw InVia micro-Raman spectrometer equipped with a notch filter with performance down to ~9 cm^{-1} and acquired over the spectral range of 10 to 200 cm^{-1}. All glasses show a broad asymmetric peak around 50 cm^{-1}, the so-called Boson peak. This Boson peak is associated with the existence of an intermediate-range order in the glass.

2.2.3 Infrared spectroscopy

Infrared (IR) spectroscopy is complementary to Raman spectroscopy because of differences in some key fundamental ways. Raman spectroscopy depends on a change in polarizability of a molecule, whereas IR spectroscopy depends on a change in the dipole moment. The combination of these two methods becomes a powerful tool when performing materials characterization.

Infrared spectra were obtained in the specular reflectance mode on a Fourier transform vacuum spectrometer across 30–5000 cm^{-1}. The Kramer- Kronig transformation was applied to the IR spectra to obtain the absorption coefficient spectra $\alpha(\nu)$ for further analysis.

2.2.4 NMR spectroscopy

In order to estimate the ratio of each Q^n phosphate groups formed in the glass structure, magic-angle-spinning (MAS) nuclear magnetic resonance (NMR) spectrometer was conducted on a Bruker Avance III 400 (9.4 T magnet, 162 MHz for ^{31}P) with a 4 mm MAS probe. Deconvolution of the ^{31}P MAS NMR spectra was done by dmfit program[63] with four or five Gaussians to quantify the Q^n and $Q^n{}_m$ -species at 1.5, –7.8, –14.2, –20, –26.2 ppm (for NAPFS glasses) and 2, –4.2, –10, –16, –23 ppm (for FPS glasses). Frequency, half-width and intensity were independent and unconstrained variables. The peak areas are quantiatively proportional to the concentration of the respective Q^n and $Q^n{}_m$ -species.

2.2.5 EPR spectroscopy

The technique of electron paramagnetic resonance (EPR) spectroscopy was used to measure the concentration of Cu^{2+} as well as look specifically at the environment and bonding type of Cu^{2+} ions in different glasses.

Measurements were recorded on an EMXmicro CW-EPR spectrometer (Bruker EMX micro EMM-6/1/9-VT control unit, ER 070 magnet, EMX premium ER04 X-band microwave bridge equipped with EMX standard resonator, EMX080 power unit) using powdered samples at room temperature. EPR data were evaluated using the Bruker Xenon software package, version 1.1b86. The SpinCountQ software module was used for quantitative analyses. X-band EPR spectra attributions were conducted on the basis of previous reports on metal phosphates[40, 45, 64-65] and borate glasses.[43-44, 50, 52]

3 Results and Discussion

3.1 Effect of structural change in fluoride-sulfate-phosphate glasses on copper doped and their electrical conductivity

3.1.1 NAPFS glasses $(100 - x - y)NaPO_3/xAlF_3/yNa_2SO_4$ (x = 0–40, y = 0–30)

NAPFS glasses' major component is sodium metaphosphate, thus, (PO_3^{2-}) Q^1 and (PO_2^-) Q^2 are the two main groups in glass network. Depending on the content of AlF_3 and Na_2SO_4 the $[Q^2]/[Q^1]$ ratio will change. For example, $[Q^2]/[Q^1]$ ratio increases with decreasing AlF_3 and Na_2SO_4 concentrations and conversely, this ratio decreases when either the amount of AlF_3 or Na_2SO_4 increases.

Physical properties of NAPFS glasses also depend on the $[AlF_3]$ and $[Na_2SO_4]$. The results in publication 3.2.1 demonstrate that the glass transition temperature T_g, Young's modulus E and volume density of bonding energy U_0/V_0 increase while molar volume V_m and Poisson ratio v decrease with the rising AlF_3 concentration in NAPFS glasses. On the contrary, the addition of Na_2SO_4 in NAPFS glasses leads to opposite trends in all properties. These changes in glass properties are explained based on changes in glass structure.

As AlF_3 is introduced into sodium phosphate, it will depolymerize the phosphate chains (break P–O–P bonds), but simultaneously it connects with phosphate groups to create strong cross-linking Al–O–P bonds between the phosphate tetrahedra. This fact was proved by Raman and ^{31}P-NMR spectroscopies. When increasing AlF_3 content, Raman spectra in NAPF showed that the $\nu_s(PO_3^{2-})$ Q^1 band at 1040 cm^{-1} converts to a Q^1_m peak at 1090 cm^{-1} (m indicates the number of non-bridging oxygen atoms connected to an aluminate polyhedron, P–O–Al linkages).[23, 66] Additionally, ^{31}P-NMR spectra also indicate the growth of new species at higher frequencies with rising AlF_3 concentration. Both of these phenomena are caused by the cleavage of P–O–P linkages and the increasing amount of Q^1_m and Q^2_m units. Five components Q^0_m (m = 0, 1, 2), Q^1, Q^1_m, Q^2 and Q^2_m were fitted in NAPF spectra[35, 67] instead of three components Q^0, Q^1 and Q^2 in pure sodium metaphosphate glass.[68] The strong cross-linkages between aluminum polyhedra and phosphate tetrahedra make a more constrained, rigid glass leading to a higher T_g.

Unlike AlF_3, the authors *Da et al.*[69] reported that sulfur is incorporated into phosphate glasses in the form of isolated SO_4^{2-} groups. We also got the same result when aluminum fluoride – sodium metaphosphate (NAPF) glasses were modified by sulfate ions. Obviously, the lack of covalent bonding between SO_4^{2-} and NAPF glass network leads to loosening of the initial glass structure; with increasing SO_3 content, a less constrained, more compliant glass structure results and decreases T_g.

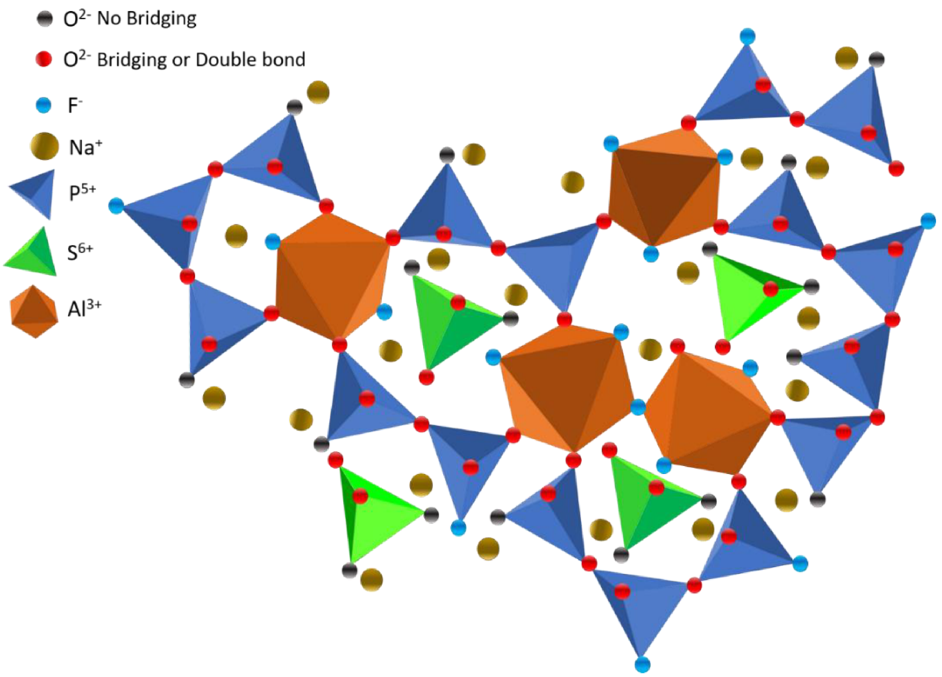

Figure 3-1: Schematic structure of NAPFS glass

3.1.2 FPS glasses (100 – x – y)MF$_n$/xSr(PO$_3$)$_2$/ySrSO$_4$ (x = 10–20, y = 3–20)

Contrary to NAPFS glasses, FPS glasses have much higher fluorine concentration compared to the other glass series, thus, the molecular structure of FPS glasses is based on an ionic metal fluoride network. In the Raman spectra in publication 3.2.1, we can recognize that Q^0 and Q^1 are dominant (with two main peaks at 1000 and 1060 cm^{-1}, respectively) over Q^2 (with very low intensity of shoulder around 1200 cm^{-1}), which is expected because of the low P_2O_5 content.[21, 69-

70] The Q^n-species are linked to fluoroaluminate entities like $Al(F,O)_6$-chains.[23] In FPS glasses, substitution of $Sr(PO_3)_2$ by $SrSO_4$ results in higher network depolymerization and the formation of more Q^0 units.[69] Like NAPFS glasses, this substitution causes a decrease of T_g as well as the decrease in constraints in the glass structure as the sulfate groups form isolated anions (absence of connection between sulfate with phosphate and fluoroaluminate groups of the initial glass).

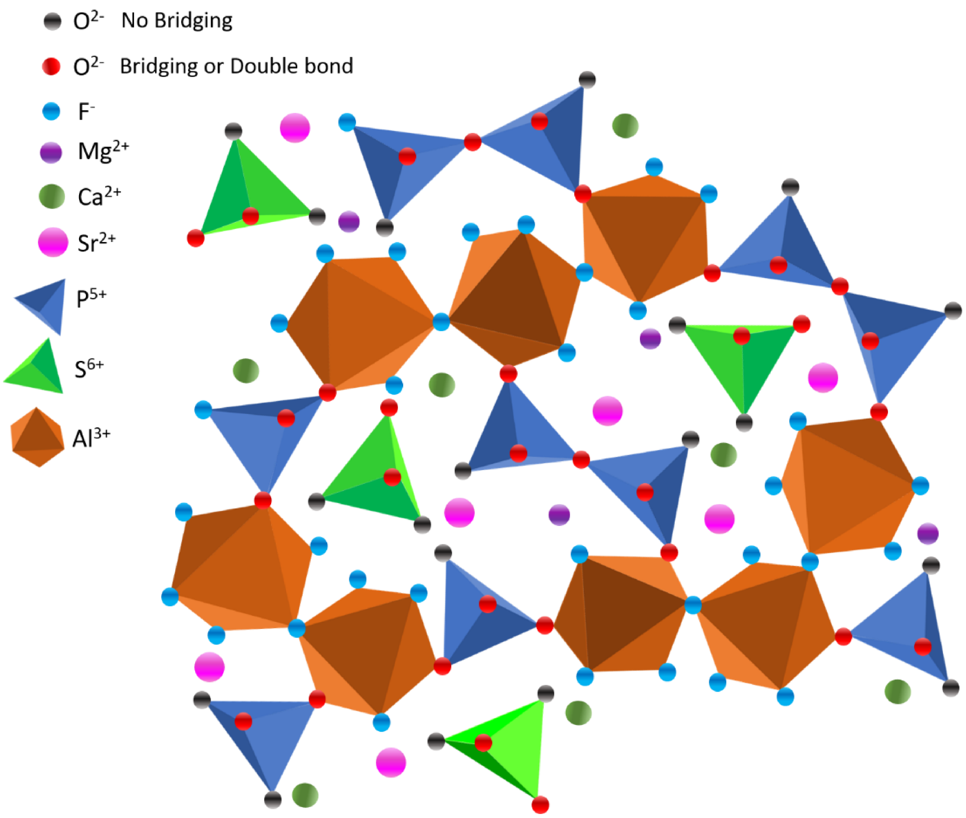

Figure 3-2: Schematic structure of FPS glass

3.1.3 Cu^{2+} in FPS glasses

All glasses were melted at both the same temperature and length of time, therefore, $[Cu^{2+}/Cu^{+}]$ ratio is assumed to depend mostly on glass composition. The results presented within are similar to the other authors[49, 71], where the $[Cu^{2+}/Cu^{+}]$ ratio decreases with increasing of $SrSO_4$ content, i.e., with increasing basicity of the glass.

The $[Cu^{2+}]$ depends mainly on basicity of the glass, however, the maximum absorption wavelength ($\lambda_{max,Cu^{2+}}$) is not influenced by this. The data from Figure 3-3 shows that although the optical basicity from FP0 to FP20 linearly increases with rising P_2O_5 content in the base fluoride glass, the absorption wavelengths are still unchanged from FP4 to FP20. On the other hand, the absorption wavelengths $\lambda_{max,Cu}^{2+}$ in FPS20, FPS15 and FPS10 glasses are shifted to shorter wavelengths when $Sr(PO_3)_2$ was replaced by $SrSO_4$ while their optical basicity only very slightly decreases; we cannot even observe such a small change in optical basicity in Figure 3-3. As mentioned above, phosphate content only occupies small part in FPS glass compositions, thus, Q^3 and Q^2 groups are less prevalent, and the phosphate groups are almost exclusively Q^0 and Q^1 groups. The publication 3.2.3 demonstrates that the $\lambda_{max,Cu}^{2+}$ depends mostly on the number of Q^1 groups: when their percentage is higher than 38%, the absorption spectra centers around 845 nm, yet if the relative amount is lower than 34%, $\lambda_{max,Cu}^{2+}$ depends on the relative amount of Q^1 species in glass matrix. When fewer Q^1 groups are formed in the glass network, the scarcity of Q^1 ligands forces most of the Cu^{2+} ions into mixed F^- /PO_4^{3-}/SO_4^{2-} or F^-/SO_4^{2-} environments, which shifts the absorption spectra to shorter wavelengths. It is clear that Cu^{2+} ions bond preferentially to phosphate Q^1 ligands, which is explained in detail in the publication 3.2.3.

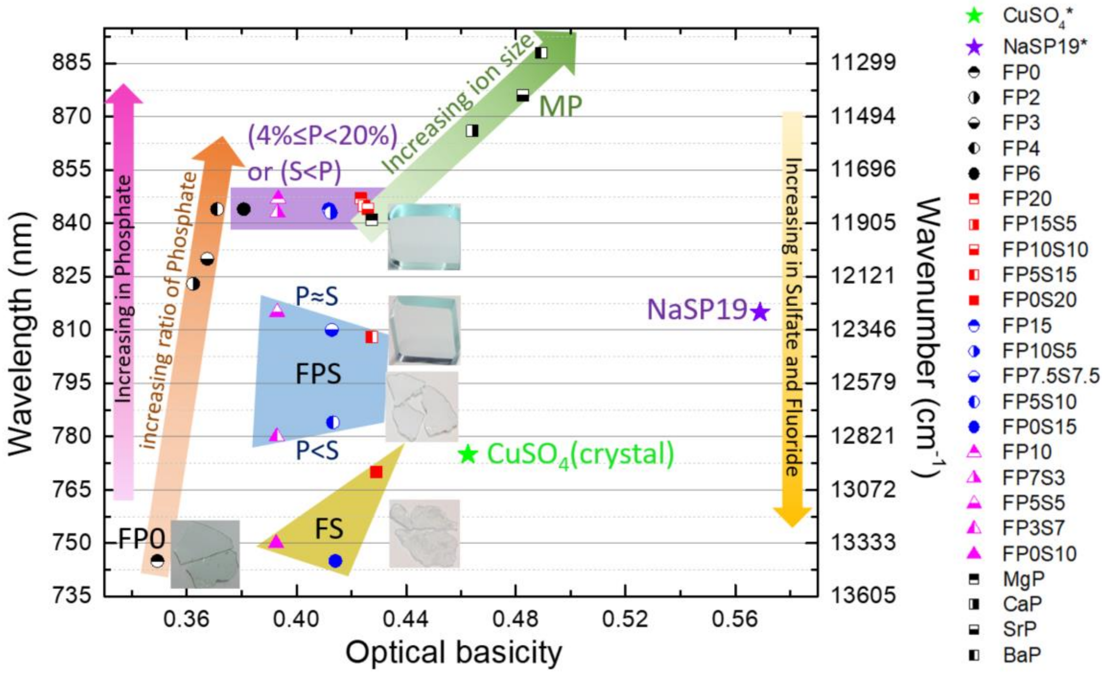

Figure 3-3: Cu^{2+} absorption wavelengths correspond to the optical basicity of MP, FP, and FPS glasses. (*These glasses were melted for references NaSP19 ($19.8Na_2O$-$42.2ZnO$-$19.1SO_3$-$18.9P_2O_5$)[69] and $CuSO_4$).

It is well known that Cu^{2+} is present as an elongated tetragonal distortion of the CuO_6 octahedral coordination in the oxide glass.[47, 72-75] Therefore, the peaks in the optical absorption spectra of Cu^{2+} in the visible range are often asymmetric and broad. They were fitted by three Gaussian curves corresponding to the energy transitions between orbitals $d_{z^2} \rightarrow d_{x^2-y^2}$, $d_{xy} \rightarrow d_{x^2-}$

$_y{}^2$, and d_{xz}, $d_{yz} \rightarrow d_{x^2-y^2}$. In this study, however, both O^{2-} and F^- ligands were available in FP and FPS glasses and the imbalance between these ligands in $Cu(O,F)_6$ octahedral sites causes rhombic distortion instead.[76-77] The Cu^{2+} broad absorption bands were resolved into four Gaussian peaks corresponding to four energy levels $d_{z^2} \rightarrow d_{x^2-y^2}$, $d_{xy} \rightarrow d_{x^2-y^2}$, $d_{yz} \rightarrow d_{x^2-y^2}$ and $d_{xz} \rightarrow d_{x^2-y^2}$. These results match perfectly with the EPR analysis of Cu^{2+} in FP and FPS glasses. EPR spectra express three signals B_1, B_2 and B_3 revealing the rhombic symmetry (rhombic g-values with $g_1 < g_2 < g_3$) of the coordination sphere.[76, 78-79]

3.1.4 Electrical conductivity in NAPFS glasses

At the same temperature, electrical conductivity and activation energy of NAPFS glasses depend mostly on the number of mobile sodium ions and the flexibility of the glass structure. The results in publication 3.2.4 show that for glasses with the same glass matrix, the electrical conductivity is higher and the activation energy is lower for increasing Na_2O content. On the contrary, glasses with differing chemical components and the same Na_2O content have different the conductivities and activation barriers demonstrating the importance of the energy of chemical bonding between Na^+ ions (charge carriers) and the glass matrix.

In sodium metaphosphate glass (Fig. 1-6), we can see that the most Na^+ ions were associated with non-bridging oxygens in Q^2 phosphate chains. Addition of AlF_3 to the sodium metaphosphate glass causes depolymerization of phosphate chains and simultaneously forms $Al(OP)_mF_n$ octahedra, as well as Al−F−Al and P−F bonds (Fig. 3-1).[35] Using the ratio of $NaPO_3$ and AlF_3, the value of m and n in $Al(OP)_mF_n$ were estimated to be on average four and two, respectively; thus, an aluminum octahedra can be considered a pseudo-Q^4 species with four Al–O–P bonds.[35] Consequently, some of the non-bridging oxygens in Q^2 phosphate chains will become linked to $Al^{(6)}$ units, Na^+ ions will be released from the phosphate network and preferentially associate with F^-, resulting in more mobile Na^+. Moreover, Figure 3-1 also illustrates that SO_3 introduced into NAPF glasses leads to the expansion of the initial glass structure (because of the lack of directional bonding between $SO_4{}^{2-}$ and NAPF glass network), which can make the network more flexible, and lower the strain energy of Na^+ ions moving through the material.

From these arguments, one must conclude that the rising concentration of Na_2O, AlF_3, and SO_3 in NAPFS glasses all lead to an increase in electrical conductivity as well as decrease in activation energy.

3.2 Index of publications

3.2.1 Formation, structure, and properties of fluoro-sulfo-phosphate poly-anionic glasses

Q. H. Le, T. Palenta, O. Benzine, K. Griebenow, R. Limbach, E. I. Kamitsos, L. Wondraczek, “Formation, structure, and properties of fluoro-sulfo-phosphate poly-anionic glasses”, J. Non-Cryst. Solids 477 (2017) 58-72.

DOI:10.1016/j.jnoncrysol.2017.09.043

Phosphate glasses exhibit high solubility for secondary anion species. This includes sulfate, fluoride or nitride ions, and enables the preparation of poly-anionic glasses. Here, we consider fluoro-sulfo-phosphates. We show that in this system, even equimolar anion mixing can be achieved without notably compromising the glass-forming ability. The derived glasses exhibit surprising stability, which enables the fabrication of bulk samples mostly without the need to employ rapid quenching techniques. In terms of molecular structure, they rely on primarily ionic bonding among the different constituents, whereby the fluoride and sulfate anions seem to act as stabilizing ionic cross-linkers between highly-depolymerized phosphate entities. Investigation of the low-frequency Raman scattering indicates characteristic variations on intermediate-range structure, where a shift in the Boson peak appears to correlate inversely with increasing sulfate content. We discuss this observation in terms of the low level of bond localization and low field strength of the sulfate anion relative to phosphate Q^0 groups. Adjusting the degree of anion competition enables to tailor super-structural heterogeneity. Beyond this, the glass system provides an interesting variety of ligand situations for the potential incorporation of optically active cation species.

Journal of Non-Crystalline Solids 477 (2017) 58–72

Contents lists available at ScienceDirect

Journal of Non-Crystalline Solids

journal homepage: www.elsevier.com/locate/jnoncrysol

Formation, structure and properties of fluoro-sulfo-phosphate poly-anionic glasses

Quyen Huyen Le[a,b], Theresia Palenta[a], Omar Benzine[a], Kristin Griebenow[a], Rene Limbach[a], Efstratios I. Kamitsos[c], Lothar Wondraczek[a,]*

[a] *Otto Schott Institute of Materials Research, University of Jena, Fraunhoferstrasse 6, 07743 Jena, Germany*
[b] *Can Tho University of Technology, 256 Nguyen Van Cu, Can Tho, Viet Nam*
[c] *Theoretical & Physical Chemistry Institute, National Hellenic Research Foundation, 48 Vassileos Constantinou Avenue, 11635 Athens, Greece*

ARTICLE INFO

Keywords:
Phosphate
Sulphate
Fluoride
Multi-anion
Anion mixing

ABSTRACT

Phosphate glasses exhibit high solubility for secondary anion species. This includes sulfate, fluoride or nitride ions, and enables the preparation of poly-anionic glasses. Here, we consider fluoro-sulfo-phosphates. We show that in this system, even equimolar anion mixing can be achieved without notably compromising the glass forming ability. The derived glasses exhibit surprising stability, what enables the fabrication of bulk samples mostly without the need to employ rapid quenching techniques. In terms of molecular structure, they rely on primarily ionic bonding among the different constituents, whereby the fluoride and sulfate anions seem to act as stabilizing ionic cross-linkers between highly-depolymerized phosphate entities. Investigation of the low-frequency Raman scattering indicates characteristic variations on intermediate-range structure, where a shift in the Boson peak appears to correlate inversely with increasing sulfate content. We discuss this observation in terms of the low level of bond localization and low field strength of the sulfate anion relative to phosphate Q^0 groups. Adjusting the degree of anion competition enables to tailor super-structural heterogeneity. Beyond this, the glass system provides an interesting variety of ligand situations for the potential incorporation of optically active cation species.

1. Introduction

Phosphate glasses count among the archetype classes of oxide glasses [1]. In a first consideration, they can be described through comparably straightforward and now well-validated structural models, where the constitutive building blocks of PO_4 tetrahedral units are interconnected across the oxygen corners. The degree of interconnection, often denoted as the degree of polymerization, depends on the presence of secondary cation species, i.e., the so-called network modifiers. For each positive modifier charge, one bridging oxygen species is transformed into a non-bridging (NBO) species, and there is only little disproportionation. This picture follows Zachariasen's original network hypothesis [2] and has been evolving over the years to include more complex parameters on intermediate structural length scales [1,3–5], and non-linear interactions among cation species [6–9]. Specific interest arises from the presence of the one double-bonded oxygen in the PO_4 tetrahedron. The other three oxygen species are available for cross-linking, following the terminology of Q-groups in which the value of i in $Q^{i\,=\,0\ldots3}$ denotes the number of bridging oxygen species per phosphate tetrahedron. When $i < 3$, the double-bond is delocalized. Polyphosphate glasses comprise of Q^3 and/or Q^2 units which form a network of crosslinked chains of PO_4 tetrahedra. An almost pure chain-structure is obtained in metaphosphate glasses, i.e., when there is exactly one positive modifier charge per PO_4. For higher content of modifier charges, the Q^2 chains become increasingly depolymerized until an ionic network of only Q^1 and Q^0 species is obtained. In such glasses, ionic crosslinking becomes the dominant structural parameter, which is why they are often called *invert* glasses. In particular for these, structural models are still evolving [10].

In terms of applications, phosphate glasses have been of significant interest as host material for rare earth ions (RE) [11–13]. This is due to the typically high solubility of virtually all RE species, the comparably low phonon energy which reduces non-radiative electronic relaxation in photoluminescence processes and, hence, potential use as laser gain medium. In addition, phosphate glasses usually provide a broader window of transparency as compared to silicate glasses, however, compromised by difficulties in controlling water content [14].

Interestingly, besides cation solubility, modification of invert

---

* Corresponding author.
E-mail address: lothar.wondraczek@uni-jena.de (L. Wondraczek).

http://dx.doi.org/10.1016/j.jnoncrysol.2017.09.043
Received 29 June 2017; Received in revised form 20 September 2017; Accepted 21 September 2017
Available online 01 October 2017

phosphate glasses is possible also through anion substitution. For example, large amounts of SO_4^{2-} can be dissolved in zinc and other orthophosphate glasses, what significantly enhances glass forming ability and the material's thermo-chemical stability [15–20]. On the other side, fluorophosphate glasses incorporate significant amounts of fluoride species in a phosphate matrix. They have originally been designed for passive optics as well as laser applications so as to achieve high optical transmittance across the ultraviolet (UV) to near-infrared (NIR) spectral range, very low partial dispersion, and low linear and non-linear refractive index [21–24]. Further modification of the fluorophosphate anion network has been considered, e.g., through incorporation of P—N bonds [25], tellurite polyhedra [26], or sulfate groups [25,27], but usually with only minor degrees of substitution. More recent findings [28,29], however, suggest that this perceived limitation has been primarily due to the high melting temperatures which were employed in these previous studies [30], causing significant loss of sulfate through melt decomposition.

In the present report, we discuss formation, structure and properties of fluoro-sulfo-phosphate glasses across a broad range of sulfate and fluoride incorporation into meta- and orthophosphate matrices. While in these glasses, ionic interactions present the dominant structural parameter, surprisingly high glass forming ability and good glass stability are found. This demonstrates how anion-mixing presents an alternative route for tailoring the structural dynamics of phosphate invert glasses.

2. Experimental procedures

High purity (optical grade) raw materials of $NaPO_3$, AlF_3, Na_2SO_4, $Sr(PO_3)_2$, $SrSO_4$, MgF_2, CaF_2, SrF_2 were used for the preparation of Na_2O-AlF_3-P_2O_5-SO_3 (NAPFS) and MgF_2-CaF_2-SrF_2-AlF_3-$Sr(PO_3)_2$-$SrSO_4$ (FPS) glasses. The nominal compositions are given in Tables 1 and 4. Batches of 100 g were melted in Pt-crucibles, in a muffle furnace for 1.5 h at 850–1000 °C, followed by homogenization for 2 h at 1000–1100 °C (exact melting conditions are given in Tables 1, 4). FPS glasses with a phosphate-to-sulfate ratio ≥ 1 (D1–D3, E1–E3, F1–F3) and NAPFS were cast into preheated graphite moulds and annealed (T_g + 50 °C) for 4 h before cooling to room temperature (RT) at a rate of about 3–5 K/h. Melts with a phosphate-to-sulfate ratio < 1 and sample A5 in the NAPFS series were rapidly quenched on a copper plate. These latter glasses were then similarly annealed from RT to T_g + 50 °C for 1 h, and cooled back to RT.

The density ρ of all glasses was determined with the Archimedes method at 25 °C in ethanol (NAPFS) or distilled water (FPS). Transition temperatures T_g were measured by differential scanning calorimetry (DSC, NETZSCH STA 449 F3 Jupiter equipped with DSC sample holders). Each measurement was done under inert atmosphere of N_2 with a controlled flow rate of 20 ml/min at a heating rate of 20 K/min. The value of T_g was extracted from the onset of the glass transition for each sample. In a similar way, the onset temperatures of crystallization were also determined by DSC, using a heating rate of 10 K/min and a home-built apparatus.

Vibrational spectroscopy (Raman and infrared) was conducted on polished samples with dimensions of 15x10x2 mm. High-frequency Raman spectra were collected over the spectral range of 50–1500 cm^{-1}, using an excitation wavelength of 514.5 nm in 90° scattering geometry on a Raman microscope. In addition, low-frequency Raman spectra were collected using a Renishaw InVia micro-Raman spectrometer equipped with a notch filter with performance down to ~9 cm^{-1}. For this, samples were similarly as with high-frequency Raman excited with a 514.5 nm Argon laser at ambient temperature, and the signal was collected on a CCD camera over the spectral range of 0 to 1375 cm^{-1} with a resolution of 2 cm^{-1}. Subsequently, empty scans were taken for the correction of air scattering at low frequencies. Data accumulation times varied between 90 s and 180 s, depending on the type of glass. For each sample, spectra were averaged over up to 10 scans. In the low-frequency region (10–200 cm^{-1}), Raman spectra of glasses typically exhibit an excess of vibrational density of states VDOS several times higher than the value predicted by the Debye model for an elastic continuum (which is a quadratic function of the frequency [31]). Such excess of vibrational density appears when plotting the reduced density of states $g(\omega)/\omega^2$ ($g_{Deb}(\omega) \approx \omega^2$) as a function of the excitation energy, and is manifested by a large asymmetric peak called "boson peak" with a maximum

Table 1

Physical and mechanical properties of the investigated NAPFS glasses: transition temperature T_g, density ρ, molar volume V_m, shear G, bulk K, Young's modulus E and Poisson ratio ν as well as atomic packing density C_g, volume density of bonding energy $< U_0/V_0 >$ and Young's modulus E, as calculated following the concept of Makishima and Mackenzie, [34] with nominal compositions (mol%) and synthesis conditions.

Series	Glass	Variable		Synthesis conditions (°C)	Thermal parameters (°C)			ρ (g/cm³)	V_m (cm³/mol)	G (GPa)	K (GPa)	E[a] (GPa)	E[b] (GPa)	C_g	$< U_0/V_0 >$ (kJ/cm³)	ν
					T_g	T_x	ΔT									
(100-x)NaPO$_3$-xAlF$_3$																
NAPF	A1	x	0	800, 1.5 h	289	–	–	2.500	40.79	14.3	29.4	36.9	31.5	0.522	30.19	0.29
	A2		10	850, 1.5 h	311	–	–	2.553	39.23	16.0	32.4	41.1	36.7	0.535	34.30	0.288
	A3		20	900, 1.5 h	325	–	–	2.616	37.61	18.5	36.0	47.3	42.3	0.55	38.42	0.281
	A4		30	1000, 1.5 h	367	–	–	2.682	36.01	22.2	41.1	56.5	48.1	0.566	42.54	0.271
	A5		40	1000, 1.5 h	412	–	–	2.753	34.42	28.3	46.5	70.5	54.4	0.583	46.66	0.247
(80-y)NaPO$_3$-20AlF$_3$-yNa$_2$SO$_4$																
NAPFS1	B1	y	0	900, 1.5 h	325	–	–	2.616	36.01	18.5	36.0	47.3	42.3	0.55	38.42	0.281
	B2		5	850, 1.5 h	327	–	–	2.725	36.83	20.8	39.8	53.2	44.3	0.573	38.60	0.277
	B3		10	850, 1.5 h	330	–	–	2.628	38.95	18.5	36.5	47.4	42.9	0.553	38.78	0.283
	B4		15	850, 1.5 h	314	–	–	2.624	39.78	17.3	35.6	44.7	43.1	0.553	38.97	0.291
	B5		20	850, 1.5 h	313	393	80	2.618	40.63	16.9	35.0	43.6	43.2	0.552	39.15	0.293
	B6		30	800, 1.5 h	288	323	35	2.631	41.96	–	–	–	–	–	–	–
70NaPO$_3$-(30-z)AlF$_3$-zNa$_2$SO$_4$																
NAPFS2	C1	z	0	1000, 1.5 h	367	–	–	2.682	36.01	22.2	41.1	56.5	48.1	0.566	42.54	0.271
	C2		5	850, 1.5 h	336	–	–	2.634	37.76	19.0	37.1	48.6	45.2	0.555	40.66	0.282
	C3		10	850, 1.5 h	330	–	–	2.628	38.96	18.5	36.5	47.4	42.9	0.553	38.78	0.283
	C4		15	850, 1.5 h	307	–	–	2.589	40.67	15.9	33.5	41.3	40.2	0.545	36.91	0.295
	C5		20	850, 1.5 h	298	366	68	2.559	42.27	15.5	32.5	40.1	37.7	0.538	35.03	0.294
Experimental error					± 2			± 0.002		± 0.1	± 0.6	± 0.7				± 0.003

[a] Determined by ultrasonic echography.

[b] Determined by the concept of Makishima and Mackenzie.

intensity at frequency ω_{BP} and followed by a more gradual decline for $\omega > \omega_{BP}$. This peak is a universal characteristic feature in disordered systems [32], appearing not only in light scattering spectra, but also in neutron scattering spectra and in the low-temperature heat capacity [33].

Infrared spectra were obtained in the specular reflectance mode on a Fourier transform vacuum spectrometer across 30–5000 cm^{-1}. Kramer-Kronig transformation was applied to the IR spectra to obtain the absorption coefficient spectra $\alpha(\nu)$ for further analysis.

Magic-angle-spinning (MAS) nuclear magnetic resonance (NMR) analyses were conducted on a Bruker Avance III 400 (9.4 T magnet, 162 MHz for ^{31}P) with a 4 mm MAS probe. One-pulse experiments were performed with 60° pulses (2 μs) and a recycle delay time of 350 s. The sample rotation frequency was 12.5 kHz. All spectra were referenced to 85 wt% H_3PO_4.

Elastic properties were characterized through ultrasonic echography on co-planar, optically polished glass plates. For this, the longitudinal c_L and transversal wave velocities c_T were determined with a piezoelectric transducer operating at frequencies of 8–12 MHz (Echometer 1077, Karl Deutsch GmbH & Co KG). The shear G, bulk K and Young's modulus E as well as the Poisson ratio ν were then calculated according to the following equations [20]:

$$G = \rho c_T^2, \tag{1}$$

$$K = \rho\left(c_L^2 - \frac{4}{3}c_T^2\right), \tag{2}$$

$$E = \rho\left[\frac{3c_L^2 - 4c_T^2}{(c_L/c_T)^2 - 1}\right], \tag{3}$$

$$\nu = \frac{c_L^2 - 2c_T^2}{2(c_L^2 - c_T^2)} \tag{4}$$

Furthermore, the Young's modulus was also approximated following the concept of Makishima and Mackenzie [34]. In this simplistic approach, E is estimated from of the atomic packing density C_g and the volume density of bonding energy $< U_0/V_0 >$, which is defined as the dissociation energy per unit volume G_i of each glass component, weighted by its molar fraction f_i:

$$E = 2C_g \sum f_i G_i \tag{5}$$

The parameter C_g in the above equation relates the theoretical molar volume $V_i = 4/3\pi N(xr_A{}^3 + yr_B{}^3)$ of the ions of a compound A_xB_y, with the molar mass M_i, the Avogadro constant N and the ionic radii r_A and r_B, respectively, to the effective molar volume of the glass: [35]

$$C_g = \rho\frac{\sum f_i V_i}{\sum f_i M_i}, \tag{6}$$

with r_A: (Na^+) = 1.02 Å; (Mg^{2+}) = 0.57 Å; (Ca^{2+}) = 1.06 Å; (Sr^{2+}) = 1.21 Å; (Al^{3+}) = 0.54 Å; (P^{5+}) = 0.17 Å; (S^{6+}) = 0.12 Å and r_B: (O^{2-}) = 1.35 Å; (F^-) = 1.33 Å [36]. The values of G_i were estimated from the molar heat of formation ΔH_f of every single glass component in its crystalline state and the respective atoms in their gaseous state, according to: [37]

$$G_i = \frac{\rho_i}{M_i}[x\Delta H_f(\text{A, gas}) + y\Delta H_f(\text{B, gas}) - \Delta H_f(\text{A}_x\text{B}_y, \text{crystal})] \tag{7}$$

Using the values of ΔH_f from Ref. [38] we obtained G_i = 72.3 kJ/cm^3 (MgF_2); 63.7 kJ/cm^3 (CaF_2); 52.0 kJ/cm^3 (SrF_2); 71.4 kJ/cm^3 (AlF_3); 32.2 kJ/cm^3 (Na_2O); 44.3 kJ/cm^3 (SrO); 119.4 kJ/cm^3 (Al_2O_3) and 35.5 kJ/cm^3 (SO_3). For P_2O_5 we adopted the value of G_i = 28.2 kJ/cm^3 as suggested by Inaba et al. [37], which has been corrected with respect to the double-bonded oxygen ion in [PO_4] tetrahedral units [1].

3. Results and discussion

3.1. General

Glass fabrication started from the well-known sodium metaphosphate, which was gradually modified by adding aluminum fluoride (NAPF-series). This series was used as a set of reference specimens, with phosphate and fluoride anions, and mixed fluorophosphate groups. Sulfate groups were then introduced as another anion species by substituting the nominal sodium metaphosphate with sodium sulfate at constant (NAPFS1) or varying (NAPFS2) fluoride content. Furthermore, a sodium-free starting point of a well-described fluorophosphate glass was chosen, in which again, phosphate was gradually replaced by sulfate without changing the cation species at varying fluoride content (FPS sub-series). All series were studied over broad composition ranges. If not otherwise stated, the respective glass forming region according to the present melting and cooling conditions spanned the reported sample compositions. Only for the pure fluoro-sulfates (FS) [25,27] or at very low phosphate content (see experimental section), glass formation required rapid quenching. Obtained glasses were visually transparent without signs of crystals or bubbles. Occasional X-ray diffraction analyses confirmed the absence of crystalline phases. Glass stability was high as qualitatively judged from the difference between T_g and T_x (Tables 1 and 4, with the above noted exceptions of FS): for the majority of glasses, T_x could not be observed within the considered temperature window at a DSC heating rate of 10 K/min. Similarly, indications of phase separation could not be detected visually by shining a green laser pointer through the glass to evaluate elastic optical scattering. In the following Tables, nominal compositions are stated. A typical absolute fluoride and sulfate loss through evaporation of ≤ 5 wt% and < 1 wt%, respectively, was estimated through EDX analyses in the NAPFS glasses. Both values are probably somewhat higher for the FPS series, in which higher melting temperatures were employed. Noteworthy, the water content of fluoride phosphate glasses is generally low as compared to that of their phosphate counterparts (facilitated through fluoride evaporation).

Physical properties of NAPF(S) and FPS glasses are presented in Tables 1–4 and plotted in Fig. 1. As seen from Fig. 1, T_g, $E^{a,b}$ and U_0/V_0 increase with the rising AlF_3 concentration in NAPF glasses. On the other hand, V_m and ν decrease as the amount of AlF_3 increases. Addition of Na_2SO_4 in NAPFS glasses leads to opposite trends in all properties. Only Young's modulus $E^{a,b}$ and volume density of bond energy U_0/V_0 of the NAPFS1 series seem to remain unchanged when AlF_3 is constant and $NaPO_3$ is replaced by Na_2SO_4. This is consistent with previous observations on FP glasses [39].

Substitution of $Sr(PO_3)_2$ by $SrSO_4$ in FPS causes a decrease of T_g and V_m. However, Young's modulus E, $< U_0/V_0 >$ and Poisson ratio ν slightly increase (Fig. 2). As will be seen later, these observations of macroscopic properties can be well-understood on the basis of structural considerations.

3.2. Structural characterization

3.2.1. Series (100-x)$NaPO_3$-xAlF_3

For referencing the following glass series, initially, the join of aluminum fluoride – sodium metaphosphate was considered (NAPF). All glasses in the NAPF series were synthesized under identical conditions. Solely variations in melting temperature depended on the content of AlF_3 in these glasses (Table 1). Changes in glass structure and properties are thus caused by the amount of AlF_3 added to the sodium metaphosphate base glass and the amount of the retained fluorine.

Raman spectra of this glass series are presented in Fig. 3a. The spectrum of the pure sodium metaphosphate glass (A1) shows two main bands at 684 and 1164 cm^{-1} which correspond to the symmetric stretching modes of the P—O—P bridges connecting Q^2 phosphate tetrahedral units (ν_s(P—O—P)) and $PO_2{}^-$, $\nu_s(PO_2{}^-)$ Q^2, respectively

Table 2
^{31}P MAS-NMR lineshape fitting parameters for NAPFS glasses.

Series	Glass	Variable		Q^0_m			Q^1			Q^1_m			Q^2			Q^2_m			Q^0: $Q^1_{0,m}$: $Q^2_{0,m}$
				δ (ppm)	fwhm (ppm)	Area (%)	δ (ppm)	fwhm (ppm)	Area (%)	δ (ppm)	fwhm (ppm)	Area (%)	δ (ppm)	fwhm (ppm)	Area (%)	δ (ppm)	fwhm (ppm)	Area (%)	
(100-x)NaPO$_3$-xAlF$_3$																			
NAPF	A1	x	0	1.5	5.0	0.53	− 7.80	6.5	4.16	–	–	–	− 19.65	7.4	95.31	–	–	–	0.53: 4.16: 95.31
	A2		10	1.5	5.0	0.83	− 7.60	7.3	8.23	− 14.28	9.8	10.47	− 19.80	8.0	69.04	− 26.20	11.8	11.43	0.83: 18.70: 80.47
	A3		20	1.5	5.0	0.57	− 7.60	7.5	10.13	− 14.10	8.6	16.77	− 19.97	8.7	54.98	− 26.20	12.2	17.55	0.57: 26.90: 72.53
	A4		30	0.5	5.5	0.47	− 7.60	8.0	5.59	− 14.25	10.9	34.57	− 20.50	10.0	40.84	− 26.78	12.5	18.52	0.47: 40.16: 59.36
	A5		40	0.0	6.0	0.41	− 7.60	9.0	2.95	− 15.10	11.4	50.10	− 21.55	11.0	28.56	− 26.80	12.9	17.99	0.50: 53.05: 46.55
(80-y)NaPO$_3$-20AlF$_3$-yNa$_2$SO$_4$																			
NAPFS1	B1	y	0	1.5	5.0	0.57	− 7.60	7.5	10.13	− 14.10	8.6	16.77	− 19.97	8.7	54.98	− 26.20	12.2	17.55	0.57: 26.90: 72.53
	B2		5	1.5	4.8	0.44	− 7.60	7.9	10.36	− 14.20	9.6	24.05	− 20.00	11.0	51.03	− 26.30	13.0	14.12	0.44: 34.41: 65.15
	B3		10	1.5	4.8	0.46	− 7.60	7.9	10.14	− 14.20	10.1	24.42	− 19.95	9.3	50.28	− 26.30	11.9	14.70	0.46: 34.56: 64.98
	B4		15	1.6	4.5	0.55	− 7.45	7.6	13.28	− 14.15	8.9	26.04	− 19.95	8.8	46.72	− 26.20	11.8	13.41	0.55: 39.32: 60.13
	B5		20	1.7	5	0.78	− 7.45	7.4	12.68	− 14.30	9.5	28.75	− 20.00	8.6	45.23	− 26.20	11.4	12.56	0.79: 41.43: 57.79
	B6		30	2.5	4.3	0.39	− 7.50	7.6	10.99	− 14.30	9.0	29.34	− 20.25	8.4	44.02	− 26.30	11.2	15.26	0.39: 40.33: 59.28
70NaPO$_3$-(30-z)AlF$_3$-zNa$_2$SO$_4$																			
NAPFS2	C1	z	0	0.5	5.5	0.47	− 7.60	8.0	5.60	− 14.25	10.9	34.57	− 20.50	10.0	40.84	− 26.78	12.5	18.52	0.47: 40.17: 59.36
	C2		5	1.8	4.5	0.60	− 7.60	7.8	11.96	− 14.20	9.2	25.07	− 20.00	9.0	46.92	− 26.65	11.4	15.45	0.60: 37.03: 62.37
	C3		10	1.5	4.8	0.46	− 7.60	7.9	10.15	− 14.20	10.1	24.42	− 19.95	9.3	50.27	− 26.30	11.9	14.70	0.46: 34.57: 64.97
	C4		15	1.6	5.0	0.84	− 7.50	7.4	12.54	− 14.30	8.3	19.62	− 19.85	7.9	54.88	− 26.10	10.2	12.12	0.84: 32.16: 67.00
	C5		20	1.9	4.5	1.40	− 7.35	7.0	14.14	− 14.10	7.2	14.00	− 19.70	7.5	63.16	− 26.05	10.0	7.30	1.40: 28.14: 70.46
Error analysis				± 0.2	± 0.5	± 0.1	± 0.15	± 0.5	± 1	± 0.2	± 0.5	± 2	± 0.2	± 0.5	± 2	± 0.2	± 0.5	± 1.5	

[40,41]. Weaker features at ~1025, 1270 and 1330 cm^{-1} can be assigned to the $\nu_s(PO_3{}^{2-})$ of the end groups in pyrophosphate dimers (Q^1), the asymmetric stretching mode $\nu_{as}(PO_2{}^{-})$ of Q^2 units and of neutral phosphate tetrahedra, ν(P═O), respectively [41]. The broad profile between 300 and 430 cm^{-1} is attributed to bending modes of Q^2 units [42].

Addition of AlF$_3$ to the sodium metaphosphate glass causes small but progressive changes in the Raman spectra at low AlF$_3$ contents. They evolve into major changes for $x \geq 30$, indicating modifications of the metaphosphate ($Q^2 = PO_3{}^{-}$) backbone. New bands appear at about 540, 630, 765, 850 and 1045–1090 cm^{-1}. Here, the feature at ~540 cm^{-1} arises from the vibrations of [Al(F,O)]$_6$ [41]. Moreover, the higher the content of AlF$_3$, the more [AlF$_4$] groups are formed in the NAPF glasses. This is proven by the increasing intensity of the band at 630 cm^{-1} [43]. According to Philip et al. [44], crystalline sodium pyrophosphate, $Na_4P_2O_7$, shows ν_s(P–O–P) at 740 cm^{-1} for P–O–P bridges connecting pyrophosphate tetrahedral units ($Q^1 = PO_{3.5}{}^{2-}$). Therefore, the new band at 765 cm^{-1} could be associated with the formation of pyrophosphate dimers, $P_2O_7{}^{4-}$, resulting from the depolymerization of metaphosphate chains. The symmetric stretching vibration of the $PO_3{}^{2-}$ end groups of the pyrophosphate units, $\nu_s(PO_3{}^{2-})$ was found at 1025 cm^{-1} for crystalline $Na_4P_2O_7$. However, charge balancing the $P_2O_7{}^{4-}$ by both Na$^+$ and Al^{3+} ions would cause the upshift of the $\nu_s(PO_3{}^{2-})$ mode, and the potential creation of P–O–Al bridging bonds with a new resonance. Hence, the bands at 1040–1090 cm^{-1} were assigned to the $\nu_s(PO_3{}^{2-})$ of Q^1 with a growing number of Q^1_m units (m indicates the number of non-bridging oxygen atoms connected to an aluminate polyhedron, P–O–Al linkages) [41,45]. In addition, the very weak bands of orthophosphate $\nu_s(PO_4{}^{3-})$ Q^0 and the stretching vibration of P–F bonds are also observed at 940 and 850 cm^{-1} for $x \geq 30$ [41,46,47]. Apparently, AlF$_3$ additions open the polyphosphate entities and insert fluoride bridges.

The symmetric stretching mode ν_s(P–O–P) (Q^2) appears initially at 684 cm^{-1}. As x increases, this band shifts to higher frequency and is seen as a shoulder at 730 cm^{-1} due to network depolymerization for $x = 40$. The down-shift and broadening of the $\nu_s(PO_2{}^{-})$ band (from 1164 to 1135 cm^{-1}) and the upshift of the ν_s(P–O–P) (Q^2) mode (from 684 to 730 cm^{-1}) are indicative of the disruption of metaphosphate chains, probably by the incorporation of Al^{3+} polyhedral units in P–O–Al linkages as noted above [48].

The continuous evolution of the IR spectra (Fig. 3b) with AlF$_3$ content is in agreement with the Raman results concerning the disruption of the metaphosphate structure. The intensity of the asymmetric stretching mode $\nu_{as}(PO_2{}^{-})$ at 1270 cm^{-1} decreases gradually [42], and two new bands grow-in at 1150 and 1210 cm^{-1} for $x = 40$. Two ν_{as}(P–O–P) bands appear initially at 875 and 995 cm^{-1} for P–O–P bridges connecting Q^2 phosphate tetrahedral units, probably in chain and ring formations [42]. As x increases, these bands lose intensity and are eventually replaced by the 945 cm^{-1} band at $x = 40$. This is typical of ν_{as}(P–O–P) in $P_2O_7{}^{4-}$ dimeric units [49]. The profile at 720–780 cm^{-1} is due to the ν_s(P–O–P) bridges, as discussed for the corresponding Raman spectra [42,47,48]. Similar to the up-shift of Raman band at 1040–1090 cm^{-1} of $\nu_s(PO_3{}^{2-})$ caused by the increasing AlF$_3$ content, the $\nu_{as}(PO_3{}^{2-})$ band also shifts from 1092 to 1150 cm^{-1} [44]. The bands at around 1200 cm^{-1} could originate from the ν_{as}(P–O–Al). The growing intensity of two bands at 415 and 630 cm^{-1} are assigned to bending modes δ(Al–F) and asymmetric stretching modes ν_{as}(Al–F) which occur as x increases from 10 to 40 (Fig. 3b) [40]. The bending modes of the phosphate network, δ(P–O) units, manifest in a broad band from 478 to 537 cm^{-1} [42]. The weaker feature at 220 cm^{-1} is due to Na$^+$ ion site vibration mode, ν(Na–O) [42].

Fig. 4a shows the ^{31}P MAS NMR spectra obtained for the set of NAPF glasses. For the pure sodium metaphosphate glass ($x = 0$), a symmetric and sharp resonance originating from Q^2 (~95%) phosphate groups is observed at − 19.65 ppm [50]. In our study, NaPO$_3$ was used as raw

Table 3
Frequencies and assignments of Raman and infrared bands recorded in this work for NAPFS glasses.

Raman (cm^{-1})	Infrared (cm^{-1})	Assignment	References
$1270–1330_{(vw)}$[a]	$1270–1287_{(vs)}$	$\nu_{as}(PO_2^-)$[b], Q^2[c] in metaphosphate chains/rings and $\nu(P=O)$	[41,42]
$1220_{(vw)}$		$\nu_3(SO_4^{2-})$	[20,47,56,57]
$1164_{(vs)}$		$\nu_s(PO_2^-)$, Q^2 in metaphosphate chains/rings	[40,41]
	$1160_{(vs)}$	$\nu_3(SO_4^{2-})$	[47]
	$1200_{(w)}$	$\nu_{as}(P–O–Al)$	
	$1092–1151_{(s)}$	$\nu_{as}(PO_3^{2-})$ Q^1	[44]
$1025–1090_{(vw\text{-}s)}$		$\nu_s(PO_3^{2-})$ Q^1 in sodium metaphosphate and Q^1_m units with P–O–Al linkages	[40,41,45]
$940_{(vw)}$		$\nu_s(PO_4^{3-})$ Q^0	[46,47]
	$995_{(s)}$	$\nu_{as}(P–O–P)$ in rings	[42]
$992_{(vs)}$	$992_{(vw)}$	$\nu_1(SO_4^{2-})$	[20,47,56,57]
	$875–945_{(s)}$	$\nu_{as}(P–O–P)$ in chains and in dimeric units	[49]
$850_{(vw)}$		$\nu_s(P–F)$	[41]
	$720–780_{(m)}$	$\nu_s(P–O–P)$ in Q^1 and Q^2	[47,48]
$765_{(w\text{-}s)}$		$\nu_s(P–O–P)$ Q^1, the upshift caused by the replacement of Al^{3+} for Na^+ ions	[44]
$696_{(s)}$-$730_{(m,\ sh)}$		$\nu_s(P–O–P)$ Q^2 in shorter metaphosphate chains and Q^1	[48]
$684–686_{(s)}$		$\nu_s(P–O–P)$ Q^2 in metaphosphate chains/rings	[40,41]
$630_{(w,\ sh)}$		$\nu_s(Al–F)$	[43]
	$630_{(sh)}$	$\nu_{as}(Al–F)$	[40]
$627_{(m)}$	$627_{(w\text{-}m)}$	$\nu_4(SO_4^{2-})$	[47,56,57]
$540_{(w\text{-}m)}$		$\nu(Al(F,O)_6)$	[41,43]
	$478–537_{(m)}$	$\delta(P–O)$	[42]
$460_{(w\text{-}m)}$		$\nu_2(SO_4^{2-})$,	[47,56,57]
	$415_{(w\text{-}m)}$	$\delta(Al–F)$	[40]
$300–430_{(m)}$		$\delta(P–O)$	[42]
	$\sim 200_{(m)}$	$\nu(Na–O)$	[42]

[a] Band intensity: vs = very strong, s = strong, m = medium, w = weak, vw = very weak, sh = shoulder.
[b] Vibration mode: ν = stretching, δ = bending, ν_s, ν_1 = symmetric stretching, ν_{as}, ν_3 = asymmetric stretching, ν_2 = symmetric bending, ν_4 = asymmetric bending.
[c] Q^i: a phosphate tetrahedron with i bridging and 4-i terminal oxygen atoms.

material to prepare this glass. During the melting process, a fraction of P_2O_5 evaporates. Hence, the ratio between Na_2O and P_2O_5 may be higher than 1, which leads to the appearance of a weak band at -7.8 ppm in the spectrum of sample A1 ($Q^1 \approx 4\%$). In addition, water can also disrupt the phosphate network, leading to Q^1 and very small amounts of Q^0 at a chemical shift of 1.5 ppm (~ 0.5%) [51].

In accordance with the increase in AlF_3 concentration, we observe a progressive shift towards higher frequencies and broadening of the ^{31}P signals (Fig. 4). This is caused by the cleavage of P–O–P linkages and the increasing amount of Q^1_m and Q^2_m units. The ^{31}P MAS NMR spectrum of the pure sodium metaphosphate glass (A1) was best-fit with three Gaussian components, see also [50]. For the other glasses, an acceptable deconvolution is obtained for five components located around 1.5, -7.6, -14.2, -20 and -26.2 ppm and reflects the chemical shifts of Q^0_m ($m = 0, 1, 2$), Q^1, Q^1_m, Q^2 and Q^2_m, respectively (Fig. 4b and 5) [52]. All data are summarized in Table 2.

Corresponding to the observations which were made through vibrational spectroscopy, for $x \geq 30$, the shoulders in the NMR spectra disappear behind the raising Q^1_m band (Fig. 4). Dollase et al. [52] demonstrated that replacing Na^+ neighbours with the stronger Al^{3+} ion around phosphate groups causes the chemical shift to decrease by 8 to 9 ppm for each additional Al^{3+} neighbour in $Na_{3-3x}Al_xPO_4$. This was similarly confirmed by Fletcher, showing that both increasing polymerization [53] and an increasing number of Al nearest neighbours to P lead to more negative chemical shift in ^{31}P NMR [53,54]. As seen in Fig. 5 and Table 2, the shift of fitted lines between Q^1–Q^1_m and Q^2–Q^2_m is ~6.5 ppm, from which we can deduce that on average, only one Na^+ ion per phosphate group was replaced by Al^{3+} ions to create P–O–Al bridging bonds ($m = 1 \gg m = 2$) [52,55]. The higher the content of $[AlF_3]$, the more disrupted are the Q^2 groups. Moreover, Al^{3+} ions seem to preferentially replace Na^+ ions in Q^1 over Q^2 groups. This analysis is in good agreement with the interpretation of the Raman and IR spectra. From this, we affirm that there is an exchange between F and O to form P–F bonds [41].

3.2.2. Series (80-y)NaPO$_3$-20AlF$_3$-yNa$_2$SO$_4$

Sulfate was introduced into NAPF by substituting sodium phosphate with sodium sulfate. This simultaneously leads to an increase in the nominal total molar fraction of sodium, since with each SO_4^{2-} group, one additional sodium ion is introduced. Hence, also the Na:P ratio is increasing. Raman spectra of glasses from the series of $(80\text{-}y)NaPO_3$-$20AlF_3$-yNa_2SO_4 (NAPFS1) compare to those of NAPF with $x = 20…30$, with additional features emerging around 460, 627 and 992 cm^{-1} (Fig. 6a). The latter grow in intensity with increasing Na_2SO_4 content (y). They are attributed to $\nu_2(SO_4^{2-})$, $\nu_4(SO_4^{2-})$ and $\nu_1(SO_4^{2-})$ modes of the sulfate ions charged-balanced by Na^+ cations [16].

The frequencies of the main peaks of the phosphate network remain practically unaffected by the addition of Na_2SO_4. There is an up-shift of the $\nu_s(P–O–P)$ mode from about 696 to 708 cm^{-1} for $y = 5$, indicating increasing depolymerization of the phosphate network. At the same time, however, the band appears to down-shift for higher degrees of substitution. This points to a re-increase of the degree of phosphate polymerization, potentially due to non-random precipitation of sodium species in the vicinity of sulfate anions. In parallel, the frequencies of $\nu_s(PO_3^{2-})$ in Q^1_m with P–O–Al linkages remain practically unaffected around 1068 cm^{-1} at unchanged AlF_3 content.

The corresponding IR spectra of NAPFS1 (Fig. 6b) similarly reflect the presence of sulfate anions through peaks growing-in at about 627 and 1160 cm^{-1} [16]. In addition, weak activation of the $\nu_1(SO_4^{2-})$ mode is observed at about 992 cm^{-1} [56]. As in the Raman spectra, the frequencies of most peaks of the phosphate network remain practically unaffected by the presence of Na_2SO_4. Again, after rising from 916 to 924 cm^{-1}, it seems that the $\nu_{as}(P–O–P)$ mode is an exception as its frequency decreases from 924 cm^{-1} ($y = 5$) to 918 cm^{-1} ($y = 20$) and then increases to 932 cm^{-1} for $y = 30$ [49]. As with the Raman data, we assign this variation to minor variations in the degree of phosphate polymerization, resulting from non-random precipitation and glass synthesis (where the sample with $y = 30$ was rapidly quenched, and the other samples were cast and cooled comparably slowly).

NMR spectra are presented in Fig. 7. There is not much variation visible among the samples of the NAPFS1 series. In fact, Q^2 groups

Table 4

Physical and mechanical properties of the FPS glasses investigated: transition temperature T_g, density ρ, molar volume, shear G, bulk K, Young's modulus E and Poisson ratio ν as well as atomic packing density C_g, volume density of bonding energy $< U_0/V_0 >$ and Young's modulus E, as calculated following the concept of Makishima and Mackenzie [34], with nominal compositions (mol%) and synthesis conditions.

Series	Glass	Variable		Synthesis conditions (°C)	Thermal parameters (°C)			ρ (g/cm^3)	V$_m$ (cm^3/mol)	G (GPa)	K (GPa)	E^a (GPa)	E^b (GPa)	C_g	$< U_0/V_0 >$ (kJ/cm^3)	ν
					T_g	T_x	ΔT									
$80(MF_n)$-$(20$-$x_1)Sr(PO_3)_2$-x_1SrSO_4, $80(MF_n) = 10MgF_2 + 21.8CaF_2 + 18.2SrF_2 + 30AlF_3$																
FPS20	D1	x_1	0	1000–1100, 2 h	485	–	–	3.512	34.29	30.2	63.8	78.4	74.2	0.626	59.24	0.295
	D2		5	1000–1100, 2 h	469	–	–	3.527	33.27	29.3	63.2	76.1	74.5	0.627	59.42	0.299
	D3		10	1000–1100, 2 h	451	–	–	3.531	32.35	27.6	60.5	71.8	74.7	0.627	59.61	0.302
	D4		15	1000–1100, 2 h	430	567	137	3.547	31.33	–	–	–	75.1	0.628	59.79	–
	D5		20	1000–1100, 2 h	395	466	71	3.555	30.39	–	–	–	75.3	0.628	59.97	–
$85(MF_n)$-$(15$-$y_1)Sr(PO_3)_2$-y_1SrSO_4, $85(MF_n) = 10MgF_2 + 23.4CaF_2 + 19.4SrF_2 + 32.2AlF_3$																
FPS15	E1	y_1	0	1000–1100, 2 h	488	–	–	3.503	32.19	29.8	63.6	77.4	76	0.627	60.64	0.298
	E2		5	1000–1100, 2 h	474	–	–	3.527	31.09	29	63.2	75.4	77.1	0.634	60.83	0.301
	E3		7.5	1000–1100, 2 h	456	–	–	3.531	30.62	28.2	61.8	73.4	76.9	0.631	60.92	0.302
	E4		10	1000–1100, 2 h	437	577	140	3.547	30.04	–	–	–	77.5	0.635	61.01	–
	E5		15	1000–1100, 2 h	402	462	60	3.555	29.10	–	–	–	79.3	0.648	61.19	–
$90(MF_n)$-$(10$-$z_1)Sr(PO_3)_2$-z_1SrSO_4, $90(MF_n) = 10MgF_2 + 30CaF_2 + 15SrF_2 + 35AlF_3$																
FPS10	F1	z_1	0	1000–1100, 2 h	461	–	–	3.427	29.89	29.4	62.9	76.3	79.2	0.631	62.75	0.298
	F2		3	1000–1100, 2 h	457	–	–	3.471	28.98	29.8	64.6	77.5	80.3	0.639	62.86	0.3
	F3		5	1000–1100, 2 h	446	–	–	3.479	28.56	28.3	62.4	73.7	80.5	0.64	62.93	0.303
	F4		7	1000–1100, 2 h	431	541	110	3.562	27.54	–	–	–	82.5	0.655	63.01	–
	F5		10	1000–1100, 2 h	400	455	55	3.527	27.29	–	–	–	81.7	0.647	63.11	–
Experimental errorc[c]					± 2			± 0.002		± 0.1	± 0.6	± 0.7				± 0.003

[a] Determined by ultrasonic echography.

[b] Determined by the concept of Makishima and Mackenzie.

[c] Standard deviation.

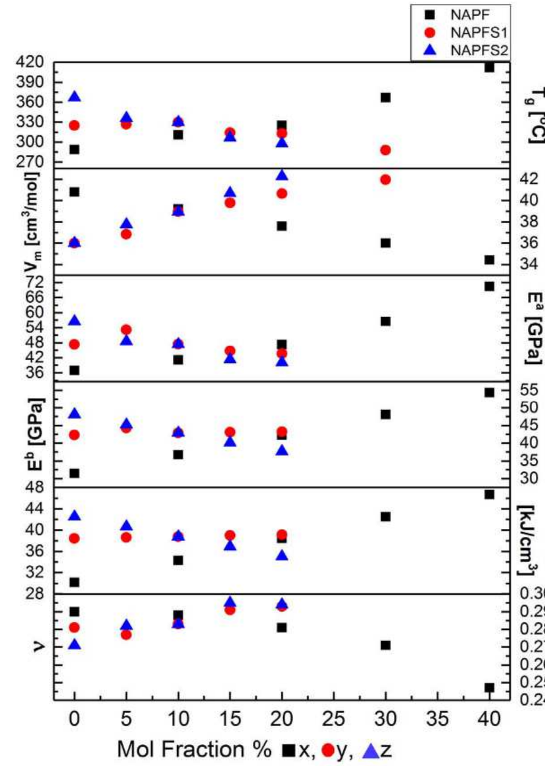

Fig. 1. Dependence of the transition temperature T_g, molar volume V_m, Young's modulus E, volume density of bonding energy $< U_0/V_0 >$ and Poisson ratio ν on the AlF_3 content (x) for the (100-x)$NaPO_3$-$x$$AlF_3$ glasses and on the Na_2SO_4 content (y, z) for the (80-y) $NaPO_3$-20AlF_3-$y$$Na_2SO_4$ and 70$NaPO_3$-(30-z)AlF_3-$z$$Na_2SO_4$ glasses respectively.

slightly decrease while the fraction of Q^1_m increases from B1 to B6 because of the reduction of the ratio between $NaPO_3$ and AlF_3 (Table 2). However, the details of the variation in —P—O—P— as seen from Raman and IR cannot be detected at this point and within the accuracy of the data (including the effect of powder preparation for NMR analysis).

It was previously reported [16] that sulfur is incorporated into phosphate glasses in the form of isolated SO_4^{2-} groups and that cation species tend to selectively precipitate in the vicinity of certain anions. This observation seems to be confirmed in the present study, at least for the considered compositional regime where we do not detect any P—O—S groups.

3.2.3. *Series 70NaPO$_3$-(30-z)AlF$_3$-zNa$_2$SO$_4$*

A second series of NAPFS was produced in which the fluoride was substituted by sulfate at a lower base content of sodium metaphosphate. Besides variations in the anion content, this means that also the typically cross-linking species of Al^{3+} is replaced by sodium cations. The Raman spectra shown in Fig. 8a exhibit bands at 460, 627 and 992 cm^{-1}, related to the sulfate anion as with NAPFS1. The ν_s(P—O—P) and $\nu_s(PO_3^{2-})$ also shift to higher frequencies from 686 to 710 cm^{-1} and 1063 to 1078 cm^{-1}, respectively, with higher AlF_3 content (as with NAPF glasses). IR spectra confirm these data (Fig. 8b). In addition, the intensity of ν_{as}(P—O—Al) at about 1200 cm^{-1} decreases with increasing z.

The ^{31}P MAS NMR spectra of the NAPFS2 series follow those of the sulfate-free series of NAPF. They are dominated by the changing AlF_3 content (Fig. 9). An increasing amount of Q^1 groups is found when more AlF_3 is present in the glasses. All data are summarized in Table 2. Assignments of vibrational bands are collected in Table 3.

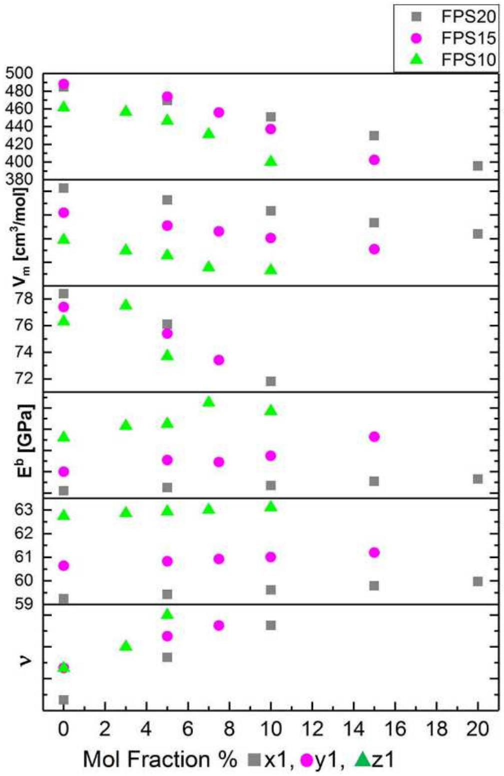

Fig. 2. Dependence of the transition temperature T_g, molar volume V_m, Young's modulus E, volume density of bonding energy $< U_0/V_0 >$ and Poisson ratio ν on the $SrSO_4$ content (x_1, y_1, z_1) for the 80(MF_n)-(20-x_1)$Sr(PO_3)_2$-$x_1$$SrSO_4$, 85($MF_n$)-(15-$y_1$)$Sr(PO_3)_2$-$y_1$$SrSO_4$ and 90(MF_n)-(10-z_1)$Sr(PO_3)_2$-$z_1$$SrSO_4$ glasses, respectively. For nominal compositions see Table 4.

3.2.4. *Series of FPS*

Contrary to NAPFS, FPS glasses contain divalent cations in place of the monovalent sodium. The ratio of F:P is varied along the series, and sulfate is introduced through substitution of strontium metaphosphate at each step of F:P-variation. The studied compositions are summarized in Table 4. Since the qualitative variations among the three sub-series of FPS20, FPS15 and FPS10 are equivalent, in the following, we focus our analysis on the FPS20 sub-series. Corresponding data on FPS15 and FPS10 are provided in the Supplementary Information.

Raman spectra for the FPS20 series are shown in Fig. 10a. For $x_1 = 0$, the two bands at 1060 and 1000 cm^{-1} reflect the pyrophosphate chain terminators, $\nu_s(PO_3^{2-})$ of Q^1, and the orthophosphate groups Q^0, $\nu_s(PO_4^{3-})$, respectively [40,41,58]. The shoulders around 1100 and 1200 cm^{-1} are assigned to contributions from $\nu_{as}(PO_3^{2-})$ of Q^1 and $\nu_s(PO_2^{-})$ of Q^2 units [16,47]. Because Q^1 is dominant over Q^2, the symmetric stretching vibration of P—O—P, ν_s(P—O—P) at 756 cm^{-1} derives from Q^1 [59]. Its resonance energy corresponds to that which was seen for ν_s(P—O—P) Q^1 in NAPF and NAPFS glasses. However, in the Raman spectra of FPS glasses, we find no evidence of P—F bonds (absence of a band at around 850 cm^{-1}) [41]. The feature at 563 cm^{-1} is indicative for both vibrations of $\nu Al(F,O)_6$ and the asymmetric bending mode of PO_4^{3-}, $\nu_4(PO_4^{3-})$, Q^0 [41,47,49]. In the depolarized Raman spectra (VH, Fig. 10b), $\nu_4(PO_4^{3-})$ exhibits highly reduced intensity with increasing x_1. The broad envelope between 300 and 400 cm^{-1} originates primarily from bending modes of phosphate units [41,42].

Similar to Na_2SO_4-substituted NAPF, when $Sr(PO_3)_2$ is partially replaced by $SrSO_4$ in 80(MF_n)-(20-x_1)$Sr(PO_3)_2$-$x_1$$SrSO_4$, the $\nu_2(SO_4^{2-})$,

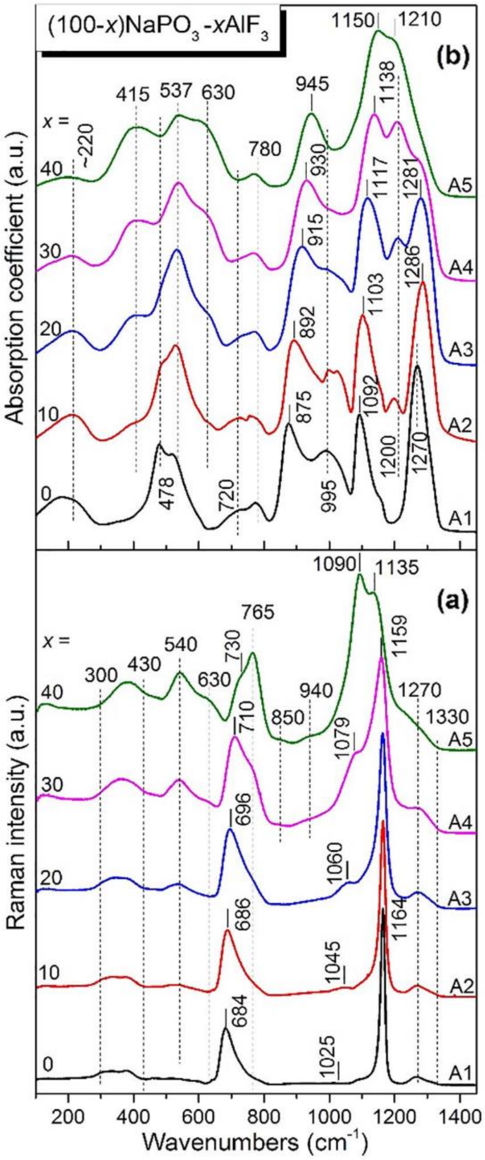

Fig. 3. Raman (a) and IR (b) spectra of NAPF glasses.

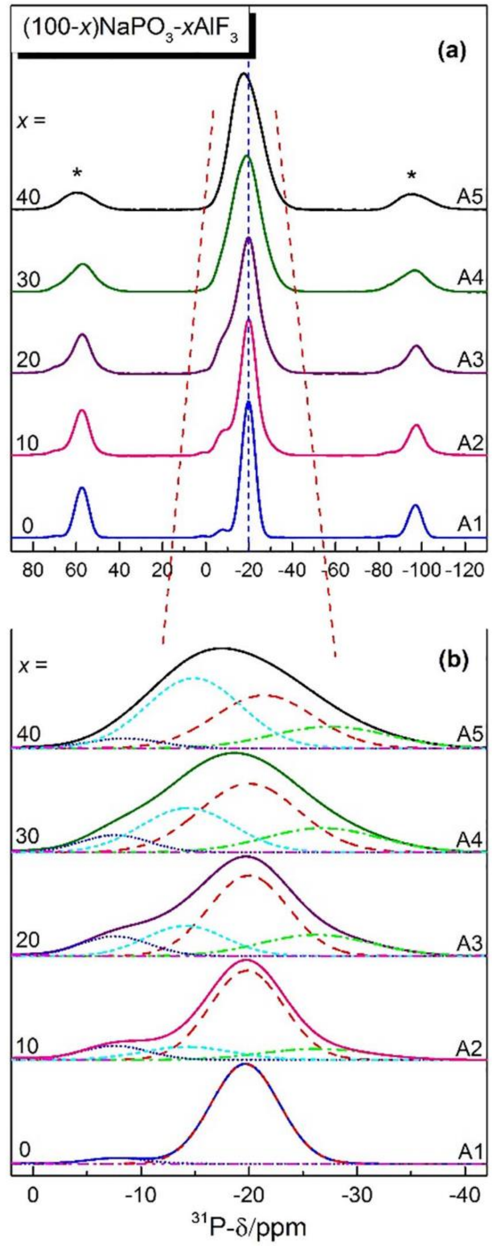

Fig. 4. (a) ^{31}P MAS NMR spectra of NAPF glasses. Spinning sidebands are indicated by asterisks. (b) ^{31}P MAS NMR spectra deconvolutions.

$\nu_4(SO_4^{2-})$ and $\nu_1(SO_4^{2-})$ modes emerge at around 460, 627 and 1000 cm^{-1}, respectively [16,20,47,56,57]. Weaker shoulders at high frequency (~1125 and 1205 cm^{-1}) are associated with the asymmetric stretching mode of sulfate anions, $\nu_3(SO_4^{2-})$ [47,56,57]. The bands of $\nu_{as}(PO_3^{2-})$ Q^1 (1100 cm^{-1}), $\nu_s(PO_2^-)$ (1200 cm^{-1}) and $\nu_3(SO_4^{2-})$ (~1125 and 1205 cm^{-1}) cannot reliably be deconvoluted because of the strong spectral overlap. Furthermore, $\nu_s(PO_4^{3-})$ (Q^0) at around 1000 cm^{-1} overlaps with ν_1 (SO_4^{2-}). However, the sulfate vibration of ν_1 (SO_4^{2-}) can also be detected in the depolarized spectra (VH, Fig. 10b). Here, the intensity of $\nu_s(PO_3^{2-})$ Q^1 at 1060 cm^{-1} is strongly reduced with increasing x_1. Even $\nu_s(PO_3^{2-})$ does not seem to appear in glass D4. In contrast to its Raman resonance, $\nu_3(SO_4^{2-})$ exhibits a strong IR signal, i.e., within 1080 to 1220 cm^{-1} (D5) [20,47]. In glass D1, it is easy to identify $\nu_{as}(Q^0)$, $\nu_{as}(Q^1)$, $\nu_{as}(Q^2)$ at 1057, 1125 and 1182 cm^{-1} (Fig. 10c) [16,47,49,60]. But there is an overlap between these peaks with $\nu_3(SO_4^{2-})$ in D2, D3 and D4, similar to the Raman spectra. The location of $\nu_4(SO_4^{2-})$ in alkali sulfophosphate glasses was identified within ~610–655 cm^{-1} [16,47,56,57]. However, this is overlapped by ν_s(Al−F), corresponding to the NAPFS glass series. The bending modes of Al−F and P−O are found at 415 and 565 cm^{-1}, respectively [40,42]. Finally, the cation motion bands (where ν(Na−O) at 220 cm^{-1} was well-separated from ν(Al−F) in NAPF and NAPFS glasses) in FPS glasses, ν(M−O) (with M = Mg, Ca, Sr) cover a broad feature below 415 cm^{-1} [42], overlapping also the location of ν(Al−F) (Fig. 10c).

The ^{31}P MAS NMR spectra obtained for the set of FPS20 glasses are summarized in Fig. 11a. When $Sr(PO_3)_2$ was replaced by $Sr(SO_4)_2$, the ratio between P/F decreases, leading to the transformation of Q^1 into

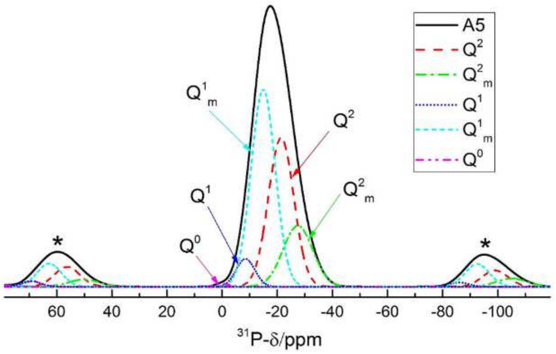

Fig. 5. ^{31}P MAS-NMR spectrum of $60NaPO_3$–$40AlF_3$ (A5). Dash curves indicate the deconvolution into individual Gaussian components. Q^0, Q^1 and Q^2 are referred to phosphate groups with NBOs coordinated by Na^+ only. Q^1_m and Q^2_m are denoted to phosphate groups with NBOs linked to both Na^+ and Al^{3+} ions.

Q^0. Analyzing NMR spectra of these glasses is compromised as compared to the case of NAPFS because the observed chemical shift is affected by the simultaneous presence of three divalent cation species, Mg^{2+}, Ca^{2+} and Sr^{2+}, instead of only the single species of Na^+. Assignment of Q^0, Q^1 and Q^2 units of the magnesium polyphosphate has been reported at around ~ (− 1, − 2.4), (− 14, − 16) and (− 29, − 32) ppm, respectively [58,61,62]. Similarly, phosphate groups of calcium phosphate glasses were reported with chemical shifts of about 2.4, (− 8, − 10) and (− 25, − 28) ppm [61,63]. The deconvolution at (− 7, − 9) and (− 21, − 26) in the resonance spectra of strontium phosphate glasses was assigned to Q^1 and Q^2 units, respectively [64]. Taking into account these and further studies [59], we simplified to the average values corresponding to Mg^{2+}, Ca^{2+} and Sr^{2+} cations. The resulting deconvolution data are summarized in Table 5. Similar to NAPFS glasses, besides Q^0, Q^1 and Q^2, also Q^0_m and Q^1_m in P—O—Al linkages were fit in this procedure. Because the content of Q^2 was generally low, we did not deconvolute its band further into Q^2_m. The obtained data correspond-well to the previous vibrational spectroscopic analyses (Fig. 12).

3.3. Intermediate-range structural heterogeneity

Anion mixing in sulfophosphate glasses has previously been reported to cause non-random distribution of sodium and zinc cation species [16,65]. Here, we used analyses of the low-frequency Raman vibrations to obtain further indications of such behavior also for the more complex case of three-fold anion mixing. For the determination of the Boson peak position, all Raman spectra were corrected for air scattering. A constant baseline was subtracted individually. In order to compare the intensities of spectra mainly in the low frequency region ($\omega < 200\ cm^{-1}$) individual bands of each sample were normalized over the integral intensity of all bands in this sample. This approach was chosen because of the complexity of the glass systems (Table 6).

To rule-out the temperature dependence of the Raman spectra, the measured intensity $I_{expt}(\omega, T)$ can be converted into the reduced Raman intensity. Shuker and Gammon proposed a model [66] which makes it possible to connect the excess of vibrational density of states $g(\omega)/\omega^2$ to this reduced intensity by means of a coupling coefficient which takes the following form:

$$I^{red}(\omega) = \frac{I_{expt}(\omega, T)}{[n(\omega, T) + 1]\omega} = C(\omega)\frac{g(\omega)}{\omega^2} \tag{8}$$

where $n(\omega,T) = [\exp(\hbar\omega/kT) - 1]^{-1}$ is the Bose-Einstein population factor or occupation number for the frequency ω and the temperature T, ħ and k are the reduced Planck and Boltzmann constants, respectively. The intensity of Raman scattered light depends not only on the vibrational density of states, but also on the coupling between photons and vibrations. C(ω) is the coupling function between light and the vibrational mode of frequency ω of the system. C(ω) is proportional to ω^α with $\alpha \in [0,2]$ depending on whether the excess of vibrational density of states (VDOS) arises from acoustic modes, local optical modes or hybrid modes. It is considered that there is no significant effect of the C(ω) on the estimation or interpretation of the Boson peak in the glass systems in this study.

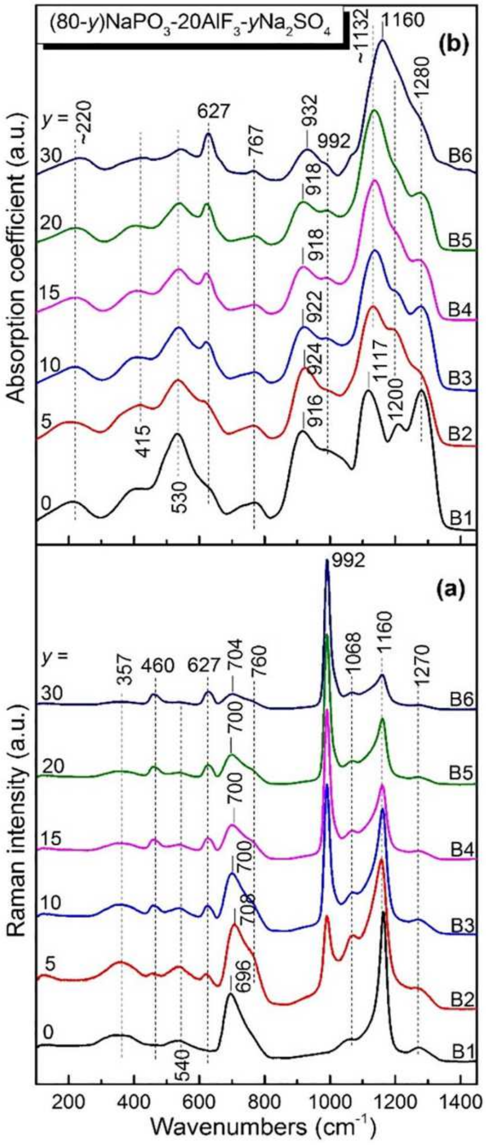

Fig. 6. Raman (a) and IR (b) spectra of NAPFS1 glasses.

The Stokes-side of the reduced low-frequency Raman spectra is shown in Fig. 13 for various samples of the FPS10 sub-series. To estimate the Boson peak frequency ω_{BP}, it is necessary to use a function which reproduces well the reduced intensity $I^{red}(\omega)$ and takes into consideration the asymmetric shape of the Boson peak. Usually in literature a log-normal function is used, the terms of this function are different according to the publications but are often very poorly explained [67,68]. For the present case, we used a log-normal function with well-explained terms,

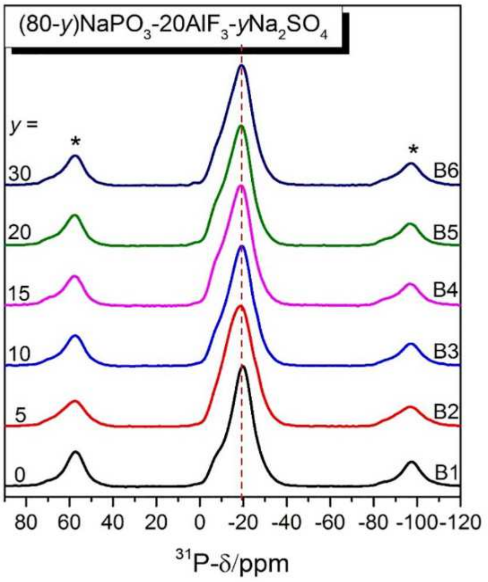

Fig. 7. ^{31}P MAS NMR spectra of NAPFS1 glasses. Spinning side-bands are marked with asterisks.

$$I(\omega) = \mathrm{A}\ \exp\left\{-ln(2)\left[\frac{ln\left(1+2\alpha\frac{\omega-\omega_{BP}}{\mathrm{w}}\right)}{\alpha}\right]^2\right\} + I_0 \tag{9}$$

Here, A is the amplitude, α is a parameter that describes the asymmetry of the function, w is the width of the function and ω_{BP} is the position of the center of Boson peak, I_0 is a parameter of reference and adjustment.

The origin or the interpretation of the Boson peak in glasses has been highly debated over the last decades. Currently, there is a general agreement that the Boson peak is a manifestation of disorder on intermediate or higher structural length scale [69–72]. Several theoretical models have been proposed to interpret the excess vibrational contribution leading to the appearance of the Boson peak [73]. The non-continuous vitreous structure model developed by Duval gives an interpretation of the presence of this excess of state density [74]. The Boson peak would be the signature of structural inhomogeneity on the scale of a few nanometers, due to the similarity of low-frequency Raman scattering spectra of glasses with those of heterogeneous materials, e.g., containing nanoparticles. The model therefore postulates the existence of "cohesive domains" within which the atoms would be more strongly linked to each other than the atoms outside these domains. According to the model in Ref. [74], and also Ref. [75], the average length scale of dynamic heterogeneity ξ ("*cohesive domains*") can be estimated from the low-frequency vibrational spectrum with the following expression.

$$\xi = c_T/2\pi c\omega_{\mathrm{BP}} \tag{10}$$

Here, c_T is the transverse sound velocity. The value of ξ is typically about 1–5 nm in the case of inorganic glasses and 2–3 nm in the case of polymers, agreeing well with the dynamic heterogeneity length scale for the structural relaxation obtained from 4-dimensional NMR [32].

Fig. 14a and b display the evolution of the Boson peak frequency ω_{BP} within the FPS, NAPF and NAPFS-glass series as a function of the addition of different chemical species. In the FPS glass series, the frequency of the Boson peak ω_{BP} for the samples of the sub-series FPS15 is greater than those of FPS20 and FPS10 series for the same $SrSO_4$ content. However, a clear trend of a decreasing frequency ω_{BP} with increasing $SrSO_4$ content can be observed for all glasses. Regarding NAPF and NAPFS-glass series, two trends are observed; first in NAPFS1 and NAPFS2 the frequency of the Boson peak ω_{BP} shifts towards low values with increasing Na_2SO_4 content while in NAPF the Boson peak shifts towards high frequencies with increasing AlF_3 content.

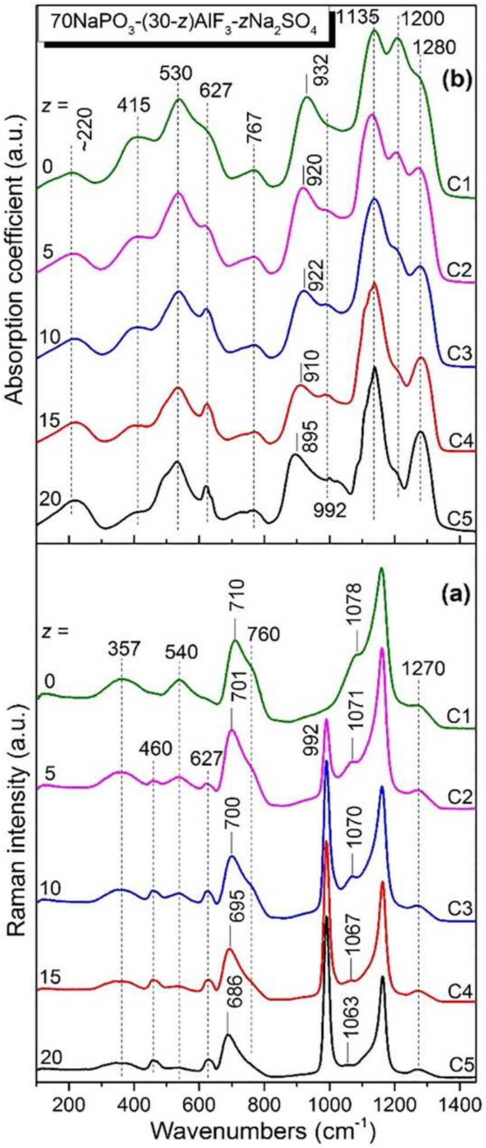

Fig. 8. Raman (a) and IR (b) spectra of NAPFS2 glasses.

According to Ref. [74], the frequency of the Boson peak ω_{BP} is inversely proportional to the average size ξ of the heterogeneous domains. Thus, a displacement of the position of the Boson peak towards higher frequency reflects higher homogeneity of the glasses and vice versa.

The differences in heterogeneity in the present glass series could probably be explained by a greater distortion in the network when adding the different chemical constituents. It seems intuitive to conclude that in the NAPF series, the increasing content of AlF_3 increases the extent of structural cross-linking, thus covering interstitial regions between domains of higher elasticity and, eventually, resulting in apparently higher homogeneity of the glass material. On the other side, higher ionicity with higher extent of anion mixing (simultaneous

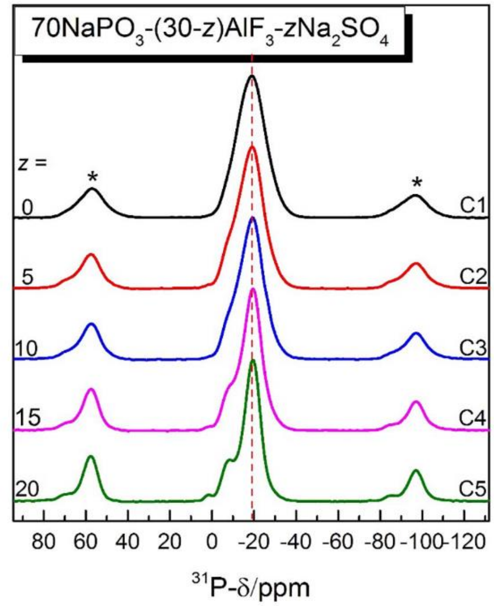

Fig. 9. ^{31}P MAS NMR spectra of NAPFS2 glasses.

presence of anions with notably different size, field strength and bond localization) would result in a higher tendency of non-random ion distribution and, thus, higher heterogeneity.

3.4. Model of the structure of mixed-anion fluoro-sulfo-phosphate glasses

From the above considerations, a model for the structure of fluoro-sulfo-phosphate glasses with high degree of anion mixing is derived (see Fig. 15). First, regular observations made by Raman and IR spectroscopy reveal the dominance of ionic interaction and the nature of the contributing ionic species. This agrees with the state of knowledge regarding related fluoro-phosphate, phosphate and sulfo-phosphate glasses as reviewed above: phosphate occurs primarily in the form of Q^0 and Q^1 groups. Depending on the phosphate content, also Q^2 is present, especially in the NAPF(S) series. The introduction of fluoride, in the presence of Al^{3+}, leads to the formation of edge-sharing AlF_6 octahedra. Furthermore, through formation of P—F-bonds, some of the phosphate groups are transformed into fluoro-phosphate groups of the type PO_3F.

There is no evidence in our data that the sulfate anion forms any super-structural units with phosphate or fluoride groups. Instead, we may consider the sulfate anion in comparison to a Q^0 group (Fig. 16): both species have very similar size [76]. However, Q^0 has three negative charges (PO_4^{3-}) where SO_4^{2-} has only two. Together, these facts lead to a much weaker field around the sulfate anion, and a lower degree of bond localization (directionality). Therefore, compared to Q^0 the environment of a quasi-spherical SO_4^{2-} group has a lower energy density and a notably higher polarizability. Considering the length of an S—O (or P—O) bond, the volume which is occupied by each group (length scale Δ_{SP} and $\Delta_P$in Fig. 16) together with its neighboring cations is in the range of a cubic nanometer. This compares-well with the length scale ξ which is extracted from the Boson frequency. We may therefore take the trends in ω_{BP} as direct evidence for the effect of SO_4^{2-} in local structural expansion. Also the strong tendency of FS melts to crystallize is confirming this picture: here, the contrast in field strength between both anion species is even higher (with an about fourfold anion polarizability of SO_4^{2-} as compared to F^-). This asymmetry leads to an even stronger tendency of non-random ion distribution and, ultimately, crystallization of the fluoride salt.

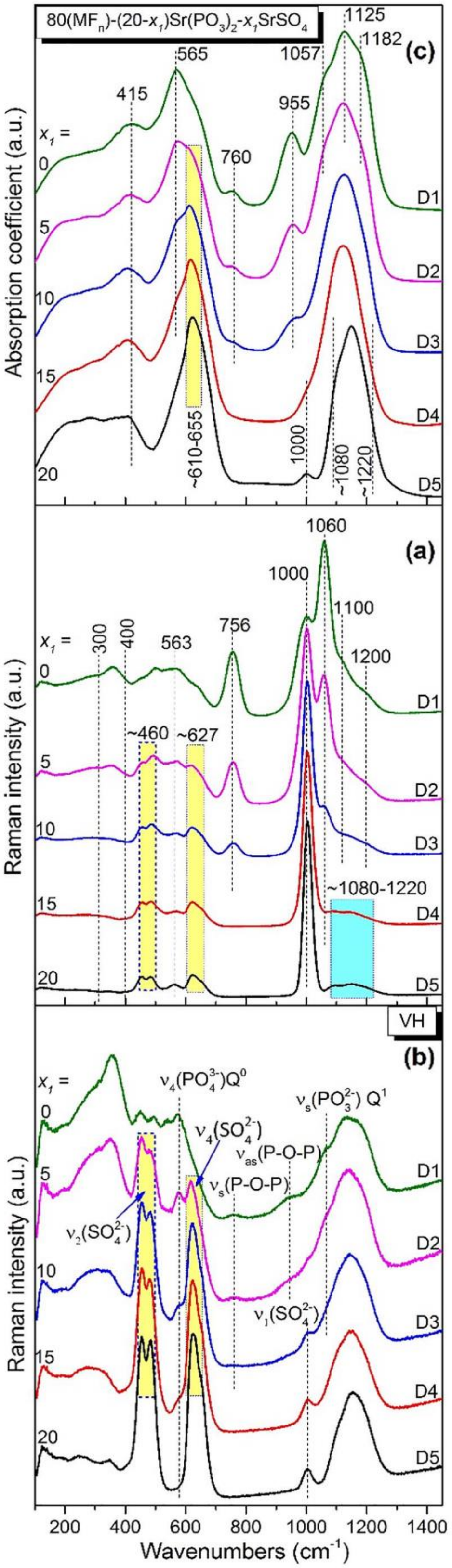

(caption on next page)

Fig. 10. Raman (a), depolarized (VH) Raman (b), and IR (c) spectra of FPS20 glasses. For nominal composition see Table 4.

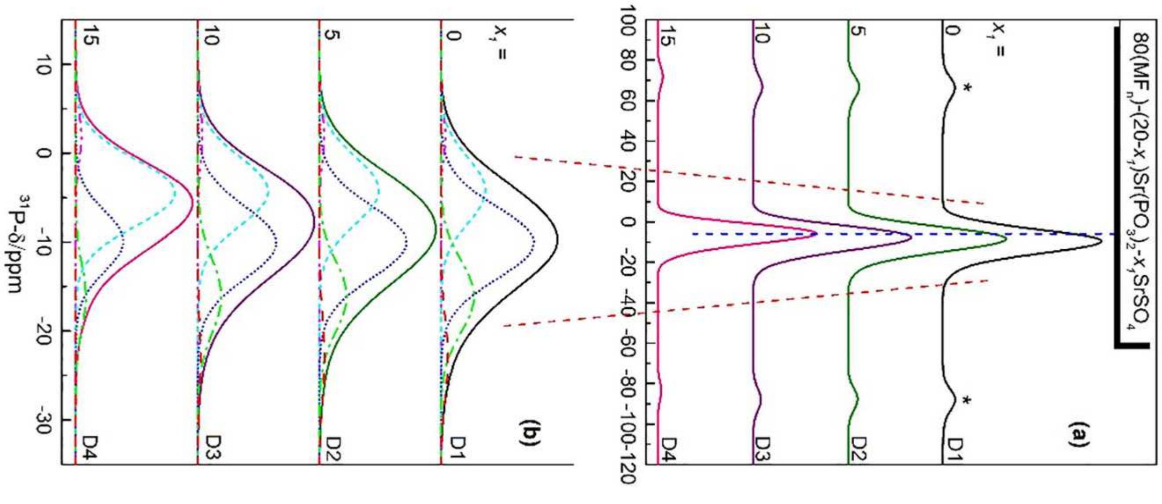

Fig. 11. (a) ^{31}P MAS NMR spectra of FPS20 glasses. Spinning sidebands are indicated by asterisks. (b) ^{31}P MAS NMR spectra deconvolutions. For nominal composition see Table 4.

4. Conclusions

We show that phosphate glasses exhibit high solubility for secondary anion species such as sulfate and fluoride groups. This enables the preparation of multi-anion glasses, in bulk form and mostly without the need for rapid quenching. Even equimolar anion mixing ratios can be achieved without notably compromising the glass forming ability. At the same time, addition of sulfate reduces the glass transition temperature, while fluoride leads to an increase of T_g. Vibrational spectroscopy at low and high frequencies, and NMR analysis were employed to obtain general information on the structure of these glasses. On short range, they exhibit primarily ionic bonding among the different

Table 5
^{31}P MAS-NMR lineshape fitting parameters for FPS glasses.

Series	Glass	Variable		Q^0			Q^0_m			Q^1			Q^1_m			Q^2_m			$Q^0_{0,m}$: $Q^1_{0,m}$: Q^2_m
				δ (ppm)	fwhm (ppm)	Area (%)	δ (ppm)	fwhm (ppm)	Area (%)	δ (ppm)	fwhm (ppm)	Area (%)	δ (ppm)	fwhm (ppm)	Area (%)	δ (ppm)	fwhm (ppm)	Area (%)	
80(MF$_n$)-(20-x_1)Sr(PO$_3$)$_2$-x_1SrSO$_4$																			
FPS20	D1	x_1	0	2.00	6.3	1.51	− 4.20	8.7	21.18	− 10.08	9.5	53.41	− 16.1	9.5	19.48	− 23.00	10.2	4.42	22.69: 72.89: 4.42
	D2		5	1.90	6.5	1.73	− 4.20	8.9	29.35	− 10.00	9.5	50.11	− 16.1	9.2	15.47	− 23.00	10.5	3.34	31.08: 65.58: 3.34
	D3		10	1.90	7.0	1.89	− 4.30	9.0	36.27	− 10.06	9.5	45.92	− 16.1	9.8	14.35	− 23.00	9.0	1.57	38.16: 60.27: 1.57
	D4		15	1.90	6.5	2.72	− 4.45	8.8	63.50	− 9.90	8.0	27.83	− 16.1	8.3	5.95	–	–	0.00	66.22: 33.78: 0.00
85(MF$_n$)-(15-y_1)Sr(PO$_3$)$_2$-y_1SrSO$_4$																			
FPS15	E1	y_1	0	2.00	7.9	1.86	− 4.20	8.9	30.53	− 9.90	9.8	48.01	− 16.0	10.4	17.21	− 23.00	10.0	2.39	32.39: 65.22: 2.39
	E2		5	2.00	7.0	2.55	− 4.35	8.7	59.20	− 9.70	8.1	31.15	− 16.0	8.4	6.61	− 23.00	8.0	0.49	61.75: 37.76: 0.49
	E3		7.5	1.90	7.0	3.46	− 4.30	8.7	66.41	− 9.80	8.0	25.87	− 16.0	8.0	4.26	–	–	0.00	69.87: 30.13: 0.00
	E4		10	2.00	7.6	1.29	− 4.00	9.5	79.93	− 9.90	8.5	16.62	− 16.0	8.0	2.16	–	–	0.00	81.22: 18.78: 0.00
90(MF$_n$)-(10-z_1)Sr(PO$_3$)$_2$-z_1SrSO$_4$																			
FPS10	F1	z_1	0	2.00	6.5	1.93	− 4.30	8.6	34.51	− 9.95	9.0	43.77	− 16.0	8.5	16.67	− 23.00	9.0	3.12	36.44: 60.44: 3.12
	F2		3	2.00	6.7	3.09	− 4.40	8.5	58.17	− 9.80	8.0	31.32	− 16.0	8.0	6.67	− 23.00	8.0	0.75	61.26: 39.99: 0.79
	F3		5	2.00	6.7	2.21	− 4.20	9.0	71.82	− 9.90	8.0	22.34	− 16.0	8.2	3.63	–	–	0.00	74.03: 25.97: 0.00
	F4		7	2.20	7.0	2.51	− 4.10	9.6	79.48	− 9.80	8.5	15.79	− 16.0	8.0	2.22	–	–	0.00	81.99: 18.01: 0.00
Error analysis				± 0.1	± 0.5	± 0.2	± 0.15	± 0.5	± 2	± 0.15	± 0.5	± 2	± 0.1	± 0.5	± 1	± 0.1	± 0.5	± 0.3	

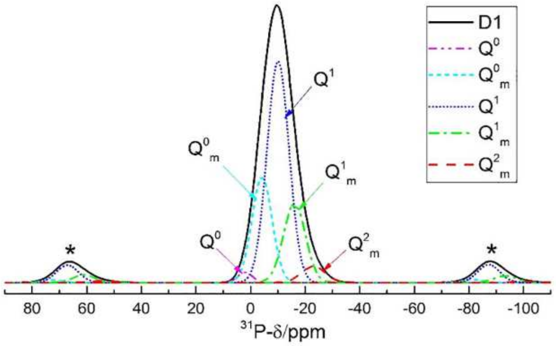

Fig. 12. ^{31}P MAS-NMR spectrum of glass D1 ($x = 0$). Dashed curves indicate the deconvolution into individual Gaussian components. Q^0 and Q^1 are referred to phosphate groups with NBOs coordinated by M^{2+} ions only (M = Mg, Ca and Sr). Q^0_m, Q^1_m and Q^2_m refer to phosphate groups with NBOs linked to both M^{2+} and Al^{3+} ions. For nominal composition see Table 4.

Table 6
Frequencies and assignments of Raman and infrared bands collected in this work for FPS glasses.

Raman (cm^{-1})	VH-polarized Raman (cm^{-1})	Infrared (cm^{-1})	Assignment	References
$1080–1220_{(w)}$		$1080–1220_{(vs)}$	$\nu_3(SO_4^{2-})$	[20,47,56,57]
$1200_{(sh,w)}$			$\nu_s(PO_2^{-})$ Q^2	[16,47]
	$1182_{(vs)}$		$\nu_{as}(PO_2^{-})$ Q^2	
$1100_{(sh,w)}$		$1125_{(vs)}$	$\nu_{as}(PO_3^{2-})$ Q^1	[16,47,49,60]
$1060_{(w\text{-}vs)}$			$\nu_s(PO_3^{2-})$ Q^1	[40,41,58]
		$1057_{(s)}$	$\nu_{as}(PO_4^{3-})$ Q^0	[49]
$1000_{(m)}$			$\nu_s(PO_4^{3-})$ Q^0	[40,41,58]
$1000_{(vs)}$	$1004_{(w)}$		$\nu_1(SO_4^{2-})$	[20,47,56,57]
$756_{(m,s)}$	$760_{(w)}$		ν_s(P–O–P) Q^1	[59]
$627_{(m)}$		$\sim 610–655_{(s)}$	$\nu_4(SO_4^{2-})$	[20,47,56,57]
$563_{(w)}$			$\nu Al(O,F)_6$ and $\nu_4(PO_4^{3-})$ Q^0	[41,47,49]
	$578_{(sh,w)}$		$\nu_4(PO_4^{3-})$ Q^0	
		$565_{(w\text{-}s)}$	δ(P–O)	[42]
$460_{(m)}$			$\nu_2(SO_4^{2-})$	[20,47,56,57]
		$415_{(m)}$	δ(Al–F)	[40]
		$< 415_{(m)}$	ν(M-O) (M = Mg, Ca, Sr)	[42]
$300–400_{(m)}$			δ(P–O)	[41,42]

constituents, whereby the fluoride and sulfate anions seem to act as stabilizing ionic cross-linkers among highly-depolymerized phosphate entities. This is in general accordance with knowledge on related phosphate, sulfophosphate and fluorophosphate glasses. Low-frequency Raman scattering indicates characteristic variations on intermediate-range structure, where a shift in the Boson peak appears to correlate inversely with the increasing degree of asymmetry in anion field strength and bond localization: Q^0 and SO_4^{2-} groups have very similar size, but generate local environments with strongly different energy density. This seems to manifest in a lower Boson frequency for glasses containing sulfate anions.

We believe that the studied suite of glasses provides an interesting route for tailoring structural dynamics. Besides, the rich variety of ligand situations which may be generated within such multi-anion surroundings is of interest for hosting optically active cation species.

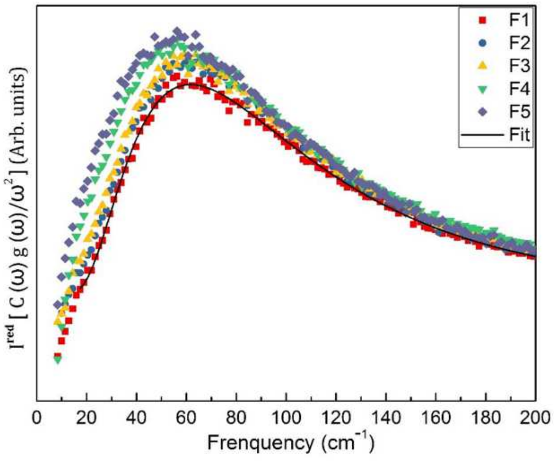

Fig. 13. Stokes-side of reduced low-frequency Raman spectra of the FPS10 sub-series after subtraction of quasi-elastic scattering (QES) contribution. The solid line represents a log-normal fit used to estimate the Boson peak's frequency. For nominal compositions see Table 4.

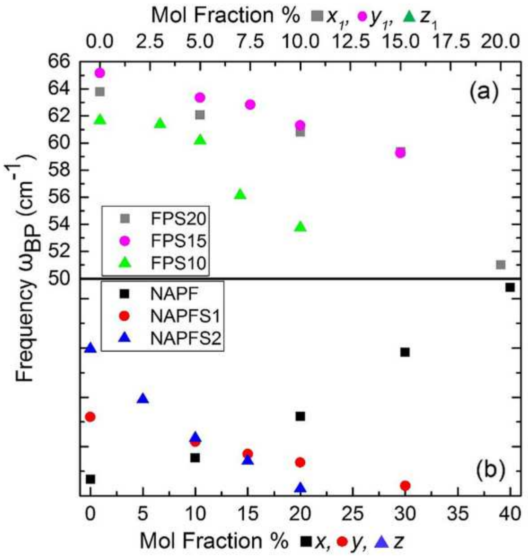

Fig. 14. (a) Variations of the boson peak frequency ω_{BP} as a function of $SrSO_4$ content (x_1, y_1, z_1) in FPS20, FPS15 and in FPS10 series respectively. (b) Variations of the Boson peak frequency ω_{BP} as a function of AlF_3 content (x) in NAPF, and Na_2SO_4 content (y, z) in NAPFS1 and NAPFS2 respectively. For nominal compositions see Tables 1 and 4.

Acknowledgements

This project has received funding from the European Research Council (ERC) under the European Union's Horizon 2020 research and innovation program (ERC grant UTOPES, grant agreement no. 681652). HQL is grateful to the Vietnam International Education Development (VIED) of the Ministry of Education and Training of Vietnam for financial support. The authors wish to thank their colleagues Sindy Fuhrmann, Uwe Hoppe, Doris Ehrt and Bruno P. Rodrigues for fruitful discussions relating to the structure of phosphate glasses and the potential role of sulfate additions. We further thank Gabi Moeller (sample preparation), Dietmar Güttler, Jelena Petrovic (thermal analyses), Christian Zeidler (optical analyses), Felix Lind and Doris Möncke (IR spectroscopy on FPS series), and Nadja Buchert (XRD) for valuable support in data acquisition.

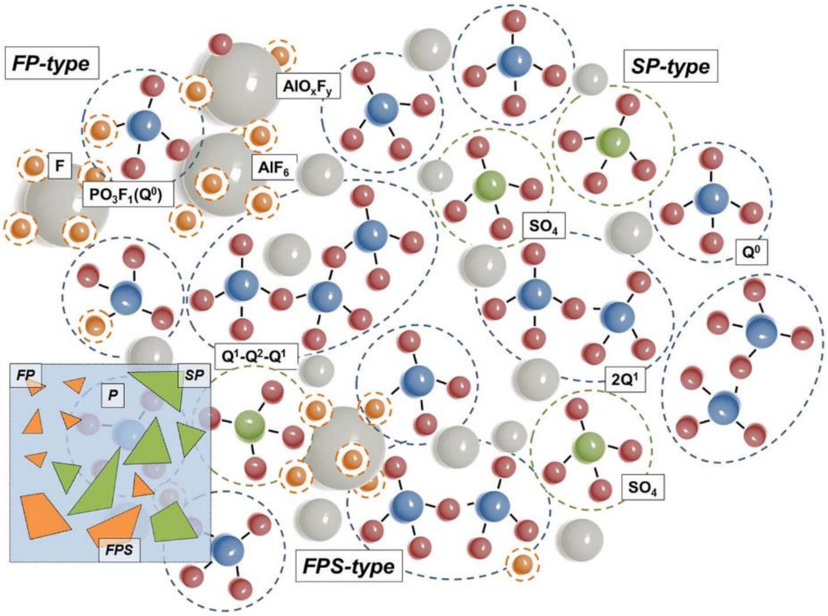

Fig. 15. Model of the structure of fluoro-sulfo-phosphate multi-anion glasses. The inset schematically depicts chemical heterogeneity in the three types of glass. The gray balls depict cation species.

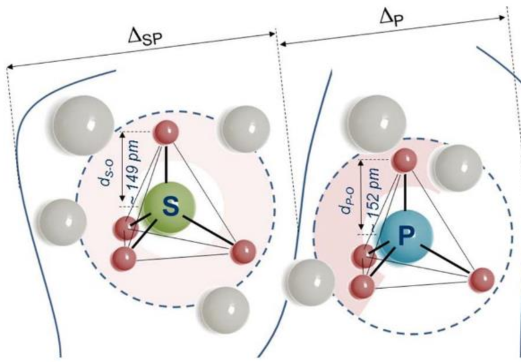

Fig. 16. Model of the structural vicinity of a phosphate Q^0 group and a sulfate anion (see text for details).

Appendix A. Supplementary data

Supplementary data to this article can be found online at https://doi.org/10.1016/j.jnoncrysol.2017.09.043.

References

[1] R.K. Brow, J. Non-Cryst. Solids 263 (2000) 1–28.
[2] W.H. Zachariasen, J. Am. Chem. Soc. 54 (1932) 3841–3851.
[3] A. Eisenberg, H. Farb, L.G. Cool, J. Polym. Sci., Part A-2 4 (1966) 855–868.
[4] U. Hoppe, J. Non-Cryst. Solids 195 (1996) 138–147.
[5] G.N. Greaves, S. Sen, Adv. Phys. 56 (2007) 1–166.
[6] B.P. Rodrigues, J. Deubener, L. Wondraczek, Front. Mater. (2016) 3.
[7] C. Calahoo, J.W. Zwanziger, J. Non-Cryst. Solids 460 (2017) 6–18.
[8] K. Griebenow, U. Hoppe, D. Möncke, E.I. Kamitsos, L. Wondraczek, J. Non-Cryst. Solids 460 (2017) 136–145.
[9] K. Griebenow, E.I. Kamitsos, L. Wondraczek, J. Non-Cryst. Solids 468 (2017) 74–81.
[10] Y. Onodera, S. Kohara, H. Masai, A. Koreeda, S. Okamura, T. Ohkubo, Nat. Commun. 8 (2017) 15449.
[11] M.J. Weber, J. Non-Cryst. Solids 123 (1990) 208–222.
[12] J.H. Campbell, T.I. Suratwala, J. Non-Cryst. Solids 263 (2000) 318–341.
[13] S. Tanabe, C. R. Chim. 5 (2002) 815–824.
[14] H. Ebendorff-Heidepriem, W. Seeber, D. Ehrt, J. Non-Cryst. Solids 163 (1993) 74–80.
[15] N. Da, S. Krolikowski, K.H. Nielsen, J. Kaschta, L. Wondraczek, J. Am. Ceram. Soc. 93 (2010) 2171–2174.
[16] N. Da, O. Grassme, K.H. Nielsen, G. Peters, L. Wondraczek, J. Non-Cryst. Solids 357 (2011) 2202–2206.
[17] S. Sirotkin, R. Meszaros, L. Wondraczek, Int. J. Appl. Glas. Sci. 3 (2012) 44–52.
[18] S. Striepe, N. Da, J. Deubener, L. Wondraczek, J. Non-Cryst. Solids 358 (2012) 1032–1037.
[19] D.C. Bassett, R. Meszaros, D. Orzol, M. Woy, Y.L. Zhang, K. Tiedemann, L. Wondraczek, S. Komarova, J.E. Barralet, J. Biomed. Mater. Res. A 102 (2014) 2842–2848.
[20] A. Thieme, D. Moncke, R. Limbach, S. Fuhrmann, E.I. Kamitsos, L. Wondraczek, J. Non-Cryst. Solids 410 (2015) 142–150.
[21] S. Tanabe, S. Yoshii, K. Hirao, N. Soga, Phys. Rev. B 45 (1992) 4620–4625.
[22] H. Ebendorff-Heidepriem, D. Ehrt, M. Bettinelli, A. Speghini, J. Non-Cryst. Solids 240 (1998) 66–78.
[23] J.F. Philipps, T. Topfer, H. Ebendorff-Heidepriem, D. Ehrt, R. Sauerbrey, Appl. Phys. B Lasers Opt. 72 (2001) 399–405.
[24] J.J. Zhang, D.B. He, Z.C. Duan, L.Y. Zhang, S.X. Dai, L.L. Hu, Phys. Lett. A 337 (2005) 480–486.
[25] D. Ehrt, T. Toepfer, Proc. SPIE 4102 (2000) 95.
[26] L.Y. Zhang, L. Wen, H.T. Sun, J.J. Zhang, L.L. Hu, J. Alloys Compd. 391 (2005) 156–161.
[27] P. Ebeling, D. Ehrt, M. Friedrich, Phosphorus Res. Bull. 10 (1999) 484–489.
[28] G.A. Kumar, A. Martinez, E. De La Rosa, J. Lumin. 99 (2002) 141–148.
[29] W.C. Wang, Q.H. Le, Q.Y. Zhang, L. Wondraczek, J. Mater. Chem. C 5 (2017) 7969–7976.
[30] P. Ebeling, PhD Thesis, University of Jena, (2000).
[31] A.A. Osipov, L.M. Osipova, Phys. Chem. Glasses: Eur. J. Glass Sci. Technol., Part B 56 (2015) 53–58.
[32] L. Hong, V.N. Novikov, A.P. Sokolov, J. Non-Cryst. Solids 357 (2011) 351–356.
[33] G. D'Angelo, G. Carini, C. Crupi, M. Koza, G. Tripodo, C. Vasi, Phys. Rev. B (2009) 79.
[34] A. Makishima, J.D. Mackenzie, J. Non-Cryst. Solids 12 (1973) 35–45.
[35] A. Makishima, J.D. Mackenzie, J. Non-Cryst. Solids 17 (1975) 147–157.
[36] R.D. Shannon, Acta Crystallogr., Sect. A: Found. Adv. 32 (1976) 751–767.
[37] S. Inaba, S. Fujino, K. Morinaga, J. Am. Ceram. Soc. 82 (1999) 3501–3507.
[38] D.R. Lide, Handbook of Chemistry and Physics, 74 ed., CRC Press, Boca Raton, 1993.
[39] R. Limbach, B.P. Rodrigues, D. Möncke, L. Wondraczek, J. Non-Cryst. Solids 430 (2015) 99–107.
[40] D. Möncke, D. Ehrt, L.L. Velli, C.P.E. Varsamis, E.I. Kamitsos, Phys. Chem. Glasses 46 (2005) 67–71.
[41] D. Möncke, D. Ehrt, L.L. Velli, C.P.E. Varsamis, E.I. Kamitsos, S. Elbers, H. Eckert, Phys. Chem. Glasses: Eur. J. Glass Sci. Technol., Part B 48 (2007) 399–402.
[42] L.L. Velli, C.P.E. Varsamis, E.I. Kamitsos, D. Möncke, D. Ehrt, Phys. Chem. Glasses 46 (2005) 178–181.
[43] L.F. Santos, R.M. Almeida, V.K. Tikhomirov, A. Jha, J. Non-Cryst. Solids 284 (2001) 43–48.
[44] D. Philip, B.L. George, G. Aruldhas, J. Raman Spectrosc. 21 (1990) 523–524.
[45] B.N. Nelson, G.J. Exarhos, J. Chem. Phys. 71 (1979) 2739–2747.
[46] Y.M. Lai, X.F. Liang, S.Y. Yang, J.X. Wang, B.T. Zhang, J. Mol. Struct. 1013 (2012) 134–137.

[47] D. Möncke, S. Sirotkin, E. Stavrou, E.I. Kamitsos, L. Wondraczek, J. Chem. Phys. (2014) 141.
[48] D. Palles, I. Konidakis, C.P.E. Varsamis, E.I. Kamitsos, RSC Adv. 6 (2016) 16697–16710.
[49] C.-P.E. Varsamis, E.I. Kamitsos, T. Minami, N. Machida, J. Phys. Chem. C 116 (2012) 11671–11681.
[50] S. Prabakar, R.M. Wenslow, K.T. Mueller, J. Non-Cryst. Solids 263 (2000) 82–93.
[51] D.S. Brauer, J. Jones, A. Clare (Eds.), Bio-Glasses: An Introduction, John Wiley and Sons, Ltd., 2012, p. 45.
[52] W.A. Dollase, L.H. Merwin, A. Sebald, J. Solid State Chem. 83 (1989) 140–149.
[53] J.P. Fletcher, S.H. Risbud, R.J. Kirkpatrick, J. Mater. Res. 5 (1990) 835–840.
[54] R.J.M. Silva, Structural Characterization of Fluorophosphate Glasses Using NMR Methodologies (Master thesis), Universidade de São Paulo, 2014.
[55] J. Schneider, S.L. Oliveira, L.A.O. Nunes, H. Panepucci, J. Am. Ceram. Soc. 86 (2003) 317–324.
[56] G.D. Chryssikos, E.I. Kamitsos, A.P. Patsis, J. Non-Cryst. Solids 202 (1996) 222–232.
[57] A. Hamilton, R.I. Menzies, J. Raman Spectrosc. 41 (2010) 1014–1020.
[58] G. Walter, J. Vogel, U. Hoppe, P. Hartmann, J. Non-Cryst. Solids 320 (2003) 210–222.
[59] R.K. Brow, C.C. Phifer, G.L. Turner, R.J. Kirkpatrick, J. Am. Ceram. Soc. 74 (1991) 1287–1290.
[60] D. Möncke, D. Ehrt, L. Velli, C.P.E. Varsamis, E.I. Kamitsos, Conference: XX, ICG, Kyoto, Japan, 2004.
[61] P. Hartmann, J. Vogel, B. Schnabel, J. Non-Cryst. Solids 176 (1994) 157–163.
[62] R.J. Kirkpatrick, R.K. Brow, SSNMR 5 (1995) 9–21.
[63] J.P. Fletcher, R.J. Kirkpatrick, D. Howell, S.H. Risbud, J. Chem. Soc. Faraday Trans. 89 (1993) 3297–3299.
[64] R. Pires, I. Abrahams, T.G. Nunes, G.E. Hawkes, J. Non-Cryst. Solids 337 (2004) 1–8.
[65] S. Reibstein, N. Da, J.P. Simon, E. Spiecker, L. Wondraczek, Phys. Chem. Glasses: Eur. J. Glass Sci. Technol., Part B 53 (2012) 61–67.
[66] R. Shuker, R.W. Gammon, Phys. Rev. Lett. 25 (1970) (222-&).
[67] B. Rossi, A. Fontana, M. Giarola, G. Mariotto, A. Mele, C. Punta, L. Melone, F. Toraldo, F. Trotta, J. Non-Cryst. Solids 401 (2014) 73–77.
[68] S. Chakraborty, V. Sivasubramanian, L.H. Singh, R.V. Krishnan, A.K. Sinha, J. Alloys Compd. 713 (2017) 95–107.
[69] H. Shintani, H. Tanaka, Nat. Mater. 7 (2008) 870–877.
[70] B. Champagnon, L. Wondraczek, T. Deschamps, J. Non-Cryst. Solids 355 (2009) 712–714.
[71] B. Mantisi, S. Adichtchev, S. Sirotkin, L. Rafaelly, L. Wondraczek, H. Behrens, C. Marcenat, N.V. Surovtsev, A. Pillonnet, E. Duval, B. Champagnon, A. Mermet, J. Phys. Condens. Matter 22 (2010) 025402.
[72] R. Zargar, J. Russo, P. Schall, H. Tanaka, D. Bonn, EPL (2014) 108.
[73] W. Schirmacher, J. Non-Cryst. Solids 357 (2011) 518–523.
[74] E. Duval, A. Boukenter, T. Achibat, J. Phys. Condens. Matter 2 (1990) 10227–10234.
[75] S.R. Elliott, Europhys. Lett. 19 (1992) 201–206.
[76] B. Gamoke, D. Neff, J. Simons, J. Phys. Chem. A 113 (2009) 5677–5684.

Supplementary Information

In Figs. S1-S2, we provide vibrational spectroscopic data of the sample series FPS10 and FPS15.

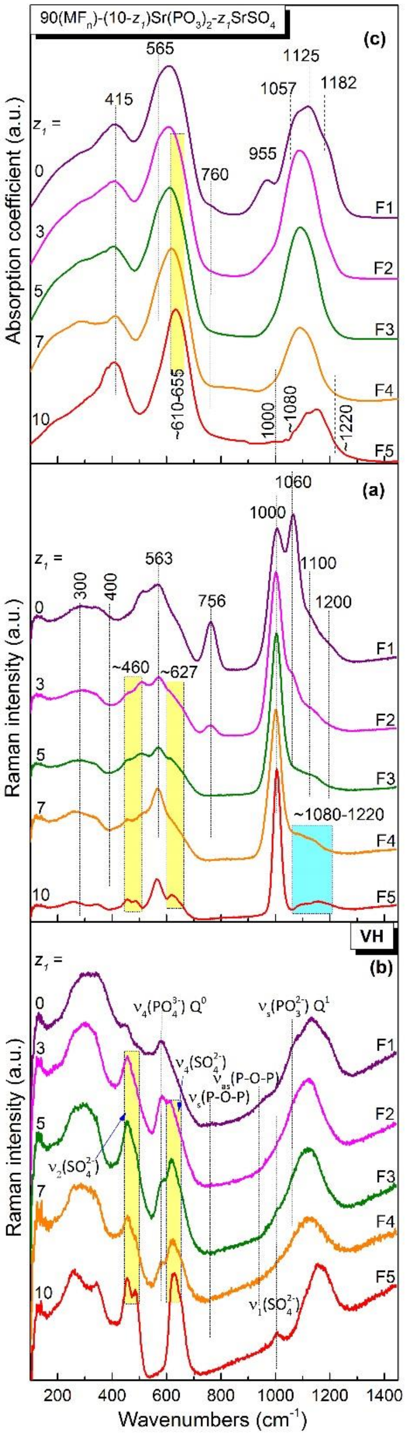

Figure S1: Raman (a), depolarized (VH) Raman (b), and IR (c) spectra of FPS10 glasses. For nominal composition see Table 4.

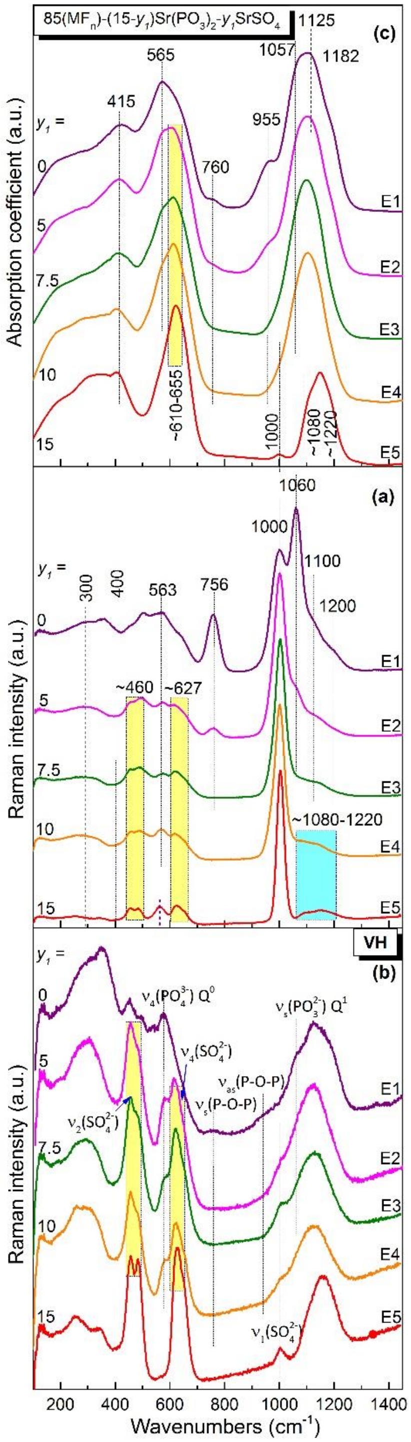

Figure S2: Raman (a), depolarized (VH) Raman (b), and IR (c) spectra of FPS15 glasses. For nominal compositions see Table 4.

3.2.2 Fluoride-sulfophosphate glasses as hosts for broadband optical amplification through transition metal activators

W. C. Wang, Q. H. Le, Q. Y. Zhang and L. Wondraczek, “Fluoride-sulfophosphate glasses as hosts for broadband optical amplification through transition metal activators”, J. Mater. Chem. C, 2017, 5, 7969-7976.

DOI: 10.1039/c7tc01853c

Unusually stable multi-anion glasses of the fluoride-sulfophosphate type (FPS) are introduced as a new host material for optically active cation species. Despite a notoriously low polymerization grade, anion mixing in this glass system enables facile manufacture of bulk or fiber devices which combine several advantages of fluoride and phosphate glasses while using the stabilizing effect of sulfate additions. Using the example of chromium doping, we demonstrate broad red photoluminescence at 734 nm and inhomogeneous broadening of the R-line at 694 nm, originating from the $^4T_2$ - $^4A_2$ and ^2E - $^4A_2$ transitions of Cr^{3+}, respectively. The luminescence mechanism is further analyzed on the basis of the corresponding Tanabe–Sugano diagram. Tailored through chemical composition, internally nucleated precipitation of a nanocrystalline fluoride phase enables switching between high-field and low-field configurations of the Cr^{3+} ion, resulting in the specific emission properties and setting the path towards FPS-based optical devices.

Journal of
Materials Chemistry C

PAPER

View Article Online
View Journal | View Issue

Check for updates

Cite this: *J. Mater. Chem. C*, 2017, **5**, 7969

Fluoride-sulfophosphate glasses as hosts for broadband optical amplification through transition metal activators†

W. C. Wang,[ab] Q. H. Le,[a] Q. Y. Zhang[b] and L. Wondraczek*[a]

Unusually stable multi-anion glasses of the fluoride-sulfophosphate type (FPS) are introduced as a new host material for optically active cation species. Despite a notoriously low polymerization grade, anion mixing in this glass system enables facile manufacture of bulk or fiber devices which combine several advantages of fluoride and phosphate glasses while using the stabilizing effect of sulfate additions. Using the example of chromium doping, we demonstrate broad red photoluminescence at 734 nm and inhomogeneous broadening of the *R*-line at 694 nm, originating from the $^4T_2 \rightarrow {}^4A_2$ and $^2E \rightarrow {}^4A_2$ transitions of Cr^{3+}, respectively. The luminescence mechanism is further analyzed on the basis of the corresponding Tanabe–Sugano diagram. Tailored through chemical composition, internally nucleated precipitation of a nanocrystalline fluoride phase enables switching between high-field and low-field configurations of the Cr^{3+} ion, resulting in the specific emission properties and setting the path towards FPS-based optical devices.

Received 28th April 2017,
Accepted 26th June 2017

DOI: 10.1039/c7tc01853c

rsc.li/materials-c

1. Introduction

Transition metal doped glasses have been receiving continuous attention in the quest for new tunable fiber lasers.[1,2] In particular, different chromium ions have been considered as interesting species, taking into account their prominent role in crystalline laser gain media, *e.g.*, Cr^{3+} in ruby lasers,[3] Cr^{4+} in YAG and forsterite,[4] or Cr^{2+} in the chalcogenide matrix.[5] While chromium ions occur in a broad variety of valence states (ranging from "+1" to "+6"), in oxide glasses, only Cr^{3+}, Cr^{5+} and Cr^{6+} are typically found.[6–8] Of particular interest are the broad near-infrared emission bands and the narrow visible emission bands which derive from the $^4T_2$ level (low-field sites) and the ^2E level (high-field sites) of Cr^{3+}, respectively. Their energetic position is dominated by the ligand-dependence of the underlying *d–d* transition.[9–11] Broadband emission at approximately 900 nm, originating from Cr^{3+} ions in a phosphate glass matrix, was reported by Sharp *et al.* as early as 1969.[12] Since then, many authors have been considering the subject. For example, Murata *et al.* provided a systematic study on the relationship of composition and redox reactions among chromium ions in multicomponent oxide glasses, reporting a redox shift from Cr^{3+} to Cr^{6+} with increasing matrix basicity.[13] Also in the form of optical fibers, significant progress has been made. For example, Cr^{3+}-doped silica fibers with a gain bandwidth covering the entire transmission range of low loss and low dispersion windows were reported in 2012, aimed at increasing the data transmission capacity in the next generation of optical communication systems.[14] Cr^{3+}-doped glass ceramic fibers were also demonstrated for potential application in broadband tunable fiber lasers.[15] However, despite these milestone findings, the preparation of efficient fiber lasers from a Cr^{3+}-doped glass has not yet been successful. Therefore, the search for suitable host materials continues.

Traditionally, phosphate glasses have been among the most prominent choices as host species for solid-state (glass) lasers, primarily due to high rare earth solubility and low phonon energy.[16–18] The structural backbone of these materials comprises a network of PO_4 tetrahedra in which three of the oxygen species provide the ability to link to a neighboring tetrahedron, while the remaining anion is linked to the central phosphorous *via* a double bond. This configuration is the fundamental basis for the specific optical properties of phosphate glasses, in particular, electronic polarizability. Secondary cation species (including rare earth or transition metal ions) can be added to this ensemble as so-called modifiers, that is, introducing chemical bonds with a more ionic character. Then, in order to charge-balance these modifier ions, not all three available edges of the phosphate tetrahedron are interconnecting, but non-bridging oxygen species are formed which interrupt the

---

[a] *Otto Schott Institute of Materials Research, Friedrich Schiller University Jena, Fraunhoferstraße 6, 07743 Jena, Germany. E-mail: lothar.wondraczek@uni-jena.de*

[b] *State Key Laboratory of Luminescent Materials and Devices, Guangdong Provincial Key Laboratory of Fiber Laser Materials and Applied Techniques, and Institute of Optical Communication Materials, South China University of Technology, Guangzhou 510641, P. R. China*

† Electronic supplementary information (ESI) available. See DOI: 10.1039/c7tc01853c

phosphate network. This is expressed in the *Q*-group nomenclature, where $Q^{n=0...3}$ refers to a phosphate entity with *n* bridging oxygen species. If $n = 2$ (the metaphosphate composition), the network comprises phosphate chains and/or rings. For $n > 2$ (ultraphosphates), these chains are crosslinked. When $n = 0...1$ (pyro-/orthophosphates), the glass comprises isolated phosphate islands in an ionic matrix. The modifying species locate between the super-structural units. Depending on charge, size and electronic structure, they interact with the local phosphate network to a different extent. Furthermore, non-linear cross-interaction among the cations leads to specific mixing effects, which are frequently made use of in the design of certain macroscopic properties.[19–21] It was found that the stability of phosphate glasses can be enhanced significantly through the introduction of sulfate anions, $[SO_4]^{2}$, both in terms of rheology (liquid fragility) and chemical properties (corrosion resistance).[22–24] Beyond this immediate, practical interest, these sulfophosphate glasses have also been identified as interesting host species for transition metal ions as they provide a very peculiar local environment of sulfate as well as phosphate entities in which ligand field splitting and local redox deviate from conventional molecular field considerations.[23,25] However, especially at high sulfate content, liquid–liquid phase separation has been observed, which prevents their use as fiber or bulk optical materials.[26]

In the present study, this leads to further extension of this chemical system by adding fluoride as another structural entity, creating fluoride-sulfophosphate glasses (FPS). As a well-known counterpart, fluorophosphate (FP) glasses combine many properties which are desired in high-performance optical applications, *e.g.*, high optical transmittance across the ultraviolet (UV) to near-infrared (NIR) spectral range, very low partial dispersion and linear and non-linear refractive index[27] (thus, high laser damage threshold), low phonon energy and the ability of incorporating large amounts of optically active species, based on the chemical and electrical properties of the fluoride anion relative to those of oxygen. Applications have been evolving on the basis of these properties primarily on the areas of (passive) optical lenses, fiber optical amplifiers, lasers and frequency converters,[28,30] with current research focusing on the effects of mixed doping with various rare earth species,[31] and also on modifying the glass matrix through the addition of further anion species.[27,32,33] For example, Kumar *et al.* studied the effect of sulfate and borate additions on the optical properties of FP glasses, reporting that sulfate acts positively on luminescence efficiency of rare earth dopants.[34,35] Important in these considerations, when the introduction of new anion species leads to an improvement of thermal stability or, *e.g.*, mechanical performance, it must not adversely affect the spectroscopic properties of the dopant species. With this in mind, FPS glasses provide an extremely complex structural environment to optically active dopant species and, according to recent findings,[36] surprising glass stability and a broad processing window. Here, we exploit these properties in a new host material for chromium-based broadband optical activity. We compare a series of Cr^{3+}-doped FPS glasses to their sulfate-free FP counterparts with varying F : P : S and F : P ratios, respectively, by means of assessing their structural and optical properties. This shows that FPS glasses provide a promising material towards broadband tunable fiber lasers.

2. Experimental

Two sets of glasses were considered in the present study, *i.e.*, a fluoride sulfophosphate (FPS) and a reference fluorophosphate (FP) series. Molar compositions were selected by starting from alkaline earth FP, $(100 - x)(MgF_2, CaF_2, SrF_2, AlF_3) - x Sr(PO_3)_2$ ($x = 0, 2, 4, 10, 15$; denoted FP0, FP2, FP4, FP10, and FP15, respectively),[27–29] and subsequently replacing $Sr(PO_3)_2$ in the FP15 composition by $SrSO_4$, $85(MgF_2, CaF_2, SrF_2, AlF_3) - (15 - y)Sr(PO_3)_2 - y SrSO_4$ ($y = 5, 7.5, 10, 15$; denoted as FP10S5, FP7.5S7.5, FP5S10, and FP0S15, respectively). All glasses were doped by adding 0.05 mol% Cr_2O_3. Only $Sr(PO_3)_2$ was dried at 120 °C for 7 h before weighting, then 100 g batches using high purity raw materials were thoroughly mixed in a plastic bottle. Batches of 100 g were melted in a muffle furnace, in Pt crucibles at 1000–1100 °C for 2 h, cooled to 830–950 °C and poured into a preheated graphite mold. The subsequent annealing process was carried out at 440–510 °C for another 2 h, followed by cooling to room temperature at the furnace rate ($\sim$ 2 K min ^{1}). Deviating from this procedure, the compositions with poor glass forming ability (FP0, FP2, FP5S10 and FP0S15) were prepared through rapid quenching by pouring the melt onto cold copper plates and immediate pressing with another copper stamp. Subsequently, annealing of these samples followed the same procedure as above. After annealing, the glass samples which were obtained through the regular method were cut into two types of specimens, *i.e.*, 20 mm × 10 mm × 1 mm and 20 mm × 10 mm × 5 mm, and both sides were polished for further spectroscopic analyses and mechanical analyses, respectively. For the quenched samples of FP2 and FP5S10, the obtained plates were polished directly without further cutting. In the case of FP0 and FP0S15, polishing was not possible because the samples were too thin (0.5–0.6 mm), so that spectroscopic analyses were performed directly on unpolished samples. Remaining glass shards were ground and sieved for differential thermal analysis (DTA) and X-ray diffraction (XRD) analysis.

The glass density was tested through the Archimedes method at 20.5 °C using distilled water as the immersion liquid. XRD was conducted on a MiniFlex600 (Rigaku, Japan) X-ray diffractometer with Cu-Kα radiation ($\lambda = 1.5406$ Å) at a tube voltage of 40 kV and a tube current of 15 mA. The glass refractive index was evaluated with a Pulfrich refractometer on samples with a thickness of 5 mm. UV-Vis-NIR absorption spectra were recorded on a Cary 5000 (Agilent) double-beam spectrophotometer with a spectral resolution of 1.0 nm. The glass transition and characteristic temperatures of crystallization were analyzed on a Differential Thermal Analyzer instrument assembled by our laboratory. Structural analyses were done by Raman spectroscopy (Renishaw, UK) using a 488 nm Argon laser as the excitation source. Static luminescence spectra were recorded on a high-resolution spectrofluorometer (Fluorolog, Horiba Jobin-Yvon), using a continuous wave 450 W Xe lamp as the excitation source and a Hamamatsu R2658P photomultiplier tube for detection.

Finally, the elastic properties were characterized by ultrasonic echography on co-planar, optically polished glass plates. The longitudinal and transversal wave velocities, c_L and c_T, were determined with a piezoelectric transducer operating at frequencies of 8–12 MHz (Echometer 1077, Karl Deutsch GmbH & Co KG).

All measurements were performed at room temperature.

3. Results and discussion

3.1. Glass formation, optical absorption and basic physical properties

As noted in the Experimental section, with the exception of the low- or no-phosphate candidates, all compositions were readily cooled into visually transparent glasses without visible bubbles, inclusions or signs of crystallization. Sample photographs are provided in the inset of Fig. 1. As expected, Cr^{3+}-doping resulted in a green tint with increasing saturation for increasing phosphate content. For FP2 and FP5S10, the green appearance evolves into a light yellowish shade, and turns to red for FP0 and FP0S15. In the latter two samples, some turbidity is seen, indicating that these samples comprise at least two phases. The red color is similar to that of ruby, where it is caused by Cr^{3+} in the alkali matrix α-Al_2O_3, in a strained six-fold coordination.[37] This implies that also in the present case, Cr^{3+} ions enter into the strong ligand field of a crystalline precipitate.[38,39] Fig. 1 shows the UV-NIR absorption spectra which correspond to the above observations. In the regularly cast samples, there are two broad absorption bands, *i.e.*, at 439 nm and 640 nm, associated with the characteristic Cr^{3+}: $^4A_2 \rightarrow {}^4T_1$ and Cr^{3+}: $^4A_2 \rightarrow {}^4T_2$ transitions. A zoom at the red region reveals two distinct shoulder bands at ~647 nm and 680 nm, corresponding to Cr^{3+}: $^2T_1 \rightarrow {}^4A_2$ and Cr^{3+}: $^4A_2 \rightarrow {}^2E$ (see Fig. S1 in the ESI†). In addition to this, a further intense absorption band is observed at ~251 nm, attributed to the charge transfer state of Cr^{6+}, indicating a strongly oxidizing effect in the quenched samples, which leads to the formation of hexavalent chromium, Cr^{6+}.

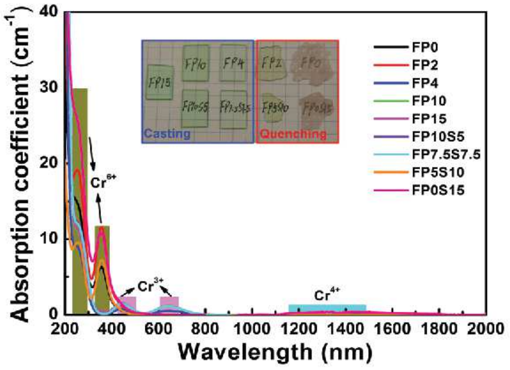

Fig. 1 Optical absorption spectra of chromium-doped FP and FPS glasses. The inset shows sample photographs (mesh spacing of 5 mm).

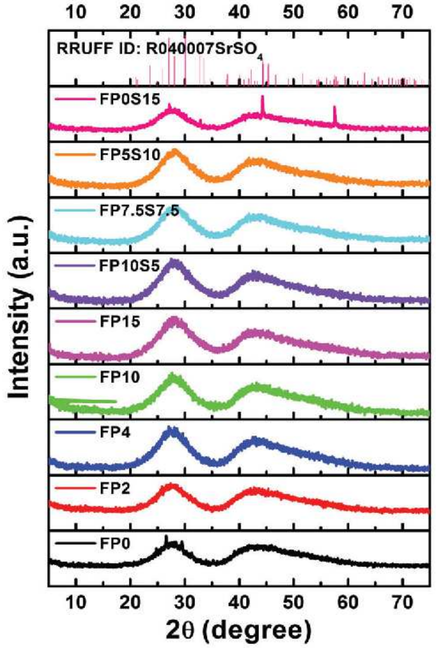

Fig. 2 XRD patterns of the chromium doped FP and FPS samples.

Noteworthily, further absorption peaks which could be characteristic of Cr^{4+} (in the spectral range of 1000–2000 nm) are detected in the quenched samples.

XRD was employed to verify the phase assembly of all samples. Diffraction patterns are shown in Fig. 2. For all samples, data are dominated by two broad, amorphous humps which reflect the glassy state. With the exceptions of FP0 and FP0S15, there are no sharp peaks which would indicate the presence of a secondary, crystalline phase. In the latter two samples, such peaks are present, that is, they are at least partially crystallized (what is in accordance with the previous optical inspection). Using Scherer's equation, a crystallite size of ~30–50 nm is approximated from the width of those diffraction peaks. Assignment to one or more specific crystallite phases is presently not possible due to the apparently low crystallite volume fraction and the unavailability of unambiguous reference data. Tentatively, a Celestine-type phase is identified in FP0S15, $SrSO_4$. For FP0, we expect one or more alkaline earth fluoride phases. Here, we speculate that the crystallite species comprise fluoride (FP0 and FP0S15) and sulfide compounds (FP0S15), subject to future analysis of the specific crystallization mechanism. The low crystallite size, high sample transparency and apparent internal nucleation suggest further exploration of corresponding glass ceramics, however, beyond the scope of the present study.

The selected physical properties of the two glass series are summarized in Table 1. Upon increasing the content of phosphate, the density of the present glasses continuously increases, *i.e.*, from 3.454 g cm ^{3} to 3.503 g cm ^{3}. When $Sr(PO_3)_2$ is replaced by $SrSO_4$, the density monotonically increases.

Table 1 Physical properties of FP and FPS glasses

Glass	Density	Refractive index (±0.0005)					Abbe's	Thermal parameters			Cutoff	Urbach		Elastic
	(g cm^{-3})	$n_{C'}$(643.84)	n_d(587.56)	n_e(546.06)	$n_{F'}$(479.98)	n_h(435.84)	number	T_g	T_x	T_p	wavelength (nm)	energy (eV)	Λth	modulus (GPa)
FP0	3.454	—	—	—	—	—	—	403	460	475	—	—	0.349	—
FP2	3.472	—	—	—	—	—	—	421	498	514	395	1.31	0.356	—
FP4	3.457	—	—	—	—	—	—	427	523	541	282	2.87	0.374	73.1 ± 0.6
FP10	3.427	1.4638	1.4652	1.4663	1.4690	1.4714	89.8 ± 17.3	445	—	—	294	3.57	0.390	76.3 ± 0.7
FP15	3.503	1.4896	1.4911	1.4925	1.4956	1.4985	81.9 ± 6.8	467	—	—	292	3.23	0.432	77.4 ± 0.7
FP10S5	3.527	1.4801	1.4816	1.4829	1.4871	1.4884	69.5 ± 5.0	448	—	—	296	3.59	0.388	75.4 ± 0.7
FP7.5S7.5	3.531	1.4726	1.4740	1.4753	1.4781	1.4808	86.1 ± 7.8	438	—	—	286	3.59	0.387	73.4 ± 0.7
FP5S10	3.540	—	—	—	—	—		425	558	584	398	1.19	0.386	—
FP0S15	3.544	—	—	—	—	—		387	465	468	—	—	0.383	—

All glasses exhibit comparably low refractive indices, in the range of 1.46–1.49, with Abbe's numbers within 69–89, that is, in the region between phosphate and fluoride-crown. Shifting from FP to FPS results in a slightly decreasing refractive index and decreasing Abbe's number.

For material processing and, for example, drawing of optical fibers, the thermal properties of the melt are of fundamental importance. The glass thermal stability is typically estimated from the characteristic temperatures, *i.e.*, the glass transition temperature T_g, the onset-temperature of crystallization T_x, and the temperature of the crystallization peak as found in a DTA scan, T_p (often associated with the maximum crystallization rate). The parameter of $\Delta T = T_x - T_g$ is then taken as the most accessible measure of glass stability, describing the temperature interval within which the super-cooled glass melt can be processed without the risk of immediate crystallization. A value of ΔT above 100 K is typically taken as an indicator of relative thermal stability such as required, *e.g.*, in a fiber drawing process. Fig. 3 displays the DTA curves of the present glasses from which the values of T_g, T_x and T_p were extracted (Table 1). For FP0, FP2, and FP0S15, ΔT is notably below 100 K, reflecting their previously observed tendency to crystallize (Experimental section). Similarly, also FP4 only narrowly reaches a ΔT of around 100 K. When sulfate is added to this composition such as in FP5S10, the glass stability is significantly enhanced. Beyond that, very high stability was found for melts with phosphate above 10 mol% and/or sulfate at or below 7.5 mol%, in which the crystallization peak could not be observed anymore in the employed experimental setting. T_g of the glasses increases significantly from 403 °C to 467 °C with increasing phosphate content, but decreases to 387 °C with the addition of sulfate. This reflects the more covalent character of bonding among the phosphate groups relative to the ionic sulfate units, which are only weakly crosslinked by the cations. In particular, this shows a significant reduction of the melting temperature while maintaining the stability of the sulfate-free glasses.

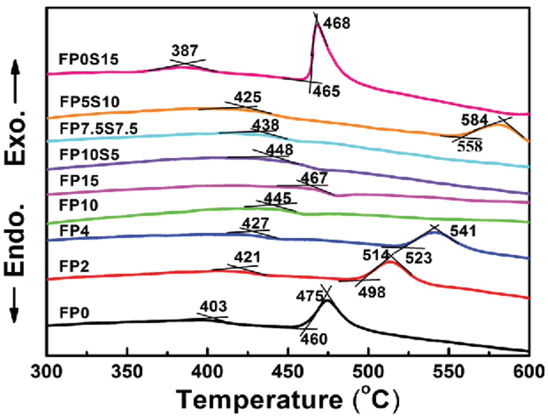

Fig. 3 Differential thermal analyses across the T_g region of FP and FPS glasses and melts.

All physical properties considered here, including glass density, refractive index, transition temperature, crystallization onset temperature, and elastic constants, are directly related to the substitution ratio between phosphate and sulfate.

For doping with transition metal elements, the local chemical properties of the matrix and, in particular, the anionic environment of the dopant are determining factors. The ability of cations to donate an electron is often approximated through mean-field approaches such as the concept of optical basicity Λ_{th}. The value of Λ_{th} is approximated from the weighted sum of the molar contributions of each component,[40]

$$\begin{aligned}\Lambda_{th} = {} & X(MgF_2)\Lambda(MgF_2) + X(CaF_2)\Lambda(CaF_2) + X(SrF_2)\Lambda(SrF_2) \\ & + X(AlF_3)\Lambda(AlF_3) + X(Sr(PO_3)_2)\Lambda(Sr(PO_3)_2) \\ & + X(SrSO_4)\Lambda(SrSO_4) \qquad (1)\end{aligned}$$

where X(i) is the molar fraction of component "i" and Λ(i) is its partial molar optical basicity. In FP glass, with an increase of phosphate content, the optical basicity of the glass increases gradually. Forming FPS by adding sulfate leads to a subsequent decrease in Λ_{th}. Data are summarized in Table 1.

3.2. Structural consideration

A structural model of FP glasses has been formulated on the basis of the ionic fluoride network into which orthophosphate (Q^0) and pyrophosphate (Q^1) groups are incorporated.[41] It has been deducted that preferential over the formation of P–F bonds, the fluorine anion associates with the Al^{3+} cation to form Al–F bonds. This leads to the formation of mixed chains of $Al(O,F)_6$ and PO_4 tetrahedra. FP glasses thus present a transition from an ionic fluoride ensemble to the polymer-like phosphate

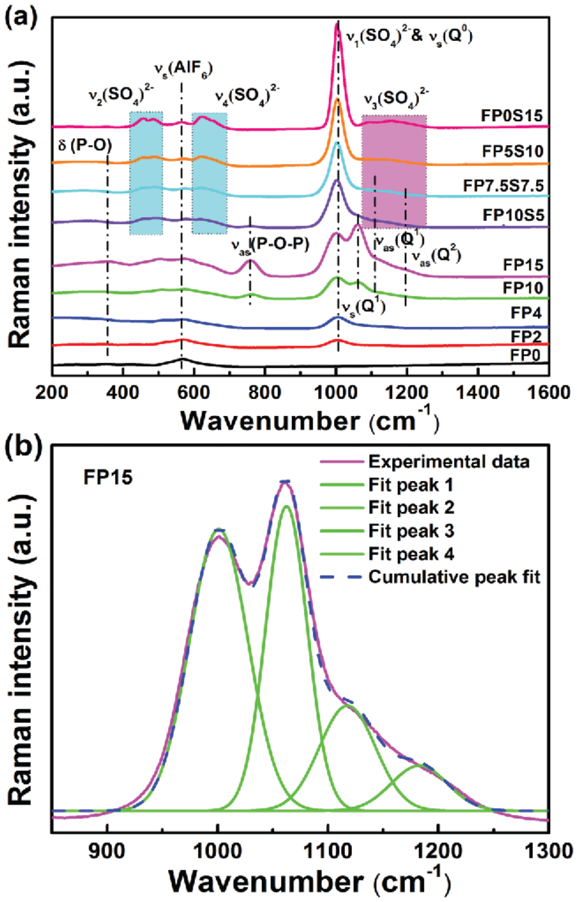

Fig. 4 (a) Raman spectra of the FP and FPS glasses and (b) example of Gaussian deconvolution on FP15 (see the text for assignment details).

network. When additional sulfate groups are introduced, the glass structure becomes more complex. In Fig. 4, Raman spectra of some FP and FPS glasses are shown to illustrate this argument. Bands were assigned on the basis of ref. 42. In addition, the broad signal at 568 cm^{-1} (in FP0) is attributed to the symmetric stretching vibration of the AlF_6 octahedron.[40] With an increase of phosphate content and a decrease of aluminum fluoride content, this peak becomes weaker and broadens due to the formation of $Al(F,O)_6$ octahedra, thereby increasing the overlap with the bending vibrations of phosphate groups in the low frequency range. In brief, on the FP series, the expected gradual increase in network polymerization is clearly seen with the increase of Q^1 and Q^2 – related contributions to the vibrational spectrum (*i.e.*, increasing fraction of bridging oxygen species). Exemplary deconvolutions of the spectral region of 850–1300 cm^{-1} are shown for FP15 in Fig. 4(b). That is, this broad Raman band is best fitted by four Gaussian functions with peaks at 1001 cm^{-1}, 1062 cm^{-1}, 1109 cm^{-1}, and 1194 cm^{-1}. These correspond to the symmetric and asymmetric stretching modes $\nu_s(Q^0)$, $\nu_{s/as}(Q^1)$ and $\nu_{as}(Q^2)$, respectively. Sulfate for phosphate substitution leads to bands evolving around 470 cm^{-1}, 624 cm^{-1}, 1000 cm^{-1} and 1157 cm^{-1}, assigned to $\nu_2(SO_4)^{2-}$, $\nu_4(SO_4)^{2-}$, $\nu_1(SO_4)^{2-}$ and $\nu_3(SO_4)^{2-}$.[22,25] Noteworthily, no Raman signal could be detected in the spectral region around 840–850 cm^{-1}, which would indicate the presence of P–F bonding.[40] In addition, it can be seen that the maximum phonon energy of the present glass increases from 1001 cm^{-1} to 1157 cm^{-1}. A lower phonon energy can increase the radiative transition probability of ions.

3.3. Luminescence properties and crystal field parameters

Photoluminescence (PL) spectra of Cr-doped FP and FPS glasses are shown in Fig. 5. A broad emission band centered at 734 nm is observed in cast glasses, resulting from the spin-allowed $^4T_2 \rightarrow {}^4A_2$ transition in Cr^{3+}.[12,13,15] Differing from this, a very intense emission band is detected in the quenched samples of FP0 and FP0S15 at ~694 nm (corresponding to the *R*-line). This band originates from the spin-forbidden transition of Cr^{3+}: $^2E \rightarrow {}^4A_2$. The accompanying broader background emission (700–900 nm) is attributed to the phonon sidebands of the $^4T_2 \rightarrow {}^4A_2$ transition. There is a positive correlation between the emission intensity and optical basicity. As the glass optical basicity increases with increasing phosphate content, also the emission intensity gradually increases. Similar behaviour was found in chromium-doped silicate glasses.[43] Noteworthily, potential interference through the effect of "photon trapping" on luminescence spectra and decay times is negligible because the samples used for spectroscopic tests are very thin. This is further confirmed by comparing the spectroscopic characteristics for different sample sizes (see Fig. S2 in the ESI†). Noteworthily, the full width at half maximum (FWHM) of the sharp peak at 694 nm is about 83 nm, which is much broader than what is typically observed in Cr^{3+}-doped crystals or glass ceramics.[44] The inhomogeneous broadening of the *R* line reflects the higher versatility of states which is available for Cr^{3+} precipitation, where each individual state provides slight differences in crystal-field splitting.[45,46] Besides the Cr^{3+} ion, also other chromium species exhibit red photoemission in some glasses. For example, Herren *et al.* observed a red emission at ~671 nm (14 900 cm^{-1}) in Cr-doped silica glass

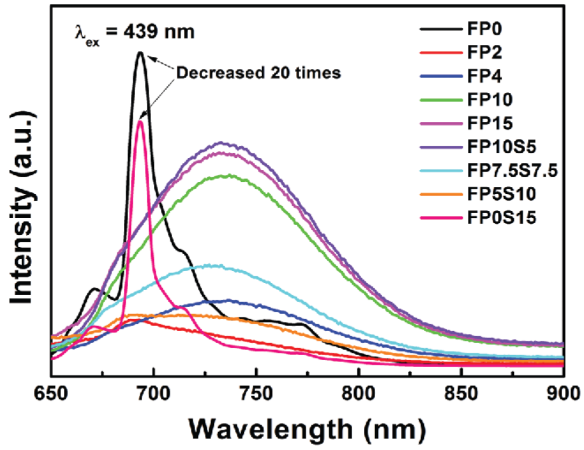

Fig. 5 PL spectra of FP and FPS glasses doped with 0.05 mol% Cr_2O_3.

which was prepared through a sol–gel method. They ascribed their observation to the presence of Cr^{5+} ions.[47] Later, the same authors specified this interpretation with a new assignment, *i.e.*, to the ligand-metal charge transfer (LMCT) transitions of Cr^{6+} ions.[48,49] They also ascribed the red band of chromium-doped sol–gel silica glass to Cr^{6+} ions being associated with Cr^{3+}, Cr^{4+} and Cr^{5+} centers.[50] Strk *et al.* obtained a red emission at 655 nm in Cr-doped silica sol–gel glasses (with excitation bands at 280 nm, 400 nm, and 500 nm).[51] Assisted through electron paramagnetic resonance spectroscopy, they proposed a charge-compensation mechanism and attributed the emission band to pairs of Cr^{6+} and Cr^{5+} ions. Clearly, both observations indicate the complexity in assigning the red emission band to either Cr^{3+} or Cr^{6+}, without a final resolution at this point.

Photoluminescence excitation (PLE) spectra of the representative FP10S5 and FP0 glasses are provided in Fig. 6. Monitoring the emission at 734 nm in FP10S5, a continuous envelope with individual bands centered at 287 nm, 425 nm, and 600 nm is observed, originating from the $^4A_2 \rightarrow {}^4T_1(^4P)$, $^4A_2 \rightarrow {}^4T_1(^4F)$, and $^4A_2 \rightarrow {}^4T_2(^4F)$ transitions of Cr^{3+}, respectively.[44] The PLE spectra of the other cast samples are similar to this. Noteworthily, the excitation peaks occur at somewhat shorter wavelengths as compared with the absorption spectra. This signifies that the low-field Cr^{3+} ions have lower luminescence efficiency.[52] Another important point is that the emission position and intensity show high correlations with the excitation wavelength, which moves to a higher wavelength (*e.g.*, from 648 nm to 734 nm) upon increasing the excitation wavelength (from 287 nm to 600 nm). Also for FP0, the PLE spectrum (monitored at 694 nm emission) consists of three broad excitation bands, here at 260 nm, 404 nm, and 540 nm, corresponding to the same transitions as above. The blue-shift relative to FPS is due to a stronger crystal field surrounding the chromium ions. Upon excitation at either of the three peak wavelengths, the position of the emission spectra remains unchanged except for the difference in intensity. An interesting point is that the emission spectra now narrow-down to a sharp line at 694 nm with a FWHM of only 4 nm, largely because of the inhomogeneous distribution of microcrystals in the quenched samples of FP0 and FP0S15.

Fig. 7 depicts the luminescence decay curves of the cast and quenched samples. The observed emission dynamics clearly deviate from a double-exponential decay function, which is taken as a result of multi-site distribution or interaction among Cr^{3+} species in the glass.[45] The average lifetime of the 734 nm emission in cast samples lies within 39.7 μs to 34.5 μs. This is much higher than what has previously been observed on Cr^{3+}-doped phosphate glass (15 μs).[12] For the quenched samples of FP2 and FP5S10, the lifetimes of the sharp emission band at 694 nm reach about 311 μs and 74.5 μs, respectively. In FP0 and FP0S15, they increase further to ~1.06 ms and 1.07 ms, respectively, but are still somewhat lower than in Cr^{3+}-doped silicate glass ceramics (2.45 ms).[44] The latter observation clearly confirms that in the quenched samples, Cr^{3+} precipitates in a crystalline environment.

The Tanabe–Sugano diagram is frequently used to analyze the energy level scheme of Cr^{3+} ([Ar]$3d^3$). For this, crystal field parameter D_q and Racah parameter B can be estimated according to[53]

$$D_q = \frac{E(^4A_2 \rightarrow {}^4T_2)}{10} \tag{2}$$

$$\frac{D_q}{B} = \frac{15(m-8)}{(m^2-10m)} \tag{3}$$

$$m = \frac{E(^4A_2 \rightarrow {}^4T_1) - E(^4A_2 \rightarrow {}^4T_2)}{D_q} \tag{4}$$

where m is determined from the resonance energy of the $^4A_2 \rightarrow {}^4T_1$ and $^4A_2 \rightarrow {}^4T_2$ transitions. Generally, the region of intermediate octahedral fields, $2.1 < D_q/B < 2.3$, was defined to separate the low-field and high-field regions.[54] In the cast glasses, the D_q, B, and D_q/B values are around 1560 cm ^{1}, 760 cm ^{1} and 2.1, respectively, whereas in the quenched samples,

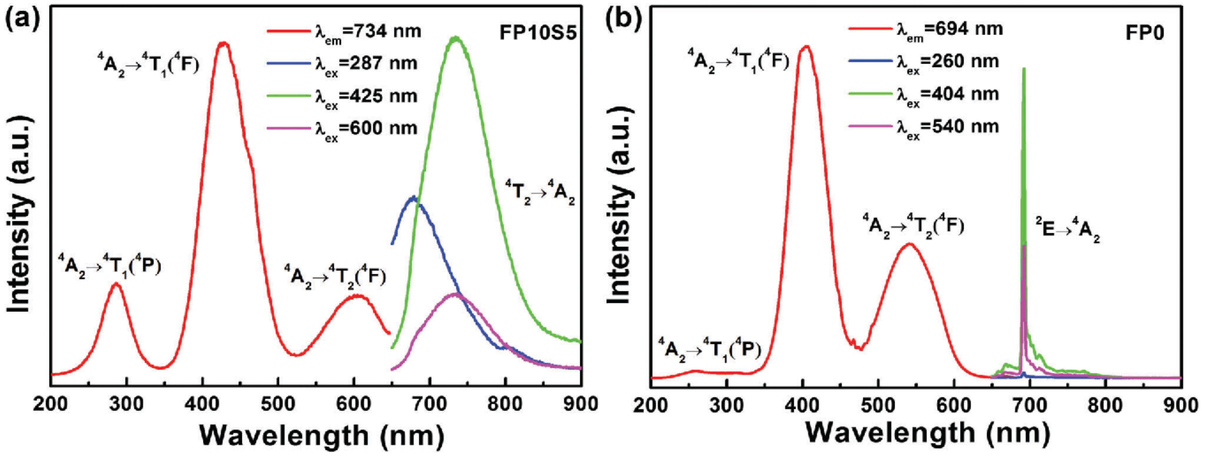

Fig. 6 PLE and PL spectra of selected (a) FP10S5 and (b) FP0 glasses doped with 0.05 mol% Cr_2O_3.

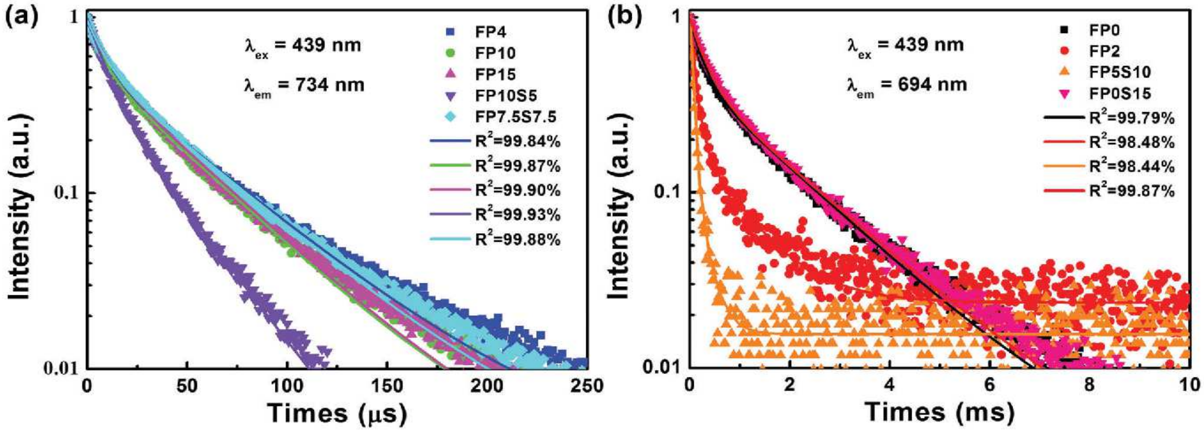

Fig. 7 Luminescence decay curves of Cr^{3+}-doped (a) casting samples and (b) quenching samples.

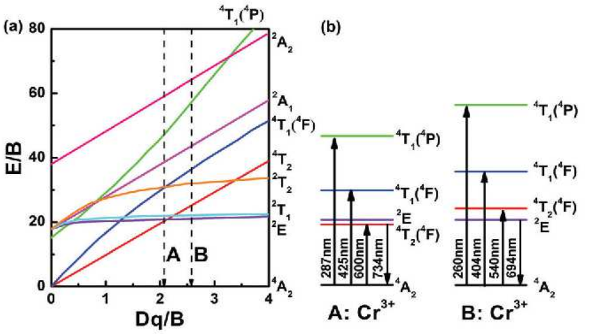

Fig. 8 (a) Tanabe–Sugano diagram and (b) energy level diagram of Cr^{3+}-doped FP and FPS glasses. Labels A and B represent the position of calculated D_q/B in FP10S5 and FP0 samples, respectively.

the values were found to be 1640 cm^{-1}, 630 cm^{-1} and 2.6. This means that the crystal field changes from a low-field to a high-field configuration as a result of varying glass compositions and quenching. We denote the two different situations as (A) and (B), as shown in Fig. 8. As can be readily seen, the $^4T_2$ state is very sensitive to D_q/B while the ^2E state is just the opposite. In situation (A), the Cr^{3+} ion locates in a lower ligand field environment, so the $^4T_2$ level is lower than the ^2E level, which results in broadband emission arising from the spin-allowed $^4T_2 \rightarrow {}^4A_2$ transition. In contrast, when the Cr^{3+} ions locate in the high crystal field (situation (B)), the ^2E level falls below the $^4T_2$ level and, thus, the spectra exhibit a sharp *R*-line originating from the spin-forbidden $^2E \rightarrow {}^4A_2$ transition.

4. Conclusions

In summary, we reported on unusually stable multi-anion glasses of the fluoride-sulfophosphate type (FPS) as a new host material for optically active cation species. Despite a notoriously low polymerization grade, anion mixing in this glass system enables the facile manufacture of bulk or fiber devices which combine several advantages of fluoride and phosphate glasses while using the stabilizing effect of sulfate added. Using the example of chromium doping, we demonstrate a broad red photoluminescence at 734 nm and an inhomogeneous broadening of the *R*-line at 694 nm, originating from the $^4T_2 \rightarrow {}^4A_2$ and $^2E \rightarrow {}^4A_2$ transitions of Cr^{3+}, respectively. The luminescence mechanism was further analyzed on the basis of the corresponding Tanabe–Sugano diagram. Tailored through chemical composition, internally nucleated precipitation of a nanocrystalline fluoride phase enables switching between high-field and low-field configurations of the Cr^{3+} ion, resulting in the specific emission properties and setting the path towards FPS-based optical devices, in particular, broadband tunable fiber amplifiers and lasers.

Acknowledgements

This project has received funding from the European Research Council (ERC) under the European Union's Horizon 2020 research and innovation programme (ERC grant UTOPES, grant agreement no. 681652). W. C. Wang gratefully acknowledges the Chinese Scholarship Council for personal support. We thank our colleagues C. Zeidler, N. Buchert, S. Fuhrmann, C. Siedler and Y. Ding for help with sample preparation and data acquisition.

References

1 G. Boulon, *Opt. Mater.*, 2012, **34**, 499.
2 M. Yasin, S. W. Harun and H. Arof, *Selected Topics on Optical Fiber Technology*, InTech, 2012.
3 T. H. Maiman, *Nature*, 1960, **187**, 493.
4 C. R. Pollock, D. B. Barber, J. L. Mass and S. Markgraf, *IEEE J. Sel. Top. Quantum Electron.*, 1995, **1**, 62.
5 S. B. Mirov, V. V. Fedorov, I. S. Moskalev and D. V. Martyshkin, *IEEE J. Sel. Top. Quantum Electron.*, 2007, **13**, 810.

6 M. Mond, D. Albrecht, E. Heumann, G. Heumann, G. Huber and S. Kück, *Opt. Lett.*, 2002, **27**, 1034.

7 J. C. Chen, Y. S. Lin, C. N. Tsai, K. Y. Huang, C. C. Lai, W. Z. Su, R. C. Shr, F. J. Kao and T. Y. Chang, *IEEE Photonics Technol. Lett.*, 2007, **19**, 595.

8 D. G. Deng, H. P. Ma, S. Q. Xu, Q. Wang, L. H. Huang, S. L. Zhao, H. P. Wang and C. X. Li, *J. Opt. Soc. Am. B*, 2010, **27**, 1659.

9 U. R. Rodríguez-Mendoza, V. Lavín, I. R. Martín and V. D. Rodríguez, *J. Lumin.*, 2004, **106**, 77.

10 H. R. Verdun, L. M. Thomas, D. M. Andrauskas, T. McCollum and A. Pinto, *Appl. Phys. Lett.*, 1988, **53**, 2593.

11 C. Deka, M. Bass, B. H. T. Chai and Y. Shimony, *J. Opt. Soc. Am. B*, 1993, **10**, 1499.

12 E. J. Sharp, J. E. Miller and M. J. Weber, *Phys. Lett. A*, 1969, **30**, 142.

13 T. Murata, M. Torisaka, H. Takebe and K. Morinaga, *J. Non-Cryst. Solids*, 1997, **220**, 139.

14 S. M. Yeh, S. L. Huang, Y. J. Chiu, H. Taga, P. L. Huang, Y. C. Huang, Y. K. Lu, J. P. Wu, W. L. Wang, D. M. Kong, K. Y. Huang, J. S. Wang, P. Yeh and W. H. Cheng, *J. Lightwave Technol.*, 2012, **30**, 921.

15 Z. J. Fang, S. P. Zheng, W. C. Peng, H. Zhang, Z. J. Ma, S. F. Zhou, D. P. Chen and J. R. Qiu, *J. Am. Ceram. Soc.*, 2015, **98**, 2772.

16 M. J. Weber, *J. Non-Cryst. Solids*, 1990, **123**, 208.

17 J. H. Campbell and T. I. Suratwala, *J. Non-Cryst. Solids*, 2000, **263**, 318.

18 S. Tanabe, *C. R. Chim.*, 2002, **5**, 815.

19 K. Griebenow, U. Hoppe, D. Möncke, E. I. Kamitsosc and L. Wondraczek, *J. Non-Cryst. Solids*, 2017, **460**, 136.

20 B. P. Rodrigues, J. Deubener and L. Wondraczek, *Front. Mater.*, 2016, **3**, 25.

21 K. Griebenow, E. I. Kamitsos and L. Wondraczek, *J. Non-Cryst. Solids*, 2017, **468**, 74.

22 N. Da, O. Grassmé, K. H. Nielsen, G. Peters and L. Wondraczek, *J. Non-Cryst. Solids*, 2011, **357**, 2202.

23 N. Da, S. Krolikowski, K. H. Nielsen, J. Kaschta and L. Wondraczek, *J. Am. Ceram. Soc.*, 2010, **93**, 2171.

24 S. Sirotkin, R. Meszaros and L. Wondraczek, *Int. J. Appl. Glass Sci.*, 2012, **3**, **44**.

25 D. Möncke, S. Sirotkin, E. Stavrou, E. I. Kamitsos and L. Wondraczek, *J. Chem. Phys.*, 2014, **141**, 224509.

26 S. Reibstein, N. Da, J. P. Simon, E. Spiecker and L. Wondraczek, *Phys. Chem. Glasses*, 2012, **53**, 61.

27 D. Ehrt and T. Töpfer, *Proc. SPIE*, 2000, **4102**, 95.

28 J. F. Philipps, T. Töpfer, H. Ebendorff-Heidepriem, D. Ehrt and R. Sauerbrey, *Appl. Phys. B: Lasers Opt.*, 2001, **72**, 399.

29 H. Ebendorff-Heidepriem, D. Ehrt, M. Bettinelli and A. Speghini, *J. Non-Cryst. Solids*, 1998, **240**, 66.

30 S. Tanabe, S. Yoshii, K. Hirao and N. Soga, *Phys. Rev. B*, 1992, **45**, 4620.

31 J. J. Zhang, D. B. He, Z. C. Duan, L. Y. Zhang, S. X. Dai and L. L. Hu, *Laser & Optronics Prog.*, 2005, **42**, 12.

32 L. Y. Zhang, L. Wen, H. T. Sun, J. J. Zhang and L. L. Hu, *J. Alloys Compd.*, 2005, **391**, 156.

33 P. Ebeling, D. Ehrt and M. Friedrich, *Phosphorus Res. Bull.*, 1999, **10**, 484.

34 G. A. Kumar, A. Martinez and E. De la Rosa, *J. Lumin.*, 2002, **99**, 141.

35 G. A. Kumar, E. De la Rosa, A. Martinez, N. V. Unnikrishnan and K. Ueda, *J. Phys. Chem. Solids*, 2003, **64**, 69.

36 Q. H. Le, D. Möncke, E. I. Kamitsos and L. Wondraczek, *Society of Glass Technology (SGT) Centenary Conference*, 2016.

37 S. Emura, H. Maeda, Y. Kuroda and T. Murata, *Jpn. J. Appl. Phys.*, 1993, **32**, 734.

38 J. Ueda and S. Tanabe, *J. Am. Ceram. Soc.*, 2010, **93**, 3084.

39 W. A. Weyl, *Coloured Glasses*, Society of Glass Technology, 2016.

40 L. L. Velli, C. P. E. Varsamis and E. I. Kamitsos, *Phys. Chem. Glasses*, 2008, **49**, 182.

41 D. Möncke, D. Ehrt, L. Velli, C. P. E. Varsamis and E. I. Kamitsos, *Int. Congr. Glass, Proc., 20th*, 2004.

42 A. Thieme, D. Möncke, R. Limbach, S. Fuhrmann, E. I. Kamitsos and L. Wondraczek, *J. Non-Cryst. Solids*, 2015, **410**, 142.

43 H. Yamazaki and S. Tanabe, *Jpn. J. Appl. Phys.*, 2005, **44**, 5011.

44 D. Q. Chen, Z. Y. Wan and Y. Zhou, *Opt. Lett.*, 2015, **40**, 3607.

45 F. Rasheed, K. P. D'onnell, B. Henderson and D. B. Hollis, *J. Phys.: Condens. Matter*, 1991, **3**, 1915.

46 S. V. Bulyarskii, A. E. Kozhevin, S. N. Mikov and V. V. Prikhodko, *Phys. Status Solidi A*, 2000, **180**, 555.

47 M. Herren, H. Nishiuchi and M. Morita, *J. Chem. Phys.*, 1994, **101**, 4461.

48 M. Moirta, N. Miyazaki, S. Murakami, M. Herren and D. Rau, *J. Lumin.*, 1998, **76&77**, 238.

49 M. Herren, K. Yamanaka and M. Morita, *Tech. Rep. Seikei Univ.*, 1995, **32**, 61.

50 M. Morita, D. Rau, S. Kajiyama, T. Sakurai, M. Baba and M. Iwamura, *Mater. Sci.-Pol.*, 2004, **22**, 5.

51 W. Stręk, P. J. Dereń, E. Łukowiak, J. Hanuza, H. Drulis, A. Bednarkiewicz and V. Gaishun, *J. Non-Cryst. Solids*, 2001, **288**, 56.

52 A. van Die, G. Blasse and W. F. van der Weg, *J. Phys. C: Solid State Phys.*, 1985, **18**, 3379.

53 C. R. Kesavulu, R. P. S. Chakradhar, R. S. Muralidhara, J. L. Rao and R. V. Anavekar, *J. Alloys Compd.*, 2010, **496**, 75.

54 F. Rasheed, K. P. O'Donnell, B. Henderson and D. B. Hollis, *J. Phys.: Condens. Matter*, 1991, **3**, 3825.

Electronic Supplementary Material (ESI) for Journal of Materials Chemistry C.
This journal is © The Royal Society of Chemistry 2017

Supporting Information

TITLE: Fluoride-sulfophosphate glasses as host for broadband optical amplification through transition metal activators

W. C. Wang,[a,b] Q. H. Le,[a] Q. Y. Zhang,[b] and L. Wondraczek*[a]

[a]Otto Schott Institute of Materials Research, University of Jena, Fraunhoferstraße 6,07743 Jena, Germany

[b]State Key Laboratory of Luminescent Materials and Devices, Guangdong Provincial Key Laboratory of Fiber Laser Materials and Applied Techniques, and Institute of Optical Communication Materials, South China University of Technology, Guangzhou 510641, P. R. China.

***Email:** lothar.wondraczek@uni-jena.de

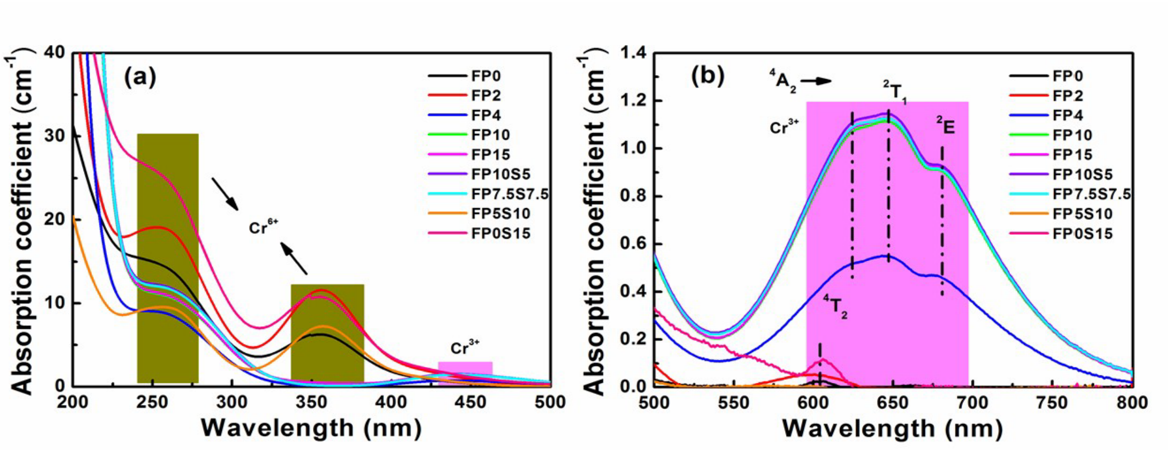

Fig. S1 Optical absorption spectra of chromium-doped FP and FPS glasses across the spectral regions of (a) 200-500 nm and (b) 500-800 nm.

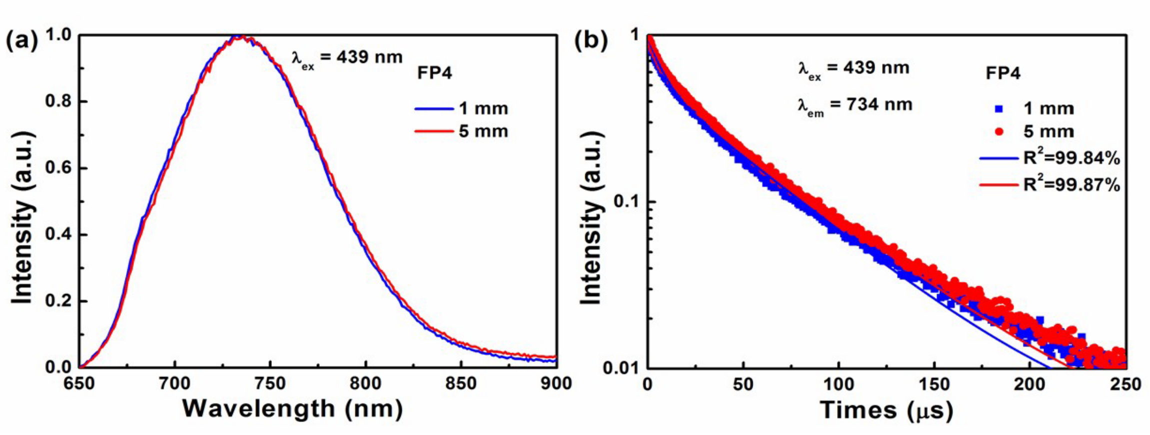

Fig. S2 (a) Emission spectra and (b) decay curves of Cr^{3+}-doped FP4 glass samples with different thickness.

3.2.3 Spectroscopic properties of Cu^{2+} in alkaline earth metaphosphate, fluoride-phosphate and fluoride-phosphate-sulfate glasses

Q. H. Le, C. Friebe, W. C. Wang, L. Wondraczek, “Spectroscopic properties of Cu^{2+} in alkaline earth metaphosphate, fluoride-phosphate and fluoride-phosphate-sulfate glasses”, J. Non-Cryst. Solids: X, 4 (2019) 100037

DOI: 10.1016/j.nocx.2019.100037

Divalent copper ions (Cu^{2+}) are not only important colorants in consumer glasses. They can also be used as a probe for assessing the local structural arrangement within a solid host. Here, we report on the incorporation of Cu^{2+} into alkaline earth metaphosphate (MP), fluoride-phosphate (FP) and fluoride-phosphate-sulfate (FPS) glasses. As a d^9 transition metal ion, Cu^{2+} exhibits a broad optical absorption band at wavelengths of 740–880 nm when incorporated into oxide glasses. The specific properties of this band are strongly affected by the local basicity of the host, which reflects in a straightforward dependence of the band position on the mean-field optical basicity in alkaline earth MP. For FP and FPS, however, distinct deviations from this simplistic correlation are found due to selective cation localization on the various oxoanions and/or halogen species. In addition, high basicity favours the formation of monovalent Cu^+. Electron paramagnetic resonance indicates a transition from tetragonally distorted octahedral coordination of Cu^{2+} in MP to rhombohedral distortion in FP and FPS glasses.

Journal of Non-Crystalline Solids: X 4 (2019) 100037

Contents lists available at ScienceDirect

Journal of Non-Crystalline Solids: X

journal homepage: www.journals.elsevier.com/journal-of-non-crystalline-solids-x

Spectroscopic properties of Cu^{2+} in alkaline earth metaphosphate, fluoride-phosphate and fluoride-phosphate-sulfate glasses

Q.H. Le[a,b], C. Friebe[c], W.C. Wang[d], L. Wondraczek[a,*]

[a] *Otto Schott Institute of Materials Research, Friedrich- Schiller-Universität, Fraunhoferstraße 6, 07743 Jena, Germany*
[b] *Can Tho University of Technology, 256 Nguyen Van Cu, Can Tho, Viet Nam*
[c] *Friedrich Schiller University, Jena Laboratory of Organic and Macromolecular Chemistry, Humboldtstr. 10, 07743 Jena, Germany*
[d] *State Key Laboratory of Luminescent Materials and Devices, Guangdong Provincial Key Laboratory of Fiber Laser Materials and Applied Techniques, Institute of Optical Communication Materials, South China University of Technology, Guangzhou 510641, PR China*

ABSTRACT

Divalent copper ions (Cu^{2+}) are not only important colorants in consumer glasses. They can also be used as a probe for assessing the local structural arrangement within a solid host. Here, we report on the incorporation of Cu^{2+} into alkaline earth metaphosphate (MP), fluoride-phosphate (FP) and fluoride-phosphate-sulfate (FPS) glasses. As a d^9 transition metal ion, Cu^{2+} exhibits a broad optical absorption band at wavelengths of 740–880 nm when incorporated into oxide glasses. The specific properties of this band are strongly affected by the local basicity of the host, which reflects in a straightforward dependence of the band position on the mean-field optical basicity in alkaline earth MP. For FP and FPS, however, distinct deviations from this simplistic correlation are found due to selective cation localization on the various oxoanions and/or halogen species. In addition, high basicity favours the formation of monovalent Cu^{+}. Electron paramagnetic resonance indicates a transition from tetragonally distorted octahedral coordination of Cu^{2+} in MP to rhombohedral distortion in FP and FPS glasses.

1. Introduction

Changes in the chemical composition of a glass impose a changing local environment on transition metal (TM) constituents. Such changes include the type and number of next neighbours (ligands) which surround the TM ion. Due to the pertinent *d-d* electronic transitions, changes in the local ligand field are often visible in the optical absorption spectra: TM-doped glasses exhibit a very broad variety of colours and shades, and certain TM species (e.g., Cu^{2+}, Cr^{3+}, Mn^{3+}, Fe^{2+}, Fe^{3+}, etc.) are among the most important colorants of consumer glasses [1]. When the respective ion exhibits an unpaired electron, additional information on the electronic state and on the ligand arrangement can be obtained by probing the resonant microwave absorption in a magnetic field (EPR). On this basis, TM dopants can be used as readily assessable indicators of the local structure of glasses.

Among the various transition metal ions, Cu^{2+} is of particular interest. Its optical absorption and EPR behaviour have been well studied in many glass matrices, including silicates, borates, phosphates and (oxo)fluorides [2–14]. Here, we now use Cu^{2+} to study the local structure of polyionic glasses which contain mixtures of different oxoanions and/or fluorides. The specific group of fluoride-phosphate-sulfate (FPS) glasses was recently discovered as a material class with the capability to admix various anion species in up to almost equimolar amounts [15]. Glasses from the FPS system exhibit non-intuitively high stability, both in terms of glass forming ability and corrosion resistance. This enables the facile fabrication of large, bulk samples, which do not notably degrade in humid air. Similar to their parent materials, phosphate and fluoride-phosphate glasses (FP), FPS glasses provide interesting host chemistries for transition metal ions as well as other optically active ion species; they exhibit a broad transmission window which extends to the deep blue or ultraviolet (UV) spectral range, relatively low partial dispersion and – owing to the presence of fluoride (or other halogenide species) – a lever for reducing the content of residual OH-groups such as required for transparency in the near-infrared spectral range [16–23]. While some initial studies have been conducted on the spectroscopic properties of Cr, Mn and Ni doped into FPS matrices [24,25], however, detailed information on the particular case of divalent copper ions and its wider properties across the involved families of glasses are presently not reported.

In oxide glasses, the Cu^{2+} ion ([Ar]$3d^9$) is usually present in octahedral coordination [26,27]. Depending on ligand situation, this octahedron can be more or less distorted. The corresponding optical absorption spectra are characterized by variations in band shape, broadness and position, owing to the strength and symmetry of the ligand field. For example, tetragonal distortion (Fig. 1a) of the CuO_6 octahedron may cause the presence of two or more overlapping absorption band [3,11,26], known as Jahn–Teller distortion [26,28–30]. The five *d*-orbitals of the octahedral complex are split into the triply-

---

[*] Corresponding author.
E-mail address: lothar.wondraczek@uni-jena.de (L. Wondraczek).

https://doi.org/10.1016/j.nocx.2019.100037
Received 20 August 2019; Received in revised form 21 September 2019; Accepted 25 September 2019

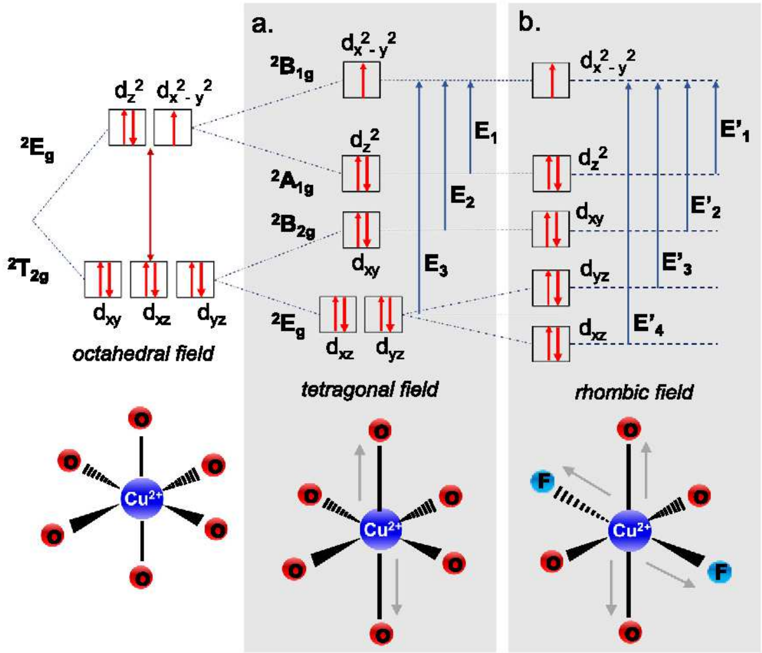

Fig. 1. Splitting of the energy levels of Cu^{2+} in MP (a), and FP and FPS (b).

degenerate $^2T_{2g}$ (lower energy) and the doubly degenerate ^2E_g (higher energy) levels. As a result of tetrahedral distortion, $^2T_{2g}$ further splits into $^2B_{2g}(d_{xy})$ and $^2E_g(d_{xz}, d_{yz})$, and the upper ^2E_g into $^2B_{1g}(d_{x^2-y^2})$ and $^2A_{1g}(d_{z^2})$ [26]. Therefore, three absorption bands are expected for Cu^{2+} in tetragonally distorted CuO_6, i.e., $^2A_{1g} \rightarrow {}^2B_{1g}$ (E_1), $^2B_{2g} \rightarrow {}^2B_{1g}$ (E_2) and $^2E_g \rightarrow {}^2B_{1g}$ (E_3) (Fig. 1a). However, depending on spectral overlap, only two components can sometimes be resolved. For example, the optical absorption spectra of Cu^{2+} in silicate, borate and nitrate glasses have been deconvoluted into two absorption bands at 794 and 1176 nm, 787 and 1111 nm, and 833 and 1111 nm, respectively [28–30]. For cupric phosphate glasses, Bae and Weinberg [26] found three components at ~ 1250, 943 and 833 nm.

Upon rhombic distortion (Fig. 1b), $^2T_{2g}$ splits into the three states of d_{xy}, d_{xz} and d_{yz}, and ^2E_g into $d_{x^2-y^2}$ and d_{z^2}. In this case, four optical absorption bands are expected [31], corresponding to the energy levels E'$_1$, E'$_2$, E'$_3$ and E'$_4$. For example, studying Cu^{2+} doped zinc potassium phosphate hexahydrate at low temperature, Madhu et al. [32] found two peaks at around 845 nm and 1300 nm, with shoulders at 750 nm and 1040 nm, respectively, which they attributed to the transitions from d_{z^2}, d_{xy}, d_{yz} and d_{xz} to $d_{x^2-y^2}$.

Usually, Cu^{2+} and Cu^+ coexist in oxide glass matrices. However, since only the Cu^{2+} ion has an unpaired electron (^2D, $S = 1/2$ and $I = 3/2$), speciation is possible not only by UV–Vis, but also by EPR spectroscopy. In this, a four-line hyperfine spectrum is expected with $m = 3/2, 1/2, -1/2, -3/2$ [33]. Axial (tetrahedral, $g_1 = g_2$ ($g_\perp$) $\neq g_3$ ($g_\parallel$)) or rhombic ($g_1 \neq g_2 \neq g_3$) distortion on the CuO_6 octahedron can then be evaluated on the spin-Hamiltonian parameters [33,34].

Combining UV–Vis optical spectroscopy and EPR analysis, we now investigate and compare the spectroscopic properties and the site geometry of Cu^{2+} when doped into alkaline earth metaphosphate (MP), FP and FPS glasses.

2. Experimental

The present study spans a series of MP, FP and FPS glasses, whereby MP covers the range of alkaline earth MPs (Mg, Ca, Sr, Ba), FPs were selected from the archetype FP reported by Ehrt et al. [35–37] with highly-mixed modifier species and increasing phosphate-for-fluoride substitution, and FPSs start from each FP with increasing sulfate-for-phosphate substitution such as reported by Le et al. [15]. All nominal compositions are summarized in Table 1. The MP glasses were prepared with a copper dopant concentration of 0.1 mol% (CuO) by regular melt-quenching. For this, batches of 70 g of analytical-grade raw materials ($Mg(PO_3)_2$, $Ca(PO_3)_2$, $Sr(PO_3)_2$ and $Ba(PO_3)_2$) were mixed in appropriate amounts and melted in a muffle furnace at 1100–1250 °C for 2 h using SiO_2 crucibles (melting temperatures given in Table 1) before casting into preheated graphite moulds. The obtained glass slabs were subsequently annealed at T_g + 50 °C for another 2 h and cooled down to room temperature (RT) at a rate of about 3–5 K/h. Similarly, FP and FPS glasses were prepared with a copper concentration of 0.05 mol% (CuO). Further details on their production are provided in Ref. [15].

The Cu^{2+} ion was studied by UV–visible and EPR spectroscopy. UV–Vis-NIR absorption spectra of 0.5–2.0 mm thick polished glass samples were recorded on a Cary 5000 (Agilent) double-beam spectrophotometer with a spectral resolution of 1.0 nm in the range from 200 to 3000 nm in direct transmission mode. From the obtained spectra, the frequency of the Cu^{2+} *d-d* transition was extracted.

X-band EPR spectra were acquired on an EMXmicro CW-EPR spectrometer (Bruker EMX micro EMM-6/1/9-VT control unit, ER 070 magnet, EMX premium ER04 X-band microwave bridge equipped with EMX standard resonator, EMX080 power unit) using powdered samples. All analyses were conducted at room temperature. EPR data were evaluated using the Bruker Xenon software package, version 1.1b86. The SpinCountQ software module was used for quantitative analyses. EPR band attributions were conducted on the basis of previous reports on metal phosphates [5,9,38,39] and borate glasses [2,6,7,12,40].

Further physical data of all glasses are available from previous studies [15,41,42] on the assumption that copper doping had a negligible effect on these properties.

Table 1
Nominal compositions (in mol%), values of λ_{max} Cu^{2+} and positions of deconvoluted absorption band maxima of MP (doped with 0.1 mol% CuO), FP and FPS (doped with 0.05 mol% CuO) glasses. The stated basicity parameters were calculated on the basis of Duffy and Ingram [43,44].

Symbol		Compositions						Synthesis conditions (°C)	T_g	Optical basicity	λ_{max} Cu^{2+}	Energy transition			
									(°C)	(Λ_{th})					
	MP	MgO	CaO	SrO	BaO	P_2O_5						$d_{xz}, d_{yz} \rightarrow d_{x^2-y^2}$		$d_{xy} \rightarrow d_{x^2-y^2}$	$d_{z^2} \rightarrow d_{x^2-y^2}$
Metal phosphate	MgP	50	0	0	0	50		1200, 1.5 h	543	0.4275	841	764		912	1124
	CaP	0	50	0	0	50		1100, 1.5 h	528	0.4642	866	795		923	1118
	SrP	0	0	50	0	50		1100, 1.5 h	490	0.4825	876	796		944	1158
	BaP	0	0	0	50	50		1100, 1.5 h	465	0.4892	888	809		949	1153
	FP	MgF_2	CaF_2	SrF_2	AlF_3	$Sr(PO_3)_2$	$SrSO_4$					$d_{xz} \rightarrow d_{x^2-y^2}$	$d_{yz} \rightarrow d_{x^2-y^2}$	$d_{xy} \rightarrow d_{x^2-y^2}$	$d_{z^2} \rightarrow d_{x^2-y^2}$
Fluoride phosphate	FP0	10	28.3	23.1	38.6	0	0	1000–1100, 2 h	400	0.3493	745	633	708	806	946
Fluoride phosphate sulfate	FP2	9.5	27.8	22.9	37.8	2	0	1000–1100, 2 h	429	0.3624	823	724	840	998	1229
	FP3	9.5	27.5	22.5	37.5	3	0	1000–1100, 2 h	436	0.3674	830	733	848	1006	1247
	FP4	9.5	27.5	21.5	37.5	4	0	1000–1100, 2 h	440	0.3710	844	753	872	1012	1193
	FP6	9.5	27	21	36.5	6	0	1000–1100, 2 h	448	0.3808	844	749	861	1045	1224
	FP10	10	30	15	35	10	0	1000–1100, 2 h	461	0.3933	847	760	885	1062	1344
	FP15	10	23.4	19.4	32.2	15	0	1000–1100, 2 h	488	0.4118	844	758	889	1072	1376
	FP20	10	21.8	18.2	30	20	0	1000–1100, 2 h	485	0.4235	847	760	886	1067	1355
	FPS10														
	FP7S3	10	30	15	35	7	3	1000–1100, 2 h	457	0.3937	843	757	883	1060	1346
	FP5S5	10	30	15	35	5	5	1000–1100, 2 h	447	0.3939	815	731	847	1002	1203
	FP3S7[a]	10	30	15	35	3	7	1000–1100, 2 h	432	0.3942	780	–	–	–	–
	FS10[a]	10	30	15	35	0	10	1000–1100, 2 h	400	0.3946	750	–	–	–	–
	FPS15														
	FP10S5	10	23.4	19.4	32.2	10	5	1000–1100, 2 h	474	0.4133	843	753	878	1057	1349
	FP7.5S7.5	10	23.4	19.4	32.2	7.5	7.5	1000–1100, 2 h	456	0.4142	810	710	825	985	1239
	FP5S10[a]	10	23.4	19.4	32.2	5	10	1000–1100, 2 h	437	0.4150	784	–	–	–	–
	FS15[a]	10	23.4	19.4	32.2	0	15	1000–1100, 2 h	403	0.4170	745	–	–	–	–
	FPS20														
	FP15S5	10	21.8	18.2	30	15	5	1000–1100, 2 h	470	0.4254	845	758	883	1062	1349
	FP10S10	10	21.8	18.2	30	10	10	1000–1100, 2 h	451	0.4275	844	756	874	1040	1297
	FP5S15	10	21.8	18.2	30	5	15	1000–1100, 2 h	430	0.4299	808	698	792	917	1091
	FS20[a]	10	21.8	18.2	30	0	20	1000–1100, 2 h	396	0.4325	770	–	–	–	–
Experimental error									± 2		± 3				

[a] Rapidly quenched samples were too thin for polishing; optical absorption data were affected by surface roughness, only $\lambda_{max,Cu2+}$ is given in those cases, but deconvolution was not done deconvolute.

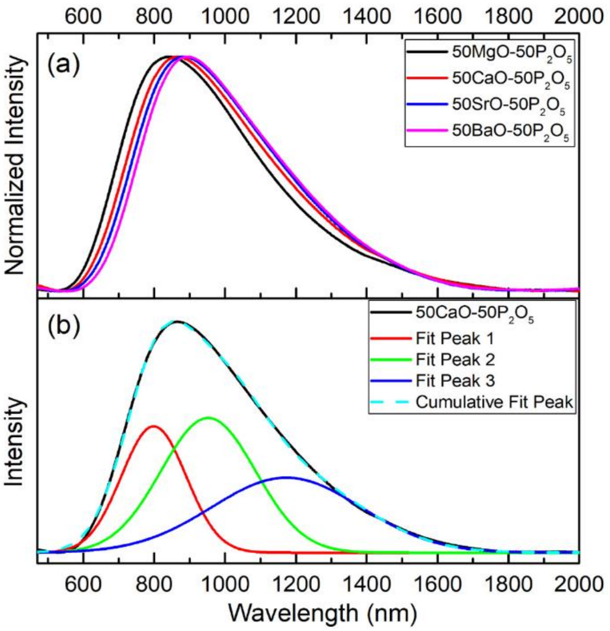

Fig. 2. (a) Optical absorption spectra of Cu^{2+} in alkaline earth MP glasses. (b) Band deconvolution of the CaP example.

3. Results and discussion

3.1. Cu^{2+} in alkaline earth metaphosphate (MP)

3.1.1. Optical spectroscopy

Near-infrared optical absorption spectra of the copper-doped alkaline earth MP glasses are provided in Fig. 2a. All spectra are readily reproduced through deconvolution into three Gaussian contributions (Fig. 2b). The locations of the band maxima of these contributions are listed in Table 1.

The variation of the overall optical absorption band maximum $\lambda_{\mathrm{max},\mathrm{Cu}^{2+}}$ with varying modifier species is also given in Table 1. The value of $\lambda_{\mathrm{max},\mathrm{Cu}^{2+}}$ increases from 841 nm to 881 nm with decreasing modifier field strength (increasing ion size) in the order of Mg to Ba. The structural origin of this variation is illustrated in Fig. 1a. While the phosphate glass network generally comprises of PO_4 structural units with zero to three bridging oxygen species ($Q^{0\ldots3}$), in the MP stoichiometry in which there is one positive modifier charge per phosphate tetrahedron, the fraction of Q^2 is usually > 90% so that a one-dimensional network is generated [42,45]. The modifier cations are placed into the interstitials between neighboring chains where they act as ionic crosslinkers [46]. In the group of Mg to Ba, the ionic radius varies from 57 to 135 pm [47]. This translates into similarly variable constraint strength. As another semi-empirical metric, also the mean-field optical basicity Λ_{th} increases from MgP to BaP (Table 1); the BaP glass has the strongest ability to donate a negative charge to the probe ion (Cu^{2+}) [39]. As a consequence, octahedral splitting decreases in the order of MgP to BaP and, thus, $\lambda_{\mathrm{max},\mathrm{Cu}^{2+}}$ red-shifts [48]. Fig. 3 illustrates this trend with Λ_{th}.

3.1.2. EPR spectroscopy

EPR spectra in the MP:Cu glasses are provided in Fig. 4. The extracted g-values are given in Table 2. Both $g_{\parallel}$ and $g_{\perp}$ are greater than the g-value of the free electron (2.00232), which indicates that Cu^{2+} has an octahedral environment elongated along one of the cubic axes, with the ground state $d_{x^2-y^2}$ ($^2B_{1g}$). The parallel component exhibits a hyperfine structure, although only three lines are clearly resolved; the fourth parallel line (at highest field) is hardly detectable on the available data. Due to line broadening, no hyperfine structure was resolved on the perpendicular component, thus, no hyperfine parameter $A_{\perp}$ was determined. By convention, the values stated for $g_{\parallel}$ and $g_{\perp}$ represent the center of the respective unresolved band. Replacement of the alkaline earth species effects systematic changes in the spin-Hamiltonian parameters (Table 2), whereby $g_{\perp}$ and $A_{\parallel}$ increase whereas $g_{\parallel}$ decreases in the direction of Mg to Ba. This is in accordance with the calculated

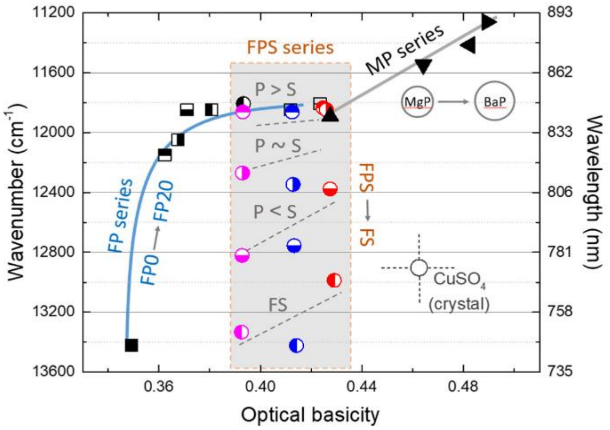

Fig. 3. Location of the Cu^{2+} absorption band maximum as a function of mean-field optical basicity for MP, FP and FPS glasses. Crystalline $CuSO_4$ is shown for reference. Lines were drawn as guides for the eye in order to highlight compositional trends.

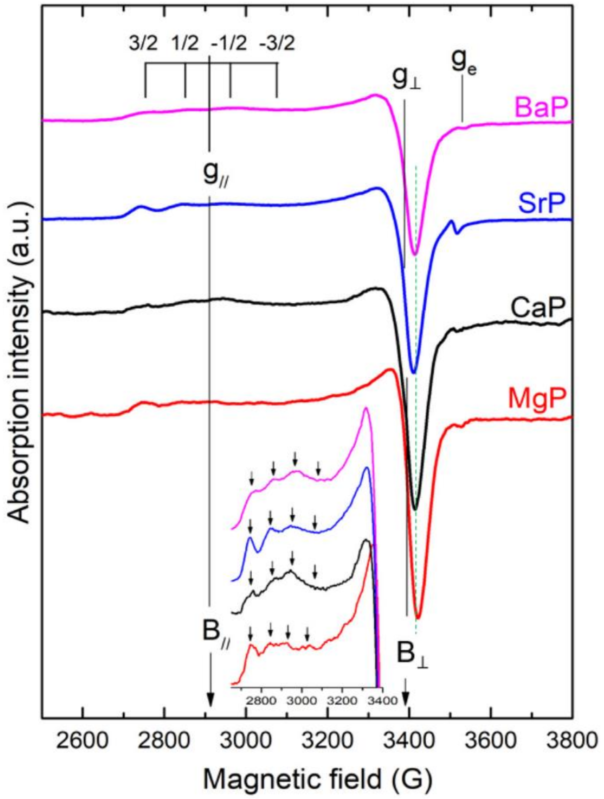

Fig. 4. Room temperature EPR spectra of MP glasses (see text for details).

Table 2
Spin-Hamiltonian parameters of Cu^{2+} doped MP and FPS glasses.

Symbol	Microwave frequency (MHz)	$g_\perp$ ($\pm$ 0.002)	$g_\parallel$ ($\pm$ 0.002)		$A_\parallel$ ($\pm$ 2) ($10^{-4}\,cm^{-1}$)	$g_\parallel/A_\parallel$ (cm)		Concentration	
MP								Cu^{2+} [mol/mg]	Error
MgP	9859.06	2.074	2.437		95	257		4.93E-09	6.6E-10
CaP	9859.06	2.079	2.426		103	236		4.74E-09	2.8E-10
SrP	9858.78	2.080	2.426		106	229		3.31E-09	5.8E-11
BaP	9859.06	2.082	2.416		111	218		2.58E-09	4.3E-10
FPS20		g_1	g_2	g_3	A_3	g_3/A_3	R		
FP20	9857.38	2.072	2.107	2.394	117	205	0.122	4.46E-09	1.4E-10
FP15S5	9843.53	2.070	2.107	2.392	117	204	0.130	4.01E-09	2.6E-10
FP10S10	9848.71	2.071	2.108	2.392	117	204	0.130	3.77E-09	1.8E-10
FP5S15	9859.90	2.070	2.111	2.380	115	207	0.152	3.17E-09	1.7E-10
FS20	9842.41	2.067	2.129	2.362	112	211	0.266	1.50E-09	1.6E-10

optical basicity, which increases from ~ 0.43 for $Mg(PO_3)_2$ to ~ 0.49 for $Ba(PO_3)_2$; relative to MgP, BaP is the softer electron donor [50,51].

For qualitatively estimating the extent of tetragonal distortion, the ratio of $g_\parallel/A_\parallel$ is used [7,51]. As a consequence of the variations in $g_\parallel$ and $A_\parallel$, also $g_\parallel/A_\parallel$ increases, i.e., from ~ 218 to 257 cm (Table 2): the extent of tetragonal distortion of the CuO_6 octahedron increases from $Ba(PO_3)_2$ to $Mg(PO_3)_2$. Similar observations have been made on MPs with other TM dopants [52], where the prevalent coordination of the matrix cation and the availability of lattice sites affect the speciation of the dopant species; $Mg(PO_3)_2$ favours a higher amount of tetrahedral MgO4 sites, whereas with increasing alkaline earth radius, increasing amounts of octahedral sites are observed [53].

In addition to studying site geometry, EPR also provides information on the abundance of Cu^{2+} species (versus Cu^+). The decrease of the g ~ 2.06 band intensity (B ~ 3415 G, Fig. 4) reflects a reduction in Cu^{2+} ion content from MgP to BaP (at constant nominal copper content). This seems to be a logical result of the increase in electronic polarizability and matrix basicity [54], where the electron donor capacity increases from MgP to BaP and, hence, Cu^{2+} is reduced to form Cu^+. Similar observations have been made in other glasses [11,55].

3.2. *Cu^{2+} in fluoride-phosphate (FP) and fluoride-phosphate-sulfate (FPS) glasses*

3.2.1. *Optical spectroscopy*

Some near-infrared optical absorption spectra of copper-doped FP and FPS glasses are shown in Fig. 5a. In comparison to the MP spectra, FP and FPS spectra appear to exhibit a more pronounced asymmetry with a wider red stretch. Here, a best fit is obtained when using four Gaussian contributions for band deconvolution, indicating rhombic distortion of the CuO_6 octahedron. The locations of the four band maxima are listed in Table 1.

The overall absorption maximum $\lambda_{max,Cu}{}^{2+}$ in FP0 is around 745 nm. When as little as 2 mol% of P_2O_5 are present in FP2, $\lambda_{max,Cu}{}^{2+}$ increases dramatically from 745 to 823 nm. It further rises to ~ 830 nm in FP3 and levels-out at ~843–847 nm for FP4-FP20 (Table 1 **and** Fig. 3). When in the FP matrix, $Sr(PO_3)_2$ is replaced by $SrSO_4$ (going from FP to FPS), $\lambda_{max,Cu}{}^{2+}$ again shifts to shorter wavelength (Table 1 **and** Fig. 3). We hypothize that this reflects a preference of the Cu^{2+} ions for $PO_4{}^{3-}$ (Q^0, orthophosphate) and $P_2O_7{}^{4-}$ (Q^1, pyrophosphate) groups as illustrated in Fig. 6. Among these two, the Q^1 group is further preferred for steric reasons. In the FPS glasses, substitution phosphate by sulfate results in higher network depolymerisation and the formation of Q^0 [56].

Previous NMR data corroborate this argument [15,57]. As shown in Fig. 7, there is a clear trend of blue-shifting $\lambda_{max,Cu}{}^{2+}$ with increasing Q^0 and decreasing Q^1. This is notwithstanding the further presence of F ligands, where also for lower F, the same trend is observed. In FS20 where there is no P, the absorption maximum of Cu^{2+} shifts back to ~ 770 nm (however, this observation must be taken with care since the pure FS underwent rapid quenching and/or might still exhibit a certain degree of devitrification) [58]. Overall, the fraction of Q^1 appears to determine $\lambda_{max,Cu}{}^{2+}$. When Q^1 exceeds around one third of the phosphate species (with the exception of FP5S15), all glasses exhibit $\lambda_{max,Cu}{}^{2+}$ in the saturation range of ~825–850 nm. On the other hand, when $Q^1 \leq 34\%$, most of the Cu^{2+} ions seem to be forced into a mixed

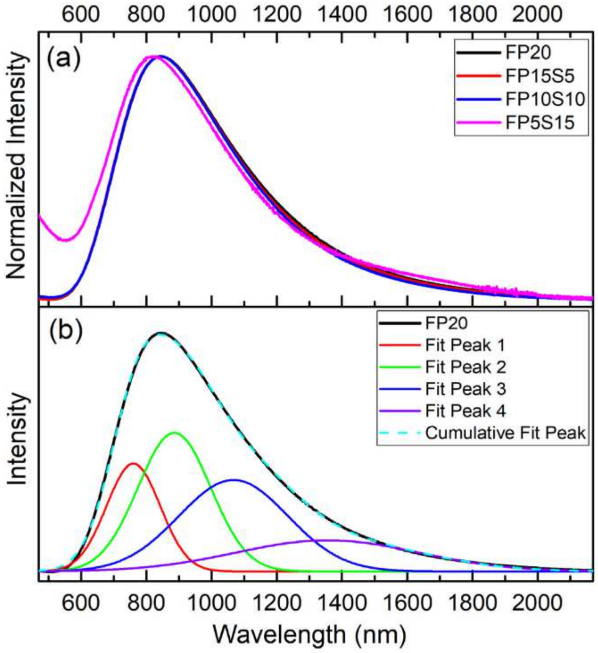

Fig. 5. (a) Optical absorption spectra of Cu^{2+} in the FPS20 series (b) Band deconvolution for the example of FP20.

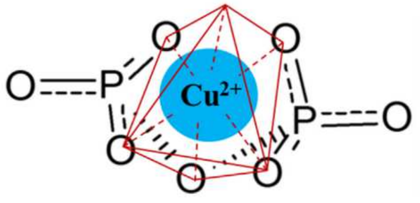

Fig. 6. Sketch of a Cu^{2+} ion forming an octahedral complex with two pyrophosphate groups.

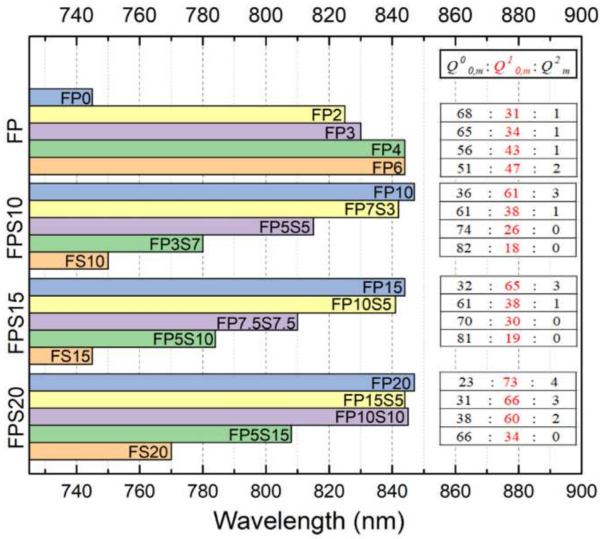

Fig. 7. Relation between the Cu^{2+} absorption band maximum and the relative abundance of Q^0, Q^1 and Q^2 phosphate units.

$F^-/PO_4{}^{3-}/SO_4{}^{2-}$ or $F^-/SO_4{}^{2-}$ environment, leading to a blue-shift of $\lambda_{max,Cu2+}$.

Contrary to the MP glasses, the change of optical basicity seems to have only little effect on the position of the absorption maximum wavelength in FP and FPS glasses (Fig. 3). In FPS glasses, there is even a shift to shorter wavelength when the sulfate content is enhanced, even thought at the same time, the mean-field basicity slightly decreases. This seems to reflect the preferential association of Cu^{2+} ions with the phosphate ligands. The imbalance of ligands may be a reason for the rhombic distortion which is indicated by the UV–Vis spectra (Fig. 5) [10,59].

3.2.2. EPR spectroscopy

Comparing EPR spectra of FPS glasses to those of the MP glasses, we find an additional band at ~ 3340 G (Fig. 8). The three signals $B_{1,2,3}$ which are corroborating our previous assumption of rhombic distortion (with $g_1 < g_2 < g_3$, Table 2) correspond to the three main axes x, y and z of the magnetic tensor [34,59,60]. As with $A_\perp$ in MP glasses, A_1 and A_2 in FPS glasses are difficult to determine because of spectral broadening, so that we calculated only A_3. Interestingly, the g-values, A_3 as well as g_3/A_3 remain nearly unaffected by changes in the chemical composition, invariable, which is consistent with the almost unchanged value of $\lambda_{max\ Cu}{}^{2+}$ in these glasses. When most Cu^{2+} ions precipitate in the vicinity of Q^1 groups (Fig. 6), the polarizability of oxygen ion surrounding Cu^{2+} does not notably change. Only in the more mixed environment of FP5S15 and FS20, changes of g and A parameters occur.

If the quantity $R = \frac{(g_2 - g_1)}{(g_3 - g_2)}$ is less than unity, the ground state or $^2B_{1g}(d_{x-y}^{2\ 2})$ is predominant, while for $R > 1$, the ground state of $^2A_{1g}(d_z{}^2)$ is expected [32,61]. In the present study, all values of R are at or below 0.3 (Table 2), indicating that the ground state is $^2B_{1g}$ $(d_{x-}^{2}{}_{y}{}^{2})$.

The concentration of Cu^{2+} ions in FPS20 series decrease from FP20 to FS20, visible in reducing intensity of the band at $g \sim 2.05$ ($B \sim$ 3425 G). We recognize that the amount of Q^0 $(PO_4{}^{3-})$ and $SO_4{}^{2-}$ increase jointly, leading to increased basicity (Table 2) and, hence, the ability to donate electrons to Cu^{2+} ions. As a result, the lowest concentration of Cu^+ ion is found in FP20. Corresponding EPR spectra and data on FPS15, FPS10 are provided in the Supplementary Information, **Fig. S1**.

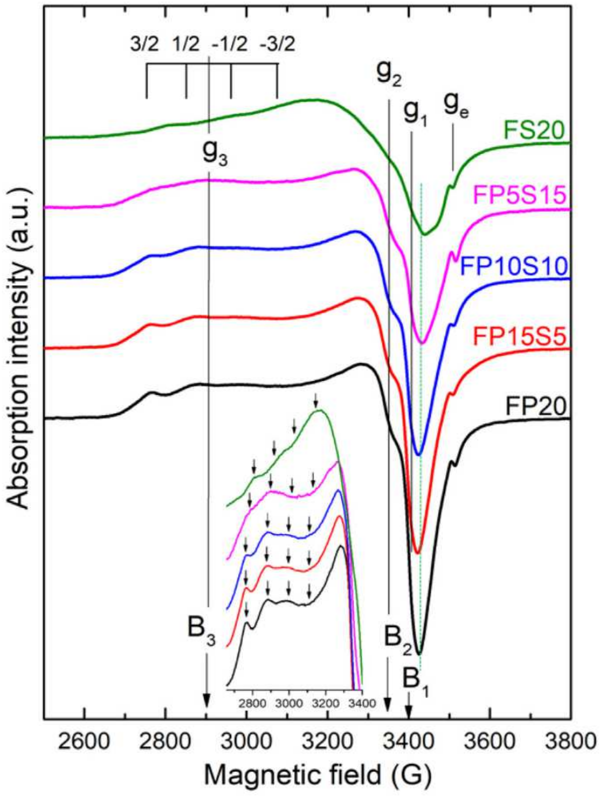

Fig. 8. Room temperature EPR spectra of FPS20 glasses.

4. Conclusions

The local environment of divalent copper ions in MP, FP and FPS glasses was studied by UV–visible and EPR spectroscopy. The broad NIR absorption band of Cu^{2+} was found to shift from about 750 nm to about 880 nm with increasing optical basicity of the host, however, distinct variations which occurred in the simultaneous presence of multiple oxoanions or fluorine ligands indicated strongly selective dopant precipitation. In MP glasses, the Cu^{2+} ligand environment exhibited characteristic Jahn-Teller distortion, related to the electron hole in the ground state of $d_{x-y}^{2\ 2}$. The NIR absorption band was best-fit using three Gaussian components corresponding to $d_z{}^2 \rightarrow d_{x-}^{2}{}_{y}{}^{2}$, $d_{xy} \rightarrow d_{x-}^{2}{}_{y}{}^{2}$, and d_{xz}, $d_{yz} \rightarrow d_{x-}^{2}{}_{y}{}^{2}$. Increasing size of the modifier cations lead to a red-shift in the absorption band maximum, but also resulted in a tendency to form more monovalent Cu^+ as a result higher lattice basicity. For the FP and FPS glass series, there was a much less pronounced dependency of the absorption band maximum on optical basicity. Instead, the spectral properties were dominated by the presence of phosphate dimer groups (Q^1, whereby higher Q^1 resulted in red-shifted absorption bands), sulfate groups ($SO_4{}^{2-}$, with higher S:P ratio leading to blue-shifted absorption) and fluorine. For these glass series, EPR indicated rhombic distortion, assumedly caused by ligand mixing. The optical absorption spectra were best fit using four contributions to account for the transitions from $d_z{}^2$, d_{xy}, d_{yz} and d_{xz} to $d_{x-}^{2}{}_{y}{}^{2}$.

Declaration of Competing Interest

The authors declare that they have no known competing financial interests or personal relationships that could have appeared to influence the work reported in this paper.

Acknowledgements

HQL is grateful to the Vietnam International Education Development program (VIED) of the Ministry of Education and Training of Vietnam for financial support. The authors wish to thank their present and former colleagues Gabi Moeller (sample preparation), Dietmar Güttler and Jelena Petrovic (thermal analyses), Christian Zeidler (optical analyses) and Doris Möncke (data discussion).

Appendix A. Supplementary data

Supplementary data to this article can be found online at https://doi.org/10.1016/j.nocx.2019.100037.

References

[1] W.A. Weyl, Coloured Glasses, Seventh reprint edition, Society of Glass Technology, Sheffield, UK, 2016.
[2] M. Peteanu, I. Ardelean, S. Filip, F. Ciorcas, J Mater Sci-Mater El 7 (1996) 165–170.
[3] S.I. Andronenko, R.R. Andronenko, A.V. Vasil'ev, O.A. Zagrebel'nyi, Glas. Phys. Chem. 30 (2004) 230–235.
[4] S. Suresh, J.C. Babu, V. Chandramouli, Phys. Chem. Glasses 46 (2005) 27–30.
[5] G. Giridhar, M. Rangacharyulu, R.V.S.S.N. Ravikumar, P.S. Rao, J. Mater. Sci. Technol. 25 (2009) 531–534.
[6] V.N. Padmini, J.L. Kumari, J.S. Kumar, S. Cole, Phys. Chem. Glasses: Eur. J. Glass Sci. Technol., Part B 52 (2011) 167–170.
[7] B. Sumalatha, I. Omkaram, T.R. Rao, C.L. Raju, J. Non-Cryst. Solids 357 (2011) 3143–3152.
[8] T.G.V.M. Rao, A.R. Kumar, C.K. Chakravarthi, M.R. Reddy, N. Veeraiah, Physica B-Condensed Matter 407 (2012) 593–597.
[9] K. Srinivasulu, I. Omkaram, H. Obeid, A.S. Kumar, J.L. Rao, Physica B-Condensed Matter 407 (2012) 4741–4748.
[10] H.M. Zhang, X. Wan, J. Struct. Chem. 54 (2013) 26–31.
[11] L.G. Back, Phys. Chem. Glasses: Eur. J. Glass Sci. Technol., Part B 56 (2015) 8–14.
[12] Z.Y. Yao, D. Moncke, E.I. Kamitsos, P. Houizot, F. Celarie, T. Rouxel, L. Wondraczek, J. Non-Cryst. Solids 435 (2016) 55–68.
[13] B. Srinivas, R.V. Kumar, A. Hameed, G. Ramadevudu, M.N. Chary, M. Shareefuddin, Optik 156 (2018) 289–296.
[14] L. Grund Bäck, S. Ali, S. Karlsson, L. Wondraczek, B. Jonson, Journal of Non-Crystalline Solids: X 3 (2019) 100029.
[15] Q.H. Le, T. Palenta, O. Benzine, K. Griebenow, R. Limbach, E.I. Kamitsos, L. Wondraczek, J. Non-Cryst. Solids 477 (2017) 58–72.
[16] M.J. Weber, J. Non-Cryst. Solids 123 (1990) 208–222.
[17] S. Tanabe, S. Yoshii, K. Hirao, N. Soga, Phys. Rev. B 45 (1992) 4620–4625.
[18] H. Ebendorff-Heidepriem, D. Ehrt, M. Bettinelli, A. Speghini, J. Non-Cryst. Solids 240 (1998) 66–78.
[19] J.H. Campbell, T.I. Suratwala, C.B. Thorsness, J.S. Hayden, A.J. Thorne, J.M. Cimino, A.J. Marker, K. Takeuchi, M. Smolley, G.F. Ficini-Dorn, J. Non-Cryst. Solids 263 (2000) 342–357.
[20] D. Ehrt, P. Ebeling, U. Natura, J. Non-Cryst. Solids 263 (2000) 240–250.
[21] J.F. Philipps, T. Topfer, H. Ebendorff-Heidepriem, D. Ehrt, R. Sauerbrey, Appl Phys B-Lasers O 72 (2001) 399–405.
[22] D. Ehrt, C. R. Chim. 5 (2002) 679–692.
[23] J.J. Zhang, D.B. He, Z.C. Duan, L.Y. Zhang, S.X. Dai, L.L. Hu, Phys. Lett. A 337 (2005) 480–486.
[24] W.C. Wang, Q.H. Le, Q.Y. Zhang, L. Wondraczek, J. Mater, Chem. C 5 (2017) 7969–7976.
[25] W.C. Wang, X. Yang, T. Wieduwilt, M.A. Schmidt, Q.-Y. Zhang, L. Wondraczek, Front Mater 6 (2019) 148, https://doi.org/10.3389/fmats.2019.00148.
[26] B.S. Bae, M.C. Weinberg, J. Non-Cryst. Solids 168 (1994) 223–231.
[27] F.A. Cotton, G. Wilkinson, C.A. Murillo, M. Bochmann, Advanced Inorganic Chemistry, 6th ed., John Wiley & Son, Inc., 1999.
[28] R. Juza, H. Seidel, J. Tiedeman, Angew. Chem. Int. Ed. 5 (1966) 85.
[29] R.F. Bartholomew, R.E. Tischer, J. Am. Ceram. Soc. 53 (1970) 130.
[30] A. Duran, J.M.F. Navarro, Phys. Chem. Glasses 26 (1985) 126–131.
[31] S.L. Reddy, T. Endo, G.S. Reddy, M.A. Farrukh (Ed.), Advanced Aspects of Spectroscopy, IntechOpen, 2012.
[32] N. Madhu, A.V. Chandrasekhar, B.J. Reddy, Y.P. Reddy, R.V.S.S.N. Ravikumar, P.S. Rao, Indian J Chem A 38 (1999) 590–591.
[33] F.E. Mabbs, D. Collison, Electron Paramagnetic Resonance of d Transition Metal Compounds, Elsevier Science, 1992.
[34] R. Aasa, P. Aisen, J. Biol. Chem. 243 (1968) 2399.
[35] D. Moncke, D. Ehrt, L.L. Velli, C.P.E. Varsamis, E.I. Kamitsos, Phys. Chem. Glasses 46 (2005) 67–71.
[36] L.L. Velli, C.P.E. Varsamis, E.I. Kamitsos, D. Moncke, D. Ehrt, Phys. Chem. Glasses: Eur. J. Glass Sci. Technol., Part B 49 (2008) 182–187.
[37] D. Ehrt, Phys. Chem. Glasses: Eur. J. Glass Sci. Technol., Part B 56 (2015) 217–234.
[38] O. Cozar, I. Ardelean, V. Simon, L. David, N. Vedean, V. Mih, Appl. Magn. Reson. 16 (1999) 473–480.
[39] S.S. Sastry, B.R.V. Rao, Physica B-Condensed Matter 434 (2014) 159–164.
[40] N.S. Rao, S. Bale, M. Purnima, C. Srinivasu, M.A. Samee, K.S. Kumar, S. Rahman, Physica B-Condensed Matter 404 (2009) 1785–1789.
[41] R. Limbach, B.P. Rodrigues, D. Möncke, L. Wondraczek, J. Non-Cryst. Solids 430 (2015) 99–107.
[42] K. Griebenow, C.B. Bragatto, E.I. Kamitsos, L. Wondraczek, J. Non-Cryst. Solids 481 (2018) 447–456.
[43] J.A. Duffy, M.D. Ingram, J. Inorg. Nucl. Chem. 37 (1975) 1203–1206.
[44] J.A. Duffy, Phys. Chem. Glasses: Eur. J. Glass Sci. Technol., Part B 52 (2011) 107–114.
[45] R.K. Brow, J. Non-Cryst. Solids 263 (2000) 1–28.
[46] B.P. Rodrigues, L. Wondraczek, J. Chem. Phys. 140 (2014) 214501.
[47] R.D. Shannon, Acta Crystallogr., Sect. A: Found. Adv. 32 (1976) 751–767.
[48] G.A. Lawrance, Introduction to Coordination Chemistry, John Wiley & Sons Ltd (2010).
[50] C. Shiyamala, R. Venkatesan, P.S. Rao, SSCom 128 (2003) 137–142.
[51] L.A. Silva, J.B. de Andrade, A.S. Mangrich, J. Braz. Chem. Soc. 18 (2007) 607–610.
[52] K. Griebenow, U. Hoppe, D. Möncke, E.I. Kamitsos, L. Wondraczek, J. Non-Cryst. Solids 460 (2017) 136–145.
[53] K. Griebenow, E.I. Kamitsos, L. Wondraczek, J. Non-Cryst. Solids 468 (2017) 74–81.
[54] J.A. Duffy, Bonding, Energy Levels, and Bands in Inorganic Solids, Longman Scientific & Technical, 1990.
[55] F.G.K. Baucke, J.A. Duffy, Phys. Chem. Glasses 34 (1993) 158–163.
[56] N. Da, O. Grassmé, K.H. Nielsen, G. Peters, L. Wondraczek, J. Non-Cryst. Solids 357 (2011) 2202–2206.
[57] D. Massiot, F. Fayon, M. Capron, I. King, S. Le Calve, B. Alonso, J.O. Durand, B. Bujoli, Z.H. Gan, G. Hoatson, Magn. Reson. Chem. 40 (2002) 70–76.
[58] W.C. Wang, R. Zhou, H.Q. Le, Q.Y. Zhang, L. Wondraczek, J. Lumin. 210 (2019) 457–463.
[59] B. Kozlevcar, P. Segedin, Croat. Chem. Acta 81 (2008) 369–379.
[60] A. Zabel, A. Winter, A. Kelling, U. Schilde, P. Strauch, Int. J. Mol. Sci. 17 (2016).
[61] D.E. Billing, R.J. Dudley, B.J. Hathaway, A.A. Tomlinso, J. Chem. Soc. A (1971) 691.

Spectroscopic properties of Cu^{2+} in alkaline earth metaphosphate, fluoride-phosphate and fluoride-phosphate-sulfate glasses

Q. H. Le [a,b], C. Friebe [c], W. C. Wang [d], L. Wondraczek [a,]*

[a]Otto Schott Institute of Materials Research, Friedrich- Schiller-Universität, Fraunhoferstraße 6, 07743 Jena, Germany
[b]Can Tho University of Technology, 256 Nguyen Van Cu, Can Tho, Vietnam
[c] Friedrich Schiller University Jena Laboratory of Organic and Macromolecular Chemistry, Humboldtstr. 10, 07743 Jena Germany
[d]State Key Laboratory of Luminescent Materials and Devices, Guangdong Provincial Key Laboratory of Fiber Laser Materials and Applied Techniques, and Institute of Optical Communication Materials, South China University of Technology, Guangzhou 510641, P. R. China

Supplementary Information

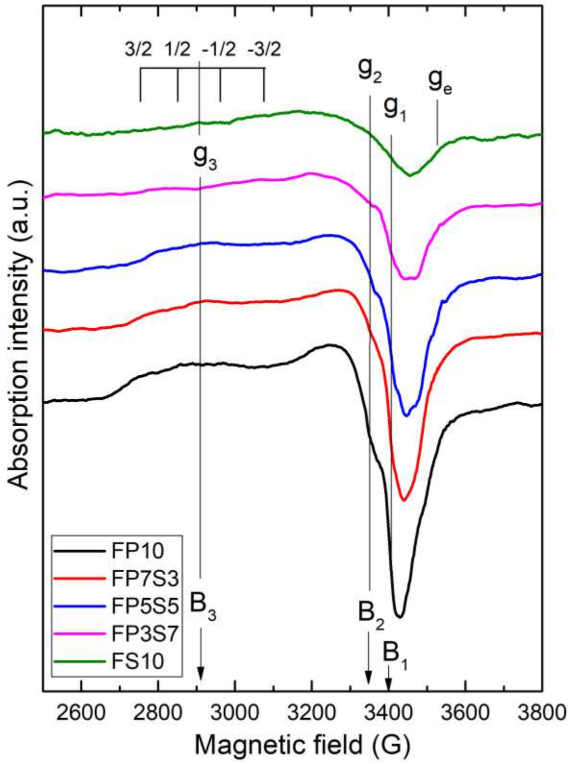

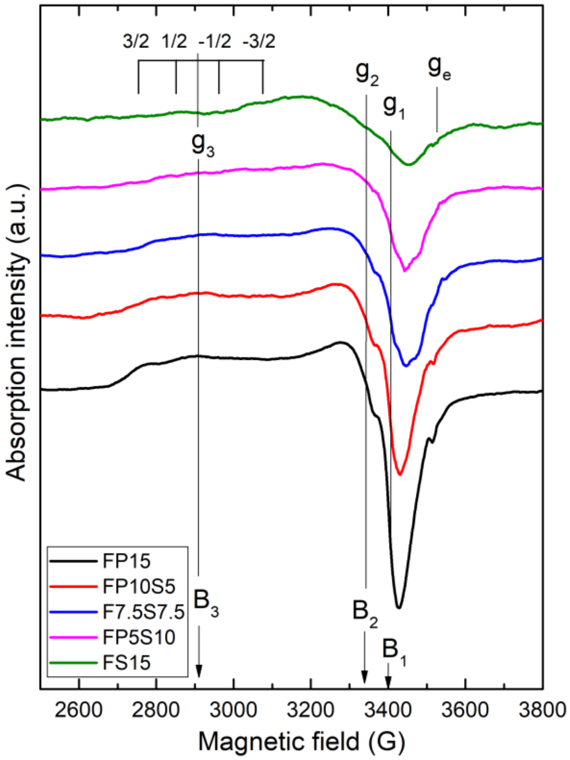

Figure S1: *Room temperature EPR spectra of FPS10 and FPS15 glasses.*

3.2.4 Optimization of electrical conductivity in the Na_2O-P_2O_5-AlF_3-SO_3 glass system

Quyen Huyen Le, Courtney Calahoo, Yang Xia, Caio B. Bragatto, Lothar Wondraczek, "Optimization of Electrical Conductivity in the Na_2O-P_2O_5-AlF_3-SO_3 Glass System", J. Am. Ceram. Soc, submitted 21-Nov-2019

Manuscript ID is JACERS-45068

We report on the individual roles of charge carrier density and network modification in sodium ion conducting glasses from the Na_2O-P_2O_5-SO_3-AlF_3 (NAPFS) system. For this, a broad range of glass compositions was considered across the series of $44Na_2O/(56 - x - y)P_2O_5/xAlF_3/ySO_3$, $47Na_2O/(53 - x - y)P_2O_5/xAlF_3/ySO_3$ and $50Na_2O/(50 - x - y)P_2O_5/xAlF_3/ySO_3$, with $x = 8, 12, 16, 20$ and $y = 0, 5, 7, 10, 12$. Impedance spectroscopy was conducted on these glasses at frequencies from 10^{-2} to 10^6 Hz and over temperatures from 50 to 250 °C, and complemented by structural analyses using Raman spectroscopy and nuclear magnetic resonance data. While the trends in dc conductivity and activation energy follow that of Na_2O content (increasing from 44 to 50 mol%), substantial enhancement of conductivity (by about two orders of magnitude) and correspondingly lower activation energy were also found for constant Na_2O concentration when adjusting SO_3 or AlF_3 within specific limits of glass structure.

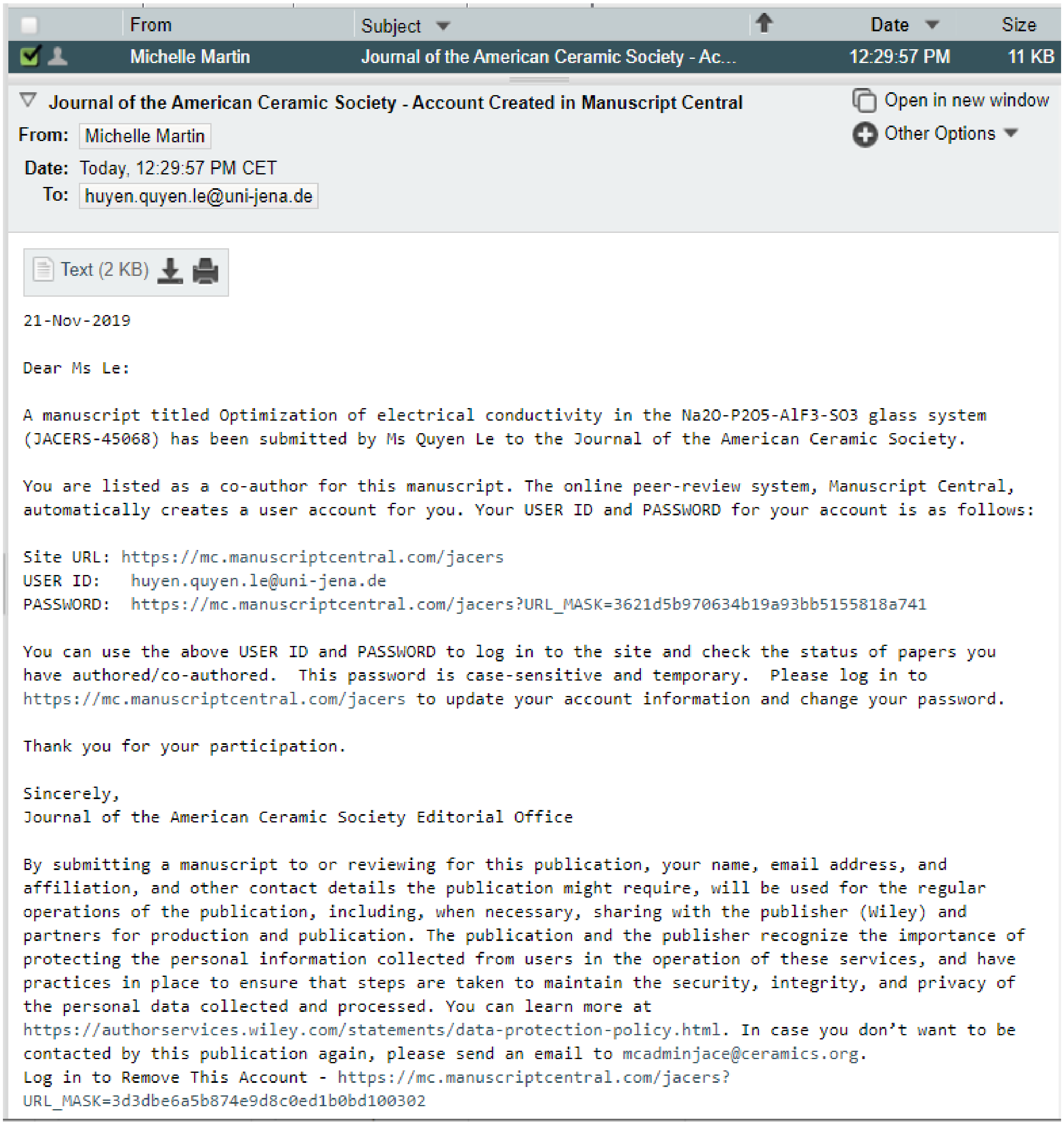

Journal of the American Ceramic Society - Account Created in Manuscript Central

From: Michelle Martin
Date: Today, 12:29:57 PM CET
To: huyen.quyen.le@uni-jena.de

21-Nov-2019

Dear Ms Le:

A manuscript titled Optimization of electrical conductivity in the Na2O-P2O5-AlF3-SO3 glass system (JACERS-45068) has been submitted by Ms Quyen Le to the Journal of the American Ceramic Society.

You are listed as a co-author for this manuscript. The online peer-review system, Manuscript Central, automatically creates a user account for you. Your USER ID and PASSWORD for your account is as follows:

Site URL: https://mc.manuscriptcentral.com/jacers
USER ID: huyen.quyen.le@uni-jena.de
PASSWORD: https://mc.manuscriptcentral.com/jacers?URL_MASK=3621d5b970634b19a93bb5155818a741

You can use the above USER ID and PASSWORD to log in to the site and check the status of papers you have authored/co-authored. This password is case-sensitive and temporary. Please log in to https://mc.manuscriptcentral.com/jacers to update your account information and change your password.

Thank you for your participation.

Sincerely,
Journal of the American Ceramic Society Editorial Office

By submitting a manuscript to or reviewing for this publication, your name, email address, and affiliation, and other contact details the publication might require, will be used for the regular operations of the publication, including, when necessary, sharing with the publisher (Wiley) and partners for production and publication. The publication and the publisher recognize the importance of protecting the personal information collected from users in the operation of these services, and have practices in place to ensure that steps are taken to maintain the security, integrity, and privacy of the personal data collected and processed. You can learn more at https://authorservices.wiley.com/statements/data-protection-policy.html. In case you don't want to be contacted by this publication again, please send an email to mcadminjace@ceramics.org.
Log in to Remove This Account - https://mc.manuscriptcentral.com/jacers?URL_MASK=3d3dbe6a5b874e9d8c0ed1b0bd100302

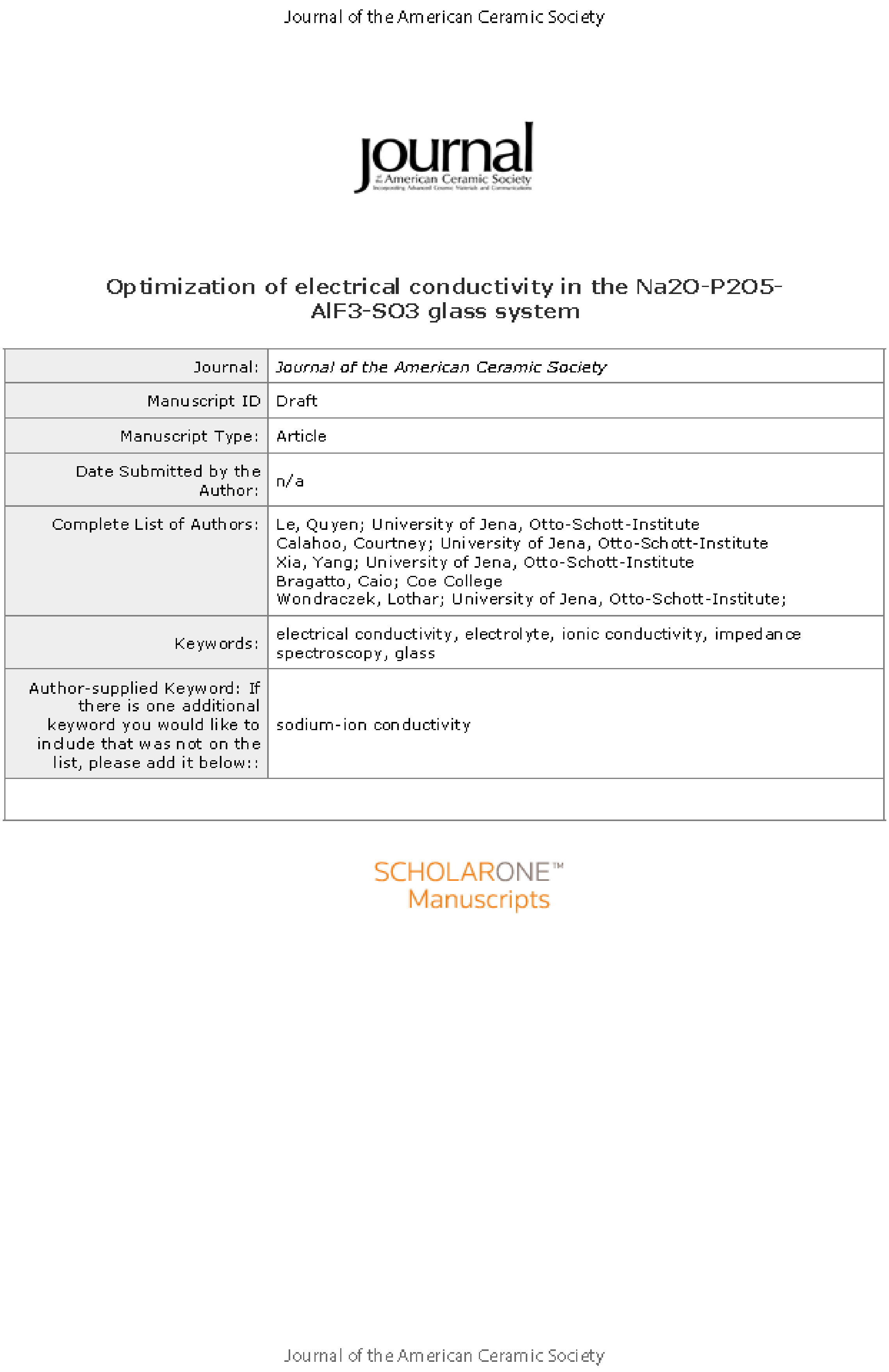

Optimization of electrical conductivity in the Na2O-P2O5-AlF3-SO3 glass system

Journal:	*Journal of the American Ceramic Society*
Manuscript ID	Draft
Manuscript Type:	Article
Date Submitted by the Author:	n/a
Complete List of Authors:	Le, Quyen; University of Jena, Otto-Schott-Institute Calahoo, Courtney; University of Jena, Otto-Schott-Institute Xia, Yang; University of Jena, Otto-Schott-Institute Bragatto, Caio; Coe College Wondraczek, Lothar; University of Jena, Otto-Schott-Institute;
Keywords:	electrical conductivity, electrolyte, ionic conductivity, impedance spectroscopy, glass
Author-supplied Keyword: If there is one additional keyword you would like to include that was not on the list, please add it below::	sodium-ion conductivity

Optimization of Electrical Conductivity in the Na_2O-P_2O_5-AlF_3-SO_3 Glass System

Quyen Huyen Le[a,b], Courtney Calahoo[a], Yang Xia[a], Caio B. Bragatto[c], Lothar Wondraczek[a,*]

[a]*Otto Schott Institute of Materials Research, University of Jena, Fraunhoferstrasse 6, 07743 Jena, Germany*
[b]*Can Tho University of Technology, 256 Nguyen Van Cu, Can Tho, Vietnam*
[c] *Department of Physics, Coe College, Cedar Rapids, Iowa 52402, United States*

Abstract

We report on the individual roles of charge carrier density and network modification in sodium ion conducting glasses from the Na_2O-P_2O_5-SO_3-AlF_3 (NAPFS) system. For this, a broad range of glass compositions was considered across the series of $44Na_2O/(56 - x - y)P_2O_5/xAlF_3/ySO_3$, $47Na_2O/(53 - x - y)P_2O_5/xAlF_3/ySO_3$ and $50Na_2O/(50 - x - y)P_2O_5/xAlF_3/ySO_3$, with $x = 8, 12, 16, 20$ and $y = 0, 5, 7, 10, 12$. Impedance spectroscopy was conducted on these glasses at frequencies from 10^{-2} to 10^6 Hz and over temperatures from 50 to 250 °C, and complemented by structural analyses using Raman spectroscopy and nuclear magnetic resonance data. While the trends in dc conductivity and activation energy follow that of Na_2O content (increasing from 44 to 50 mol%), substantial enhancement of conductivity (by about two orders of magnitude) and correspondingly lower activation energy were also found for constant Na_2O concentration when adjusting SO_3 or AlF_3 within specific limits of glass structure.

* lothar.wondraczek@uni-jena.de

1. Introduction

The development of solid-state electrolytes is one key technological advance required for a safer, cleaner future. Sodium ion conducting glasses have attracted attention because of their possible application as solid electrolytes in sodium ion batteries (SIBs). Since the sodium ion is both heavier and larger than lithium, the energy density of SIBs is not expected to exceed that of the Li analogues.[1] On the other hand, sodium is naturally abundant and its relative ease of extraction can outweigh its inherent shortcomings for applications in which energy density is not a critical issue. For example, SIBs might be the better choice in terms of operating cost, battery durability or safety of operation.[2,3] This is particularly the case when using oxide electrolytes; however, with presently only two well-known oxide materials (β-alumina and NASICON), the selection of suitable electrolytes is small compared to the number of potential lithium ion conductors: not only is there still a need to improve and optimize sodium ion conductivity, but also the fundamental interrelations between material chemistry, structure and sodium mobility must be better understood.

Here, we report on sodium ion conductivity in complex ionic glasses of the type Na_2O-AlF_3-P_2O_5-SO_3 (NAPFS). In this system, chemical ordering is tailored through anion mixing up to equimolar fractions.[4] In order to determine the effect of the individual glass components, in particular, AlF_3 and SO_3, on sodium ion mobility, three series of NAPFS glasses were considered in detail (Series I: $44Na_2O/(56 - x - y)P_2O_5/xAlF_3/ySO_3$; Series II: $47Na_2O/(53 - x - y)P_2O_5/xAlF_3/ySO_3$; Series III: $50Na_2O/(50 - x - y)P_2O_5/xAlF_3/ySO_3$, with $x = 8, 12, 16, 20$ and $y = 0, 5, 7, 10, 12$). The purpose of this research was to investigate how the concentration of charge carriers (Na_2O content) and the structural changes (AlF_3 and SO_3 content) individually affected the mobility of sodium ions, as deduced from trends in electrical conductivity, and to connect this information to structural insights from Raman and NMR spectroscopy.

2. Experimental

Na_2O-P_2O_5-SO_3-AlF_3 (NAPFS) glasses were prepared using $NaPO_3$, Na_2CO_3, $(NH_4)_2HPO_4$, $(NH_4)_2SO_4$ and AlF_3 (*p.a.*). In order to ensure comparability of experimental data, all glasses were melted in Pt crucibles using the same melting protocol and conditions. Raw materials were mixed to yield an equivalent of ~ 50 g of glass per sample, and heated in an electrical furnace at 780 °C for 1.5 h. The obtained glass melts were cast into preheated graphite moulds and annealed at $T_g + 50$ °C for 3 h, and then cooled down to room temperature (RT) at a rate of ~ 3 − 5 K/h. Nominal compositions of all glasses are provided in Table 1. In total, 60 different glass compositions were included in this study, selected for constant sodium ion concentration per series, systematically varying fractions of anion species within each series, and increasing sodium ion concentration from series I to series III.

The densities ρ of all glasses were determined with the Archimedes method at 25 °C in ethanol. The glass transition temperatures T_g were measured by differential thermal analysis (NETZSCH STA 449 F3 Jupiter equipped with DSC sample holders). In order to ensure good thermal contact with the sensor, bulk pieces of glass (approx. 30 mg) were polished on one side. Platinum crucibles were used for each measurement under N_2 atmosphere with a controlled flow rate of 20 ml/min at a heating rate of 20 K/min. The value of T_g was determined from the onset of the glass transition for each sample. All data are provided in **Table 1**.

Structural analyses were performed on polished samples by Raman spectroscopy (Renishaw, UK). Micro-Raman spectra were collected over the spectral range of 80 – 1600 cm^{-1}, using an excitation wavelength of 514 nm (Argon laser) in the 90° scattering configuration.

For the electrical measurements, glass samples with a flat surface of roughly 1–1.5 cm^2 and a thickness of 0.2 cm were cut and polished on both sides. Gold layers were sputtered with an Anatech Hummer 10.2 for 300 seconds, with an average current ranging from 15 to 20 mA. The impedance measurements were performed on a Novocontrol Alpha-A spectrometer paired with a Novotherm Temperature Control System at frequencies from 10^{-2} to 10^6 Hz and temperatures from 50 to 250 °C with intervals of 25 °C. For clarity, Table 1 only presents the conductivity values taken at 50, 150 and

250 °C; we observed a linear increase of electrical conductivity with temperature for all glasses (**Figure 1a**). The activation energy was determined following the same procedure for all samples.[5] The half-circle of the Nyquist plot (*Z'* x −*Z''*) was fit in order to determine the direct current resistance (R_{DC}, in Ω), from which, along with the geometry factor of the sample (*l*/*A*, where *l* is the thickness in cm and *A* the area of the sample in cm^2), the electrical conductivity (σ, in S·cm^{-1}) was obtained:

$$\sigma = \left(\frac{1}{R_{DC}}\right)\left(\frac{l}{A}\right).$$

An example Nyquist plot of the $47Na_2O$-$30P_2O_5$-$7SO_3$-$16AlF_3$ composition measured at 50 – 250 °C with 25 °C steps is provided in **Figure 1b**. The R_{DC} conductivity as a function of temperature is shown in **Figure 1a**. To calculate the activation energy of ion conductivity (E_A, in eV), the following Arrhenius relation was used, where σ_0, T and k_B are the pre-exponential factor, temperature and Boltzmann's constant, respectively,

$$\sigma T = \sigma_0 \exp\left(-\frac{E_A}{k_B T}\right).$$

An example of the Arrhenius plot for the $47Na_2O$-$30P_2O_5$-$7SO_3$-$16AlF_3$ composition is given in **Figure 1c**.

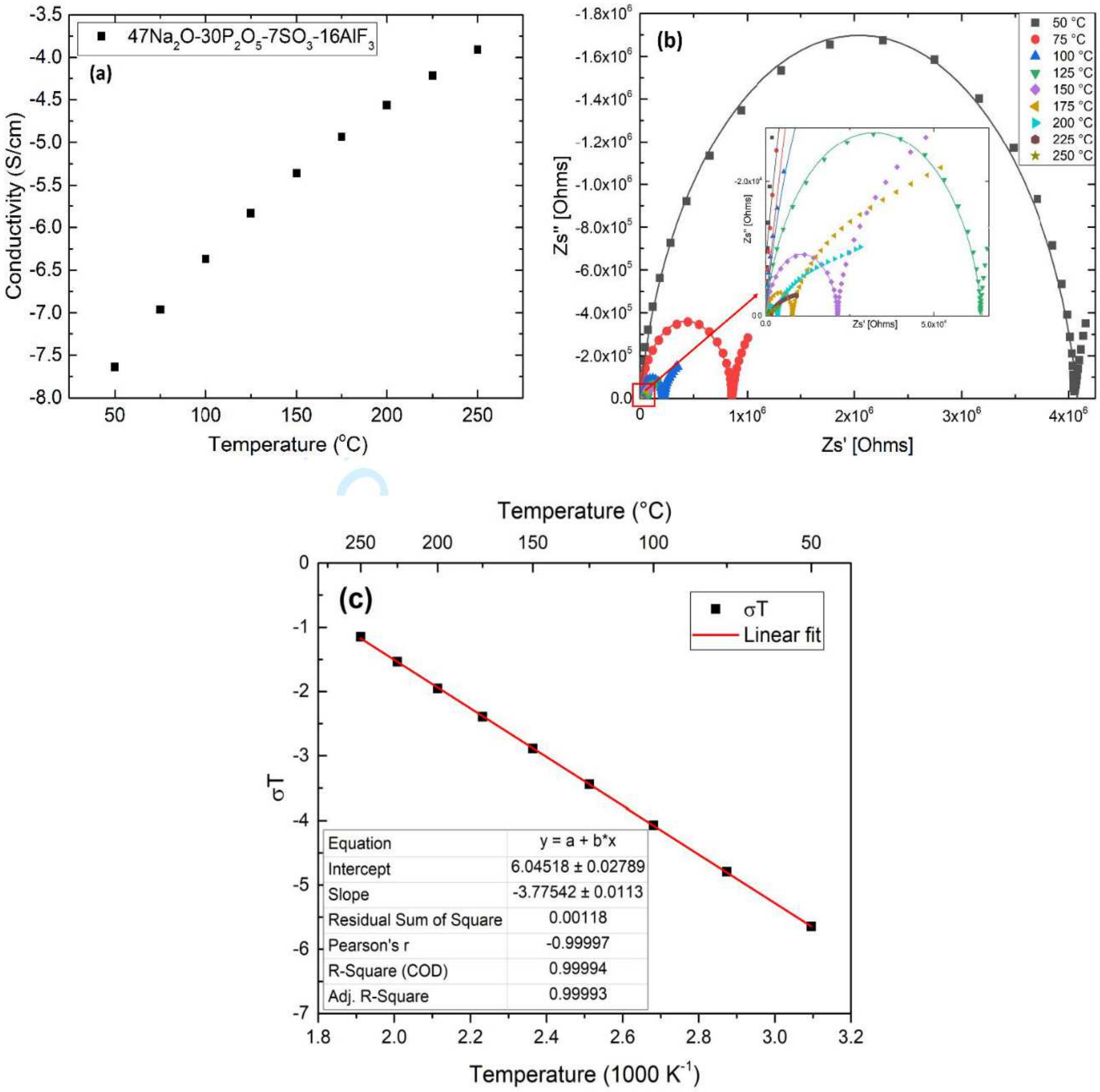

Figure 1: **(a)** Temperature dependence of the electrical conductivity of glass 47Na$_2$O-30P$_2$O$_5$-7SO$_3$-16AlF$_3$, **(b)** Nyquist plots of glass 47Na$_2$O-30P$_2$O$_5$-7SO$_3$-16AlF$_3$ at various temperatures (labels), **(c)** Arrhenius plot for the 47Na$_2$O-30P$_2$O$_5$-7SO$_3$-16AlF$_3$ glass.

Table 1: Nominal composition (mol%), density ρ, glass transition temperature T_g, electrical conductivity (σ), activation energy of electrical conductivity (E_A) and Na ions per cm³ with nominal compositions (mol%) of the present glasses. For reference, the relative variation (%) of Na ions per cm³, electrical conductivity at 50°C and activation energy per step of partially replacing P_2O_5 by Na_2O, AlF_3 and SO_3 are also provided

Group	Na_2O	P_2O_5	AlF_3	SO_3	Density	T_g	log σ (S/cm)			E_A	Na	Percentage increase of			Percentage increase of			Percentage increase of		
					(cm^3 mol^{-1})	(°C)	50°C	150°C	250°C	(eV)	(10^{22} cm^{-3})	Na	log σ 50°C	E_A	Na	log σ 50°C	E_A	Na	log σ 50°C	E_A
												%	%	%	%	%	%	%	%	%
					± 0.005	± 2	± 0.13	± 0.07	± 0.05	± 0.008		when P_2O_5 is partially replaced by Na_2O			when P_2O_5 is partially replaced by AlF_3			when P_2O_5 is partially replaced by SO_3		
IA	44	48	8	0			no glass formation													
	44	43	8	5	2.549	327	-8.43	-5.86	-4.23	0.815	1.364				5.08	-0.82	-2.11			
	44	41	8	7	2.546	328	-8.30	-5.79	-4.17	0.803	1.380				5.34	1.62	-2.60	1.58	1.59	-1.51
	44	38	8	10	2.552	321	-8.16	-5.67	-4.11	0.801	1.410				5.47	1.01	-2.43	3.00	1.70	-0.26
	44	36	8	12	2.556	319	-7.99	-5.63	-4.08	0.781	1.431				5.56	1.87	-2.47	2.10	2.00	-2.41
IB	44	44	12	0			no glass formation													
	44	39	12	5	2.582	339	-8.50	-5.86	-4.26	0.798	1.415				5.98	2.32	-4.05			
	44	37	12	7	2.582	335	-8.16	-5.73	-4.17	0.782	1.433				6.23	1.50	-2.28	1.83	3.98	-2.01
	44	34	12	10	2.587	332	-8.07	-5.66	-4.10	0.781	1.464				5.92	4.48	-4.57	3.12	1.09	-0.09
	44	32	12	12	2.591	331	-7.84	-5.50	-4.00	0.762	1.486				5.78	3.59	-3.30	2.19	2.85	-2.45
IC	44	40	16	0	2.627	366	-8.78	-6.43	-4.50	0.808	1.428				5.30	0.79	-3.39			
	44	35	16	5	2.626	360	-8.30	-5.89	-4.21	0.766	1.474				5.60	4.35	-1.26	4.65	5.40	-5.26
	44	33	16	7	2.629	355	-8.04	-5.69	-4.15	0.764	1.495				5.44	5.12	-4.78	2.09	3.17	-0.20
	44	30	16	10	2.625	350	-7.71	-5.42	-3.94	0.745	1.523				5.89	3.74	-2.98	2.81	4.08	-2.42
	44	28	16	12	2.624	347	-7.56	-5.31	-3.83	0.737	1.544				5.94	3.50	-4.09	2.06	1.95	-1.16
ID	44	36	20	0	2.659	386	-8.71	-6.19	-4.56	0.781	1.481									
	44	31	20	5	2.659	380	-7.94	-5.62	-4.14	0.756	1.531							4.96	8.79	-3.17
	44	29	20	7	2.657	375	-7.63	-5.40	-4.02	0.727	1.550							1.93	3.96	-3.76
	44	26	20	10	2.657	372	-7.42	-5.23	-3.81	0.723	1.582							3.25	2.69	-0.58
	44	24	20	12	2.655	369	-7.30	-5.12	-3.70	0.707	1.603							2.11	1.70	-2.29

IIA	47	45	8	0	2.549	326	-8.66	-6.30	-4.70	0.842	1.447				5.76	0.22	-2.88			
	47	40	8	5	2.555	325	-8.28	-5.95	-4.47	0.809	1.497	13.30	1.86	-0.75	6.29	0.23	-2.69	5.02	4.45	-3.90
	47	38	8	7	2.555	322	-8.20	-5.79	-4.16	0.802	1.516	13.64	1.20	-0.04	6.36	2.46	-4.18	1.92	0.93	-0.81
	47	35	8	10	2.566	316	-7.89	-5.49	-3.89	0.780	1.553	14.34	3.30	-2.59	5.33	2.57	-3.60	3.69	3.78	-2.80
	47	33	8	12	2.567	311	-7.73	-5.38	-3.88	0.764	1.574	14.35	3.31	-2.17	5.54	3.96	-2.94	2.11	2.02	-1.99
IIB	47	41	12	0	2.588	334	-8.64	-6.10	-4.44	0.818	1.504				5.94	1.35	-1.30			
	47	36	12	5	2.599	341	-8.26	-5.82	-4.24	0.787	1.560	14.50	2.89	-1.34	5.96	4.48	-3.51	5.55	4.47	-3.72
	47	34	12	7	2.597	337	-8.00	-5.62	-4.10	0.769	1.580	14.67	2.05	-1.66	6.24	4.48	-3.72	1.99	3.15	-2.32
	47	31	12	10	2.588	337	-7.69	-5.36	-3.91	0.752	1.606	14.20	4.82	-3.75	6.63	5.33	-5.32	2.66	3.89	-2.21
	47	29	12	12	2.590	330	-7.42	-5.15	-3.68	0.742	1.629	14.33	5.37	-2.64	6.71	3.43	-5.43	2.32	3.41	-1.33
IIC	47	37	16	0	2.627	361	-8.52	-6.04	-4.39	0.807	1.564	13.58	2.89	-0.13	6.39	3.30	-4.47			
	47	32	16	5	2.632	356	-7.89	-5.56	-4.10	0.760	1.619	14.49	5.03	-0.78	6.24	1.65	-3.97	5.56	7.49	-5.87
	47	30	16	7	2.633	352	-7.64	-5.36	-3.91	0.740	1.642	14.68	5.01	-3.11	5.87	0.54	-1.54	2.28	3.15	-2.54
	47	27	16	10	2.627	353	-7.28	-5.17	-3.71	0.712	1.673	14.91	5.66	-4.52	5.94	1.04	-0.47	3.05	4.74	-3.84
	47	25	16	12	2.627	349	-7.17	-5.09	-3.65	0.702	1.697	15.25	5.20	-4.78	6.00	1.04	-2.42	2.40	1.47	-1.44
IID	47	33	20	0	2.667	397	-8.24	-5.85	-4.29	0.771	1.628	14.67	5.35	-1.25						
	47	28	20	5	2.664	380	-7.76	-5.62	-4.04	0.729	1.682	15.13	2.36	-3.50				5.42	5.91	-5.38
	47	26	20	7	2.657	367	-7.60	-5.38	-3.93	0.729	1.701	15.10	0.42	0.19				1.90	2.05	-0.08
	47	23	20	10	2.649	362	-7.20	-5.04	-3.65	0.708	1.732	14.97	3.01	-2.04				3.12	5.22	-2.80
	47	21	20	12	2.648	358	-7.09	-4.95	-3.56	0.685	1.757	15.32	2.79	-3.13				2.45	1.48	-3.37
IIIA	50	42	8	0	2.566	328	-8.63	-6.06	-4.37	0.827	1.588	14.11	0.39	-1.77	6.40	3.15	-3.66			
	50	37	8	5	2.566	326	-8.18	-5.69	-4.20	0.802	1.640	14.31	1.16	-0.84	6.45	2.09	-7.60	5.21	5.19	-3.00
	50	35	8	7	2.566	324	-8.04	-5.62	-4.11	0.779	1.661	14.54	1.92	-2.85	6.60	5.08	-5.97	2.15	1.69	-2.82
	50	32	8	10	2.564	317	-7.73	-5.43	-4.02	0.744	1.694	14.13	1.98	-4.65	6.86	6.76	-2.97	3.29	3.84	-4.60
	50	30	8	12	2.567	315	-7.53	-5.20	-3.75	0.734	1.719	14.52	2.53	-3.97	7.36	6.22	-2.72	2.50	2.57	-1.29
IIIB	50	38	12	0	2.606	343	-8.35	-5.88	-4.28	0.797	1.652	14.75	3.32	-2.55	6.46	3.83	-4.25			
	50	33	12	5	2.601	342	-8.01	-5.58	-3.99	0.741	1.704	14.47	3.00	-5.84	6.56	8.02	-3.33	5.26	4.15	-6.96
	50	31	12	7	2.601	343	-7.63	-5.36	-3.77	0.733	1.727	14.77	4.55	-4.67	6.28	7.36	-4.01	2.30	4.70	-1.11
	50	28	12	10	2.600	342	-7.21	-5.03	-3.59	0.722	1.763	15.66	6.19	-4.03	6.40	3.07	-3.13	3.55	5.54	-1.56
	50	26	12	12	2.607	341	-7.06	-4.90	-3.49	0.714	1.793	16.34	4.83	-3.74	5.54	2.73	-2.36	3.00	2.01	-1.03

IIIC	50	34	16	0	2.642	369	-8.03	-5.65	-4.15	0.763	1.716	15.27	5.75	-5.48	5.86	2.62	-1.90			
	50	29	16	5	2.633	369	-7.37	-5.20	-3.78	0.716	1.770	15.07	6.60	-5.67	6.50	-3.96	3.04	5.36	8.32	-6.07
	50	27	16	7	2.627	365	-7.07	-4.92	-3.58	0.704	1.790	14.80	7.43	-4.96	6.41	-4.87	4.36	2.02	4.02	-1.81
	50	24	16	10	2.624	361	-6.99	-4.88	-3.51	0.699	1.827	15.43	3.96	-1.81	6.46	-2.47	2.57	3.68	1.17	-0.65
	50	22	16	12	2.617	348	-6.87	-4.78	-3.38	0.697	1.848	15.17	4.14	-0.61	6.51	-3.00	1.90	2.13	1.67	-0.24
IIID	50	30	20	0	2.664	377	-7.82	-5.55	-4.05	0.748	1.775	14.74	5.09	-2.94						
	50	25	20	5	2.659	363	-7.66	-5.40	-3.92	0.738	1.835	15.32	1.27	1.21				6.00	2.12	-1.34
	50	23	20	7	2.649	361	-7.41	-5.18	-3.73	0.734	1.854	15.34	2.41	0.74				1.92	3.18	-0.54
	50	20	20	10	2.644	359	-7.16	-4.98	-3.56	0.717	1.892	15.95	0.55	1.19				3.73	3.42	-2.36
	50	18	20	12	2.635	358	-7.08	-4.91	-3.50	0.711	1.913	15.68	0.23	3.79				2.18	1.16	-0.88
											Average variation	**14.78**	**3.42**	**-2.30**	**6.08**	**2.46**	**-2.76**	**3.12**	**3.42**	**-2.35**

Results and Discussion

3.1. NAPFS glass molecular structure

To understand the mechanism of electrical conductivity, the structure of NAPFS glasses was initially elucidated through a combination of previous Raman and ^{31}P-NMR spectroscopic observations (from Le *et al.*[4]), along with ^{19}F-NMR and ^{27}Al-NMR spectroscopy data (from Calahoo *et al.*[6]). These previous data were re-analysed band deconvolution. **Figure 2** shows the Raman spectrum of 70NaPO$_3$-5Na$_2$SO$_4$-25AlF$_3$ glass, where each of the individual Gaussian peaks corresponds to a molecular vibration as described by Le *et al.*.[4] Since the considered structural characterization techniques are sensitive to whether a phosphate is bonded to another phosphate tetrahedron or an aluminium octahedron (P−O−P or P−O−Al bonds, respectively), we differentiate Q^n-species using an extra subscript indicating aluminum bonding, *e.g.*, Q^1_{Al} and Q^2_{Al}.The symmetric stretches of the Q^1 phosphate tetrahedra, $v_s(Q^1)$, as well as the short chain and long chain/ring of Q^2-units, $v_s(Q^2)$, are found at higher frequencies when AlF$_3$ is added and P−O−Al linkages are formed. Specifically, the Q^1 peak located at 1010 cm^{-1} becomes a Q^1 with aluminum neighbours at 1068 cm^{-1} (assigned as Q^1_{Al}) and the Q^2 peaks, originally found at 1130 and 1160 cm^{-1} correspond to a single Q^2_{Al} peak at 1185 cm^{-1}. The peak assignments for $v_s(Q^1)$, $v_s(Q^2)$, $v_s(Q^1_{Al})$ and $v_s(Q^2_{Al})$, and the relative amounts of species from the Raman spectra deconvolution agree well with the ^{31}P-NMR results for the same composition (**Figure 3**).

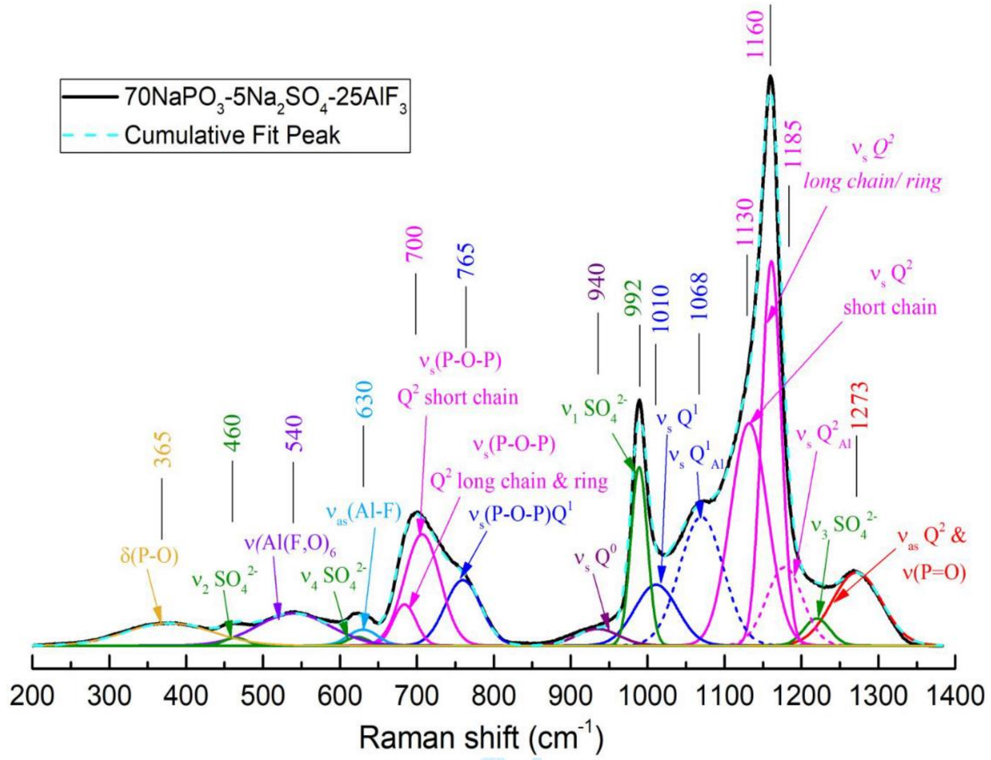

Figure 2: Deconvoluted Raman spectrum of $70NaPO_3$-$5Na_2SO_4$-$25AlF_3$ glass in Le *et al.*[4] Labels indicated positions of individual Gaussian peaks.

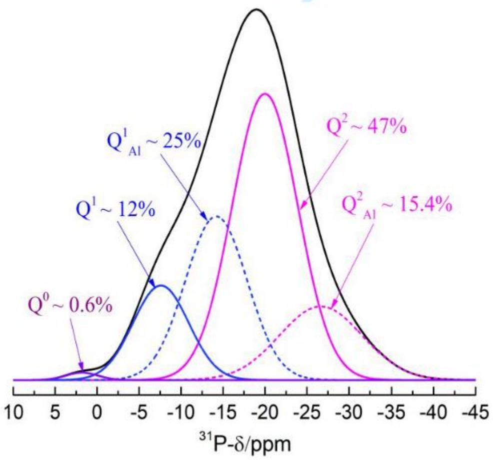

Figure 3: ^{31}P-MAS NMR spectra deconvolutions of $70NaPO_3$-$5Na_2SO_4$-$25AlF_3$ in Le *et al.*[4]

In our glasses with AlF_3 as the source of aluminum, the ^{27}Al-NMR spectra indicate that almost all aluminum atoms have six-fold coordination (even at high [Al/P] where four-fold Al is expected to form, fluorine content forces octahedral coordination).[6-8] Consequently, we expect all investigated compositions to have octahedral aluminum sites. Previously published ^{19}F-NMR of similar Na_2O-P_2O_5-AlF_3 (NAPF) glasses found three different fluorine species: non-bridging fluorine, $Al{-}F{\cdot\cdot}Na^+$ (located at −170 ppm), fluoride bridges, Al−F−Al (−147 ppm), and covalent P−F bonds (−75 ppm).[6,8] The existence of aluminum-fluoride bonds in the current series was confirmed by Raman spectroscopic analysis, at 540 cm^{-1} ($\nu Al(F,O)_6$) and 630 cm^{-1} (ν_{as} Al−F) in **Figure 2**. The current Raman results, combined with previous NMR data on NAPF glasses, and with other literature[6,8,9] indicate that aluminum links to phosphate units through P−O−Al linkages to form $Al(OP)_4F_2$ octahedra. We observe in **Figure 4** that higher AlF_3 content leads to an increased number of P−O−Al bonds for all NAPFS series (as indicated by the respective growth of the Q^1_{Al} and Q^2_{Al} Raman bands at 1068 and 1090 cm^{-1}). Additionally, we expect higher AlF_3 content to result in more Al−F−Al linkages (from previous ^{19}F-NMR).[6,8] As observed elsewhere, these strong, directional bonding interactions are responsible for the decrease in Poisson ratio, and for increasing glass transition temperature and Young's modulus.[4,10]

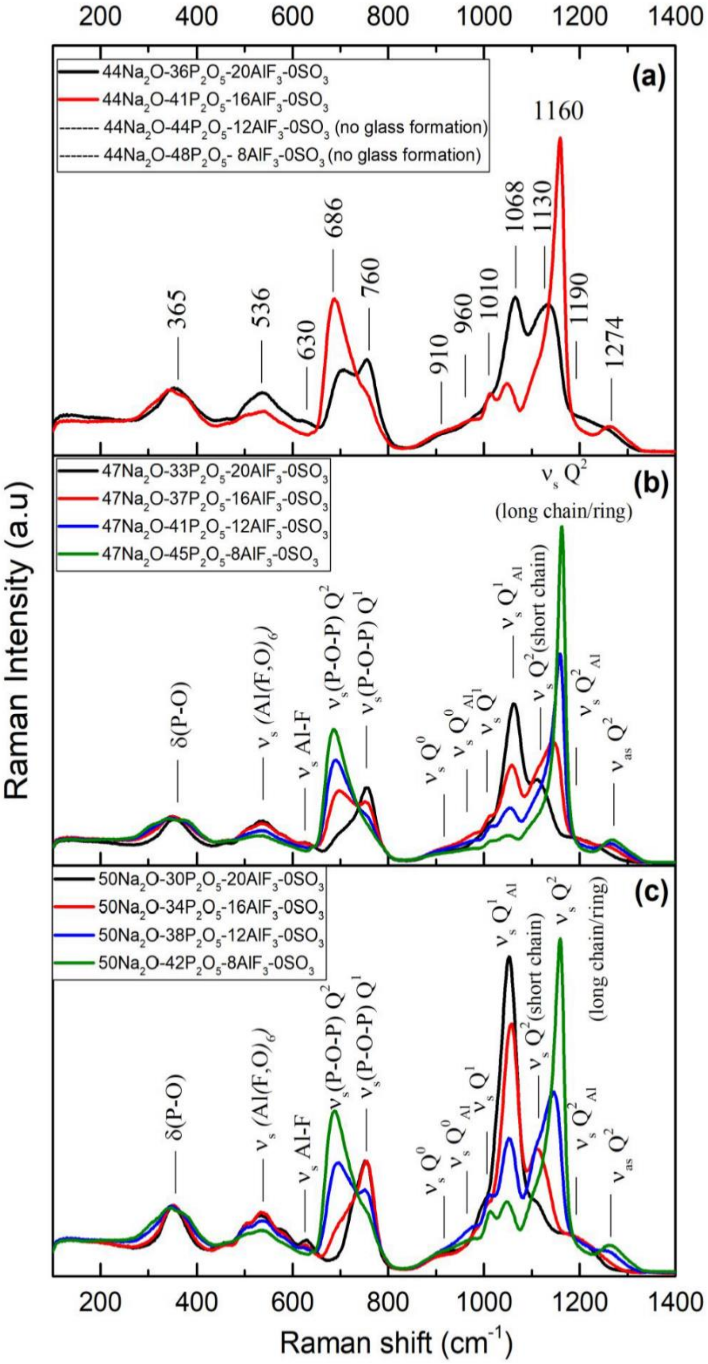

Figure 4: Structural effect of AlF_3 addition at three constant sodium concentrations. Raman spectra of series (a) $44Na_2O/(56 - x)P_2O_5/xAlF_3$, (b) $47Na_2O/(53 - x)P_2O_5/xAlF_3$ and (c) $50Na_2O/(50 - x)P_2O_5/xAlF_3$ (x = 8, 12, 16 and 20 mol%).

In order to better separate the individual effects of AlF_3 and SO_3 addition on the $NaPO_3$ glass structure, comparisons of the appropriate Raman spectra are provided in **Figure 5**. From **Figure 5a**, we find that when P_2O_5 is replaced by AlF_3 (at constant Na_2O and SO_3 content), the intensities of $v_s(Q^1$, P–O–P) species at 760 cm^{-1} and $v_s(Q^1{}_{Al})$ units at 1065 cm^{-1} increase while the $v_s(Q^2$, P–O–P) at 690 cm^{-1} and $v_s(Q^2)$ at 1060 cm^{-1} sharply decrease. Evidently, AlF_3 additions disrupt the metaphosphate chains to form links between the phosphate series *via* Al–O–P bonds. On the other hand, when [Na_2O] and [AlF_3] remain unchanged (**Figure 5b**), the substitution of P_2O_5 by SO_3 causes only slight changes in the Raman spectra. As expected for a decrease in P_2O_5 content (fewer P–O–P bonds), an increase in SO_3 content results in a decrease in the intensity of $v_s(Q^2$, P–O–P) and $v_s(Q^2{}_{Al})$ peaks at 690 and 1160 cm^{-1}, respectively, however, the intensities of $v_s(Q^1$) and $v_s(Q^1{}_m)$ bands remain mostly unaffected. It was previously reported that sulfate anions ($SO_4{}^{2-}$) may facilitate the depolymerization of metaphosphate chains.[4,11] As for the present glasses, however, the results presented in **Figure 5** do not indicate that $SO_4{}^{2-}$ additions results in a larger amount of depolymerized phosphate species. In comparison to AlF_3 addition, sulfate does not cause significant depolymerization of the phosphate network (only that which is caused by lower P_2O_5 content), because unlike aluminum, sulfate does not bond directly to the phosphate network, *i.e.*, it does not form P–O–S bonds. Sulfate exists predominantly in the form of isolated $SO_4{}^{2-}$ tetrahedra associated with Na^+.[11] As the formation of bridging oxygens is avoided, introduction of sulfur trioxide into NAPF glasses results in an increase in Poisson ratio,[12] and a reduction in both the glass transition temperature and Young's modulus.[4] If we consider the relatively strong, covalent Al–O–P bond with its bridging oxygen, AlF_3 and SO_3 have the opposite effect on connectivity of the glass network.

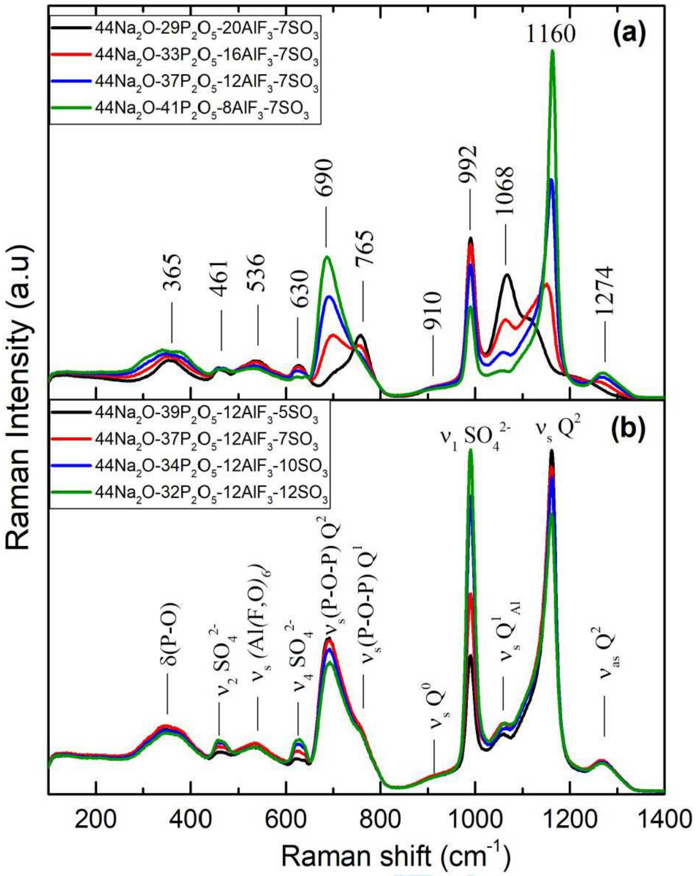

Figure 5: **Structural effects of AlF_3 vs. SO_3 addition**. Raman spectra of series (a) $44Na_2O/(49 - x)P_2O_5/xAlF_3/7SO_3$ and (b) $44Na_2O/(44 - y)P_2O_5/12AlF_3/ySO_3$ ($x = 8$, 12, 16 and 20 mol%, $y = 0$, 5, 7, 10, 12 mol%).

3.2. Effect of composition on electrical conductivity

In glasses, electrical conductivity and the activation energy of ion transport depend on two major factors: the electrostatic binding energy of the charge carrier ions to move freely (E_B) and the strain energy of the glass matrix (E_S).[13] In the present study, the sodium content [Na^+] is much higher than [F^-], thus, sodium cations are expected to be the major contributor to electrical conductivity. The most immediate way to enhance the net conductivity is to enhance the number of charge carriers without reducing their mobility. In order to tailor E_B and E_S, however, the relative amounts of the glass components can be adjusted in other ways. Since both parameters rely on the nature of the pertinent chemical bonding, the glassy matrix must be chosen so as to make sodium cations more mobile, for example, through manipulating local bond polarizability, network rigidity and chemical ordering. As seen from **Figure 6**, the electrical conductivity increases and the activation energy decreases with increasing Na_2O, AlF_3 or SO_3 content. While this trend is shown only for a temperature of 50 °C, it was observed for all temperatures measured (**Figure S1**, the only difference is that higher temperatures result in a smaller spread of conductivities, *i.e.*, weaker compositional dependence; at higher temperatures, the differences in E_S might be wiped-out by thermal softening).

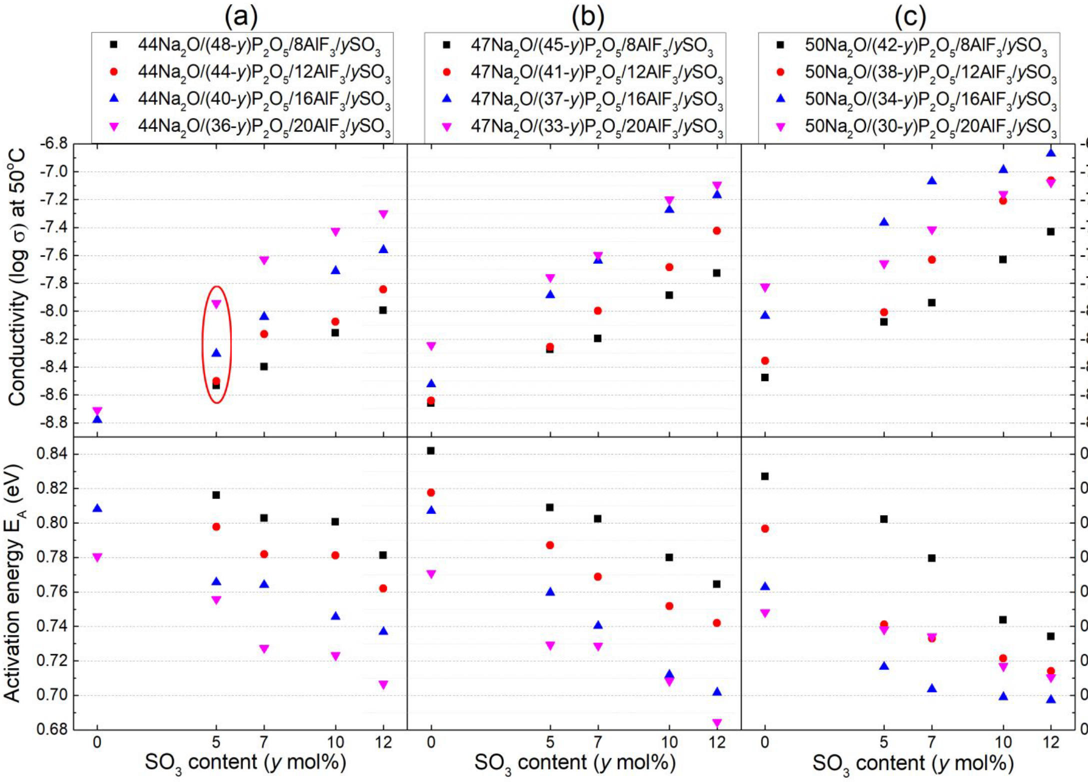

Figure 6: **Dependence of electrical conductivity on AlF_3 and SO_3 content at 50°C**. (a) series I: $44Na_2O/(56 - x - y)P_2O_5/xAlF_3/ySO_3$; (b) series II: $47Na_2O/(53 - x - y)P_2O_5/xAlF_3/ySO_3$; (c) series III: $50Na_2O/(50 - x - y)P_2O_5/xAlF_3/ySO_3$, with x = 8, 12, 16, 20 and y = 0, 5, 7, 10, 12). The circled data is discussed in terms of AlF_3 content in Section 3.2.2.

When comparing conductivity, an important parameter is the charge carrier density, in our case, the number of Na ions per cm^3 (Na^+/cm^3). As can be seen from **Table 1**, when P_2O_5 is partially replaced by Na_2O or SO_3, the average relative increase in Na^+/cm^3 for each substitution step is 14.78% and 3.12%, respectively. Although the sodium density increase for each substitution step is much higher for replacing P_2O_5 with Na_2O than for the replacement of P_2O_5 with SO_3, the average increase in electrical conductivity at 50 °C and the decrease in activation energy are very similar (around 3.42% and −2.3%, respectively). The substitution of P_2O_5 by AlF_3 leads to an increase of the sodium density as well (6.08%), yet, for each substitution step the average increase in electrical conduction is only 2.46% (lower than substitution by either Na_2O or SO_3), but the activation energy still decreases as compared to the other two substitutions, i.e., by about −2.76%. Since the trends in conductivity cannot simply be explained by changes in charge carrier density (Na^+/cm^3) and all chemical substitutions have similar effects on $E_{A,}$ we believe the structure of these glasses to be of import. To better understand how individual chemical components affect the ionic conduction, the structures of the appropriate compositional series are analysed and discussed below.

3.2.1. Na_2O effect

When metal oxides (Me_2O) are introduced into the pure Q^3 phosphate network, they cleave P–O–P linkages to form polar bonds of the type $P–O–Me^+$, *i.e.*, non-bridging oxygens (NBOs), in the glass bulk.[14] Since sodium interacts with the glass network mostly through ionic bonding, we can deduce that as $[Na^+]$ and [NBOs] increase, the electrical conductivity becomes higher. Nonetheless, the relationship between conductivity and Na^+ content is non-linear as variations in free volume and the ionic bonding of the NBOs can also restrain the movement of the Na^+ ions as compared to a glass network with lower E_B (and the same $[Na^+]$).

This non-linear relationship between [NBOs] and [Na$^+$] is demonstrated by the conductivities of the NAPFS glasses plotted in **Figure 7**. Although the glasses with the highest Na_2O concentration (50 mol%) also have the highest electrical conductivity, the conductivity is also dependent on AlF_3 concentration. When [AlF_3] < 20 mol% (**Figures 7a-c**), the conductivity and energy barrier in NAPFS glasses depend strongly on the Na_2O concentration. At the highest AlF_3 concentration (20 mol**%, Figure 7d**), this dependence is much less pronounced.

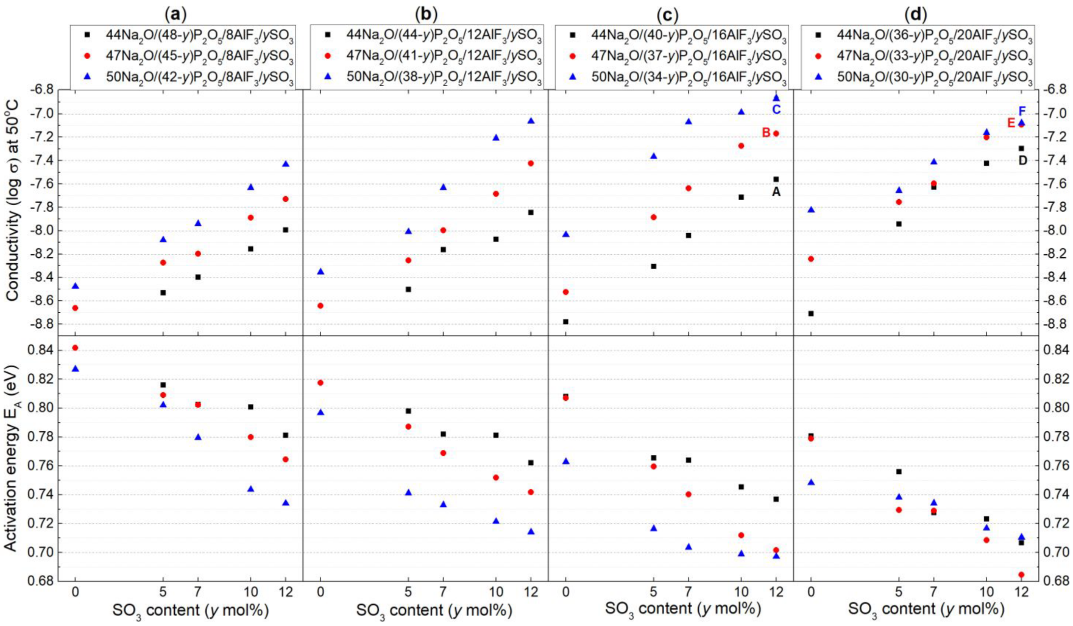

Figure 7: Dependence of electrical conductivity on Na_2O and SO_3 content for constant [AlF_3]: (a) 8 mol% (b) 12 mol% (c) 16 mol% and (d) 20 mol%. Illustrative compositions are labelled A, B, and C and D, E, and F.

The Raman spectra in **Figure 8** highlight the structural differences between the glasses with 16 mol% AlF_3 (labelled A, B, C in **Figure 7c**) and those with only 20 mol% AlF_3 (labelled D, E, F in **Figure 7d**). As expected, the intensity of the $\nu_s(Q^2)$ band decreases, while the $\nu_s(Q^1_{Al})$ peak at 1060 cm^{-1} rises sharply from the incidental higher [Al/P] ratio (Q^1 appears to not be affected substantially). AlF_3 forms $Al(OP)_4F_2$ octahedra in the glass with mostly Al–F··Na$^+$ terminal bonds, which are so strongly preferred that the fluoride has been known to capture Na^+ ions from the sodium phosphate network (and possibly encourage the re-formation of P–O–P bonds).[8] The higher conductivity in **Figure 7c** can then be explained by higher $[AlF_3/P]$ content resulting in higher average ionicity from larger relative amounts of $Al–F··Na^+$ terminal bonds.

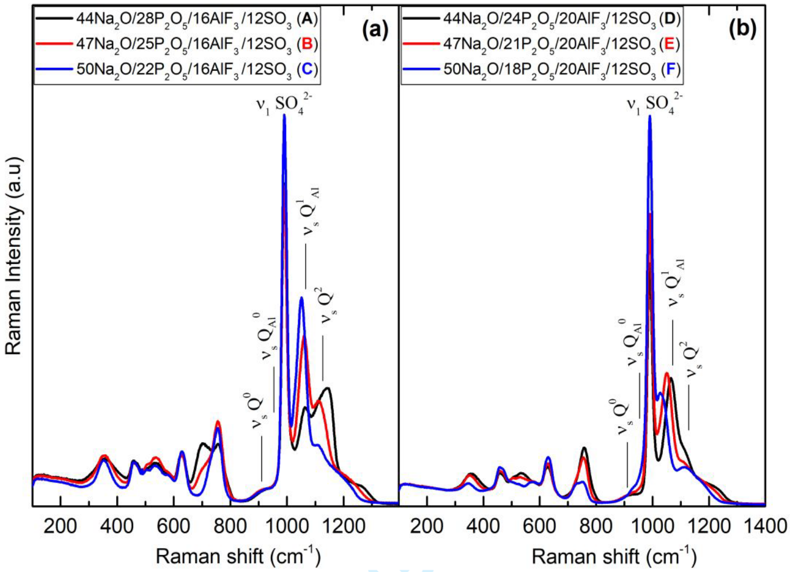

Figure 8: **Effect of Na_2O addition at constant AlF_3 and SO_3 concentrations**. Raman spectra of glasses with (a) < 20 mol% AlF_3, labelled A, B, C in Figure 7c and (b) > 20 mol% AlF_3, labelled D, E, F in Figure 7d.

On the other hand, the Raman spectra in **Figure 8b** do not show as clear trends in intensities of the $v_s(Q^2)$ and $v_s(Q^1{}_{Al})$ bands as a function of Na_2O content. To emphasize the underlying structural changes, **Figure 9** depicts the deconvolution of Raman spectra of the three glasses with greater than 20 mol% AlF_3. Although the spectra were fit with many peaks, the increase of Q^0 species with respect to sodium content (Q^0 and $Q^0{}_{Al}$ peaks located at 925 – 975 cm^{-1}) is clearly seen, while the intensity of the $v_s(Q^1)$ peak remains fairly constant. Since at 20 mol% AlF_3, the $[Na_2O]/([Na_2O]+[P_2O_5])$ ratio is 0.74, it is expected from literature that the glass structure should be composed of only pyrophosphate and orthophosphate units.[15] From this, we assume that the amount of Q^0 species in glass series $50Na_2O/(30$

$- x)P_2O_5/xSO_3/20AlF_3$ is responsible for the smaller conductivity increase (as a function of $[Na_2O]$) as compared to the $47Na_2O/(33 - x)P_2O_5/xSO_3/20AlF_3$ and $44Na_2O/(36 - x)P_2O_5/xSO_3/20AlF_3$ series in **Figure 7d**.

The relative amounts of Q^3, Q^2, Q^1 and Q^0 species in glass depends strongly on the modifier-to-former ratio, *i.e.*, Na_2O/P_2O_5 ratio.[14,16] If $[Na_2O]/([Na_2O]+[P_2O_5])$ is higher than 0.7, phosphate invert glasses are formed exclusively by orthophosphate and pyrophosphate species.[15,16] Sodium phosphate compositions formed of only orthophosphate ($Q^0 = PO_4^{3-}$) and pyrophosphate ($Q^1 = P_2O_7^{4-}$) species have both high $[Na^+]$ and [NBO]/[P]. The high [NBO]/[P] of the Q^0 and Q^1 units results in strong ionic bonds between the sodium charge carriers and the phosphate network, thus counteracting the higher conductivity provided by the added $[Na^+]$. Then, the large population of Q^0 species in the > 20 mol% AlF_3 series results in a stronger binding energy, trapping some of the Na^+ charge carriers. As a result, the conductivity of glasses with > 20 mol% AlF_3 (D, E, F in **Figure 7d**) does not have the same trends as the three series with < 20 mol% AlF_3 (**Figures 7a, 7b, and 7c**).

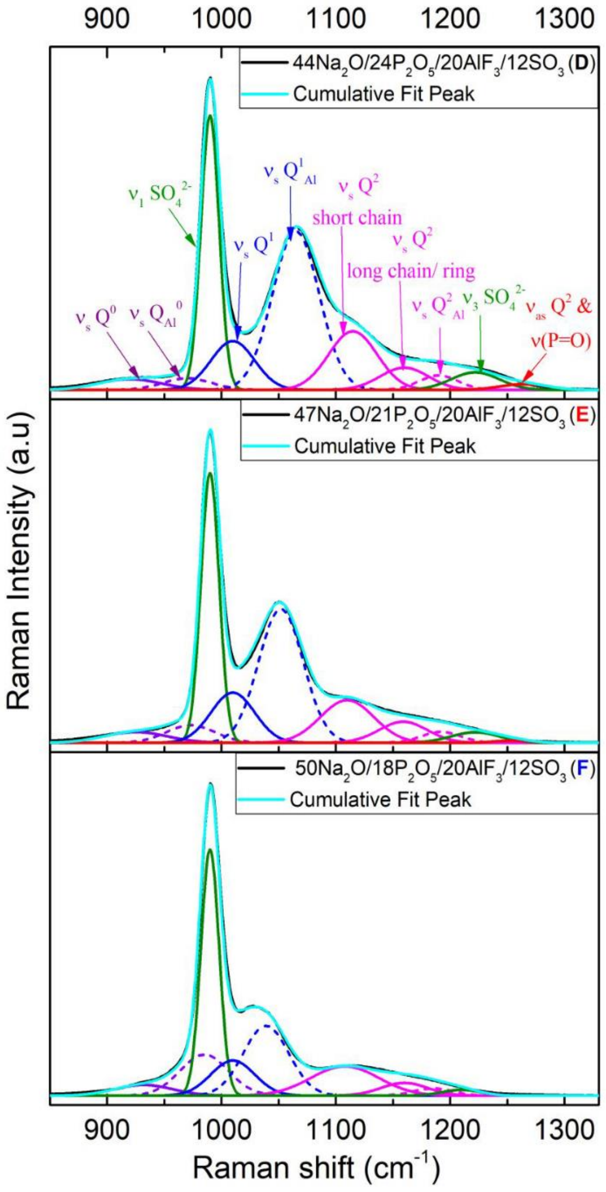

Figure 9: Effect of Na$_2$O addition at high AlF$_3$ and SO$_3$ concentrations. Deconvoluted Raman spectra of glasses with greater than 20 mol% AlF$_3$, labelled D, E, F in Figure 7d.

3.2.2. AlF$_3$ effect

In addition to the depolymerization of the glass network caused by Na$_2$O, also AlF$_3$ disrupts the phosphate chains. The effects of AlF$_3$ on electrical conductivity and activation energy are visible in

Figure 6, where the Na_2O and SO_3 content are held constant. For example, the series with the Na_2O content, ($44Na_2O/(51 - x)P_2O_5/xAlF_3/5SO_3$ [**Figure 6a**, encircled by the red ellipse]) demonstrates that increasing AlF_3 content (from 8 to 20 mol%) leads to higher electrical conductivity, with a significant rise at 20 mol% AlF_3. This phenomenon occurs similarly for 7, 10 and 12 mol% SO_3 in **Figure 6a** and can be observed for all σ at different temperatures (σ plots of 150 and 250 °C are provided in **Figure S1**). **Figure 6a** also shows the expected inverse relationship between activation energy and AlF_3 content, and again, there are larger decreases in E_A for the higher AlF_3 contents (especially between 16 and 20 mol%).

However, for the intermediate concentration of Na_2O, (**Figure 6b**, series $47Na_2O/(53 - x - y)P_2O_5/xAlF_3/ySO_3$), the large 'jump' or increase of electrical conductivity always appears at 16 mol% AlF_3 instead of at 20 mol% (like the lowest [Na_2O] in **Figure 6a**). Indeed, the values of conductivity at 20 mol% AlF_3 are only slightly higher than those for 16 mol% AlF_3. The slight rise in conductivity is generally accompanied by an equally small drop in the activation energy (low SO_3 compositions appear to be exceptions). In contrast, there is a different phenomenon which occurs at the highest [Na_2O], (**Figure 6c**, series of $50Na_2O/(50- x - y)P_2O_5/xAlF_3/ySO_3$): the conductivity values at the highest AlF_3 content (20 mol%) are lower than those at 16 mol%. Predictably, the activation energy also has the lowest values at 16 mol% AlF_3 content, but then rises again at 20 mol% AlF_3 content (again zero SO_3 content is different).

The expected trend with increasing AlF_3 is observed in almost every NAPFS series, with the exception of the glass series with the highest sodium *and* aluminum fluoride content, $50Na_2O/(30 - y)P_2O_5/20AlF_3/ySO_3$ (pink triangles in **Figure 6c**), where instead the conductivity and E_A are lower and higher, respectively, than in the series with less AlF_3 content. This is similar to the unexpectedly small increase in conductivity observed at the highest AlF_3 content when Na_2O was increased (Section 3.2.1), yet here the amount of Na_2O is constant (so instead, high AlF_3 content must be responsible for the lower conductivity).

The Raman spectra in **Figure 4** agree with the conductivity trends for [AlF_3] found in **Figure 6**. They show depolymerization of the phosphate backbone due to the formation of $Al(OP)_4F_2$ octahedra: simultaneous increasing intensity of $v_s(Q^1{}_{Al})$ at 1068 cm^{-1}, rapidly decreasing intensity of $v_s(Q^2)$ at 1130 cm^{-1}, and disappearance of the band at 1160 cm^{-1} ($v_s(Q^2)$, long chain/ring)). The more ionic $F^{\cdot\cdot}Na^+$ bonding leads to higher Na^+ mobility. Even more convincingly, the $v_s(Q^1{}_{Al})$ intensity at 1068 cm^{-1} increases sharply at the same AlF_3 content where the conductivity 'jumped' in **Figure 6**. A large increase in $Q^1{}_{Al}$ at constant 44 Na_2O mol% is observed between 16 to 20 mol% (**Figure 4a**). For 50 Na_2O mol% (**Figure 4c**), the increase in $Q^1{}_{Al}$ occurs at lower AlF_3 content, *i.e.*, between 12 and 16 mol%. For the intermediate amount of Na_2O (47 mol%), it is more difficult to tell from **Figure 4**. If the spectra are deconvoluted, the larger increase in $Q^1{}_{Al}$ is in between 12 and 16 AlF_3 mol% (as expected from the jump in conductivity in **Figure 6b**). It is important to remember that for each constant sodium concentration, there are at least five series of four glasses each that show this correlation between a large increase in σ and $Q^1{}_{Al}$ intensity.

Calculating the aluminum to phosphorus ratio [Al]/[P] for the compositions shown in **Figure 6** and **Figure 4**, the data provided in **Table 2** reveal that σ is roughly correlated with [Al]/[P]: a higher ratio leads to higher σ, until [Al]/[P] reaches some threshold (such as in the case of 50 mol% Na_2O and 20 mol% AlF_3, where σ decreases). Assuming that each aluminum creates an $Al(OP)_4F_2$ octahedron and four Al–O–P bonds, the ratio [Al–O–P]/[P] shows a similar trend: slightly more than one Al–O–P bond per phosphorus tetrahedra ($\approx$ 1.25 [Al–O–P]/[PO_4^{3-}]) does not hinder conductivity and σ is mostly determined by the number of ionic $F^{\cdot\cdot}Na^+$ bonds. However, greater than 1.25 [Al–O–P]/[PO_4^{3-}] (approximately 1.5 [Al–O–P]/[PO_4^{3-}]) does not result in much of an improvement in conductivity and surprisingly, 1.75 – 2 [Al–O–P]/[PO_4^{3-}] lowers σ.

Table 2: Aluminum per phosphate tetrahedra and Al–O–P bond per phosphate tetrahedra as determined from composition.

	44 mol % Na_2O		47 mol % Na_2O		50 mol % Na_2O	
	[Al/P]		[Al/P]		[Al/P]	
Mol% AlF_3	Low SO_3	High SO_3	Low SO_3	High SO_3	Low SO_3	High SO_3
8 AlF3	0.08	0.11	0.09	0.12	0.10	0.13
12 AlF3	0.14	0.19	0.15	0.21	0.16	0.23
16 AlF3	0.20	0.29	0.22	0.32	0.24	0.36
20 AlF3	0.28	0.42	0.30	0.48	0.33	0.56
	[Al–O–P]/[P]		[Al–O–P]/[P]		[Al–O–P]/[P]	
Mol% AlF_3	Low SO_3	High SO_3	Low SO_3	High SO_3	Low SO_3	High SO_3
8 AlF3	0.33	0.44	0.36	0.48	0.38	0.53
12 AlF3	0.55	0.75	0.59	0.83	0.63	0.92
16 AlF3	0.80	1.14	0.86	1.28	0.94	1.45
20 AlF3	1.11	1.67	1.21	1.90	1.33	2.22

The electrical conductivity and the corresponding activation energy are strongly affected by the amount of AlF_3 in NAPFS glasses, yet like Na_2O, the relationship is complex and non-linear. In **Figure 10** we use valence unit (VU) theory[6,17] to explain how sodium ions initially become more ionic and mobile with increasing AlF_3 content, and then become less conductive at too high AlF_3 content. VU theory proposes that strong cations have VUs equal to their valence shared by the number of bonds they form. For example, tetrahedral P^{5+} has +5 VUs shared among four bonds. Additionally, bonds to an oxygen atom must sum up to −2 VUs. For example, **Figure 10a** shows that the phosphorus of Q^2 species cannot give 2 VU to each of its NBOs, and to sum up to −2 VU must gain the remaining electron density from Na^+ ions ($P{-}O{\cdots}Na^+$).

When adding aluminum fluoride to a sodium metaphosphate glass (**Figure 10b**), AlF_3 depolymerizes the phosphate chains, and forms $Al(OP)_4F_2$ octahedra (Al–O–P bonds). Based on previous results (especially the chemical shifts of the ^{19}F NMR),[6,8] $Al{-}F{\cdot\cdot}Na^+$, Al−F−Al, and P−F bonds exist. Since phosphorus is forced to bond with aluminum, Na^+ ions are released from NBOs, and preferentially associate with terminal fluorine ions instead. Generally, the increase in σ and the lower activation barrier when AlF_3 content increases are due to reduced directionality of these new bonds between sodium and fluorine. The Al–F··Na^+ and P–F··Na^+ bonds shown in **Figure 10b** demonstrate that sodium must donate only 0.5 VUs to the terminal fluorines. The Raman analysis in Section 3.2.1 (**Figure 4**) and literature[4,7,9] suggest that pyrophosphate (Q^1) and orthophosphate (Q^0) units are formed almost exclusively upon high Na_2O and AlF_3 addition; this is illustrated in **Figure 10c** for [AlF_3] being higher to approximately equal to [P_2O_5]. Although the Q^0 and Q^1 species form relatively directional Al–O–P bonds, VU theory indicates that $Al(OP)_4F_2$ octahedra donate only 0.5 VUs to an oxygen neighbour, causing the NBOs of Q^0_{Al} to strongly attract Na^+ ions (in order to fill their 2 VUs).

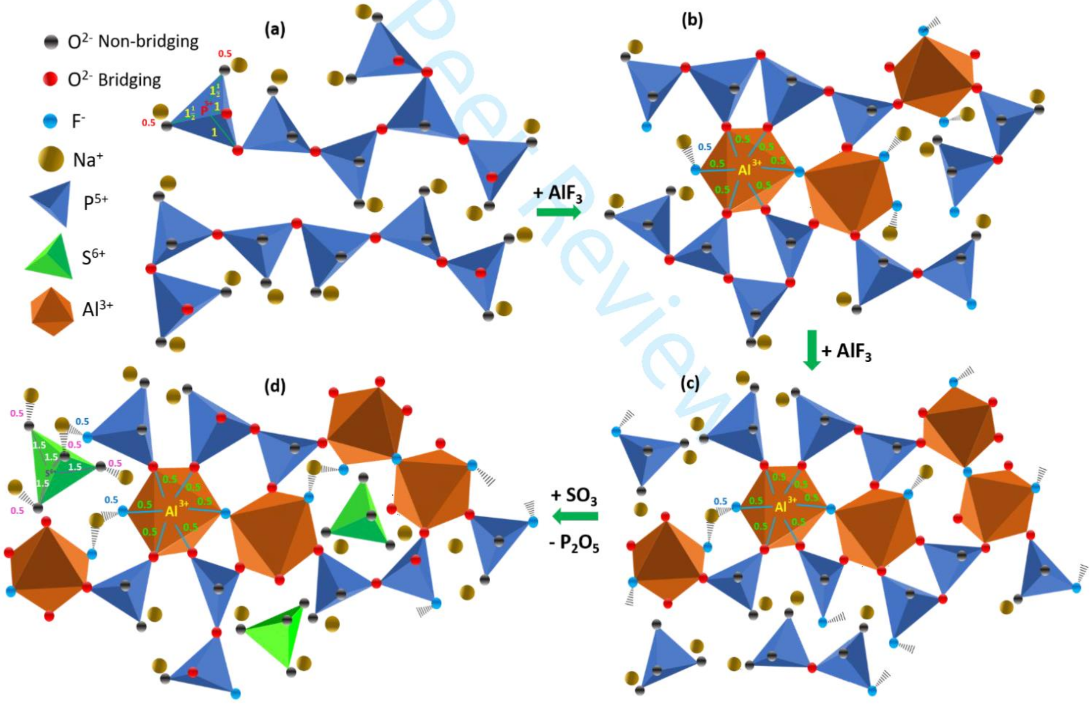

Figure 10: Structural models of (a) pure $NaPO_3$, (b) $NaPO_3$ + 8 or 12 mol% AlF_3 (c) $NaPO_3$ + 16 or 20 mol% AlF_3, (d) $NaPO_3$ + 16 or 20 mol% AlF_3 + SO_3. The VU calculation is shown for a Q^2 phosphate, $Al(OP)_2F_2$ and SO_4^{2-} polyhedra, all with sodium neighbours.

In **Figure 11**, we compare the [VU]/[NBO] ratio of all of the possible Q^0 and Q^1 species, depending on the number of aluminum and fluorine neighbors (Q^0, Q^0_F, Q^0_{Al}, Q^0_{2Al}; Q^1, Q^1_F, Q^1_{Al}, Q^1_{2Al}). For simplicity, we made P–F bonds equivalent to Al–F bonds and assumed that the oxygen in Al–O–P bonds needs 1.5 VU from the phosphorus (based on only gaining 0.5 VU from the Al). It is clear, in addition to creating ionic $F^{\cdot\cdot}Na^+$ bonds, that the P–F bonds (found in Q^0_F and Q^1_F) also reduce the VU or electron density per NBO that is necessary from each sodium, therefore making the bond weaker between NBO and sodium. On the other hand, aluminum addition has the opposite effect: one or two Al–O–P bonds substantially increases the electron density required from each sodium ([VUs]/[NBO]) until it is at a maximum of 1 VU/NBO for Q^0_{2Al} and Q^1_{2Al} species. As discussed in Section 3.2.1, Q^0 and Q^0_{Al} species reduce the conductivity significantly, so if [VU = 0.75]/[NBO] hinders conductivity, Q^1_{Al} should also reduce sodium mobility; this may be true, but according to the conductivity trends, the added mobility from fluorine ($F^{\cdot\cdot}Na^+$, P–F bonds) appears to compensate until Q^0_{2Al} and Q^1_{2Al} units dominate the structure. According to the [Al–O–P]/[PO_4^{3-}] calculations (**Table 2**), phosphate tetrahedra with two aluminum neighbors dominate at the same compositions where there are significant increases in the Raman Q^0_{Al} and Q^1_{Al} peaks, revealing Raman spectroscopy's weakness as it is unable to differentiate between Q-species with one or two aluminum neighbors. However, it follows that as more aluminum is added (at constant [Na_2O]), more Q-species with two aluminum neighbors will be formed.

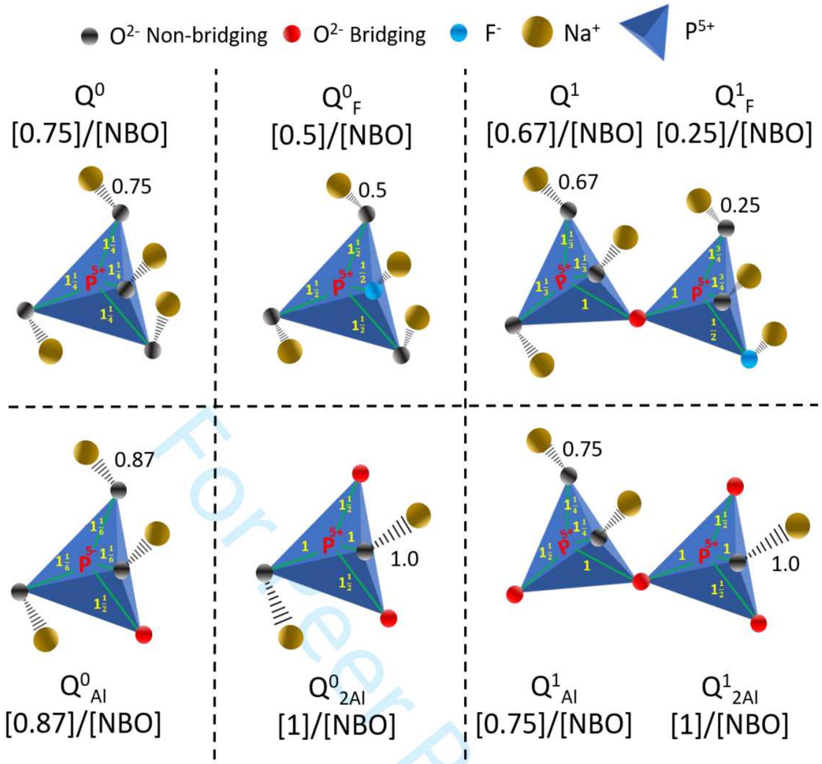

Figure 11: Antagonistic effects of fluorine and aluminum on the NBOs of phosphate tetrahedra according to Valence Unit theory. For example, Q^0 requires 3 Na^+ shared among 4 NBOs giving it [0.75 VU]/[NBO]. The size of the NBOs corresponds roughly with the electron density required from Na^+.

Nonetheless, the conductivity trends, compositional analysis and VU theory make clear that aluminum neighbors result in higher binding energies between NBOs and sodium. Then, a large fraction of the Na^+ ions become trapped by the more electron-deficient NBOs. VU theory (**Figure 11**) helps elucidate the reason that Q^0_{2Al} and Q^1_{2Al} species appear to hinder conduction compared with Q^0_{Al} and Q^1_{Al} species; it confirms that the $Na^+\cdot\cdot O$ bond is stronger, *i.e.*, has higher binding energy, in phosphate tetrahedra with more aluminium neighbours. Therefore, when Q^0_{2Al} and Q^1_{2Al} species are the majority, the average mobility of the sodium ions is lower than in the case shown in **Figure 10b** (when Q^0_{Al} and Q^1_{Al} species are the most common). This creates a unique situation, where despite having more ionic $F\cdot\cdot Na^+$ bonds and P–F bonds reducing the attraction of NBOs, the additional attraction of the sodium cations to the electron-deficient NBOs created by Al addition leads to a decrease in electrical conductivity and an increase in activation energy.

3.2.3. SO_3 effect

From examining **Figure 12** we discern that electrical conduction and activation energy are closely tied to the amount of SO_3 content introduced into NAPFS glass. Since the Raman results did not show any bonding of sulfate to the phosphate backbone (**Figure 5**, in agreement with previous studies[4,11,18]) SO_4^{2-} adds as isolated pseudo-Q^0 species and is known to lead to the loosening of the initial glass structure. Further confirmation is provided by the decrease in T_g when adding more SO_3 into the glass compositions (**Table 1**). This result is absolutely opposite with the study of Thilo and Blumental,[19] where the authors put forward the hypothesis that sulfur can connect to phosphate groups and form sulfopolyphosphate chains.

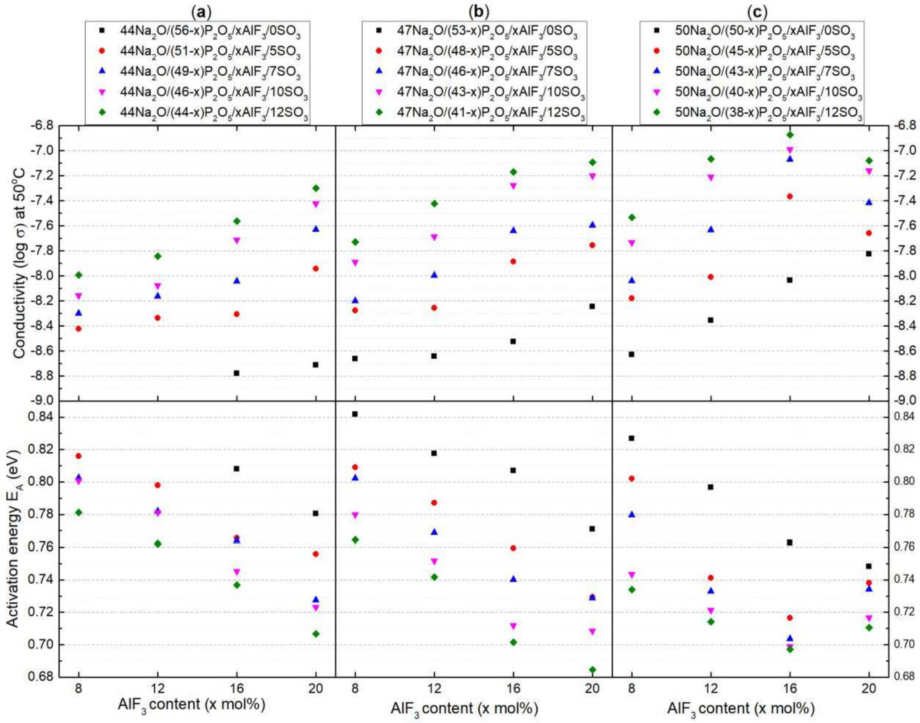

Figure 12: **Dependence of electrical conductivity on both AlF_3 and SO_3 content when $[Na_2O]$ is held constant**: (a) 44 mol% (b) 47 mol% and (c) 50 mol%.

To refute Thilo and Blumental[19] further, we compare the Raman spectra of two glass series in **Figure 13**: $47Na_2O/(53-x)P_2O_5/xAlF_3/0SO_3$ and $47Na_2O/(48-x)P_2O_5/xAlF_3/5SO_3$ with $x = 8, 12, 16, 20$. When P_2O_5 was replaced by 5 mol% of SO_3, the vibrational energies change as expected upon the addition of AlF_3, with only slightly more Q^1_{Al} units for the higher [Al/P] ratio (5 mol% SO_3). There are no new Raman peaks with the exceptions of additional features emerging around 460, 627 and 992 cm^{-1} corresponding to symmetric bending $\nu_2(SO_4^{2-})$, asymmetric bending $\nu_4(SO_4^{2-})$ and symmetric stretching $\nu_1(SO_4^{2-})$ modes of the sulfate ions, all charge-balanced by Na^+ cations.[4,11,20,21] Given the lack of structural changes in the phosphate backbone upon SO_3 addition (in comparison to AlF_3 addition), we confirm that sulfate exists mainly in the form of isolated SO_4^{2-} tetrahedra associated with Na^+. We posit that without P–O–S bridges, pseudo-Q^0 SO_4^{2-} ions will create glass regions with non-directional bonding character and high flexibility, and thus, the movement of Na^+ ions in the glass matrix will be easier, *i.e.*, have lower strain energy, in these regions.

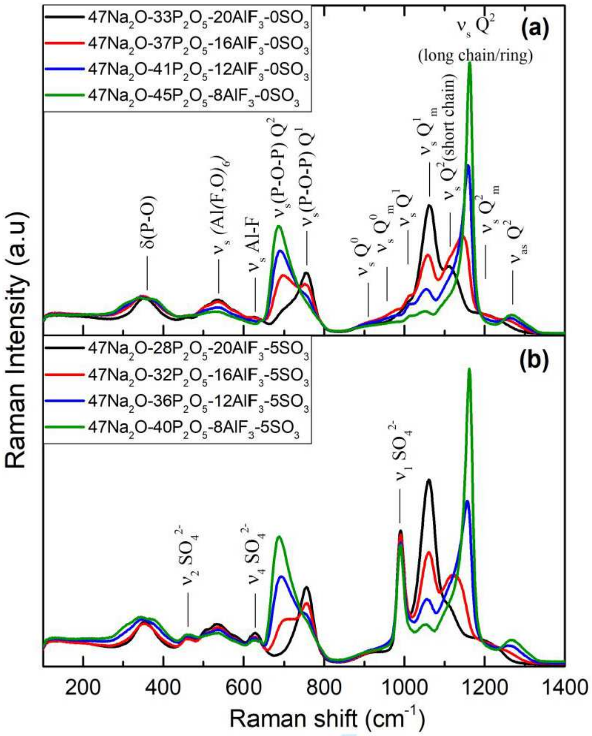

Figure 13: **Structural effect of AlF_3 addition at two constant SO_3 concentrations**. Raman spectra of series (a) $47Na_2O/(53 - x)P_2O_5/xAlF_3/0SO_3$ and (b) $47Na_2O/(48 - x)P_2O_5/xAlF_3/5SO_3$ (x = 8, 12, 16 and 20 mol%).

Upon the substitution of P_2O_5 by SO_3 at constant [Na_2O], a number of Na^+ ions are liberated from the P_2O_5 network. Although these Na^+ ions continue to bond to SO_4^{2-}, the binding energy between Na^+ and $S–O^-$ is weaker than that of the pair of Na^+ and $P–O^-$, thus the mobility of Na^+ is higher in the presence of sulfate. According to VU theory (**Figure 10d**), an isolated SO_4^{2-} tetrahedron will require an equal amount of electron density from its cation neighbours (0.5 VU in pink) as a Q^2 species, but less than a phosphate Q^0 or Q^1 species. Also, Ganguli *et al.* argue that the addition of sulfate makes a more conductive glass than pure metaphosphate because of the higher partial charge on the oxygen in a $P–O^-$ bond compared to the oxygen in an $S–O^-$ bond.[22] According to Pauling's rules of packing, both $P–O^-$

and S–O⁻ are ionocovalent bonds; the electronegativities of oxygen, phosphorus and sulfur are 3.44, 2.19 and 2.58, respectively. Thus, the difference in electronegativity of P–O⁻ is greater than that of S–O⁻, and the oxygen in P–O⁻ has a stronger 'pull' on the shared electron pairs as compared to the oxygen in S–O⁻. As a result, the Na^+ ions located near P–O⁻ bonds are trapped in deeper potential wells, while the Na^+ ions present in the coulombic potential wells near S–O⁻ bonds are expected to be more easily liberated.[22] Therefore, as more SO_3 content was added, the mobility of the sodium cations increased linearly and the activation energies became lower (as seen in **Figure 12**). Addition of SO_3 decreased both the strain energy of the glass matrix and the binding energy (the energy of bonds between the glass matrix and charge carriers), and therefore, the electrical conductivity increased.

4. Conclusion

Improvement of both the conductivity and activation energy significantly depends on the quantity of charge carriers (Na^+ ions), however, the mobility of Na^+ ions is also greatly affected by modification of the glass structure, *i.e.*, introduction of AlF_3 and SO_3. This was demonstrated when P_2O_5 was partially replaced by Na_2O, AlF_3 or SO_3: even though the addition of each chemical component affects the charge carrier density (Na^+/cm^3) differently, the electrical conductivity and activation energy still increase or decrease similarly. This indicated that structural changes due to compositional variation were at play. Raman and NMR spectroscopy revealed that AlF_3 depolymerized the Q^2 chain-like sodium metaphosphate structure to form bridging oxygen-like Al–O–P bonds, as well as terminal $Al–F{\cdot\cdot}Na^+$ and $P–F{\cdot\cdot}Na^+$ bonds. Valence unit theory helped explain the reason why terminal fluoride bonds were found to greatly increase conductivity (formation of weaker $NBO{\cdot\cdot}Na^+$ and $F{\cdot\cdot}Na^+$ bonds), but highly depolymerized Q^n species with two aluminum neighbors hinder sodium conductivity substantially. These concomitant, antagonistic effects led to smaller increases in σ at constant sodium additions and a reversal in σ trends for AlF_3 addition. The correlation between σ and SO_3 content is simpler, where isolated SO_4^{2-} ions with weaker bonding between the oxygen and sodium resulted in linearly increasing conductivity.

Based on the relationships found within, Na_2O and SO_3 should be increased as much as possible in NAPFS glasses in order to improve conductivity and energy of activation (until crystallization occurs). The correlation with AlF_3 content is more complex; AlF_3 depolymerizes the phosphate network significantly, therefore, raising [AlF_3] in NAPFS glasses to increase the electrical conductivity is limited by the ratio of [Al/P] (since $Q^0{}_{2Al}$ and $Q^1{}_{2Al}$ species possess substantially higher binding energies between the Na^+ and NBOs).

Acknowledgements

This project received funding from the European Research Council (ERC) under the European Union's Horizon 2020 research and innovation program (ERC grant UTOPES, grant agreement no. 681652). HQL is grateful to the Vietnam International Education Development (VIED) of the Ministry of Education and Training of Vietnam for financial support. Parts of the study were supported by the European Commission through its European Social Fund (ESF) for Thuringia. We acknowledge fruitful discussion and collaboration with all members of the Hy-NIB project consortium. The authors are thankful to Gabi Moeller (sample preparation), Nadja Buchert and Jelena Petrovic (thermal analyses), Christian Zeidler (Raman measurement) and Lingqi Su (impedance analyses) for valuable support in data acquisition.

References

1. Xu GL, Amine R, Abouimrane A, Che HY, Dahbi M, Ma ZF, et al. Challenges in Developing Electrodes, Electrolytes, and Diagnostics Tools to Understand and Advance Sodium-Ion Batteries. Adv Energy Mater 2018;8(14).
2. Pan HL, Hu YS, Chen LQ. Room-temperature stationary sodium-ion batteries for large-scale electric energy storage. Energ Environ Sci 2013;6(8):2338-60.
3. Bella F, Colo F, Nair JR, Gerbaldi C. Photopolymer Electrolytes for Sustainable, Upscalable, Safe, and Ambient-Temperature Sodium-Ion Secondary Batteries. ChemSuschem 2015;8(21):3668-76.
4. Le QH, Palenta T, Benzine O, Griebenow K, Limbach R, Kamitsos EI, et al. Formation, structure and properties of fluoro-sulfo-phosphate poly-anionic glasses. J Non-Cryst Solids 2017;477:58-72.
5. Braunger ML, Escanhoela CA, Fier I, Walmsley L, Ziemath EC. Electrical conductivity of silicate glasses with tetravalent cations substituting Si. J Non-Cryst Solids 2012;358(21):2855-61.
6. Calahoo C, Petrovic J, Le QH, Werner-Zwanziger U, Zwanziger J, Wondraczek L. Structural Relaxation in Polyanionic Sodium Fluorophosphate Glasses. Front Mater 2019;6(165).
7. Möncke D, Ehrt D, Velli LL, Varsamis CPE, Kamitsos EI, Elbers S, et al. Comparative spectroscopic investigation of different types of fluoride phosphate glasses. Phys Chem Glasses: Eur J Glass Sci Technol, Part B 2007;48(6):399-402.
8. Bradtmuller H, Zhang L, de Araujo CC, Eckert H, Möncke D, Ehrt D. Structural Studies of NaPO3-AlF(3) Glasses by High-Resolution Double-Resonance Nuclear Magnetic Resonance Spectroscopy. J Phys Chem C 2018;122(37):21579-88.
9. Möncke D, Eckert H. Review on the structural analysis of fluoride-phosphate and fluoro-phosphate glasses. J Non-Cryst Solids: X 2019;3:100026.
10. Limbach R, Rodrigues BP, Moncke D, Wondraczek L. Elasticity, deformation and fracture of mixed fluoride-phosphate glasses. J Non-Cryst Solids 2015;430:99-107.
11. Da N, Grassme O, Nielsen KH, Peters G, Wondraczek L. Formation and structure of ionic (Na, Zn) sulfophosphate glasses. J Non-Cryst Solids 2011;357(10):2202-6.
12. Striepe S, Da N, Deubener J, Wondraczek L. Micromechanical properties of (Na,Zn)-sulfophosphate glasses. J Non-Cryst Solids 2012;358(6-7):1032-7.
13. Anderson OL, Stuart DA. Calculation of Activation Energy of Ionic Conductivity in Silica Glasses by Classical Methods. J Am Ceram Soc 1954;37(12):573-80.
14. Sokolov IA, Murin IV, Kriyt VE, Pronkin AA. Structure and Electrical Conductivity of Glasses in the Na2O-Na2SO4-P2O5 System. Glass Phys Chem 2011;37(4):351-61.
15. Brauer DS, Möncke D. Introduction to the structure of silicate, phosphate and borate glasses. In: Boccaccini AR, Brauer DS, Hupa L, editors. Bioactive Glasses: Fundamentals, Technology and Applications: The Royal Society of Chemistry; 2016. p. 61 - 88.
16. Brow RK. Review: the structure of simple phosphate glasses. J Non-Cryst Solids 2000;263(1-4):1-28.
17. Bunker BC, Kirkpatrick RJ, Brow RK. Local-Structure of Alkaline-Earth Boroaluminate Crystals and Glasses .1., Crystal Chemical Concepts Structural Predictions and Comparisons to Known Crystal-Structures. J Am Ceram Soc 1991;74(6):1425-9.
18. Arkhipov VG, Ivanova LV, Mamoshin VL, Buler PI, Lushchai OI, Galnykina LM. Spectroscopic investigation of structural peculiarities of sulphate-phosphate glasses containing alkalis. J Appl Spectrosc 1986;45:460-4.
19. Thilo E, Blumenth.G. Zur Chemie Der Kondensierten Phosphate Und Arsenate .48. Uber Sulfatophosphate. Z Anorg Allg Chem 1966;348(1-2):77-&.
20. Möncke D, Sirotkin S, Stavrou E, Kamitsos EI, Wondraczek L. Partitioning and structural role of Mn and Fe ions in ionic sulfophosphate glasses. J Chem Phys 2014;141(22).

21. Thieme A, Moncke D, Limbach R, Fuhrmann S, Kamitsos EI, Wondraczek L. Structure and properties of alkali and silver sulfophosphate glasses. J Non-Cryst Solids 2015;410:142-50.

22. Ganguli M, Bhat MH, Rao KJ. Lithium ion transport in Li2SO4-Li2O-P2O5 glasses. Solid State Ion 1999;122(1-4):23-33.

Figure 1: (a) Temperature dependence of the electrical conductivity of glass $47Na_2O-30P_2O_5-7SO_3-16AlF_3$, **(b)** Nyquist plots of glass $47Na_2O-30P_2O_5-7SO_3-16AlF_3$ at various temperatures (labels), **(c)** Arrhenius plot for the $47Na_2O-30P_2O_5-7SO_3-16AlF_3$ glass.

Figure 2: Deconvoluted Raman spectrum of $70NaPO_3-5Na_2SO_4-25AlF_3$ glass in Le *et al.*[4] Labels indicated positions of individual Gaussian peaks.

Figure 3: ^{31}P-MAS NMR spectra deconvolutions of $70NaPO_3-5Na_2SO_4-25AlF_3$ in Le *et al.*[4]

Figure 4: **Structural effect of AlF_3 addition at three constant sodium concentrations**. Raman spectra of series (a) $44Na_2O/(56 - x)P_2O_5/xAlF_3$, (b) $47Na_2O/(53 - x)P_2O_5/xAlF_3$ and (c) $50Na_2O/(50 - x)P_2O_5/xAlF_3$ (x = 8, 12, 16 and 20 mol%).

Figure 5: **Structural effects of AlF_3 vs. SO_3 addition**. Raman spectra of series (a) $44Na_2O/(49 - x)P_2O_5/xAlF_3/7SO_3$ and (b) $44Na_2O/(44 - y)P_2O_5/12AlF_3/ySO_3$ (x = 8, 12, 16 and 20 mol%, y = 0, 5, 7, 10, 12 mol%).

Figure 6: **Dependence of electrical conductivity on AlF_3 and SO_3 content at 50°C**. (a) series I: $44Na_2O/(56 - x - y)P_2O_5/xAlF_3/ySO_3$; (b) series II: $47Na_2O/(53 - x - y)P_2O_5/xAlF_3/ySO_3$; (c) series III: $50Na_2O/(50 - x - y)P_2O_5/xAlF_3/ySO_3$, with x = 8, 12, 16, 20 and y = 0, 5, 7, 10, 12). The circled data is discussed in terms of AlF_3 content in Section 3.2.2.

Figure 7: **Dependence of electrical conductivity on Na_2O and SO_3 content for constant [AlF_3]**: (a) 8 mol% (b) 12 mol% (c) 16 mol% and (d) 20 mol%. Illustrative compositions are labelled A, B, and C and D, E, and F.

Figure 8: **Effect of Na_2O addition at constant AlF_3 and SO_3 concentrations**. Raman spectra of glasses with (a) < 20 mol% AlF_3, labelled A, B, C in Figure 7c and (b) > 20 mol% AlF_3, labelled D, E, F in Figure 7d.

Figure 9: **Effect of Na_2O addition at high AlF_3 and SO_3 concentrations**. Deconvoluted Raman spectra of glasses with greater than 20 mol% AlF_3, labelled D, E, F in Figure 7d.

Figure 10: Structural models of (a) pure $NaPO_3$, (b) $NaPO_3$ + 8 or 12 mol% AlF_3 (c) $NaPO_3$ + 16 or 20 mol% AlF_3,

(d) $NaPO_3$ + 16 or 20 mol% AlF_3 + SO_3. The VU calculation is shown for a Q^2 phosphate, $Al(OP)_2F_2$ and SO_4^{2-} polyhedra, all with sodium neighbours.

Figure 11: Antagonistic effects of fluorine and aluminum on the NBOs of phosphate tetrahedra according to Valence Unit theory. For example, Q^0 requires 3 Na^+ shared among 4 NBOs giving it [0.75 VU]/[NBO]. The size of the NBOs corresponds roughly with the electron density required from Na^+.

Figure 12: **Dependence of electrical conductivity on both AlF_3 and SO_3 content when [Na_2O] is held constant**: (a) 44 mol% (b) 47 mol% and (c) 50 mol%.

Figure 13: **Structural effect of AlF_3 addition at two constant SO_3 concentrations**. Raman spectra of series (a) $47Na_2O/(53-x)P_2O_5/xAlF_3/0SO_3$ and (b) $47Na_2O/(48-x)P_2O_5/xAlF_3/5SO_3$ (x = 8, 12, 16 and 20 mol%).

Figure S1: **Dependence of electrical conductivity on AlF_3 and SO_3 content at 50, 150 and 250°C**. (a) series I: $44Na_2O/(56-x-y)P_2O_5/xAlF_3/ySO_3$; (b) series II: $47Na_2O/(53-x-y)P_2O_5/xAlF_3/ySO_3$; (c) series III: $50Na_2O/(50-x-y)P_2O_5/xAlF_3/ySO_3$, with x = 8, 12, 16, 20 and y = 0, 5, 7, 10, 12).

Optimization of Electrical Conductivity in the Na_2O-P_2O_5-AlF_3-SO_3 Glass System

Quyen Huyen Le[a,b], Courtney Calahoo[a], Yang Xia[a], Caio B. Bragatto[c], Lothar Wondraczek[a,*]

[a]*Otto Schott Institute of Materials Research, University of Jena, Fraunhoferstrasse 6, 07743 Jena, Germany*
[b]*Can Tho University of Technology, 256 Nguyen Van Cu, Can Tho, Vietnam*
[c] *Department of Physics, Coe College, Cedar Rapids, Iowa 52402, United States*

Supplementary Information

Figure S1: **Dependence of electrical conductivity on AlF_3 and SO_3 content at 50, 150 and 250°C**. (a) series I: $44Na_2O/(56 - x - y)P_2O_5/xAlF_3/ySO_3$; (b) series II: $47Na_2O/(53 - x - y)P_2O_5/xAlF_3/ySO_3$; (c) series III: $50Na_2O/(50 - x - y)P_2O_5/xAlF_3/ySO_3$, with $x = 8, 12, 16, 20$ and $y = 0, 5, 7, 10, 12$).

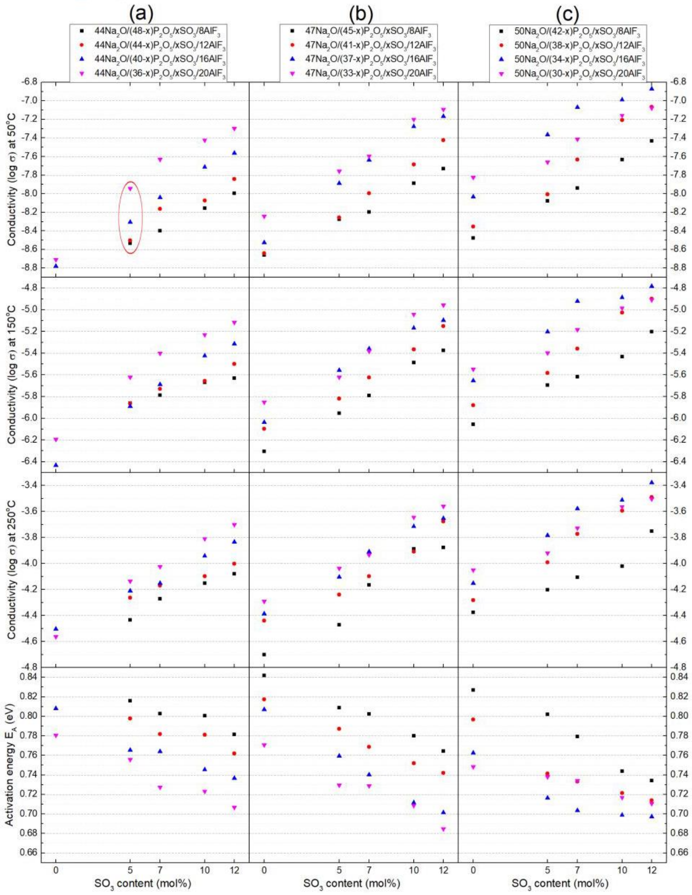

4 Summary

The aim of this research was to study the relationships between the formation, structure, and properties of the new glass system, fluoro-sulfo-phosphate poly-anionic glasses, specifically focusing on the effect of the glass structure on optical properties and electrical conductivity. In this project, the fluoro-sulfo-phosphate glass system can be divided into two groups: the FPS series [$(100–x–y)MF_n$ / $xSr(PO_3)_2$ / $ySrSO_4$ ($x + y \leq 20\%$, M = Mg^{2+}, Ca^{2+}, Sr^{2+}, Al^{3+}) with $F^– > P_2O_5 + SO_3$] were studied as new host materials for optically active cation species, while the NAPFS series [$(100–x–y)AlF_3$ / $xNaPO_3$ / yNa_2SO_4 ($x + y \geq 80\%$), with $F^– < P_2O_5 + SO_3$], whose compositions possess high sodium concentrations, and thus, high ionic conductivity and low activation energy, were investigated for their future application in solid-state sodium-ion batteries.

Raman spectra showed that the glass structure of FPS glasses (with low phosphate content) is dominated by pyro- and orthophosphate whereas in NAPFS glasses (with high phosphate content) the phosphate network is less depolymerised and metaphosphate chains are more abundant. ^{27}Al MAS NMR data indicated that six-fold aluminum is dominant in both FPS and NAPFS glass systems. Terminal fluoride $Al–F_T$, bridging fluoride Al–F–Al and Al−O−P linkages also exist in both glass systems. However, the presence of P–F bonding was found only in NAPFS but not in FPS glasses. Sulfate exists predominantly in the form of isolated $SO_4^{2–}$ tetrahedra associated with modifier cations in glass network.

To better understand the effect of multi-anion FPS glasses on the dopant species, Cu^{2+} was used as a probe for assessing the local structural arrangement within a solid host and studied by both UV-vis and EPR spectroscopy. Here, the local environments of Cu^{2+} in fluoride-phosphate (FP) and fluoride-phosphate-sulfate (FPS) glasses were compared with the Cu^{2+} environment in alkaline earth metaphosphate (MP). In the MP glasses, the Cu^{2+} ligand environment exhibited an elongated tetragonal distortion of the CuO_6 octahedra, where the asymmetric and broad NIR absorption band of Cu^{2+} was found to shift from approximately 740 nm to 880 nm with increasing optical basicity. The absorption bands were fitted by three Gaussian components corresponding to $d_{z^2} \rightarrow d_{x^2-y^2}$, $d_{xy} \rightarrow d_{x^2-y^2}$, and $d_{xz}, d_{yz} \rightarrow d_{x^2-y^2}$. Unlike the strong dependence of site geometry of Cu^{2+} in MP glasses, there was a much less pronounced correlation of the absorption band maximum on optical basicity in the glasses which contain fluorine, the FP and FPS glass series. The spectral properties were dominated by the presence of pyrophosphate groups (Q^1, more Q^1 led to red-shifted absorption bands), sulfate groups (SO_4^{2-}, with higher S:P ratio resulting in blue-shifted absorption) and fluorine (F, more F also led to blue-shifted absorption bands). The optical absorption spectra were fit best using four contributions to account for the transitions from d_{z^2}, d_{xy}, d_{yz} and d_{xz} to $d_{x^2-y^2}$. In agreement with the optical absorption spectra analysis, EPR spectroscopy also indicated Cu^{2+} had a tetragonally distorted octahedral coordination in MP and a rhombohedral distortion in FP and FPS glasses.

FPS glasses with high fluoride content are characterized by low refractive index, an exceptional partial dispersion as well as high transmission from the ultraviolet (UV) to the infrared (IR) region, and since they contain various anion species they provide an extremely complex structural environment for optically active dopant species. With chromium doping, for example, we find a broad red photoluminescence at 734 nm and an inhomogeneous broadening of the *R*-line at 694 nm, originating from the $^4T_2 \rightarrow {}^4A_2$ and $^2E \rightarrow {}^4A_2$ transitions of Cr^{3+}, respectively. The luminescence mechanism was further analyzed on the basis of the corresponding Tanabe–Sugano diagram. Tailored through chemical composition, homogeneously nucleated precipitation of a nanocrystalline fluoride phase enabled switching between high-field and low-field configurations of the Cr^{3+} ion, resulting in the specific emission properties and setting the path towards FPS-based optical devices, in particular, broadband tunable fiber amplifiers and lasers.

Electrical conductivity and activation energy of NAPFS glasses depend strongly on the electrostatic binding energy of the charge carrier ions to move freely (E_B) and the strain energy of the glass matrix (E_S). Besides simply increasing the concentration of charge carriers (Na^+ ions), the chemical components of the glass can also be adjusted to improve the electrical conductivity. Through an investigation of 58 samples, one must conclude that the increase in the electrical conductivity and decrease in the activation energy correspond to increasing Na_2O, AlF_3 and SO_3 content. Based on the relationships found within, Na_2O and SO_3 should be increased as much as possible in NAPFS glasses to improve conductivity and activation energy (until crystallization occurs). The correlation with AlF_3 content is more complex; AlF_3 depolymerizes the phosphate network significantly, therefore, raising AlF_3 in NAPFS glasses to increase the electrical conductivity is limited by the ratio of Na_2O/P_2O_5 in the glasses (since Q^0 and Q^1 species possess substantially higher binding energies between the Na^+ and NBOs).

5 Zusammenfassung

Das Ziel dieser Arbeit war die Erfassung des Zusammenhangs zwischen der Glasbildung, der Struktur und der Eigenschaften eines neuen Glassystems, den Fluoro-Sulfo-Phosphatgläsern. Insbesondere wurde hierbei der Einfluss der Glasstruktur auf die optischen Eigenschaften und die elektrische Leitfähigkeit untersucht. In diesem Projekt haben wir die Fluoro-Sulfo-Phosphatgläser in zwei Gruppen unterteilt: Der FPS-Serie $[(100–x–y)MF_n / xSr(PO_3)_2 / ySrSO_4$ $(x + y \leq 20\%$, M = Mg^{2+}, Ca^{2+}, Sr^{2+}, Al^{3+}) mit $F^- > P_2O_5 + SO_3]$ wurden als neues Trägermaterial für optisch aktive Kationen untersucht, während die NAPFS Serie $[(100–x–y)AlF_3 / xNaPO_3 / yNa_2SO_4$ $(x + y \geq 80\%)$, mit $F^- < P_2O_5 + SO_3]$, mit hohen Anteilen an Natriumionen und daher einer hohen ionischen Leitfähigkeit und einer geringen Aktivierungsenergie, als zukünftige Materialien für Solid-State Batterien erforscht wurden.

Raman-Spektren zeigen, dass die Glasstruktur der FPS-Serie (mit geringen Phosphatanteilen) von Pyro- und Orthophosphatgruppen geprägt ist, während NAPFS-Gläser (mit hohen Phosphatanteilen) nur geringe Anteile an depolymerisierten Phosphatgruppen und mehr Metaphosphatgruppen aufweist. ^{27}Al MAS NMR-Daten indizieren, dass überwiegend echsfach-koordinierte Aluminiumionen sowohl in FPS-, als auch in NAPFS-Gläsern vorherrschen. Terminale Fluoride $Al–F_T$, Brückenfluoride Al–F–Al und Al–O–P Bindungen sind in beiden Glassystemen vorhanden. Im Gegensatz dazu sind P–F-Bindungen nur in NAPFS-, aber nicht in FPS-Gläsern aufzufinden. Sulfat existiert überwiegend als isolierter SO_4^{2-}-Tetraeder, zusammen mit Netzwerkwandler-Kationen im Glasnetzwerk.

Um den Effekt von Multi-Anionen FPS-Gläsern besser zu verstehen, wurde eine Dotierung, Cu^{2+}, gewählt, mit der die lokale Anordnung im festen Trägermaterial anhand von UV-Vis - und EPR-Spektroskopie untersucht wurde. Die lokale Umgebung von Cu^{2+} in Fluoridphosphaten (FP) und Fluorid-Phosphat-Sulfaten (FPS) wurde mit der lokalen Umgebung von Cu^{2+} in Erdalkali-Metaphosphaten (MP) verglichen. In MP - Gläsern ist die Ligandenumgebung von Cu^{2+} durch eine verlängerte tetragonale Verzerrung in CuO_6-Oktaedern geprägt, in dem sich die asymmetrische, breite NIR-Absorptionsbande von Cu^{2+} mit steigender optischer Basizität von ca. 740 nm auf 880 nm verschiebt. Die Absorptionsbande wurde mit drei Gauss-Kurven gefittet, entsprechend den Übergängen von $d_{z^2} \rightarrow d_{x^2-y^2}$, $d_{xy} \rightarrow d_{x^2-y^2}$ und d_{xz}, $d_{yz} \rightarrow d_{x^2-y^2}$. Während in MP-Gläsern aber die Lage des Absorptionsmaximums stark von der Geometrie des koordinierten Cu^{2+} abhängt, ist diese

Korrelation in der FP- und FPS-Serie, welche Fluoride enthalten, deutlich schwächer ausgeprägt. Die Spektren waren hier deutlich geprägt durch die Anwesenheit von Pyrophosphat-gruppen (Q^1, mehr Q^1 führte zu einer Rotverschiebung der Absorptionsbande), Sulfatgruppen (SO_4^{2-}; höhere Anteile an Sulfaten führten zu einer Blauverschiebung) und Fluoriden (F; mehr F führte ebenfalls zu einer Blauverschiebung der Absorptionsbande). Die UV-Vis- Absorptionsspektren konnten am besten mit vier Beiträgen, unter der Berücksichtigung der d_{z^2}, d_{xy}, d_{yz} und d_{xz} zu $d_{x^2-y^2}$ Übergänge gefittet werden. Die Spektren der EPR-Messungen von MP zeigten, in Übereinstimmung mit den optischen Spektren, Hinweise auf Cu^{2+} in tetragonal verzerrter, oktaedrischer Koordinierung, und die von FP-und FPS-Gläsern mit rhomboedrischer Verzerrung.

FPS-Gläser mit hohem Anteil an Fluoriden weisen einen niedrigen Brechungsindex, eine außergewöhnliche partiale Dispersion und eine hohe Transmission vom UV- bis in den IR-Bereich auf. Da sie diverse Anionen enthalten, bieten sie eine extrem komplexe strukturelle Umgebung für optisch aktive Dotierungen. Dotierung mit Chromionen, z.B., führt zu einer breiten Photolumineszenz bei 734 nm und einer inhomogenen Verbreiterung der *R*-Linie bei 694 nm, jeweils hervorgerufen durch die $^4T_2 \rightarrow {}^4A_2$ und $^2E \rightarrow {}^4A_2$ Übergänge durch Cr^{3+}. Der Mechanismus der Lumineszenz wurde weiterhin auf Basis des Tanabe-Sugano-Diagramms analysiert. Durch Anpassung der chemischen Zusammensetzung ermöglicht die homogene Ausfällung von nanokristallinen Fluoridphasen den Wechsel zwischen Hochfeld- und Niedrigfeld-Konfiguration des Cr^{3+}. Durch die Einstellung der spezifischen Emissionseigenschaften wird dadurch der Weg Richtung FPS-basierten optischen Geräten, in Speziellem anpassbare Breitband-Faserverstärker und Laser geebnet.

Die elektrische Leitfähigkeit und die Aktivierungsenergie der NAPFS-Gläser hängt stark von der elektrostatischen Bindungsenergie der Ladungsträger (E_B) und die Verzerrungsenergie der Glasmatrix (E_S) ab. Daneben ermöglicht die Erhöhung der Konzentration an Ladungsträgern (Na^+-Ionen), d.h. die Anpassung der Glaszusammensetzung, die Anpassung der elektrischen Leitfähigkeit. Eine Studie an 58 Proben führte zu der Annahme, dass der Anstieg der elektrischen Leitfähigkeit und das Absenken der Aktivierungsenergie durch den Anstieg der Anteile an Na_2O, AlF_3 und SO_3 hervorgerufen wird. Auf der Annahme basierend sollte der Anteil an Na_2O und SO_3 im NAPFS-Glas so hoch wie möglich eingestellt werden (bis die Kristallisation eintritt), um die Leitfähigkeit und Aktivierungsenergie zu verbessern. Die Korrelation mit dem Anteil an AlF_3 ist etwas komplexer; AlF_3 depolymerisiert das Phosphatnetzwerk signifikant, wodurch der Anstieg der elektrischen Leitfähigkeit durch Anheben des AlF_3-Anteils im NAPFS-Glas durch das Verhältnis von Na_2O/P_2O_5 limitiert ist (da Q^0- und Q^1-Spezies eine höhere Bindungsenergie zwischen Na^+ und NBO aufweisen).

6 Bibliography

[1] A. K. Varshneya, in *Fundamentals of Inorganic Glasses*, Academic Press, San Diego, **1994**, pp. 13-25.

[2] K. J. Rao, *Structural Chemistry of Glasses*, Elsevier Science Ltd, The Netherlands, **2002**.

[3] A. Ponton, S. Warlus, P. Griesmar, *JCIS* **2002**, *249*, 209-216.

[4] K. L. Kearns, S. F. Swallen, M. D. Ediger, T. Wu, Y. Sun, L. Yu, *J. Phys. Chem. B* **2008**, *112*, 4934-4942.

[5] J. E. Shelby, in *Introduction to Glass Science and Technology*, 2nd ed., The Royal Society of Chemistry, UK, **2005**, pp. 7-25.

[6] X. Zhang, M. Cresswell, in *Inorganic Controlled Release Technology* (Eds.: X. Zhang, M. Cresswell), Butterworth-Heinemann, Boston, **2016**, pp. 17-55.

[7] M. D. Ediger, C. A. Angell, S. R. Nagel, *JPhCh* **1996**, *100*, 13200-13212.

[8] H. A. A. Sidek, I. T. Collier, R. N. Hampton, G. A. Saunders, B. Bridge, *Philosophical Magazine B-Physics of Condensed Matter Statistical Mechanics Electronic Optical and Magnetic Properties* **1989**, *59*, 221-232.

[9] W. Vogel, *Glass Chemistry*, 2nd ed., Springer-Verlag, **1994**.

[10] R. J. Kirkpatrick, R. K. Brow, *SSNMR* **1995**, *5*, 9-21.

[11] R. K. Brow, *J. Non-Cryst. Solids* **2000**, *263*, 1-28.

[12] D. S. Brauer, in *Bio-Glasses: An Introduction* (Eds.: J. Jones, A. Clare), John Wiley and Sons, Ltd., **2012**, p. 45.

[13] D. Ehrt, W. Seeber, *J. Non-Cryst. Solids* **1991**, *129*, 19-30.

[14] D. Ehrt, M. Carl, T. Kittel, M. Muller, W. Seeber, *J. Non-Cryst. Solids* **1994**, *177*, 405-419.

[15] W. Seeber, D. Ehrt, *Ber Bunsen Phys Chem* **1996**, *100*, 1593-1595.

[16] D. Ehrt, *Curr Opin Solid St M* **2003**, *7*, 135-141.

[17] F. X. Gan, *J. Non-Cryst. Solids* **1995**, *184*, 9-20.

[18] J. Lucas, F. Smektala, J. L. Adam, *J. Fluorine Chem.* **2002**, *114*, 113-118.

[19] J. J. Videau, J. Portier, B. Piriou, *J. Non-Cryst. Solids* **1982**, *48*, 385-392.

[20] D. Ehrt, *Structure and properties of fluoride phosphate glasses, Vol. 1761*, SPIE, **1993**.

[21] D. Möncke, D. Ehrt, L. L. Velli, C. P. E. Varsamis, E. I. Kamitsos, *Phys. Chem. Glasses* **2005**, *46*, 67-71.

[22] L. L. Velli, C. P. E. Varsamis, E. I. Kamitsos, D. Möncke, D. Ehrt, *Phys. Chem. Glasses* **2005**, *46*, 178-181.

[23] D. Möncke, D. Ehrt, L. L. Velli, C. P. E. Varsamis, E. I. Kamitsos, S. Elbers, H. Eckert, *Phys. Chem. Glasses: Eur. J. Glass Sci. Technol., Part B* **2007**, *48*, 399-402.

[24] L. L. Velli, C. P. E. Varsamis, E. I. Kamitsos, D. Moncke, D. Ehrt, *Phys. Chem. Glasses: Eur. J. Glass Sci. Technol., Part B* **2008**, *49*, 182-187.

[25] F. L. Galeener, J. C. Mikkelsen, *SSCom* **1979**, *30*, 505-510.

[26] J. J. Hudgens, S. W. Martin, *J. Am. Ceram. Soc.* **1993**, *76*, 1691-1696.

[27] R. K. Brow, D. R. Tallant, J. J. Hudgens, S. W. Martin, A. D. Irwin, *J. Non-Cryst. Solids* **1994**, *177*, 221-228.

[28] K. Meyer, A. Barz, D. Stachel, *J. Non-Cryst. Solids* **1995**, *191*, 71-78.

[29] U. Hoppe, G. Walter, A. Barz, D. Stachel, A. C. Hannon, *J. Phys.: Condens. Matter* **1998**, *10*, 261-270.

[30] K. Suzuya, D. L. Price, C. K. Loong, S. W. Martin, *J. Non-Cryst. Solids* **1998**, *232*, 650-657.

[31] U. Hoppe, *J. Non-Cryst. Solids* **1996**, *195*, 138-147.

[32] F. Liebau, in *Structure and Bonding in Crystals, Vol. 2* (Eds.: M. O'Keeffe, A. Navrotsky), Academic Press, USA, **1981**, pp. 197-232.

[33] R. K. Brow, C. A. Click, T. M. Alam, *J. Non-Cryst. Solids* **2000**, *274*, 9-16.

[34] D. Ehrt, *Phys. Chem. Glasses: Eur. J. Glass Sci. Technol., Part B* **2015**, *56*, 217-234.

[35] H. Bradtmuller, L. Zhang, C. C. de Araujo, H. Eckert, D. Möncke, D. Ehrt, *J. Phys. Chem. C* **2018**, *122*, 21579-21588.

[36] S. Lee, S. Hwang, M. Cha, H. Shin, H. Kim, *JPCS* **2008**, *69*, 1498-1500.

[37] Y. H. Elbashar, *Process Appl Ceram* **2015**, *9*, 169-173.

[38] D. K. Shen, K. T. Wang, X. H. Huang, Y. X. Chen, J. H. Bai, *J. Non-Cryst. Solids* **1982**, *52*, 151-158.

[39] S. Suresh, J. C. Babu, V. Chandramouli, *Phys. Chem. Glasses* **2005**, *46*, 27-30.

[40] G. Giridhar, M. Rangacharyulu, R. V. S. S. N. Ravikumar, P. S. Rao, *Journal of Materials Science & Technology* **2009**, *25*, 531-534.

[41] N. S. Rao, S. Bale, M. Purnima, C. Srinivasu, M. A. Samee, K. S. Kumar, S. Rahman, *Physica B-Condensed Matter* **2009**, *404*, 1785-1789.

[42] V. Kamalaker, G. Upender, M. Prasad, V. C. Mouli, *Indian J Pure Ap Phy* **2010**, *48*, 709-715.

[43] V. N. Padmini, J. L. Kumari, J. S. Kumar, S. Cole, *Phys. Chem. Glasses: Eur. J. Glass Sci. Technol., Part B* **2011**, *52*, 167-170.

[44] B. Sumalatha, I. Omkaram, T. R. Rao, C. L. Raju, *J. Non-Cryst. Solids* **2011**, *357*, 3143-3152.

[45] K. Srinivasulu, I. Omkaram, H. Obeid, A. S. Kumar, J. L. Rao, *Physica B-Condensed Matter* **2012**, *407*, 4741-4748.

[46] B. Srinivas, R. V. Kumar, A. Hameed, G. Ramadevudu, M. N. Chary, M. Shareefuddin, *Optik* **2018**, *156*, 289-296.

[47] B. S. Bae, M. C. Weinberg, *J. Non-Cryst. Solids* **1994**, *168*, 223-231.

[48] A. Goldstein, M. Vulfson, *J. Am. Ceram. Soc.* **2007**, *90*, 3680-3682.

[49] L. G. Back, *Phys. Chem. Glasses: Eur. J. Glass Sci. Technol., Part B* **2015**, *56*, 8-14.

[50] Z. Y. Yao, D. Moncke, E. I. Kamitsos, P. Houizot, F. Celarie, T. Rouxel, L. Wondraczek, *J. Non-Cryst. Solids* **2016**, *435*, 55-68.

[51] B. S. Reddy, S. Buddhudu, *Bull. Mater. Sci.* **2007**, *30*, 481-486.

[52] M. Peteanu, I. Ardelean, S. Filip, F. Ciorcas, *J Mater Sci-Mater El* **1996**, *7*, 165-170.

[53] S. I. Andronenko, R. R. Andronenko, A. V. Vasil'ev, O. A. Zagrebel'nyi, *Glass Phys. Chem* **2004**, *30*, 230-235.

[54] B. V. Padlyak, W. Wojtowicz, V. T. Adamiv, Y. V. Burak, I. M. Teslyuk, *AcPPA* **2010**, *117*, 122-125.

[55] A. Drzewiecki, B. Padlyak, V. Adamiv, Y. Burak, I. Teslyuk, *Nukleonika* **2013**, *58*, 379-385.

[56] H. Tuller, in *Springer Handbook of Electronic and Photonic Materials* (Eds.: S. Kasap, P. Capper), Springer International Publishing, Cham, **2017**, pp. 1-1.

[57] H. Gerischer, in *The CRC Handbook of Solid State Electrochemistry* (Eds.: P. J. Gellings, H. J. M. Bouwmeester), CRC Press, Inc, USA, **1997**.

[58] K. F. Brennan, *Introduction to Semiconductor Devices: For Computing and Telecommunications Applications*, Cambridge University Press, Cambridge, **2005**.

[59] R. A. Mckee, *Solid State Ion.* **1981**, *5*, 133-136.

[60] in *Diffusion in Solids: Fundamentals, Methods, Materials, Diffusion-Controlled Processes*, Springer Berlin Heidelberg, Berlin, Heidelberg, **2007**, pp. 55-67.

[61] J. X. Zhu, Q. He, X. J. Kuang, S. Ye, *J. Mater. Chem. C* **2019**, *7*, 9211-9218.

[62] C. Calahoo, J. Petrovic, Q. H. Le, U. Werner-Zwanziger, J. Zwanziger, L. Wondraczek, *Front Mater* **2019**, *6*.

[63] D. Massiot, F. Fayon, M. Capron, I. King, S. Le Calve, B. Alonso, J. O. Durand, B. Bujoli, Z. H. Gan, G. Hoatson, *Magn. Reson. Chem.* **2002**, *40*, 70-76.

[64] O. Cozar, I. Ardelean, V. Simon, L. David, N. Vedean, V. Mih, *Appl. Magn. Reson.* **1999**, *16*, 473-480.

[65] S. S. Sastry, B. R. V. Rao, *Physica B-Condensed Matter* **2014**, *434*, 159-164.

[66] B. N. Nelson, G. J. Exarhos, *J. Chem. Phys.* **1979**, *71*, 2739-2747.

[67] W. A. Dollase, L. H. Merwin, A. Sebald, *J. Solid State Chem.* **1989**, *83*, 140-149.

[68] S. Prabakar, R. M. Wenslow, K. T. Mueller, *J. Non-Cryst. Solids* **2000**, *263*, 82-93.

[69] N. Da, O. Grassme, K. H. Nielsen, G. Peters, L. Wondraczek, *J. Non-Cryst. Solids* **2011**, *357*, 2202-2206.

[70] D. Möncke, S. Sirotkin, E. Stavrou, E. I. Kamitsos, L. Wondraczek, *J. Chem. Phys.* **2014**, *141*.

[71] F. G. K. Baucke, J. A. Duffy, *Phys. Chem. Glasses* **1993**, *34*, 158-163.

[72] R. Juza, H. Seidel, Tiedeman.J, *Angew Chem Int Edit* **1966**, *5*, 85-&.

[73] R. F. Bartholomew, R. E. Tischer, *J. Am. Ceram. Soc.* **1970**, *53*, 130-+.

[74] A. Duran, J. M. F. Navarro, *Phys. Chem. Glasses* **1985**, *26*, 126-131.

[75] F. A. Cotton, G. Wilkinson, C. A. Murillo, M. Bochmann, *Advanced Inorganic Chemistry*, 6th ed., John Wiley & Son, Inc., **1999**.

[76] B. Kozlevcar, P. Segedin, *Croat. Chem. Acta* **2008**, *81*, 369-379.

[77] H. M. Zhang, X. Wan, *J. Struct. Chem.* **2013**, *54*, 26-31.

[78] R. Aasa, P. Aisen, *J. Biol. Chem.* **1968**, *243*, 2399-&.

[79] A. Zabel, A. Winter, A. Kelling, U. Schilde, P. Strauch, *Int J Mol Sci* **2016**, *17*.

ANRECHNUNG DER PUBLIKATIONSÄQUIVALENTE

Publikation 1: Formation, structure and properties of fluoro-sulfo-phosphate poly-anionic glasses, J. Non-Cryst. Solids 477 (2017) 58-72.

	Autor 1: Q. H. Le	Autor 2: T. Palenta	Autor 3: O. Benzine	Autor 4: K. Griebenow	Autor 5: R. Limbach	Autor 6: E. I. Kamitsos	Autor 7: L. Wondraczek
Konzeption des Forschungsansatzes	x						
Planung der Untersuchungen	x						
Datenerhebung	x						
Datenanalyse und Interpretation	x						
Schreiben des Manuskriptes	x						
Vorschlag Anrechnung Publikationsäquivalente	1						

Publikation 2: Fluoride-sulfophosphate glasses as hosts for broadband optical amplification through transition metal activators, J. Mater. Chem. C, 2017, 5, 7969-7976.

	Autor 1: W. Wang	Autor 2: Q. H. Le	Autor 3: Q. Zhang	Autor 4: L. Wondraczek
Konzeption des Forschungsansatzes		x		
Planung der Untersuchungen		x		
Datenerhebung		x		
Datenanalyse und Interpretation		x		
Schreiben des Manuskriptes				
Vorschlag Anrechnung Publikationsäquivalente		1		

Publikation 3: Ni-doped fluorosulfates with broad NIR luminescence, Journal of Luminescence 210 (2019) 457–463.

	Autor 1: W. Wang	Autor 2: R. Zhou	Autor 3: Q. H. Le	Autor 4: Q. Zhang	Autor 5: L. Wondraczek
Konzeption des Forschungsansatzes			x		
Planung der Untersuchungen			x		
Datenerhebung					
Datenanalyse und Interpretation					
Schreiben des Manuskriptes					
Vorschlag Anrechnung Publikationsäquivalente			0.3		

Publikation 4: Structural relaxation in polyanionic sodium fluorophosphate glasses, Front Mater 2019, 6, 165.

	Autor 1: C. Calahoo	Autor 2: J. Petrovic	Autor 3: Q. H. Le	Autor 4: U. W. Zwanziger	Autor 5: J. Zwanziger	Autor 6: L. Wondraczek
Konzeption des Forschungsansatzes			x			
Planung der Untersuchungen			x			
Datenerhebung						
Datenanalyse und Interpretation						
Schreiben des Manuskriptes						
Vorschlag Anrechnung Publikationsäquivalente			0.5			

Publikation 5: Spectroscopic properties of Cu^{2+} in alkaline earth metaphosphate, fluoride-phosphate and fluoride-phosphate-sulfate glasses, J. Non-Cryst. Solids: X 2019, 4, 100037

	Autor 1: Q. H. Le	Autor 2: C. Friebe	Autor 3: W. Wang	Autor 4: L. Wondraczek
Konzeption des Forschungsansatzes	x			
Planung der Untersuchungen	x			
Datenerhebung	x			
Datenanalyse und Interpretation	x			
Schreiben des Manuskriptes	x			
Vorschlag Anrechnung Publikationsäquivalente	1			

Publikation 6: Optimization of electrical conductivity in the Na_2O-P_2O_5-AlF_3-SO_3 glasse system, J. Am. Ceram. Soc. 2019, submitted

	Autor 1: Q. H. Le	Autor 2: Y. Xia	Autor 3: C. Calahoo	Autor 4: L. Wondraczek
Konzeption des Forschungsansatzes	x			
Planung der Untersuchungen	x			
Datenerhebung	x			
Datenanalyse und Interpretation	x			
Schreiben des Manuskriptes	x			
Vorschlag Anrechnung Publikationsäquivalente	1			

Erklärung zu den Eigenanteilen der Promovendin/des Promovenden sowie der weiteren Doktorandinnen/Doktoranden als Co-Autorinnen/-Autoren an den Publikationen und Zweitpublikationsrechten bei einer kumulativen Dissertation

Für alle in dieser kumulativen Dissertation verwendeten Manuskripte liegen die notwendigen Genehmigungen der Verlage ("Reprint permissions") für die Zweitpublikation vor.

Die Co-Autorinnen/-Autoren der in dieser kumulativen Dissertation verwendeten Manuskripte sind sowohl über die Nutzung, als auch über die oben angegebenen Eigenanteile der weiteren Doktorandin-nen/Doktoranden als Co-Autorinnen/-Autoren an den Publikationen und Zweitpublikationsrechten bei einer kumulativen Dissertation informiert und stimmen dem zu *(es wird empfohlen, diese grundsätzliche Zustimmung bereits bei Einreichung der Veröffentlichung einzuholen bzw. die Gewichtung der Anteile parallel zur Einreichung zu klären).*

Die Anteile der Promovendin/des Promovenden sowie der weiteren Doktorandinnen/Doktoranden als Co-Autorinnen/Co-Autoren an den Publikationen und Zweitpublikationsrechten bei einer kumulativen Dissertation sind in der Anlage aufgeführt.

Quyen Huyen Le 25. November, 2019 Jena ________________

Ich bin mit der Abfassung der Dissertation als publikationsbasierte Dissertation, d.h. kumulativ, einver-standen und bestätige die vorstehenden Angaben

Prof. Dr.-Ing. Lothar Wondraczek 25. November, 2019 Jena ________________

SELBSTSTÄNDIGKEITSERKLÄRUNG

Ich erkläre, dass ich die vorliegende Arbeit selbstständig und nur unter Zuhilfenahme der angegebenen Hilfsmittel, persönlichen Mitteilungen und Quellen angefertigt habe. Weder diese Arbeit, noch die darin enthaltenen Abschnitte wurden zuvor als Dissertation an dieser oder einer anderen Hochschule eingereicht.

Jena, 25. November, 2019

Quyen Huyen Le